AN EXPERIMENTAL AND ANALYTICAL INVESTIGATION OF FLOW BOILING HEAT TRANSFER UNDER MICROGRAVITY CONDITIONS

BY

MASAKI MISAWA

A DISSERTATION PRESENTED TO THE GRADUATE SCHOOL
OF THE UNIVERSITY OF FLORIDA IN PARTIAL FULFILLMENT
OF THE REQUIREMENTS FOR THE DEGREE OF
DOCTOR OF PHILOSOPHY

UNIVERSITY OF FLORIDA

1993

UNIVERSITY OF FLORIDA LIBRARIES

To my parents, Kiyoo Misawa and Kayoko Misawa, for their
unconditional suport.
And to my fiance, Masako Imai, for her incomparable love.

ACKNOWLEDGEMENTS

The author would like to express his greatest appreciation for the insightful guidance, criticisms and appraisals, and most of all, incessant encouragement and support provided by his academic advisor, Professor Samim Anghaie. Through his enthusiasm and commitment to this project, an opportunity to perform the Learjet experiment was given, for which the author had been wishing since the beginning of this study. The author is indebted to Professor Nils J. Diaz, the director of Innovative Nuclear Space Power Institute (INSPI), for financial and spiritual support for this project. The technical assistance and discussions provided by Assistant Professor James F. Klausner in the Department Mechanical Engineering is sincerely acknowledged. The author also expresses great appreciation to his previous supervisor in the University of Tokyo, Professor Shunsuke Kondo, who steered the author to this study and continuously encouraged even after the author left for the United States.

The assistance and advice from Dr. Shintaro Enya and Dr. Toshikazu Yano in the Research Institute in Ishikawajima-Harima Heavy Industries Co., Ltd. are greatly appreciated. Upon conducting the drop tower experiments, Mr. Sugawara and Mr. Tanaka provided invaluable assistance even after hours and sometimes on weekends, which is greatfully acknowledged.

The numerous technical and nontechnical discussions with Mr. James White, Dr. Yoichi Watanabe, Dr. Se-wong Chung, Dr. Ratan Kumar, and Dr. Engin Erkman were unexceptionably valuable and contributed to the accomplishment of this work in various ways. Mr. Gary Chen helped the computational work of this study. His contribution is greatly appreciated. The assistance and friendship offered by the graduate students and secretaries in the INSPI were all precious and unforgettable.

The flight experiment was conducted in the Lewis Research Center (LeRC), National Aeronautics and Space Administration (NASA) on September 16, 1992. Without the assistance and advice from Mr. Eric Neumann from NASA LeRC, successful completion of the flight experiment would not have been possible.

Lastly, the author wishes to express a special thanks to his fiancee, Masako Imai, for her continual support, cheering, and patience throughout the program. Also, she suggested the air-driven piston system for this work. She provided the author with great comfort and relief during his years at INSPI.

TABLE OF CONTENTS

page

ACKNOWLEDGEMENTS iii

LIST OF TABLES vii

LIST OF FIGURES ix

KEY TO SYMBOLS xiv

ABSTRACT xviii

CHAPTER 1 INTRODUCTION 1

- 1.1 Background 1
- 1.2 Scope of the Study 4

CHAPTER 2 PREVIOUS EFFORTS FOR MICROGRAVITY BOILING . . 7

- 2.1 Pool Boiling in Microgravity 8
- 2.2 Forced Convective Boiling in Microgravity . . 24

CHAPTER 3 EXPERIMENTAL DESIGN AND PROCEDURE 34

- 3.1 Drop Tower Experiment 34
- 3.2 Learjet Flight Experiment 42

CHAPTER 4 FLOW PATTERN, VOID FRACTION, AND PRESSURE DROP UNDER MICROGRAVITY CONDITIONS 56

- 4.1 Observation of Flow Patterns 57
- 4.2 Void Fraction 79
- 4.3 Velocity and Temperature Profiles 96
- 4.4 Pressure Drop 114

CHAPTER 5 GRAVITY EFFECTS ON SUBCOOLED BOILING HEAT TRANSFER 128

- 5.1 Flight Experiment Results 128
- 5.2 Forced Convective Single-Phase Flow 163
- 5.3 Onset of Nucleate Boiling 170
- 5.4 Subcooled Boiling Heat Transfer 181
- 5.5 Gravity Effects on Boiling Mechanisms . . . 219

CHAPTER 6 SUMMARY AND RECOMMENDATIONS 229

6.1 Discussion 229
6.2 Conclusions 238
6.3 Recommendations 240

APPENDICES 248

A STATIC PRESSURE CALCULATION 248
B ERROR ANALYSIS 252
C THERMAL PROPERTIES OF FREON 113 258

REFERENCES 269

BIOGRAPHICAL SKETCH 275

LIST OF TABLES

Table 2-1 Heat transfer data for nucleate boiling from an electrically heated wire[8] . . 9

Table 2-2 Effects of gravity on heat transfer mechanisms in pool boiling 15

Table 3-1 Channel assignments on the multiplexer cards 54

Table 4-1 Test conditions for flow pattern observation in drop tower experiments . 58

Table 4-2 Vapor volume fraction and flow patterns in drop tower experiments 65

Table 4-3 Computed wall shear stresses and wall temperatures of laminar two-phase flow for Case D0FP4. 106

Table 4-4 Computed wall shear stresses and wall temperatures of turbulent two-phase flow for Case F1035 112

Table 4-5 Test conditions for pressure drop measurement in drop tower experiments 117

Table 5-1 Learjet flight experiment conditions . 129

Table 5-2 Summary of experimental conditions for Learjet flight experiments 131

Table 5-3 Critical radii for nucleation and predicted wall superheats at the ONB . 176

Table 5-4 Boiling and evaporation heat fluxes at TW15 estimated by Chen's and Larsen-Tong's methods 218

Table 5-5 Fractions of subcooled heat transfer components under 1.0g and 0.01g for Case F1035 at TW15 (z=0.4375m) 221

Table B-1 Values and confidence intervals of measrued quantities 253

LIST OF FIGURES

Figure 2-1 Boiling curves obtained by Merte and Clark under microgravity conditions[6] . 11

Figure 2-2 Pool boiling curves for water under normal and microgravity conditions. (a) Total heat flux, and (b) Latent heat transport[20] 16

Figure 2-3 Boiling curves in subcooled Freon 113 under normal and microgravity conditions[21] 18

Figure 2-4 Subcooled pool boiling of Freon 113 under normal and microgravity conditions[21] . 19

Figure 2-5 Critical heat flux as a function of inlet velocity for upward and downward flow of liquid nitrogen in a 0.505" diameter tube[11] 28

Figure 3-1 Schematic diagram of a drop tower flow boiling loop 35

Figure 3-2 Test section used in drop tower experiments 37

Figure 3-3 A 15m drop tower facility and flow boiling loop mounted on a drop module . 40

Figure 3-4 Schematics of Learjet flight research instrument 43

Figure 3-5 Flow boiling loop used in the Learjet flight experiment 45

Figure 3-6 Test section with thermocouples and pressure transducers 46

Figure 3-7 A 0.178mO.D. air-driven plastic piston . 49

Figure 3-8 Air driving pressure vs. liquid flow rate for the piston system 50

Figure 3-9 Electrical power and interconnect diagram 53

Figure 4-1 Dominant forces under the conditions of drop tower experiments 60

Figure 4-2 Characteristic flow patterns in a vertical tube under various acceleration levels 61

Figure 4-3 Flow pattern transitions during the free fall 66

Figure 4-4 Flow pattern transitions on the Dukler flow regime map 76

Figure 4-5 Binary images of vapor phase distributions in the radial directions . 80

Figure 4-6 Local flow conditions near the bubble detachment point under microgravity conditions. (a) Vapor-phase distribution and (b) Bubble behavior after detachment 85

Figure 4-7 Void fraction profiles predicted by the drift flux model 89

Figure 4-8 Void fraction profiles predicted by Sekoguchi's model 90

Figure 4-9 Void fraction profiles predicted by the slip model 91

Figure 4-10 Two-phase flow properties under 1.0g and 0.02g for Case D0FP4 calculated by Sato's method 102

Figure 4-11 Two-phase flow properties under 1.0g and 0.02g for Case F1035 calculated by Sato's method 109

Figure 4-12 Pressure drop measurement along a vertical test section in drop tower experiments 115

Figure 4-13 Total pressure drops measured in drop tower experiments. L=0.5m, D=5x5mm, q"w=2.93kW/m^2 119

Figure 4-14 Total pressure drops in a vertical tube under 1.0g and 0.02g conditions . . . 120

Figure 4-15 Influence of gravity on pressure drop components in a vertical tube 124

Figure 4-16 Frictional pressure drop gradient in a vertical tube under 1.0g and 0.02g conditions 126

Figure 5-1 Acceleration histories recorded by an on-board accelometer during the Learjet flight experiment 132

Figure 5-2 Variation of flow properties for Case F1015 during the flight experiment . . 136

Figure 5-3 Variation of flow properties for Case F1020 during the flight experiment . . 143

Figure 5-4 Variation of flow properties for Case F1035 during the flight experiment . . 150

Figure 5-5 Flow boiling evolution in a vertical pipe in the subcooled region 162

Figure 5-6 Single-phase heat transfer in a vertical tube in Learjet flight experiments . . 167

Figure 5-7 Liquid and vapor equilibrium temperature profiles at the onset of nucleate boiling 172

Figure 5-8 Onset of nucleate boiling measured in the Learjet flight experiment. 174

Figure 5-9 Liquid and vapor equilibrium temperatures near the heating surface 178

Figure 5-10 Thermal equilibrium qualities for the Learjet flight experiment 186

Figure 5-11 Actual quality profiles calculated by the modified Sekoguchi's method 188

Figure 5-12 Void fraction profiles predicted by Sekoguchi's and Ahmad's methods . . . 189

Figure 5-13 Growth of superheated layer and bubble diameter in the axial direction . . . 191

Figure 5-14 Variation of forced convective factor under microgravity conditions 193

Figure 5-15 Increase in boiling heat flux in the flow direction 195

Figure 5-16 Boiling curves calculated by Rohsenow's correlation under various gravity conditions 198

Figure 5-17 Schematic diagram of the heat balance for a single bubble in subcooled flow . . 204

Figure 5-18 Typical bubble growth predicted by the mass transport model for Case F1035 . 209

Figure 5-19 Contribution of evaporation heat flux predicted by Larsen-Tong's correlation 215

Figure 5-20 Contribution of boiling heat flux predicted by Chen's correlation . . . 217

Figure 5-21 Ratios of heat flux components for Case F1035 predicted by the present analysis 223

Figure 5-22 Two-phase flow heat transfer rate measured under normal(1.0g) and microgravity (0.01g) conditions . . . 225

Figure 6-1 Transparent annular flow channel for observation of vapor phase evolution . 236

Figure 6-2 A proposed two-phase flow channel for measurement of bubble-induced heat transfer 238

Figure A-1 Static pressure balance in a varying gravity field 241

Figure B-1 Variation of liquid density as a function of pressure 282

Figure B-2 Variation of vapor density as a function of pressure 283

Figure B-3 Variation of latent heat as a function of pressure 284

Figure B-4 Variation of liquid specific heat as a function of pressure 285

Figure B-5 Variation of liquid viscosity as a function of pressure 286

Figure B-6 Variation of liquid thermal conductivity as a function of pressure 287

Figure B-7 Variation of thermal diffusivity as a function of pressure 288

Figure B-8 Variation of Prandtl number as a function of pressure 289

Figure B-9 Variation of Jakob number as a function of pressure 290

Figure B-10 Variation of Ja*a^0.5 as a function of pressure 291

KEY TO SYMBOLS

a	Thermal diffusivity	[m^2/s]
A_T	Total heat transfer area	[m^2]
b_h	Ratio of the superheated layer thickness to bubble height	[-]
C_0	Distribution parameter	[-]
C_1	Condensation parameter	[-]
c_{pl}	Specific heat of liquid	[J/kg/K]
d_0	Initial thickness of microlayer	[m]
D	Channel diameter	[m]
g	Gravitational constant	[m/s^2]
g_0	Normal gravitational acceleration	[m/s^2]
G	Mass flux	[$kg/m^2/s$]
h_{bo}	Boiling heat transfer coefficient	[$W/m^2/K$]
h_{fc}	Forced convective heat transfer coefficient	[$W/m^2/K$]
h_{fg}	Latent heat of vaporization	[J/kg]
h_{f0}	Single-phase heat transfer coefficient	[$W/m^2/K$]
h_{TP}	Two-phase heat transfer coefficient	[$W/m^2/K$]
j	Volumetric flux	[m/s]
k	Thermal conductivity	[W/m/K]
L	Total test section length	[m]
m	Mass transfer rate	[kg/s]

M	Molecular weight	[kg/mol]
N	Number of nucleation sites	[-]
P	Pressure	[Pa]
q''_w	Wall heat flux	[W/m^2]
q''_{ev}	Evaporation heat flux	[W/m^2]
q''_{ag}	Bubble agitation heat flux	[W/m^2]
q''_{con}	Condensation heat flux	[W/m^2]
q''_{fc}	Forced convective heat flux	[W/m^2]
r	Radius	[m]
R	Radius of flow channel	[m]
r_{crit}	Critical radius	[m]
R_i	Radius of bubble base	[m^2]
R_{113}	Gas constant of Freon 113 (=44.5)	[J/kg·K]
s	Slip ratio	[-]
T_d	Bulk temperature at bubble detachment	[K]
T_f	Bulk temperature	[K]
T_{fi}	Inlet bulk temperature	[K]
T_g	Vapor temperature	
T_i	Liquid-vapor interface temperature	[K]
T_s	Saturation temperature	[K]
T_w	Wall temperature	[K]
ΔT_{sat}	Superheat	[K]
ΔT_{sub}	Subcooling	[K]
ΔT^*	Dimensionless temperature $(=(T_s-T_f)/(T_s-T_d))$	[-]
u_f	Liquid velocity	[m/s]

u_{gj}	Drift velocity	[m/s]
v_f	Liquid specific volume	[m^3/kg]
v_g	Vapor specific volume	[m^3/kg]
v_{fg}	Relative specific volume (= $v_g - v_f$)	[m^3/kg]
x	Thermal equilibrium quality	[-]
x_a	Actual quality	[-]
X_{lt}	Martinelli parameter	[-]
y	Distance from the wall	[m]
y^*	Dimensionless distance (= y/R)	[-]
z	Distance from inlet	[m]
z_{sc}	Significant boiling length	[m]

Greek symbols

α	Void fraction	[-]
β	Expansion coefficient	[-]
δ_T	Dimensionless superheated layer thickness	[-]
ϵ	Ratio of bubble agitation heat flux to evaporation heat flux	[-]
ϵ'	Turbulent eddy diffusivity	[m^2/s]
ϵ''	Bubble-induced eddy diffusivity	[m^2/s]
η	Evaporation area ratio ($=\pi R_i^2 \cdot N/A_T$)	[-]
λ_0	Interface wave length	[m]
μ	Viscosity	[Pa·s]
ν	Kinematic viscosity	[m^2/s]
ρ	Density	[kg/m^3]
σ	Surface tension	[N/m]

τ	Shear stress	$[N/m^2]$
ϕ	Constant defined in Eq.(5-37)	[-]
φ	Superheat ratio $=\Delta T_{sat}/(\Delta T_{sat}+\Delta T_{sub})$	[-]

Dimensionless numbers

Bo	Boiling number	$q''/(h_{fg}\cdot G)$, or
Bo	Bond number	$(\rho_f-\rho_g)g\cdot D/(\sigma/D)$
Fr	Froude number	$u_{f0}{}^2/(g\cdot D)$
Fr^*	Modified Froude number	$G\cdot x_a/[(\rho_f-\rho_g)\rho_g\cdot D]^{1/2}$
Gr	Grashof number	$D^3\cdot\rho^2{}_f\cdot g\cdot\beta\cdot\Delta T/\mu_f$
Ja	Jakob number	$\Delta T\cdot c_{pl}\cdot\rho_f/(h_{fg}\cdot\rho_g)$
Nu	Nusselt number	$h\cdot D/k$
Pr	Prandtl number	a/ν
Re	Reynolds number	$u_{f0}\cdot D/\mu_f$
We	Weber number	$\rho_f\cdot u_{f0}{}^2/(\sigma/D)$

Abstract of Dissertation Presented to the Graduate School
of the University of Florida in Partial Fulfillment of the
Requirements for the Degree of Doctor of Philosophy

AN EXPERIMENTAL AND ANALYTICAL INVESTIGATION OF FLOW BOILING HEAT TRANSFER UNDER MICROGRAVITY CONDITIONS

By

Masaki Misawa

August 1993

Chairperson: Dr. Samim Anghaie
Major Department: Nuclear Engineering Sciences

An experimental and analytical investigation of saturated and subcooled flow boiling under microgravity conditions was conducted to study gravity effects on two-phase flow boiling heat transfer. Optical measurement of Freon 113 two-phase flow patterns in a 0.5m long, 5mm×5mm vertical channel uniformly heated with transparent conductive films identified bubbly, slug, and annular flow under microgravity conditions. A significantly different void distribution was observed in bubbly flow. Velocity and temperature distributions in the radial direction in bubbly flow were calculated by Sato and Sadatomi's method. The distributions were changed by the increased void fraction and coalescence of bubbles under microgravity conditions. Analysis of experimental results showed that the bubble-induced turbulence, accounting for a large fraction of heat transfer in normal gravity, became smaller under microgravity conditions. Effects of gravity on bubble agitation were less pronounced in turbulent flow than in laminar flow because of the inherent turbulence. A substantial increase in void fraction resulted in an increase in the accelerational and frictional pressure drops in the low-quality range, suggesting that the pressure drop in the subcooled region is also significant in microgravity.

Motivated by the observed changes in flow and heat transfer rates in the subcooled region under microgravity conditions, the author designed, fabricated, and tested an additional forced convective boiling rig aboard NASA's low-gravity Learjet. A 0.5m long, 11.3mm diameter vertical copper tube was heated uniformly with a constant heat flux of 23.9kW/m^2. Freon 113 in the once-through flow line was pumped by air-driven pistons to reduce the system transient time. An increase in wall superheats observed near the test section exit during the 18 seconds of microgravity implies a decrease in bulk convection in the absence of buoyancy force. The heat transfer analysis showed that the reduced gravitational acceleration affected the subcooled two-phase heat transfer through an increase in void fraction and stagnation of coalesced bubbles. The contribution of evaporation heat transfer was small in the low heat-flux range. The overall two-phase flow heat transfer coefficient in vertical upward flow was decreased under microgravity conditions.

CHAPTER 1
INTRODUCTION

1.1 Background

Heat transport is an essential issue associated with all large-power systems used in space where environment is characterized by low-gravity and vacuum. The heat transport process in space is divided into two categories: a) heat transport from spacecraft to environment, and b) heat transport inside the spacecraft. For heat rejection from the spacecraft, thermal radiation is the only method available in space. This problem has been intensively discussed since the early stage of space development and several new versions of radiator systems have been proposed[1][2].

Heat transport and fluid behavior inside the spacecraft are practically identical to ground-based systems when single-phase flow media are employed. However, as heat transport requirements grow to the 30 kilowatt-meters level and beyond[3], the existing single-phase transport systems become inefficient due to significant temperature drop along the flow direction. Temperature drop is highly undesirable for the radiator-dependent systems since the emissive power decreases proportional to the 4th power of radiator temperature. Although passive flow recirculation devices such as heat-pipes are the alternatives, they are not applicable to the transport capacities in excess of 50 kilowatt-meters[3]. The circulating two-phase flow involving phase change is capable of transporting thermal energy with small temperature drops. Because of unexpected flow behavior in the absence of gravity, however, the use of two-phase flow has been intentionally avoided regardless of its favorable features. Analysis of two-phase flow under microgravity conditions is formidable because most of the correlations derived in normal-gravity environments are empirical in nature. These correlations cannot be applied to microgravity conditions without considering the gravity effects on heat transfer mechanisms. The gravity term appearing in the ground-based correlations needs to be regarded as another variable under microgravity conditions.

The experimental efforts to investigate the effects of gravity on boiling heat transfer began in the middle 1950's when the need for scientific and practical applications of fluid technology in space became increasingly obvious. Siegel[4] published a comprehensive review of low-gravity effects on heat transfer that encompasses the efforts conducted before 1966. His review covers the four fundamental areas of heat transfer; namely, free convection, pool boiling, forced-convection boiling, and forced-convection condensation.

For pool boiling in saturated liquids, quite a few experimental data was collected under microgravity conditions[5][6][7]. Siegel[4] reported that although gravity had little effect on nucleate boiling on wires in saturated liquid, an increase in heat transfer coefficient was observed for flat plate heaters upon the change of gravity. Keshock and Siegel[8][9] also reported that the bubble growth rates in water and a 60% by weight aqueous-sucrose solution at saturation temperature were insensitive to gravity change in microgravity. However, Keshock's experiments were conducted in the drop tower facility providing a 1.0 second microgravity duration. It is possible that the microgravity condition was terminated before the wall temperature became steady.

Compared to the amount of pool boiling database, little information is available to date on the forced convective boiling. Papell[11] investigated the threshold velocity beyond which the critical heat flux was insensitive to the flow direction. Evans[12] observed bubble distributions over the tube cross section of an adiabatic flow under microgravity conditions and found that they were similar to that of vertical flow in normal gravity.

More recently, a landmark experiment for the low-gravity two-phase flow was conducted by Chen, Downing, Parish, and Keshock[13]. They observed flow patterns by a high speed camera and measured total pressure drops in adiabatic straight and curved test sections. Only slug and annular flow were observed. The measured pressure drops in a 6.7m, 15.8mm ID horizontal test section during microgravity operation exceeded those measured during the ground testing by 20% at the same qualities. This change is caused by the transition of flow patterns from stratified to slug or annular flows.

Determination of flow regime boundaries is another controversial task. Colin, Fabre, and Dukler[14] observed the gas-liquid two-phase flow pattern and attempted to find the regime-transition criteria. The results were mapped on a flow regime diagram as a function of liquid and gas superficial velocities. The predicted criterion agreed with the boundary between slug and annular flow.

More recently, Reinarts, Best, and Hill[15] measured two-phase condensation heat transfer rates of Freon 12 in microgravity. The results showed that the condensation heat transfer was significantly reduced during the microgravity period. An attempt was made to obtain the similar form of Nusselt number with Dittus-Boelter equation assuming homogeneous flow. However, gravity effects on heat transfer was not clearly shown in their modeling and the correlation derived was highly empirical.

1.2 Scope of the Study

Although numerous efforts have been devoted to microgravity pool boiling for the past 30 years, the fundamental mechanism behind the observed phenomena is yet unclear. This is mainly due to the highly empirical nature of the existing correlations obtained in normal gravity. The main objective of the present work was to identify the influence of gravity on the heat transfer mechanisms in flow boiling. To accomplish this goal, first, theoretical bases of existing correlations for heat transfer and pressure drop were examined. Second, the following specific tasks were selected:

- observation of flow patterns in microgravity,
- measurement of total pressure drops of flow boiling in a straight tube,
- measurement of void fractions in saturated and subcooled boiling, and
- measurement of two-phase heat transfer coefficients in microgravity.

Two sets of microgravity flow boiling loops were built and tested under different microgravity environments. The first series of experiments were conducted in a 15m drop tower facility providing 1.25 seconds of free fall. Flow pattern observation and pressure drop measurement were the main objectives of this series of experiments.

The second series of experiments were conducted aboard the NASA Learjet allowing approximately 18 seconds of microgravity conditions. The newly designed flow loop and data acquisition system were mounted on two racks matching with the requirements of flight experiments. To maintain the inlet conditions constant and reduce the transient time, a once-through flow line driven by pressurized pistons was employed. The main objective of this experiment was to measure the heat transfer coefficients in subcooled flow boiling under microgravity conditions. The investigation on the subcooled region was particularly motivated by the observation of significantly different flow patterns in the subcooled region during the drop tower experiments. An attempt was made to obtain velocity profiles and temperature distributions in the subcooled regions under microgravity conditions, using a method proposed by Sato and Sadatomi[16]. Their method was chosen in the present analysis because the contribution of bubble agitation to be affected by gravity change was differentiated from forced convection heat transfer. Since the number of data sets obtained from the present experiments was small, emphasis was placed on scrutinizing particular data sets from various aspects, rather than deriving new correlations for microgravity conditions.

Collected data on flow patterns, pressure drops, and two-phase heat transfer coefficients were compared with respective data obtained in normal gravity using the similar test conditions. Through comparison, the influence of gravity change on forced convection, evaporation, and bubble agitation was investigated. The validity of several existing mechanistic correlations for two-phase heat transfer was examined.

CHAPTER 2
PREVIOUS EFFORTS FOR MICROGRAVITY BOILING

The influence of gravity on pool boiling and forced convection boiling are reviewed in this section. Bubble growth in the subcooled and saturated liquid, detachment from the wall, and nucleate boiling heat transfer for pool boiling are essential issues of relevance to forced convective boiling. However, very few existing correlations have ever been applied to low-gravity environments due to lack of understanding of two-phase flow behaviors under variable gravities.

The initial approach is thus to investigate the influence of gravity on the parameters governing flow and heat transfer. First, previous studies on the influence of gravity in pool boiling are reviewed. This section also includes a discussion of the role of the buoyancy force during the bubble detachment. Second, several experimental results for forced convective boiling under microgravity conditions are reviewed. The major achievements and findings for both pool boiling and forced convective boiling are listed at the end of this chapter. Finally, the motivation of the present study and unique features of the present equipment are introduced.

2.1 Pool Boiling in Microgravity

Investigation of the gravity effects on pool boiling is of critical importance to understand the bubble growth through the superheated layer in flow boiling.

Reduced gravity experiments performed in the early 1960s are noteworthy. Sherley[5] obtained boiling curves for LH_2 under both normal and microgravity conditions using a drop tower and a KC-135 aircraft. Little difference was observed between the normal and microgravity boiling curves. Sherley concluded that the effect of gravity on the nucleate boiling was negligible. However, it should be noted that results of Sherley's work can only draw qualitative conclusions since the actual gravity level and other flow conditions during the microgravity experiments are not shown in the literature.

Siegel and Keshock[8] detected changes in superheats of vertical and horizontal wires in distilled water, ethyl alcohol, and 60% by weight aqueous-sucrose solution. As listed in Table 2-1, a decrease in superheat by 2-3°C in microgravity was observed for the horizontal wires in water and ethyl alcohol, while an increase in superheat was observed for vertical wires. No effect of gravity on the superheat was observed for sucrose solution. This fact suggests that bubble growth and detachment controls nucleate boiling heat transfer without the influence of surface tension. Siegel et al. also analyzed the effect of gravity on the contact angle through visual observation filmed by a high speed camera and found

Table 2-1 Heat transfer data for nucleate boiling from an electrically heated wire[8].

Fluid	Horizontal wire				Vertical wire			
	Earth gravity, $1g_e$		Reduced gravity, $0.014g_e$		Earth gravity, $1g_e$		Reduced gravity, $0.014g_e$	
	Heat flux Q/A Btu/(hr)(sq.ft)	Temp. difference T_w-T_s, °F	Heat flux Q/A Btu/(hr)(sq.ft)	Temp. difference T_w-T_s, °F	Heat flux Q/A Btu/(hr)(sq.ft)	Temp. difference T_w-T_s, °F	Heat flux Q/A Btu/(hr)(sq.ft)	Temp. difference T_w-T_s, °F
Distilled water	30,300	15.3	30,200	11.3	29,100	11.3	29,100	13.8
	50,100	16.7	50,000	14.5	48,700	14.2	48,900	17.6
	90,700	18.5	90,600	16.5	62,800	15.9	62,900	19.5
					69,400	17.3	69,700	21.8
Ethyl alcohol	28,700	32.2	28,700	30.2	28,300	27.1	28,300	28.2
	48,300	33.1	48,200	31.3	47,800	30.1	47,800	31.2
	62,500	33.1	62,500	31.9				
60% by weight aqueous-sucrose solution	30,000	37.3	30,000	37.3	31,000	64.3	31,000	65.8
	49,900	44.9	49,900	44.9	51,200	64.1	51,000	67.1
	64,700	50.3	64,700	50.3	66,200	79.0	66,400	83.9
	92,100	58.4	92,100	58.4	93,800	87.1	94,000	94.5

that the gravity change affects the contact angle only slightly for the above fluids.

Clodfelter[7] investigated the effect of gravity on the critical heat flux (CHF) for 0.5mm platinum horizontal wires and 6.4mm wide ribbons in distilled water using a 16.8m drop tower facility and an airplane. The CHF measured at gravity fields less than 0.01g was about 0.15times the normal gravity value. The comparison with the theoretical $g^{1/4}$ dependence showed that the existing CHF correlations qualitatively agree with the measured CHF in microgravity as well. However, little information is available on the CHF when zero gravity is approached. Since the fundamental wave length on the liquid-vapor interface is a function of gravity, the existing CHF correlations should be reassessed in the low gravity range.

A comprehensive boiling curve for microgravity pool boiling was first obtained by Merte and Clark[6]. Figure 2-1 shows the boiling curves for liquid nitrogen obtained under normal and microgravity conditions. In the nucleate boiling region, the gradient of the curve, namely, the heat transfer coefficient, in microgravity was almost the same as that under normal gravity. However, the corresponding heat fluxes at the same superheat had slightly decreased. The CHF in microgravity decreased by a factor of 2. In the film boiling region, both the heat flux and heat transfer coefficient decreased probably due to the increased irregularity of the

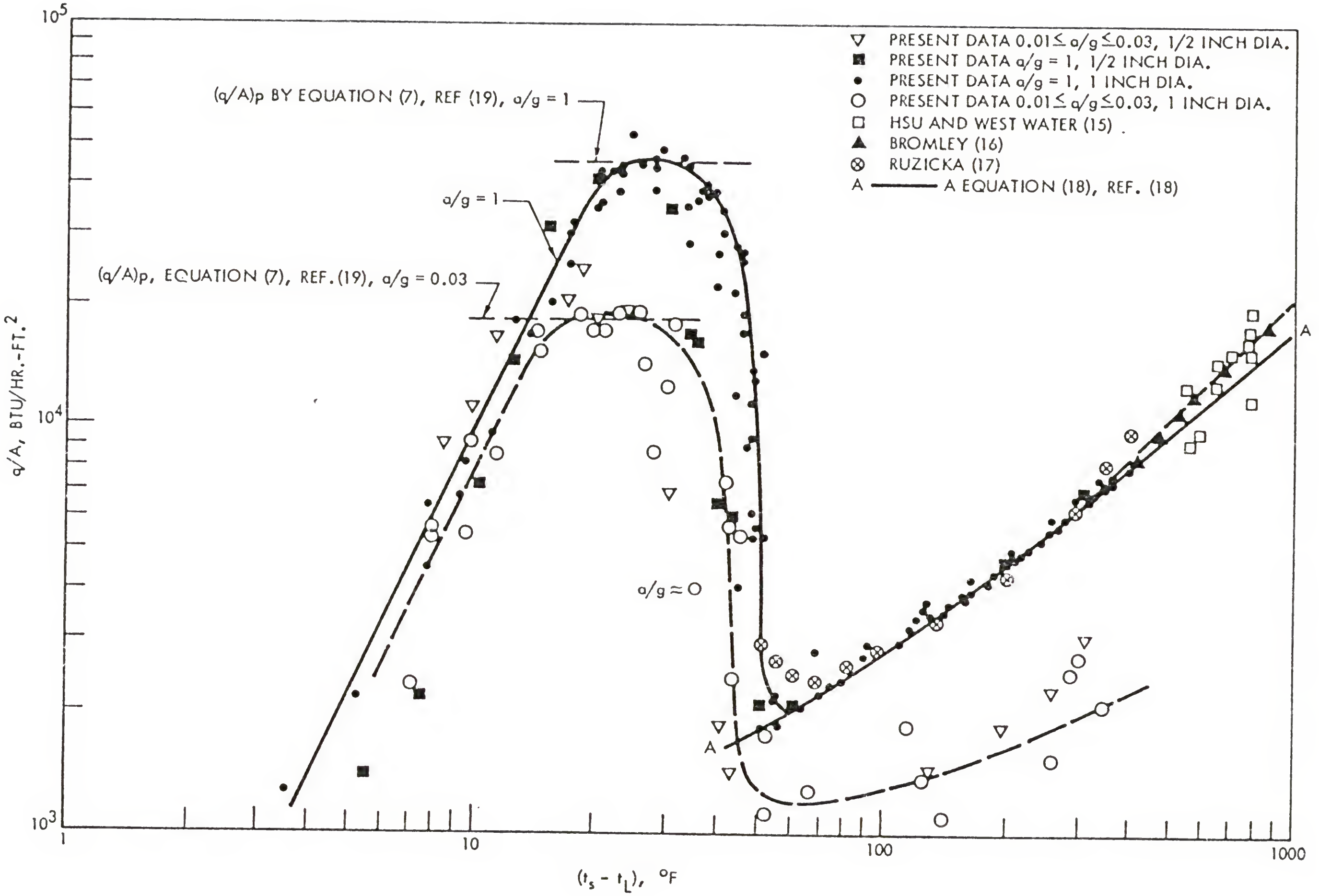

Figure 2-1 Boiling curves obtained by Merte and Clark under microgravity conditions[6].

interface. These results from Merte's pool boiling experiment suggest that the overall performance of heat exchangers to be used under microgravity conditions are poorer than in normal gravity when operated near the critical heat flux region.

The influence of gravity on pool boiling heat transfer was examined using widely accepted correlations in normal gravity. Pool boiling is categorized into four regions in terms of the dominant heat transfer mechanism. The following theoretical and semi-empirical correlations for each region were particularly selected because the gravity term was explicitly included the following:

1) Natural Convection (Re > 2000) (Jakob [17])

$$Nu=0.14\left[\left(\frac{\beta g\Delta TD^3\rho_f^2}{\mu_f^2}\right)\left(\frac{C_{pl}\mu}{k}\right)_f\right]^{1/3} \tag{2-1}$$

2) Nucleate Boiling (q"=constant) (Rohsenow [18])

$$\frac{C_{pl}(T_w-T_s)}{h_{fg}}=C\left\{\frac{q''}{\mu_f h_{fg}}\left[\frac{\sigma}{g(\rho_f-\rho_g)}\right]^{1/2}\right\}^{0.33}(Pr_f)^{1.7} \tag{2-2}$$

3) Critical Heat Flux (Zuber [10])

$$q''_{crit}=\frac{\pi}{24}h_{fg}\rho_g\left[\frac{\sigma g(\rho_f-\rho_g)}{\rho_g^2}\right]^{1/4}\left(\frac{\rho_f+\rho_g}{\rho_f}\right)^{1/2} \tag{2-3}$$

4) Film Boiling (Frederking/Clark [19])

$$Nu=0.14\left\{\frac{L^3\rho_g(\rho_f-\rho_g)}{\mu_g^2}\left(\frac{c_p\mu}{k}\right)_g\left[\frac{h_{fg}}{c_{pg}(T_w-T_s)}+0.5\right]g\right\}^{1/3} \tag{2-4}$$

Although all of the above correlations include the gravity term, the physical background for each equation is different. In natural convection, the difference in specific weight at different temperatures causes a convective motion within the liquid. In nucleate boiling, the buoyancy force acting on the vapor bubble is one of the dominant forces upon bubble detachment. Both the critical heat flux and film boiling heat flux are ruled by the Kelvin-Helmholtz instability of the liquid-vapor interface. However, the above correlations derived under normal gravity conditions assume the gravitational acceleration constant. All heat fluxes predicted by the above correlations approach zero when gravity becomes extremely small. Under such conditions, the soundness of these equations is doubtful.

The above correlations were all derived through dimensional analysis. The exponents attached to the dimensionless numbers were empirically obtained through curve fitting premised on a constant value for the gravitational constant, g=9.8m/s. Under variable conditions, however, the terms or dimensionless numbers related to the gravity term are expected to vary significantly from those in normal gravity. In addition, as a result of the diminished gravity force, the surface tension and Marangoni forces become dominant and control momentum and heat transfer. It is likely that those values such as the Grashof number or the Laplace constant are overestimated under microgravity conditions. Thus, the exponents obtained under normal gravity conditions should be re-evaluated under microgravity conditions considering the effect of variable gravity.

Table 2-2 summarizes the gravity effects predicted from the above correlations. The ratio of the pool boiling heat flux in normal gravity to that in microgravity was calculated from Merte's experiments conducted in the drop tower. It is noted that the CHF data obtained in his experiments roughly follow $g^{1/4}$ as predicted in Eq.(2-3). Latent heat transport and bulk turbulent process are the two major mechanisms of boiling heat transfer. The dominant component has yet to be determined even under normal gravity conditions. The microgravity environment, free from buoyancy-driven convection, offers an ideal stage to study the problem proposed above.

Schwartz and Adelberg[20] investigated the significance of latent heat transport of saturated water at 1 atm under microgravity conditions using an airplane providing a low gravity duration of 8 - 10 seconds. Figure 2-2 shows that the ratios of heat transport due to evaporation to the total heat flux increased as the acceleration level was reduced. The values of latent heat were calculated from the volume of vapor

Table 2-2 Effects of gravity on heat transfer mechanism in pool boiling.

	Boiling Curve*	Gravity effect on heat flux**	(q_{0g}''/q_{1g}'') predicted***	(q_{0g}''/q_{1g}'') measured*
Natural convection	$h_{0g} < h_{1g}$	$g^{1/4}$ (laminar)	---	---
	$h_{0g} < h_{1g}$	$g^{1/3}$ (turbulent)	---	---
Nucleate boiling	$h_{0g} < h_{1g}$	$g^{1/2}$	---	0.46
CHF	$h_{0g} < h_{1g}$	$g^{1/4}$	0.25	0.32
Film boiling	$h_{0g} < h_{1g}$	$g^{1/2}$ (turbulent)	0.40	0.22

* Based on the results of Merte's experiments.

** Assumed $g=0.098 m/s^2$.

*** Ratios are obtained from $(g_{0g}/g_{1g})^n$.

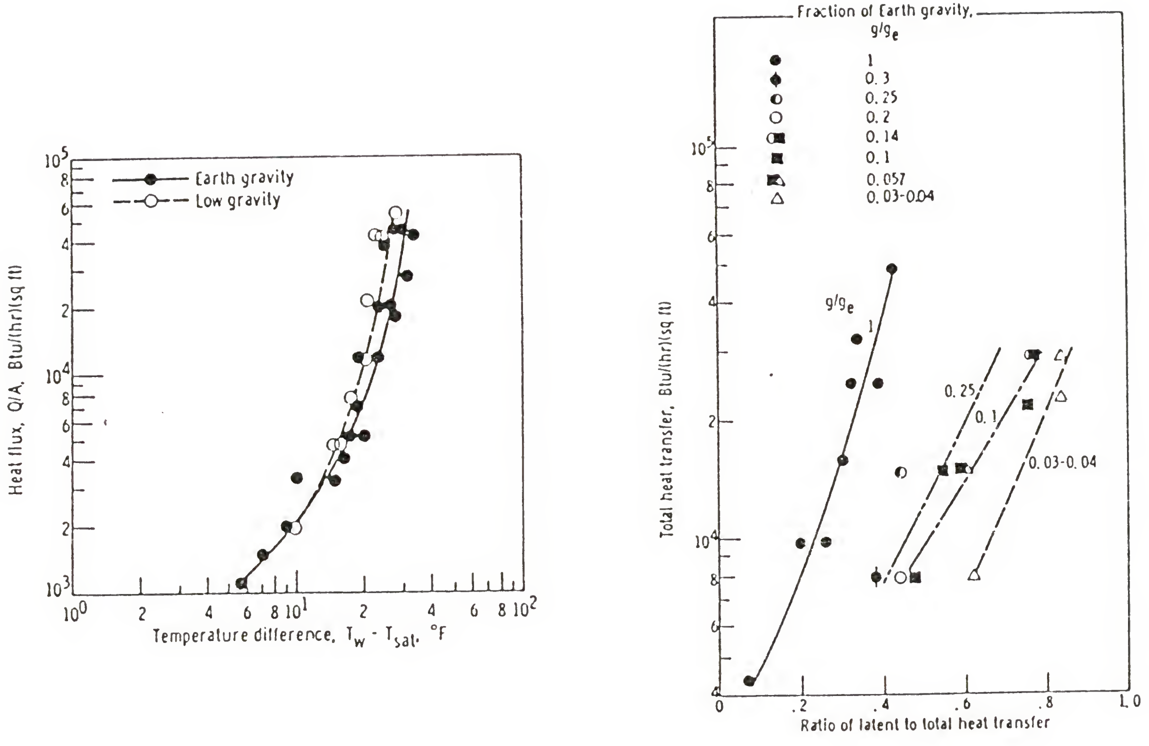

(a) (b)

Figure 2-2 Pool boiling curves for water under normal and microgravity conditions. (a) Total heat flux, and (b) Latent heat transport[20].

bubbles in photographs. The total heat flux remained unchanged in normal and microgravity. This is presumably due to the suppression of natural convection caused by the loss of buoyancy force. It is considered that under microgravity conditions, the heat transport due to natural convection was replaced by the enhanced evaporation to maintain the same total heat flux.

More recently, Zell, Straub, and Weinzierl[21] obtained a boiling curve near the onset of nucleate boiling for a gold film in saturated and subcooled Freon 113 under microgravity conditions. The experiment was conducted in a sounding rocket providing about 6 minutes of microgravity conditions on the order of 10^{-6}g, which is an extremely long and small acceleration level compared with previous microgravity environments. Figure 2-3 displays the comparison of boiling curves in normal and microgravity conditions near the onset of nucleate boiling. The boiling curves indicated that the superheat to initiate the nucleation in microgravity becomes larger than in normal gravity, and that the slope of the boiling curve after the onset of nucleate boiling is significantly smaller than in normal gravity. A prominent difference in bubble growth on the heated surface in saturated Freon 113 under microgravity conditions is shown in Figure 2-4. The growing bubbles covered the total heating area until they reached the boundary of a container, and then broke into pieces. It appeared that the buoyancy force was not strong

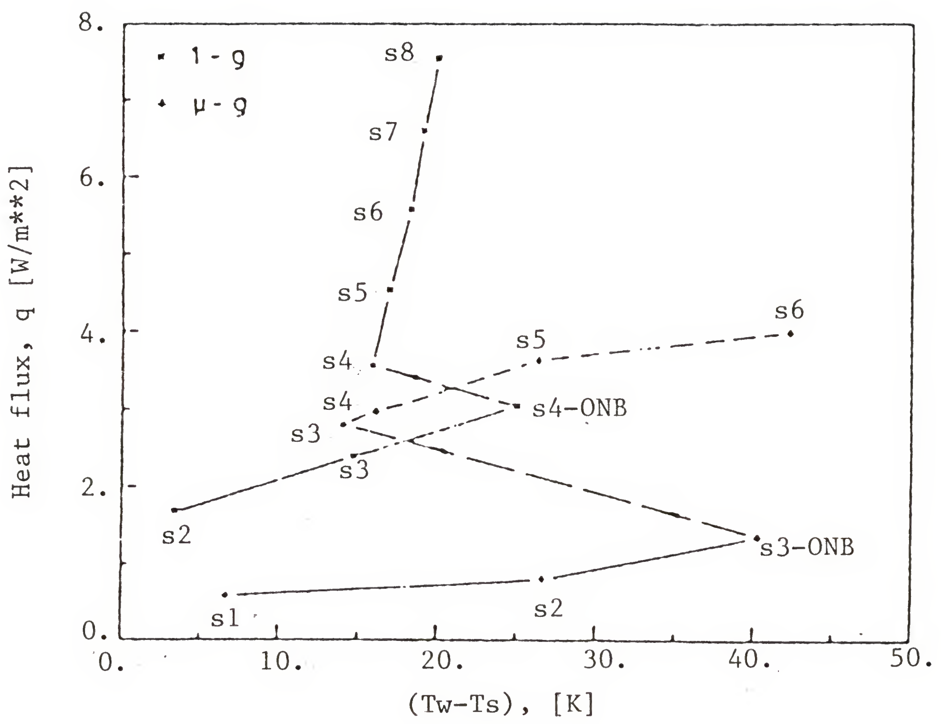

Figure 2-3 Boiling curves in subcooled Freon 113 under normal and microgravity conditions[21].

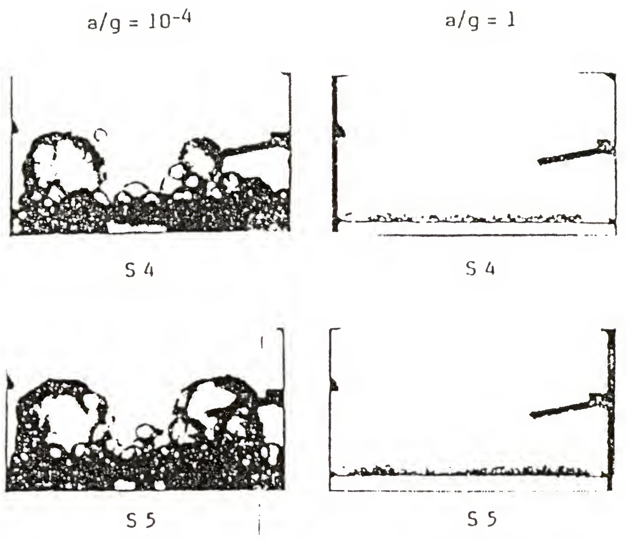

Figure 2-4 Subcooled pool boiling of Freon 113 under normal and microgravity conditions[21].

enough to detach the bubble in saturated Freon. This experiment suggests that a steady state for saturated pool boiling may not be reached since bubbles do not detach from the wall and keep growing. This observation of pool boiling phenomena indicate that the heat transfer is expected to deteriorate under microgravity conditions.

Ervin, Merte, Keller, and Kirk[22] conducted transient nucleate boiling experiments in a drop tower facility and observed boiling phenomena of subcooled Freon 113 on a 400Å thick gold film sputtered on a quartz substrate. The boiling spread across the heater surface at the moment of boiling inception and the propagation process was classified into six distinct categories. Ervin et al. reported that the energetic type of boiling propagation on the heating surface occurred uniquely in microgravity. It is assumed that the energetic boiling propagation was due to build-up of enthalpy in the superheated layer.

Bubble growth in pool boiling is mainly controlled by the surface condition of the heater and the thermal properties of the fluid. Zuber[23] derived a correlation for the growth of a single bubble in homogeneous saturated liquid

$$D(t) = \frac{\pi}{2}\left[\frac{4k_f\,(T_w - T_s)}{h_{fg}\rho_g\,(\pi\alpha)^{1/2}}\,t^{1/2} - \frac{2q''}{h_{fg}\rho_g}\,t\right] \tag{2-5}$$

The rate of growth predicted by the above equation is proportional to $t^{1/2}$ and agreed with the experimental results. Eq.(2-5) also indicates that the growth rate is independent of gravity unless other conditions are changed. However, according to the results reported by Merte et al.[6] and Ervin et al.[22], the wall superheats changed for the same heat fluxes in microgravity as the boiling progressed. Zell et al.[21] concluded that gravity dependent mechanisms such as bubble agitation and natural convection were completely compensated by the phase change mechanism under microgravity conditions, which may influence the growth rate of bubbles.

The bubble detachment diameter in pool boiling is another non-consensus issue under both normal and microgravity conditions. Fritz[24] considered the balance of the buoyancy force and the surface tension force at the moment of detachment. The model can be applied to the bubble growth with small growth rates such as gas bubbles. However, there exist dynamic forces for a rapidly growing bubble that affects the bubble detachment. An analysis of the forces acting on the bubble in normal and microgravity was conducted by Keshock and Siegel[9]. Inertia of liquid initially assists the bubble detachment. However, it opposes the detachment after the growth rate is decelerated. They concluded that the bubble detachment in saturated water did not occur in the absence of gravity because the surface tension force exceeded the sum of the buoyancy force and inertia force.

Cochran, Adylott, Frysinger[62] reported that the effect of gravity became small as subcooling increased. A horizontal chromel strip was heated in distilled water at 1 atm with variable subcooling and subjected to 2.3 seconds of microgravity free fall. The vapor volume of a single bubble was measured as a function of time from the beginning of growth until the end of detachment. For subcooling more than 16.7°C, the effect of gravity on the vapor volume was negligible. It is inferred that this is due to the increased recondensation of vapor bubbles and that the detachment diameter is determined by the thickness of the thermal boundary layer. The effect of gravity on the number of nucleation sites was also investigated. The visual observations detected little influence of gravity on the number of nucleation sites. However, the above conclusions conflict with the results from Siegel and Keshock's experiments[8], reporting a decrease in heater temperature. To investigate the gravity effect on nucleation, close observation of activated nucleation sites on the heating surface with visual aids is necessary.

Recently, Klausner and Zeng[26] proposed an unified bubble detachment model to predict vapor bubble departure diameters in both pool and flow boiling conditions. A new expression to describe the drag force acting on the bubble was obtained through numerical techniques. The force balances horizontal and perpendicular to the heating surface were considered separately to explain the mechanism of sliding bubbles before they lift off the wall. Klausner et al. concluded that the magnitude of the surface tension force accounts for only a fraction of other forces such as unsteady drag and is not significant at the points of departure. For the lift-off diameter of a bubble, a simple force balance between the buoyancy and the inertia forces may be used. They also pointed out that the departure process is strongly dependent on the pressure through the bubble growth rate.

The following is a list of major results from pool boiling experiments under microgravity conditions:

a) Significance of the surface tension in nucleate boiling was examined using different heater geometries and fluids. When the surface tension is dominant upon bubble detachment, gravity effects on the nucleate boiling was insignificant[8].

b) The slope of the boiling curve obtained under microgravity in the nucleate boiling region remained almost the same, indicating that the heat transfer coefficient was unchanged. However, CHF and film boiling roughly followed $g^{1/4}$ and $g^{1/2}$, respectively, as predicted by the existing correlations[6].

c) The heat transfer coefficient near the ONB was significantly reduced. The wall superheat that initiate nucleate boiling was increased[21].

e) The bubble detachment diameter in saturated liquid became significantly large under microgravity[21].

d) For constant heat fluxes, the fraction of latent heat transfer tends to increase as the acceleration level decreases[20]. Bulk turbulent convection appeared to be suppressed due to the lack of buoyancy-driven flow.

f) In subcooled pool boiling, the effect of gravity was negligible for subcoolings of over 16.7K. The number of nucleation sites was unchanged under microgravity[8].

g) The contact angle appeared unchanged under microgravity conditions[9].

2.2 Forced Convective Boiling in Microgravity

Compared to abundant research work for pool boiling, only a limited amount of study has been performed on forced convective boiling in microgravity. This is because microgravity environments are difficult to simulate and quite often costly to create in laboratories. Although the characteristic period of bubble formation is on the order of 10^{-3} seconds, at least several minutes are required for conventional forced convective boiling loops to reach steady states. The drop tower facilities provide 2 - 6 seconds of low-gravity environment, while the microgravity aircraft such as Learjet or KC-135 provide about 20 seconds. Regardless of difficulties described above, several compact flow boiling loops have been built and tested aboard the reduced-gravity airplanes. These experimental results are reviewed in the following paragraph and major contributions are summarized at the end.

For a better understanding of the changes in two-phase flow under microgravity, visual observation of the flow pattern change is necessary. Evans[12] observed the bubble distribution of an air-water mixture in a 12.7mm diameter, 45.7cm long adiabatic plastic tube under microgravity conditions and found that the flow patterns were similar to that of vertical upward flow under normal gravity. Bubbly, slug, and annular flow patterns were the three major flow regimes classifying the void distributions for two-phase flow under normal and microgravity conditions. Current issues under this topic are to investigate the phase transition mechanism and thus to determine the boundaries of these flow patterns. Although several researchers[13][14] proposed flow regime maps applicable to microgravity conditions, conclusive results have not yet been obtained.

Information on the pressure drop is essential for the design of heat exchangers in space. Unfortunately, only a limited amount of research has been done in this area.

Chen, Downing, Parish, and Keshock[13] measured the pressure drop in 15.8mm diameter, 1.83m long straight and curved tubes using Freon 114. A mixture of vapor and liquid with the quality ranging from 0.05 to 0.9 was produced in a swirl flow evaporator and introduced into an adiabatic transparent test section allowing for the observation of flow patterns. The measured total pressure drops in microgravity were larger than those obtained in the horizontal test section in normal gravity for the same qualities. However, the direct comparison of pressure drops is questionable because the flow patterns are different. Besides, in adiabatic systems, the bubble formation on the wall in the nucleate boiling region is neglected and the frictional component of pressure drop is underestimated.

Adiabatic dispersed flow experiments using water and n-butyl benzoate of identical densities were carried out under normal gravity conditions by Sridhar, Chao, and Soo[27]. Pressure drops along a 2.44m long, 45mm square horizontal test section were measured by changing the ratio of n-butyl benzoate in the mixture to simulate the variation of void fraction. It was observed that the frictional pressure drop was unaffected by large changes in the volume fraction of benzoate drops and their size distribution. However, the adiabatic systems fail to simulate the void fraction distribution near the wall. In actual heat exchangers, the bubble formation on the heated wall needs to be considered in the nucleate boiling region since the momentum of flow is lost substantially near the wall.

Klausner[25] studied the influence of gravity on two-phase flow by changing the orientation of flow. Heat transfer, pressure drop, and void fraction of Freon 11 in a 19.1mm diameter, 1.48m long copper tube was measured in vertical up-flow, vertical down-flow, and horizontal flow configurations. The observed flow pattern was mainly in the annular flow regime. Gravity exerts its influence on vapor volume fraction through changes in the relative velocity between the liquid and vapor phase. It is also found that both the ebullition process and bulk turbulent convection of flow boiling are affected by gravity through the thickness of the liquid film in the annular flow range.

Under normal gravity conditions, heat transfer in vertical and horizontal tubes are different. Under microgravity conditions, however, the absence of buoyancy force cancels the difference due to flow orientation with respect to the gravity field. Papell, Simoneau, and Brown[11] investigated the effect of flow orientation on the CHF for liquid nitrogen flowing through a vertical heated tube 1.28cm in diameter at 0.516MPa with a subcooling of 10.6K and found that the CHF was independent of the flow orientation beyond flow velocities greater than 1.95m/sec(Figure 2-5). This velocity corresponds to a Froude number of 31.2, indicating that the inertia force is about 30 times larger than the gravity force.

Papell[28] also observed the forced convective boiling of distilled water in a 7.9mm diameter stainless tube in microgravity. A short flow interruption at the beginning of zero gravity conditions was reported, followed by an increase in the heat transfer coefficient on the order of 16%. This observation agrees with Siegel's results from the pool boiling experiments, in which the heat transfer coefficients had

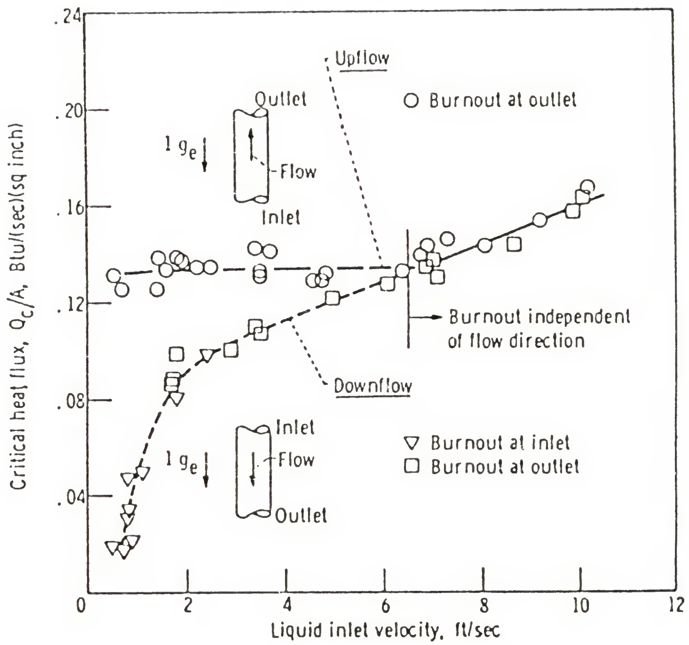

Figure 2-5 Critical heat flux as a function of inlet velocity for upward and downward flow of liquid nitrogen in a 0.505" diameter tube [11].

increased under microgravity conditions. For pool boiling, as the bubble size becomes larger, the number of bubbles emitted from the wall becomes smaller when a constant heat flux is applied. Zell et al. observed such formation of large bubbles in their microgravity experiments. If evaporation is a dominant heat transfer mechanism, the heat transfer rate of flow boiling systems shows similar tendency to that of pool boiling systems. However, the contributions of convective and evaporation heat transfer is still unclear under microgravity conditions. Precise measurement of single-phase heat transfer rate, void fraction, and wall temperatures along the flow axis is needed to resolve this issue. Unfortunately, these data were not available in Papell's experiment.

Feldmanis[29] conducted a flight experiment aboard a KC-135 microgravity aircraft and measured temperatures and pressures in a closed, forced convective boiling and condensing loop. An increase in the system pressure and an attenuation of pressure oscillations in the 9.53mm diameter, 0.91mm long evaporator was observed during the period of microgravity. No noticeable temperature change in the bulk temperature was observed at the outlet. Quantitative analysis had not been made since the data on the flow rate and thermal equilibrium quality were not measured. The pressure oscillations are probably caused by the formation of slug bubbles which are usually observed in the beginning of saturated boiling. Feldmanis agreed on the increase in heat transfer rate in microgravity, the fact first pointed out by Papell, and explained such an increase in terms of the transition of flow patterns from the bubbly to slug flow. As a pioneering work in microgravity flow boiling, his experiment introduced a number of questions as well. However, the discussion was speculative due to lack of experimental evidence.

Crowley and Sam[30] observed stable operation of the two-phase test rig aboard the NASA KC-135 aircraft under microgravity conditions. However, the wall temperatures on a condenser during the microgravity trajectories appear to be in transients. The system pressure increased about 5% (15kPa) in microgravity and correspondingly saturated fluid temperatures in the system increased by 1K to 2K. Crowley et al. reported that the heat transfer rates in the evaporator remained constant in microgravity. This result, however, contradicts the findings of Feldmanis and Papell. Since wall temperature profiles of the evaporator are not shown in the report, it is difficult to confirm their statement. The thermal equilibrium quality, flow patterns, and void fraction should be measured simultaneously to evaluate the heat transfer rate in microgravity.

Standley and Fairchild[31] examined an operation of a R-11 two-phase pumped loop system aboard the NASA KC-135 microgravity aircraft as a preliminary run for subsequent suborbital rocket tests. Mass fluxes were 100kg/m^2/s and

144kg/m^2/s and heater powers were 280W and 420W. The use of R11 allowed thermal equilibrium qualities large enough to exceed 85% of the void fraction at the boiler exit. The magnitude of temperature increases in the boiler fluid and on the boiler wall were both 1 to 2K, indicating a slight decrease in heat transfer rate under microgravity conditions. This fact opposes the findings of Papell, Feldmanis, and Crowley et al. Note that the flow pattern at these high qualities is annular, in which thin liquid film remaining on the heating wall surrounds vapor flow at the center. Standley et al. postulated that the above temperature increase was due to change in two-phase heat transfer mechanism. Due to lack of mechanistic models and limited database for microgravity flow boiling, their hypothesis has not been verified yet.

The following is a list of major results and findings made by previous investigators for flow boiling under microgravity conditions:

a) Beyond a certain value of Froude number, the effect of gravity on CHF can be negligible since the inertia force becomes dominant over the gravity force[11].

b) The three similar flow patterns were observed under microgravity although the structure of each flow pattern was different[12].

c) Several flow regime maps have been proposed to determine the boundaries of each flow regime for microgravity use[13]. However, none of them successfully classified the flow patterns observed in microgravity.

d) The total pressure drop in the horizontal straight and curved test section for two-phase flow increased probably due to flow pattern change[13].

e) The heat transfer coefficient under microgravity was increased by 16%[11]. However, other investigators contended otherwise[30].

The review of previous work has revealed a substantial lack of database on flow boiling in microgravity. Especially, the change of two-phase flow heat transfer rate in microgravity is unclear. Regardless of strenuous experimental work done in the past, no mechanistic models capable of accounting for gravity change has been proposed yet. This is because the drop towers or microgravity aircraft cannot provide enough period of microgravity for each component of flow boiling loops. The effects of gravity on boiling, condensing, and adiabatic two-phase mixtures are still unidentified. All the previous experimental facilities reviewed here consist of evaporators, condensers, pumps, and flow lines operated simultaneously under unknown influence of gravity. As Feldmanis pointed out, 19 seconds or less is too short for reaching equilibrium for the entire flow loop because of long transit time in the flow loop. Within a limited amount of time allowed for drop tower and flight experiments, focused items need to reach a steady state to measure temperatures, pressures, and flow rates under thermal equilibrium conditions.

The present study focuses exclusively on convective flow boiling under microgravity conditions. To eliminate the feedback effect on the boiling section, pumps were replaced with a once-through flow line and two separate reservoirs. The pistons equipped with the reservoirs are driven by pressurized air provided from a high pressure tank through a pressure regulator. Under the test conditions considered here, the transit time in a 0.5m boiling test section is approximately 2 to 5 seconds. Test conditions were deliberately confined to low flow rates and low heat fluxes, since the influence of gravity may be less significant in high flow rates where the inertia force is overwhelmingly larger than the buoyancy force.

CHAPTER 3
EXPERIMENTAL DESIGN AND PROCEDURE

3.1 Drop Tower Experiment

A simple flow boiling loop using Freon 113 was built for the drop tower experiment. Schematic diagram of the boiling loop is shown in Figure 3-1. The loop mainly consists of the boiling test section, vapor-liquid separator, cooler, positive-displacement gear pump, and pre-heater. The vapor generated in the test section was released into the atmosphere and only liquid was recovered and recirculated. The preheater, consisting of a coiled copper tube wrapped with an adjustable 100W heater, allowed fine adjustment of subcooling at the inlet of the test section by controlling the applied voltage to the heater. The liquid recovered in the separator was cooled while passing through the cooler immersed in iced water. The selection of a positive-displacement gear pump, capable of providing a constant liquid flow rate regardless of the pressure in the downstream, was made to deal with the unexpected pressure change in the boiling test section. Each component was connected with 4mm I.D. Teflon and copper tubes. Flow rate was controlled by throttling the flow with a valve on the line bypassing the pump.

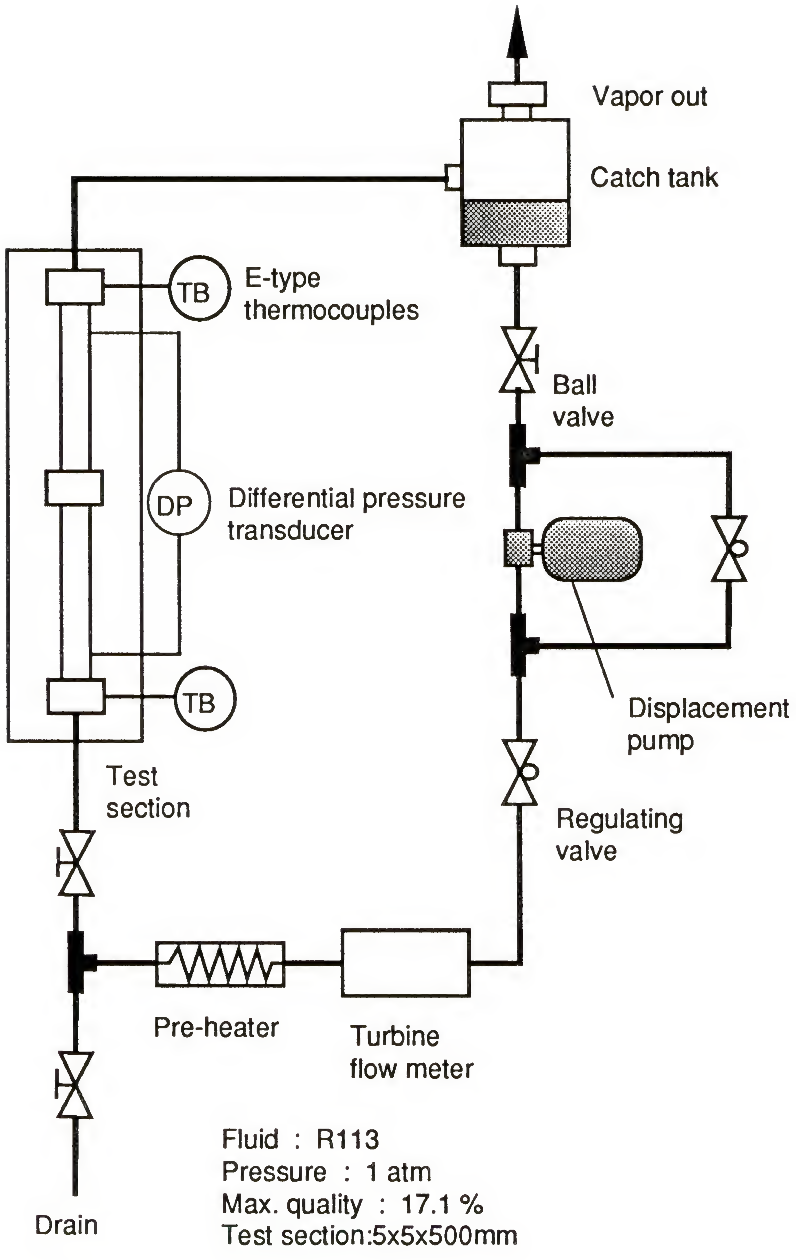

Figure 3-1 Schematic diagram of a drop tower flow boiling loop.

Mass flow rate was measured in the upstream of the boiling test section with a turbine flowmeter which is insensitive to flow orientation and gravity change. The measurable range of the flow meter was 0 - 300cc/min. Since the loop is open to ambient at the separator, pressure at the exit was assumed 1atm. Bulk temperatures at the inlet and outlet temperatures were measured by two C-C type thermocouples immersed in the flow. The junctions of the thermocouples were placed at the center of the flow.

The volume flow rate and bulk temperatures at the inlet and exit of the test section were measured on real time and the output signals were transmitted to a high speed sampling recorder.

3.1.1 Flow Pattern Observation

The first series of the drop tower experiment was intended to observe the flow patterns. A rectangular transparent boiling test section allowed visual observation of the boiling process on the heating surface and flow pattern development along the flow direction. Figure 3-2 shows details of the boiling test section and its cross section view. Four pyrex plates pressed by stainless steel plates were fastened together to form a 5mmx5mmx500mm square channel, inside which transparent electric heaters were coated. The heaters consist of a thin film made of Cl_2Sn and its total resistivity of four surfaces was 308Ω. A 110V of dc power was

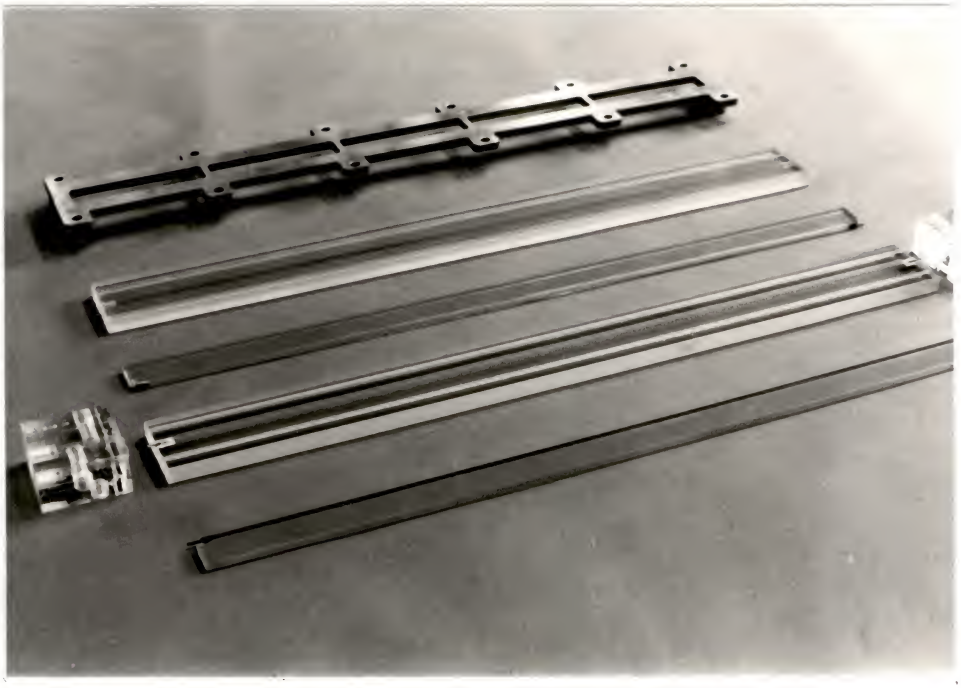

(a) Test section overview

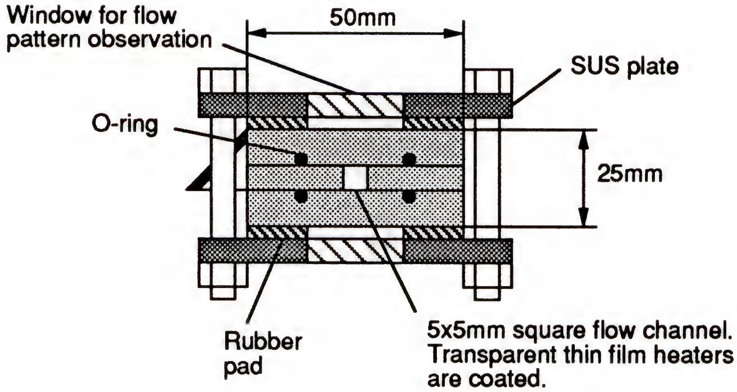
Window for flow pattern observation
50mm
SUS plate
O-ring
25mm
Rubber pad
5x5mm square flow channel. Transparent thin film heaters are coated.

(b) Cross section

Figure 3-2 Test section used in drop towerexperiments.

applied to the heater to produce 55.4W of total electrical input into the test section. It was found later that an average of 54% of electrical power was used to heat the fluid passing through the channel. The resulting heat flux in the test section was 2.9kW/m^2. The exit qualities ranged from -4.5% to 17.5% in the present study. The electrical power for the test section and preheater was continuously supplied by extension cables during the free fall.

Outside the test section, a 30mmx120mm surface mirror was attached beside the flow channel. The reflected image of flow patterns through 20mmx100mm windows were photographed with a 35mm still camera with back-lit configuration. The camera, triggered with a remote controller at the top of the drop tower, was motor-driven and capable of taking 5 frames every 0.25 seconds during 1.25 seconds of free fall.

3.1.2 Pressure Drop Measurement

The main objective of the second series of the drop tower experiment was to measure pressure drops under microgravity conditions. The same flow loop was used except for the test section. The test section used in the pressure drop measurement consists of a 4mm I.D. SUS tube wrapped uniformly with a nichrome wire whose total resistance was 13.0 ohms. A 26V dc power was applied to this heater to generate 52W of electrical power input. Heat loss to the ambient was measured by reading the temperature drop across the insulator around the test section. Approximately 12% of heat flux was lost to the ambient and the resulting net heat flux transferred to the flow was 6.63kW/m^2. The test section was arranged vertically to reduce the transient time from 1.0g to 0.02g.

A diaphragm-type differential pressure transducer was used to measure pressure drops along the test section. Pressure taps were made at the inlet and exit of the channel and connected to the high pressure and low pressure ports on the transducer by 4mm I.D. flexible tubes filled with liquid Freon R113. Under variable-gravity conditions, the static pressure inside the leading tubes needs to be considered since it also changes with gravity. The differential pressure was sampled every 2 msec. during the free fall and recorded in the same high speed sampling recorder used in the flow pattern experiment.

The above two-phase loop was mounted on a two-staged, 500mm diameter cylindrical drop module with four 5cm diameter, 1m long spikes underneath to mitigate the impact of landing which was expected to be on the order of 50g. The velocity of the module at the end of the free fall was calculated to be 19.4m/s. Upon landing, the four spikes were almost completely buried into the sand. The drag shield hanging from the module was used to reduce the air drag induced during the free fall. The test module with the fluid loop mounted is shown in Figure 3-3(a). The total weight of the test module was 87kg. The magnitude of gravity during the free fall was previously

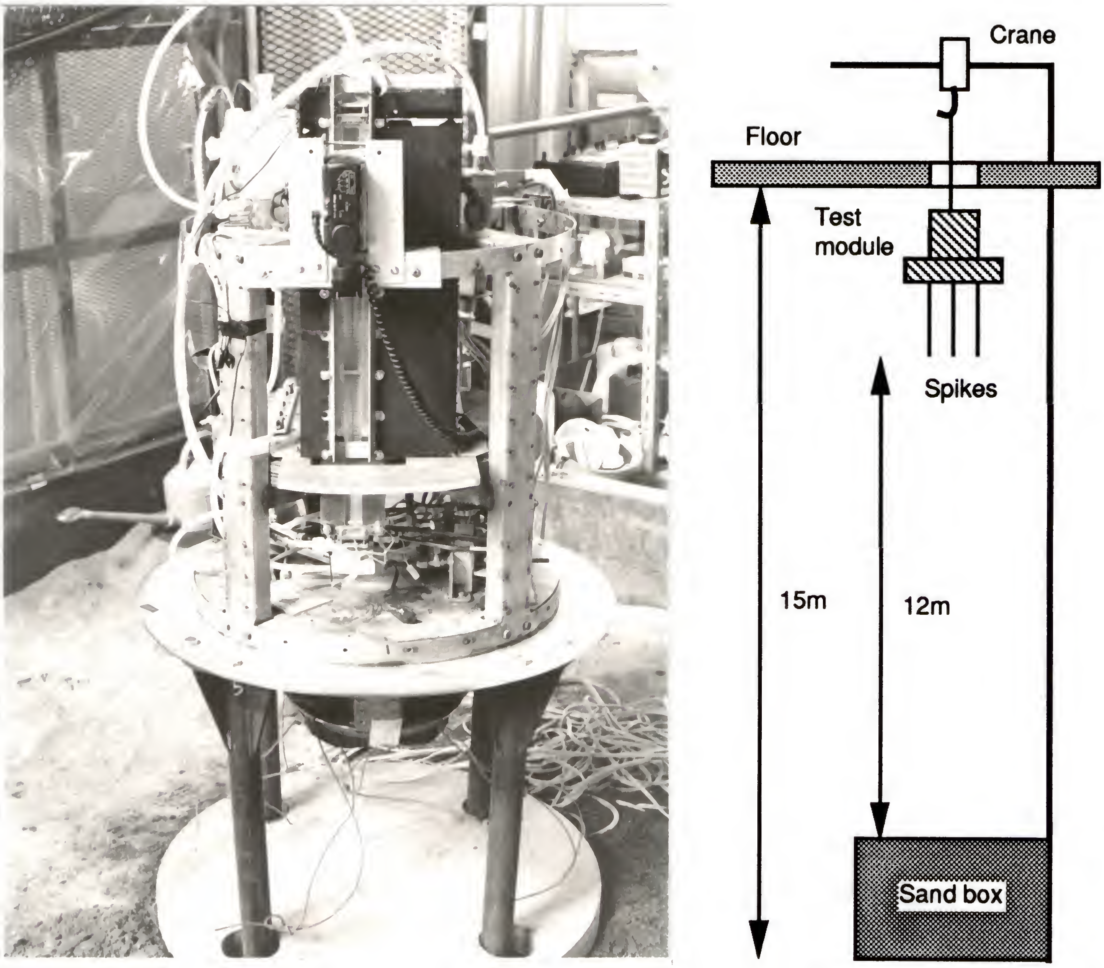

(a) Drop module

(b) Drop tower

Figure 3-3 A 15m drop tower facility and flow boiling loop mounted on a drop module.

measured with an accelerometer and found to be 0.02g. The experiment was conducted in a 15m drop tower facility owned by Ishikawajima Harima Heavy Industry Inc., Yokohama, Japan, in June and July, 1989. The free fall distance of the drop tower facility was 12m (Figure 3-3(b)) and allowed a microgravity duration of 1.25 seconds.

3.1.2 Pressure Drop Measurement

First, the pump and measurement systems were turned on and the flow was initiated. After leaks on the flow lines were checked, the voltage on the preheater was gradually increased until a desired inlet temperature was attained. Then, the main heater was turned on and boiling was started. It took approximately 3 - 4 minutes before the boiling was stabilized and a steady state was reached. Meanwhile, the batteries of the camera motor and remote controller were checked. Using the built-in crane, the operator lifted up the drop module to the top of the tower slowly with maintaining vertical attitude. About 30 seconds were waited until the swinging motion of the module completely damped out. Then, the keblar wire hanging the module was cut either manually or automatically with a video-monitored scissors. Simultaneously, the motor-driven camera was triggered and photographed 5 to 6 frames of flow patterns during the free fall consecutively. After landing, the heater power was turned off and the data stored in the recorder were printed out.

3.2 Learjet Flight Experiment

The experimental package, as shown in Figure 3-4(a) and (b), consists of two racks that meet dimensional requirements of the NASA Learjet and a boiling test section. Rack No.1 contained the entire flow boiling apparatus, while Rack No.2 contained a computer and data acquisition system. The test section stood vertically between the two racks. The flow boiling apparatus mainly consisted of a boiling test section, two 0.178mO.D. acrylic plastic pistons, coiled preheater, condenser, high pressure air tank, and flow meter system. Schematic diagram of the experimental apparatus is shown in Figure 3-5. Specifications of each component are described in the ensuing text.

Test section. Figure 3-6 shows a detailed schematic of the test section. The test section consisted of a 1.28cm diameter, 0.56m long (0.48m for heated length) copper tube with 0.711mm wall thickness, a WATLOW 500W coiled cable heater, and one flow pattern window at the end of the copper tube. The mineral-insulated, stainless-sheath heating cable with 3.2mm diameter was coiled around the copper tube and covered approximately 24% of the surface. The cable was clamped every 5cm to secure solid contact with the tube. The test section was covered with 12.3mm thickness ceramic fiber

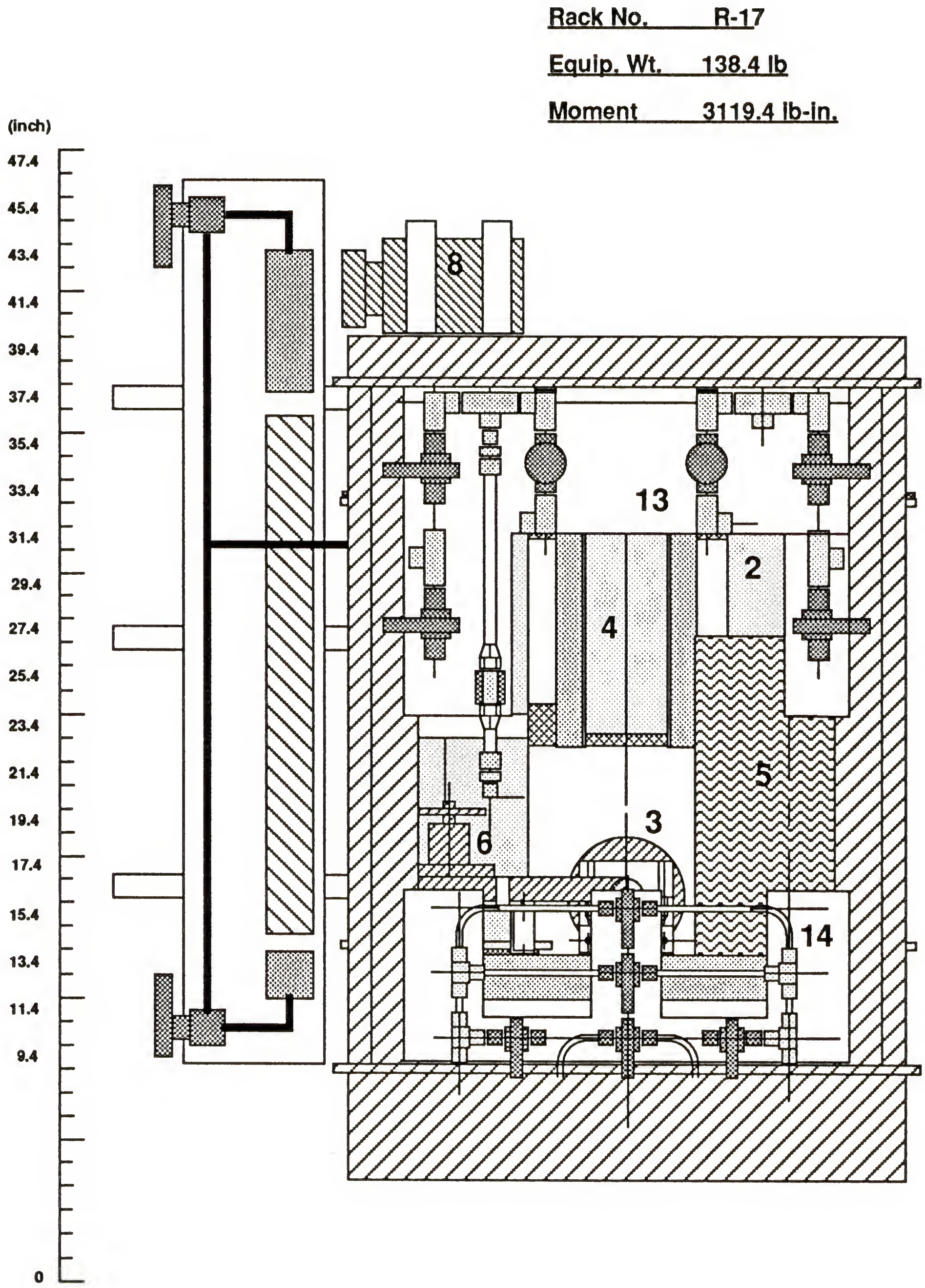

(a) Rack No.1

Figure 3-4 Schematics of Learjet flight research instrument.

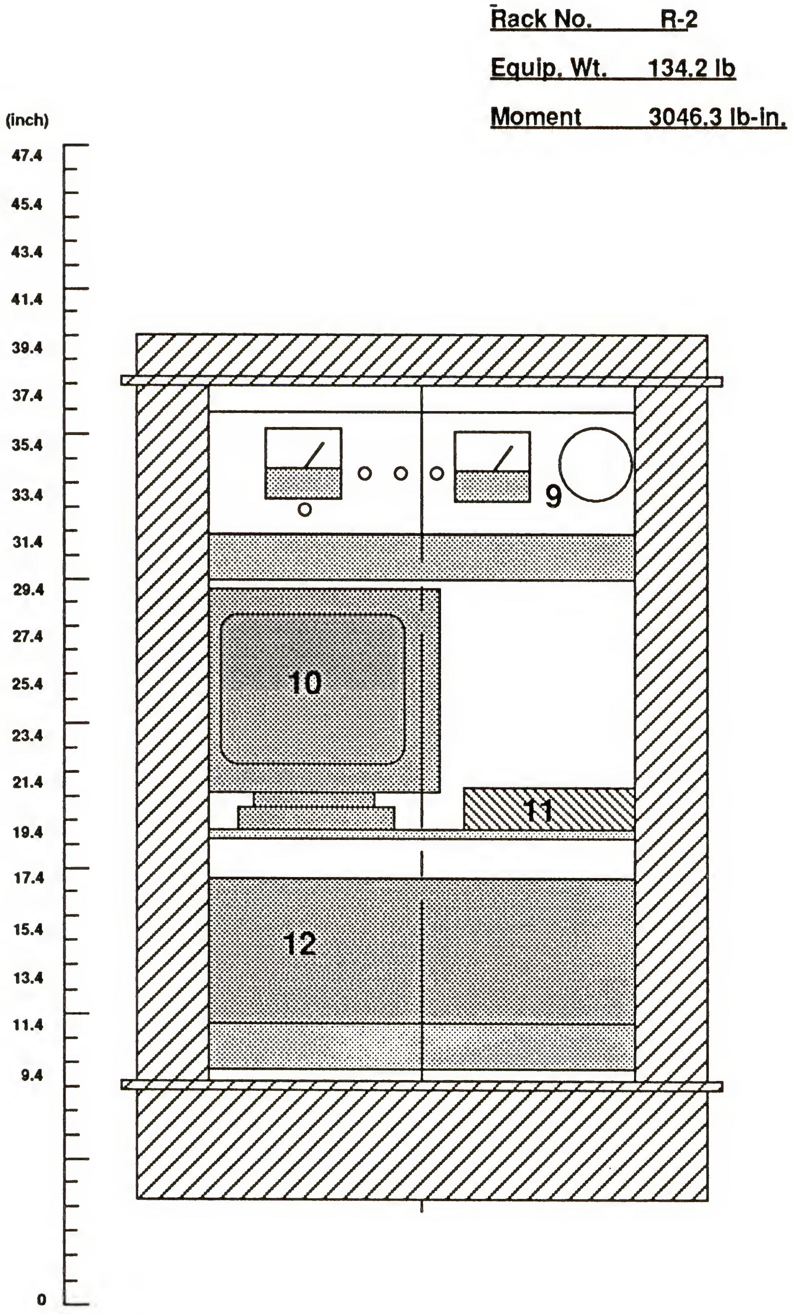

(b) Rack No.2

Figure 3-4 Schematics of Learjet flight research instrument.

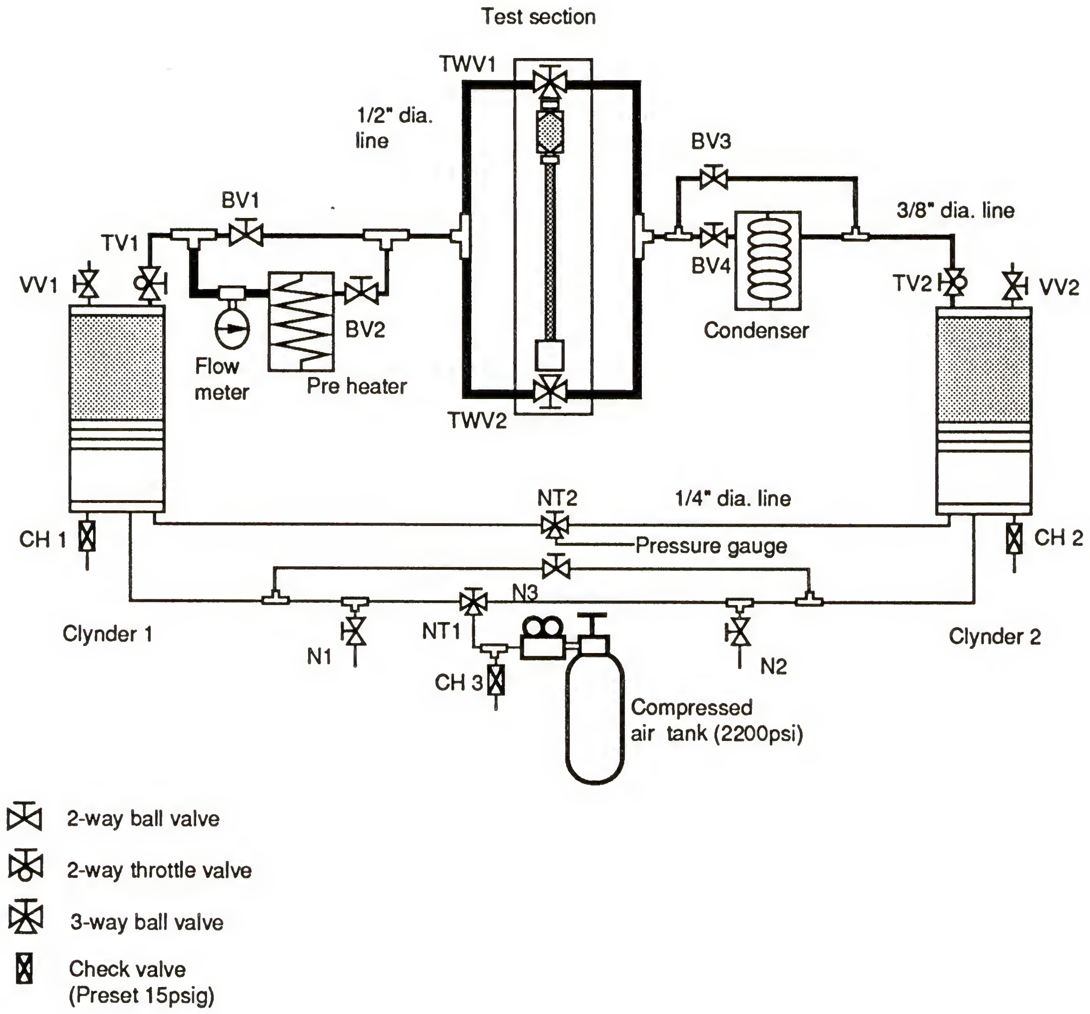

Figure 3-5 Flow boiling loop used in the Learjet flight experiment.

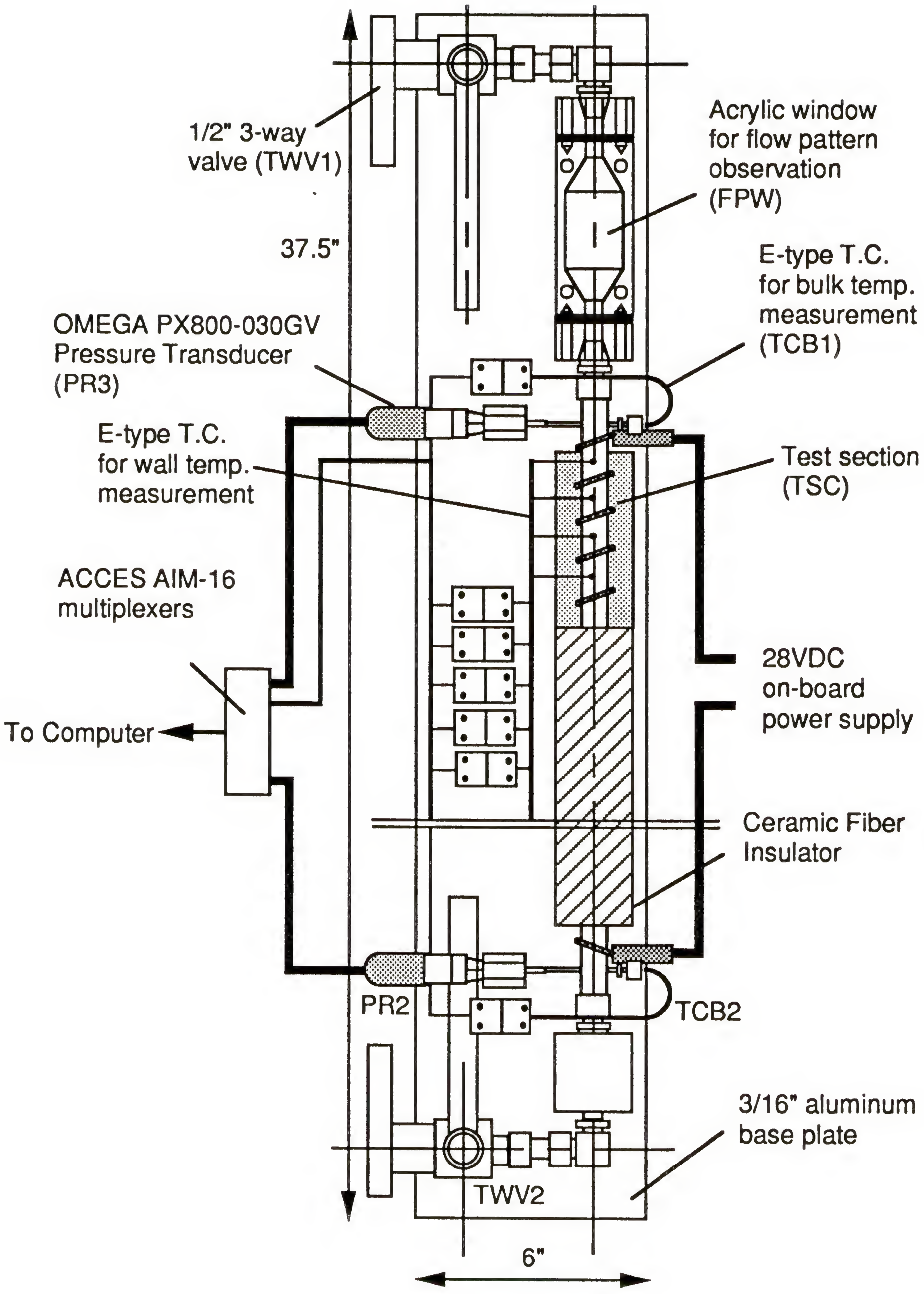
1/2" 3-way valve (TWV1)
37.5"
OMEGA PX800-030GV Pressure Transducer (PR3)
E-type T.C. for wall temp. measurement
ACCES AIM-16 multiplexers
To Computer
Acrylic window for flow pattern observation (FPW)
E-type T.C. for bulk temp. measurement (TCB1)
Test section (TSC)
28VDC on-board power supply
Ceramic Fiber Insulator
PR2
TCB2
3/16" aluminum base plate
TWV2
6"

Figure 3-6 Test section with thermocouples and pressure transducers.

insulating strips to minimize the heat loss to ambient. Two sets of thermocouples were installed inside and outside the insulator to measure the heat loss. The measurement showed that about 15% of heater power was dissipated through the insulator.

Two 12.8mm three-way valves were connected at the ends of the test section to change the orientation of the flow. The entire test section was fastened on a 4.8mm thickness aluminum plate arranged vertically. An array of 17 E-type thermocouples equally spaced on the copper tube measured outside wall temperature change during the experiment. The bulk fluid temperatures were measured by 1.58mm diameter stainless sheathed thermocouples mounted on both ends of the test section. The thermocouple junctions at the tip of the sheath extended 6.4mm into the flow. The accuracy of the temperature measurement determined by calibration was on the order of ±0.5°C.

Two OMEGA gauge pressure transducers (PX800-030GV and PX800-050GV) were mounted at the inlet and outlet of the test section perpendicular to flow to measure the system static pressure as well as the pressure drop across the test section. Nominal accuracy of the transducers is ±0.1%, or on the order of ±27.6Pa for both transducers. The voltage output signal was digitized and converted into psig unit through an ACCES 12-bit data acquisition system.

A mixture of vapor and liquid passed through the flow pattern window at the exit of the test section. The flow channel was formed between two transparent acrylic blocks 2.2mm apart from each other. The blocks were fastened with screws and sealed with Nitrile seals. This thin flow area was designed to prevent overlapping of vapor phase distributed in the liquid and provides a 4x5cm view for flow pattern observation. Flow patterns were recorded by a video camera on high speed mode.

Plastic pistons and pressurized air tank. Before the test, about 9.8 liters of liquid Freon 113 was contained in Piston 1. The pistons were made of 3.2mm acrylic plastic cylinder and 19.1mm end plates hermetically sealed with nitrile O-rings. The interior of the cylinder was divided by a free piston which also served as a boundary between liquid and pressurized air(Figure 3-7). Three O-rings on the piston were lubricated with NOSOL Uta 350, a product of Kluber Lubrication which is compatible with Freon 113.

Piston 1 was pressurized up to 68.9kPa with compressed air stored in a high pressure tank. A regulator controls air flew into the cylinders and maintained pressure constant even in the expanded volume. Figure 3-8 shows the calibration curve for compressed air pressure vs. flow rate. Since the flow rate increased linearly with the air pressure, the required flow rate was obtained by controlling the air pressure.

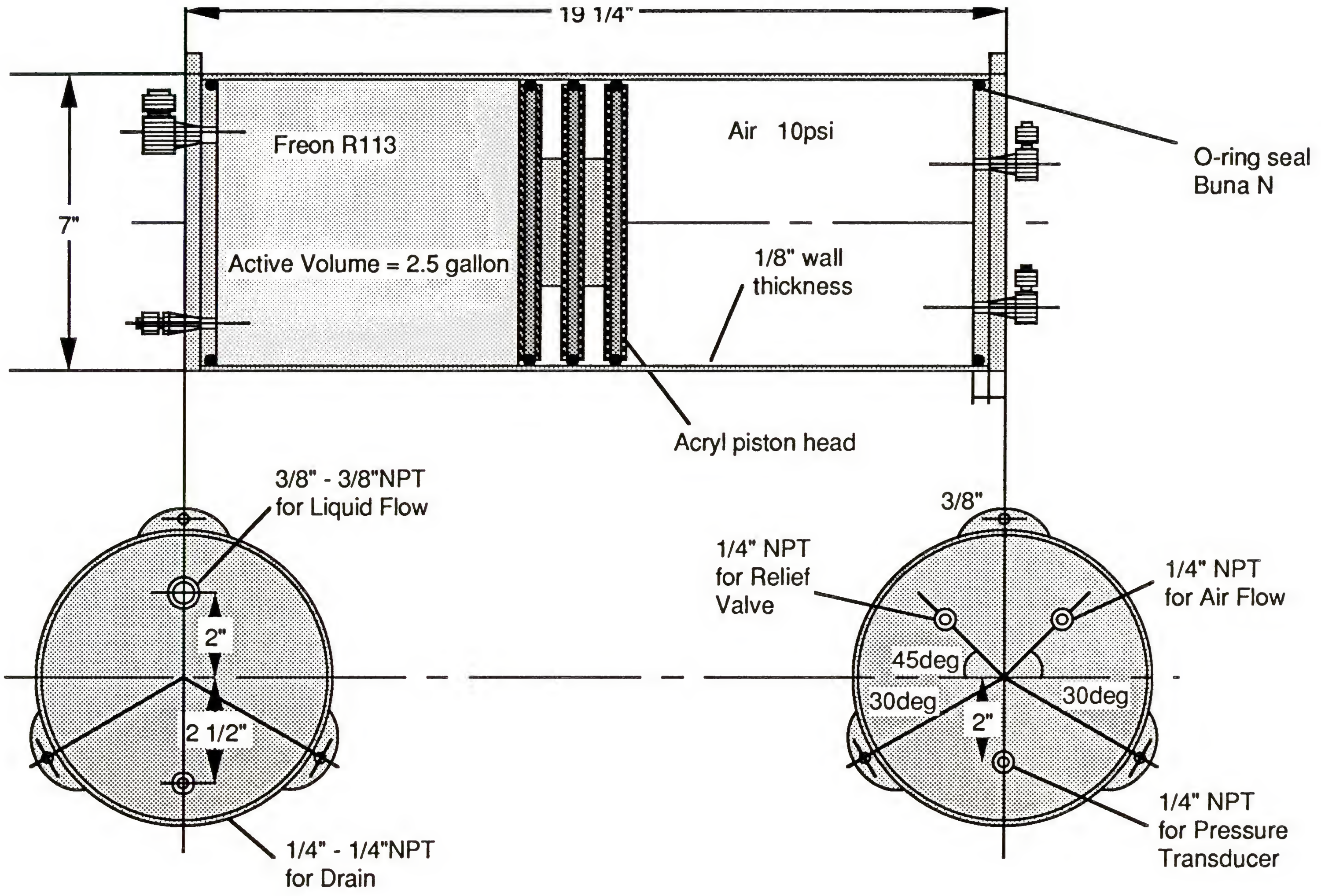

Figure 3-7 A 0.178mO.D. air-driven plastic piston.

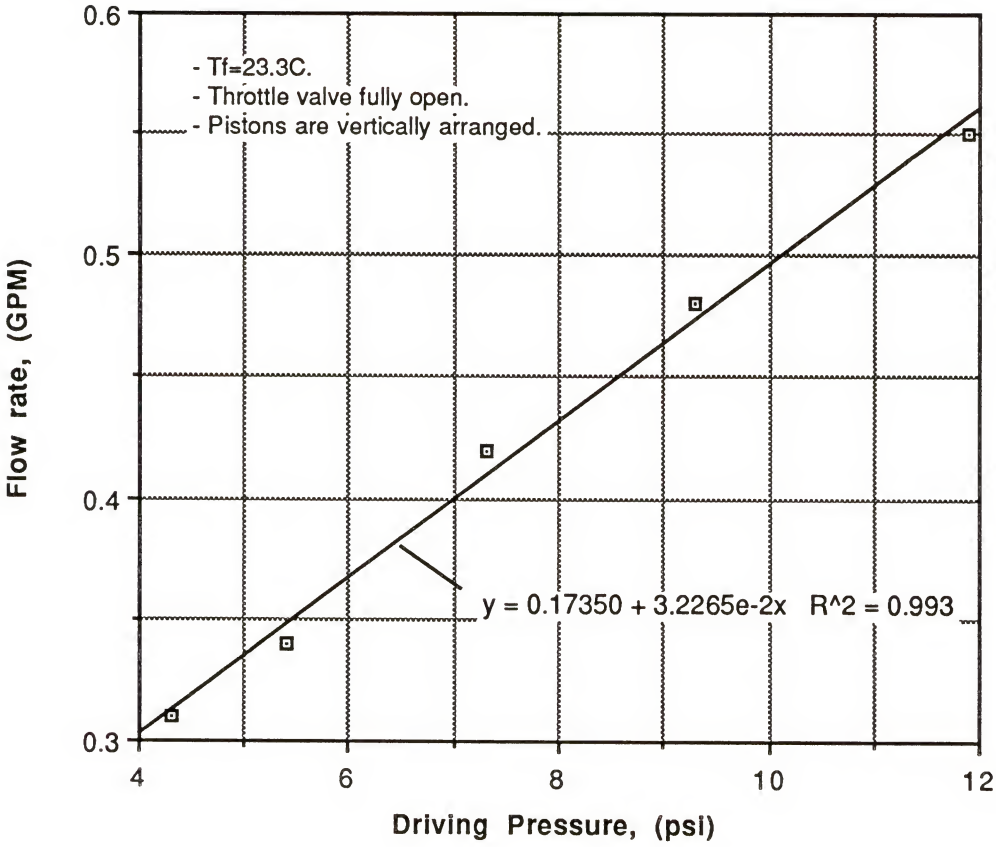

Figure 3-8 Air driving pressure vs. liquid flow rate for the piston system.

Preheater and condenser. The preheater, located in the upstream of the test section, consisted of 9.5mm diameter, 3.4m long coiled copper tube and a 600W heavily insulated heating tape. Although the preheater was originally installed to reduce inlet subcooling, we found during the ground operation that start-up period of the preheater was about 3 minutes, which would sacrifice the number of trajectories available during the flight. Therefore, the preheater was not activated during the present experiments and the test conditions were confined to high subcoolings.

After leaving the test section, a mixture of vapor and liquid was completely condensed inside a 9.5mm diameter, 2.3m copper tube coiled and immersed in ice and water contained in a well-insulated therm flask. Inlet and outlet temperatures were constantly monitored and recorded throughout the experiment. Although the temperature of the iced water was not monitored, previous ground tests showed that it was approximately 1°C.

Flow meter and signal conditioner. An OMEGA turbine flow meter (FTB-201), which was insensitive to the gravity change, measured the liquid flow rate and sent voltage signal to a data acquisition system through a signal conditioner (FLSC-28). The flow meter and signal conditioner were calibrated separately before the experiments and showed an accuracy on the order of ±0.126cc/sec.

Electrical controls. Rack No.2 contained a power control unit and a data acquisition system. The power control unit for the main heater was housed in a 50.8cm long by 12.7cm high by 7.6cm deep aluminum enclosure. The control of power was made by switching the circuit with different resisters. An ammeter indicated the current provided to the main heater (Figure 3-9). The controller draw the nominal 28V dc power from the aircraft power system and provided regulated current to the main heater. The controller was protected by a 20 amp fuse on the power input line. A relay switch activated by 12V dc was used to prevent electrical shock.

The personal computer for data acquisition and a light for flow pattern recording were connected directly to the nominal 60Hz 115VAC power system on board.

Data acquisition system. The data acquisition system included an ACCES 12bit A/D converter installed inside an IBM compatible 286 personal computer and two 16 channel multiplexers. All 32 channels were assigned to properties such as temperatures, pressures, and flow rate, and scanned these data at interval of about 0.7 seconds (Table 3-1). The minimum time interval was determined by the performance of the host computer. On the other hand, the channel-to-channel scanning interval was on the order of a micro second. Since this interval was much smaller than the transient time of thermal properties, it was regarded that the properties were practically sampled at the same time. The outputs from

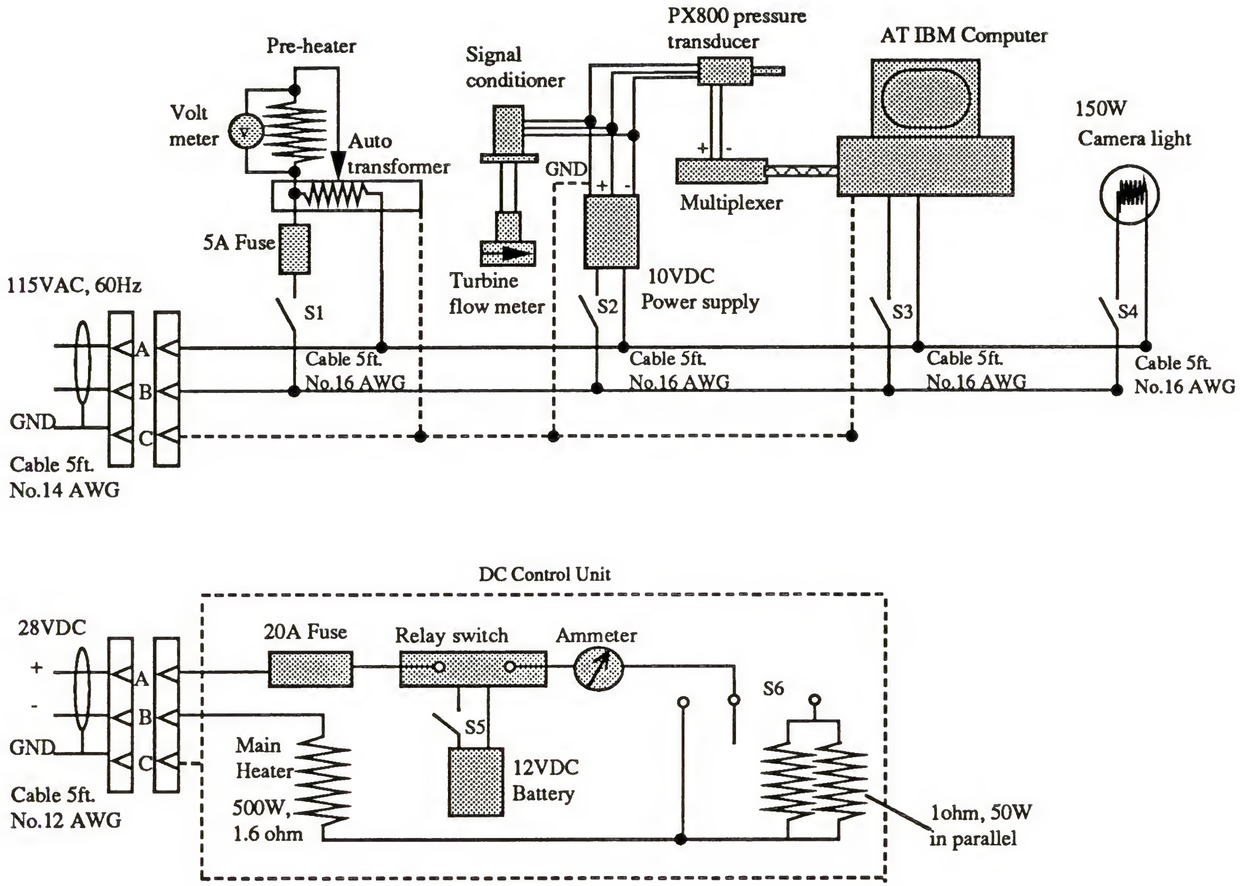

Figure 3-9 Electrical power and interconnect diagram.

Table 3-1 Channel assignments on the multiplexer card.

Channel	Gain	Properties	Unit
0	---	Thermocouple cold junction	(-)
1	x100	TW1 (Inlet Wall temperature)	(C)
2	x100	TW2	(C)
3	x100	TW3	(C)
4	x100	TW4	(C)
5	x100	TW5	(C)
6	x100	TW6	(C)
7	x100	TW7	(C)
8	x100	TW8	(C)
9	x100	TW9	(C)
10	x100	TW10	(C)
11	x100	TW11	(C)
12	x100	TW12	(C)
13	x100	TW13	(C)
14	x100	TW14	(C)
15	x100	TW15	(C)
16	x100	TW16	(C)
17	x100	TW17 (Exit Wall temperature)	(C)
18	x100	Condenser inlet temperature	(C)
19	x100	Condenser exit temperature	(C)
20	x100	Bulk temperature at the inlet	(C)
21	x100	Bulk temperature at the exit	(C)
22	x100	Insulator inside temperature	(C)
23	x100	Insulator outside temperature	(C)
24	x100	Preheater inlet temperature	(C)
25	x100	Preheater exit temperature	(C)
26	x100	Cylinder 1 exit temperature	(C)
27	x100	Preheater inlet temperature	(C)
28	x50	Air pressure in Cylinder 1	(psig)
29	x100	Test section inlet pressure	(psig)
30	x100	Test section exit pressure	(psig)
31	x1	Volume flow rate	(GPM)

thermocouples and pressure transducers on the order of 1/1000 volt was amplified 100 times in the multiplexers. The calibrated data was stored in a 320K virtual memory. Resolution of the present data acquisition system was 2.44mV. The corresponding resolutions for the temperature, pressure,and flow rate were 0.41°C, 48.1Pa, and 0.132cc/sec, respectively.

CHAPTER 4
FLOW PATTERN, VOID FRACTION, AND PRESSURE DROP UNDER MICROGRAVITY CONDITIONS

Selection of appropriate models for hydrodynamic and heat transfer analyses in two-phase flow depends on the prediction of topology of the flow or commonly known as flow patterns. The particular flow pattern is determined by the system pressure, flow rate, heat flux, channel geometry, and gravity level. The influence of the gravity on flow patterns had not been intensively discussed until the application of two-phase flow in space became a practical issue. However, it is easily imagined that the buoyancy-induced motion of the vapor phase would become weak or disappear in microgravity. The first task of the present study is, therefore, to identify the flow patterns under microgravity conditions and obtain an insight into the influence of gravity on two-phase flow structure.

In this chapter, the results of flow pattern observations in drop tower experiments and Learjet flight experiments are presented. Flow patterns in microgravity were compared to those obtained in normal gravity under similar flow conditions and their differences were discussed. Next, results from the pressure drop measurement in drop tower experiments were reported. The influence of gravity on each component of pressure drop was examined.

4.1 Observation of Flow Patterns

Four test conditions were chosen to study flow patterns and boiling evolution in the channel. The experimental conditions in these tests are summarized in Table 4-1. Flow rates and subcoolings in the tests were $37.7 kg/m^2/sec$ and $114.4 kg/m^2/sec$, and 4.6K and 17.0K, respectively. Two relatively high and low subcoolings were selected to investigate the influence of gravity on bubble growth in the superheated layer. The test section was arranged vertically in the test module to minimize the transient effects due to gravity change.

The experimental domain of these tests may be characterized by Froude number, Weber number, and Bond number. These dimensionless groups are defined as

$$Fr = \frac{u_{f0}^2}{gD} \tag{4-1}$$

$$We = \frac{\rho_f u_{f0}^2}{\sigma/D} \tag{4-2}$$

$$Bo = \frac{(\rho_f - \rho_g) gD}{\sigma/D} \tag{4-3}$$

where u_{f0} denotes the liquid velocity at the inlet of the test section, g the gravity constant on the ground ($9.8 m/s^2$), D the diameter of the tube, and σ the surface tension. Fr is the ratio of the inertia to the gravity force, while We is the ratio of the inertia to the surface tension force. Bo is

Table 4-1 Test conditions for flow pattern observation in drop tower experiments.

Case	DOFP1	DOFP2	DOFP3	DOFP4
Mass flow rate ($kg/m^2/s$)	37.7	37.7	114.4	114.4
Inlet subcooling (K)	4.6	17.0	4.6	16.9
Heat flux (kW/m^2)	2.9	2.9	2.9	2.9
Exit quality (%)	17.5	9.2	3.7	-4.5
Flow orientation at exit	vertical up	vertical up	vertical up	vertical up

defined as the ratio of gravity to surface tension forces. Gravitational acceleration reduces to about 1/100 of normal gravity for airplane experiments, and about 1/50 for drop tower experiments. Figure 4-1 shows the variation of Fr, We, and Bo for the drop tower experiments. Under normal gravity conditions, the gravity force is significantly larger than the other forces. Under microgravity conditions, the magnitudes of surface tension and liquid inertia become comparable to that of gravity. Bo for normal and microgravity conditions were 20.4 and 0.41, respectively, indicating that the surface tension became as important as the gravity force. The above result shows that 0.02g of microgravity level in the drop tower experiment was capable of successfully simulating the hydrodynamic aspect of microgravity two-phase flow phenomena.

During the drop tower experiment, growth of flow patterns in a uniformly heated transparent channel was photographed every 0.25 seconds with a motor-driven 35mm still camera during the 1.25 seconds of free fall. Schematic diagrams and photographs of typical flow patterns observed under micro and normal gravity conditions are shown in Figure 4-2(a) and (b). There were three distinguishable flow patterns in vertical upward flow in normal gravity: bubbly, slug, and annular flow. Under microgravity conditions, three flow patterns were also identified; although their details were quite different from the corresponding patterns in normal gravity.

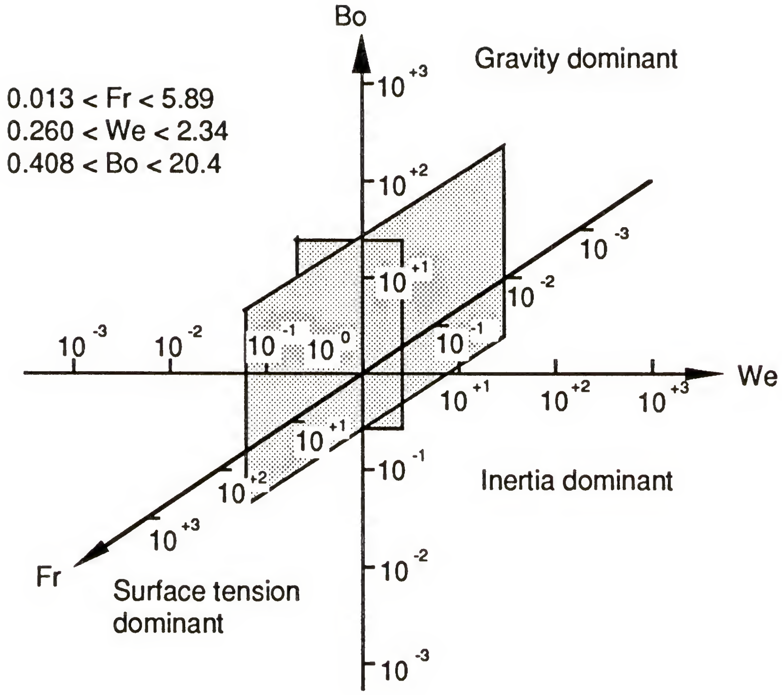

Figure 4-1 Dominant forces under the conditions of the drop tower experiment.

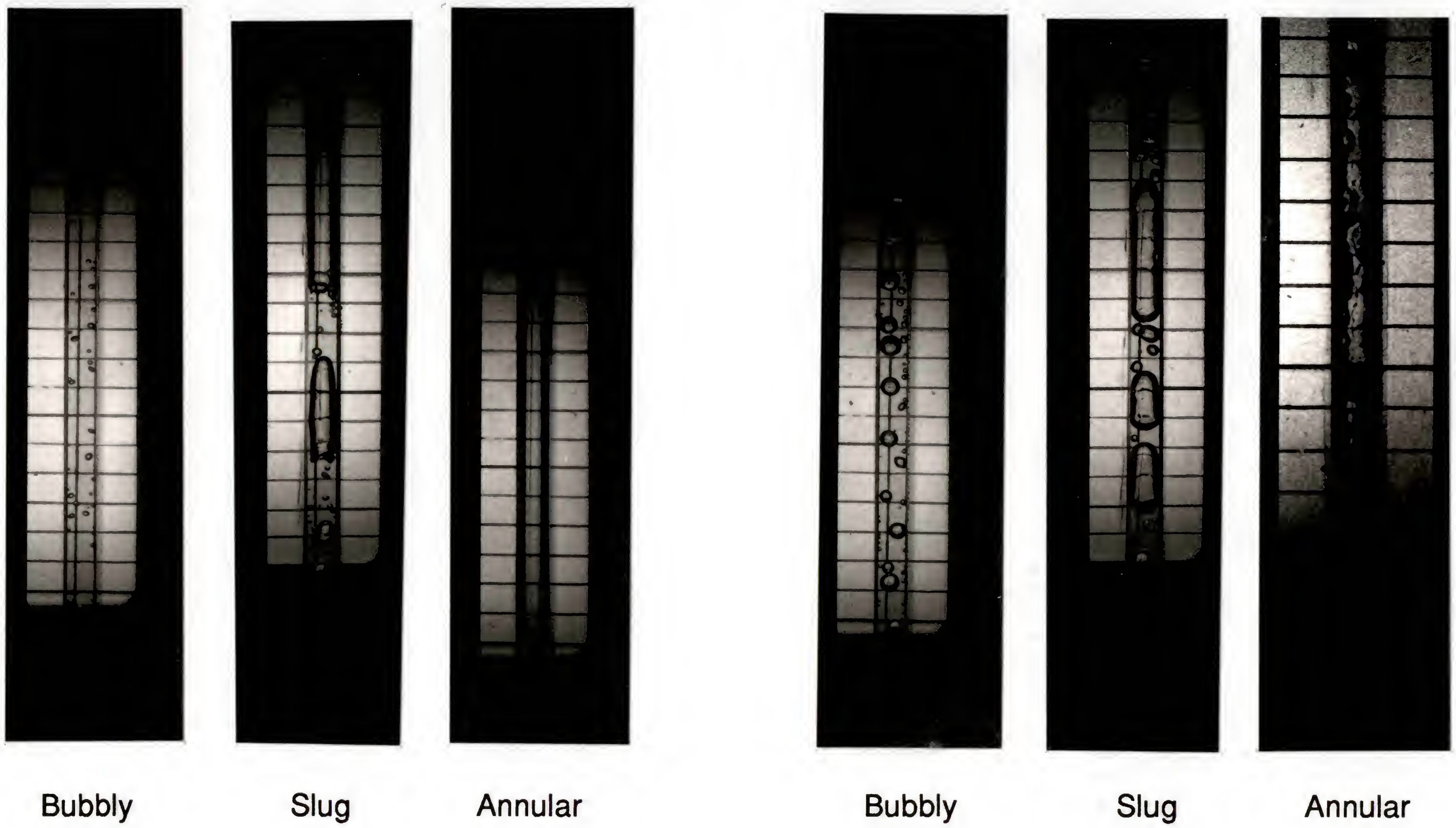

(a) $g/g_o=1.0$

(b) $g/g_o=0.02$

Figure 4-2 Characteristic flow patterns in a vertical tube under various acceleration levels.

In the bubbly flow region, two types of bubbles exist in terms of the way they are formed and the process they contribute to the heat transfer. Those observed on the wall are nucleation bubbles as a result of direct evaporation from a thin microlayer. They transfer significant amount of heat from the wall. The size of these bubbles are determined by hydrodynamic force balance and local thermal conditions on the nucleation site. Relatively large bubbles observed in the liquid core region are formed after several detached nucleation bubbles coalesce into a single larger bubble in the course of their migration into the flow. In vertical flow systems where the buoyancy force acts in the direction of the flow axis, bubble motion in the liquid is accompanied by momentum and heat exchange on a local level. This process causes further turbulence even in laminar flow and promotes heat transfer.

The photographs in Figure 4-2 indicates that the size of nucleation bubbles was similar under normal and microgravity conditions, whereas the size of coalesced bubbles in microgravity was approximately 3-4 times larger than under normal gravity conditions. It is also shown that the nucleation bubbles were constantly removed by the liquid flow even under microgravity conditions without assistance of the buoyancy force. Bubble growth is mainly controlled by the thermal condition of a thin superheated layer adjacent to the heating wall. On the other hand, the formation of coalesced bubbles is governed by relative motion of vapor phase. The almost spherical shape of each bubble indicates that the relative velocity was extremely small or zero.

It is considered that the size of a coalesced bubble is related to the Helmholtz instability of the liquid-vapor interface having relative motion. The wavelength of an interface that leads to instability is a function of the Laplace constant defined as

$$\lambda_0 = 2\pi\sqrt{\frac{\sigma}{(\rho_f - \rho_g)\,g}} \tag{4-4}$$

where λ_0 is the wave length to provide a minimum slip velocity maintaining interface stability. As the acceleration level g becomes smaller, λ_0 becomes longer. Under the gravity level of 0.02g, λ_0 is 7.1 times longer than that of normal gravity. There seems to be a certain relation between the enlarged bubble size and the extended stabilizing wavelength under microgravity conditions.

Small bubbles were observed between the heating surface and the vapor core in both slug and annular flow regimes. This phenomenon was more pronounced in the annular flow regime in which small bubbles were trapped in a liquid film. The existence of these small bubbles significantly perturbs the surface of the liquid film formed on the heating surface. In the annular flow, this highly disturbed, irregular liquid interface causes an increase in pressure drop.

The results of flow pattern observation along with the exit quality and superficial velocities are summarized in Table 4-2. The term "Frothy" was used to describe a liquid film containing small bubbles. Flow patterns of upper 30cm part of the test section were photographed by a motor-driven still camera. The transition of flow patterns from 1-g to 0.02-g under the four experimental conditions are shown in Figure 4-3(a) through (h). Figure 4-3(a) and (c) for the exit qualities of 17.1% and 9.5%, respectively, indicate that once the annular flow regime is established in normal gravity, the pattern sustains under microgravity conditions. Figure 4-3(e) and (f) shows a transition of flow pattern from bubbly to slug in the lower part and from slug to annular flow in the upper part of the channel. The flow pattern transition under Case DOFP4 shown in Figure 4-3(g) and (h) suggest that the shear stress and velocity profiles under microgravity conditions were quite different from those in normal gravity. Since the thermal equilibrium quality at the exit for this case was -1.7%, the bulk temperature of the liquid flow was still less than the saturation temperature in normal gravity. The bubbles tend to recondense upon touching the cooler liquid flow. As a result, most bubbles were observed near the wall region rather than in the liquid core.

The second series of experiments was conducted using a NASA Learjet which provides approximately 18 seconds of microgravity conditions(0.01g). The flow patterns were

Table 4-2 Vapor volume fraction and flow patterns in drop tower experiments.

Location z(m)	X (%)	U_g (m/s)	U_l (m/s)	$\langle\beta\rangle$ 1.0g	$\langle\beta\rangle$ 0.02g	$\langle\alpha\rangle$ 1.0g	$\langle\alpha\rangle$ 0.02g	Flow patterns 1.0g	Flow patterns 0.02g
0.5-0.4	17.5	0.86	0.02	0.79	0.79	0.59	0.79	Annular	Annular-Frothy
0.4-0.3	10.9	0.64	0.02	0.53	0.62	0.38	0.53	Slug	Annular-Frothy
0.5-0.4	9.2	0.48	0.02	0.47	0.77	0.25	0.77	Slug-Annular	Annular
0.4-0.3	2.7	0.26	0.03	0.24	0.50	0.11	0.50	Bubbly-Slug	Slug
0.5-0.4	3.7	0.42	0.07	0.29	0.49	0.14	0.49	Slug	Slug-Frothy
0.4-0.3	1.6	0.01	0.08	0.08	0.42	0.03	0.42	Bubbly	Slug-Frothy
0.5-0.4	-4.5	---	---	0.04	0.23	0.02	0.23	Bubbly	Bubbly(large)
0.4-0.3	-6.7	---	---	0.04	0.08	0.01	0.08	Bubbly	Bubbly(large)

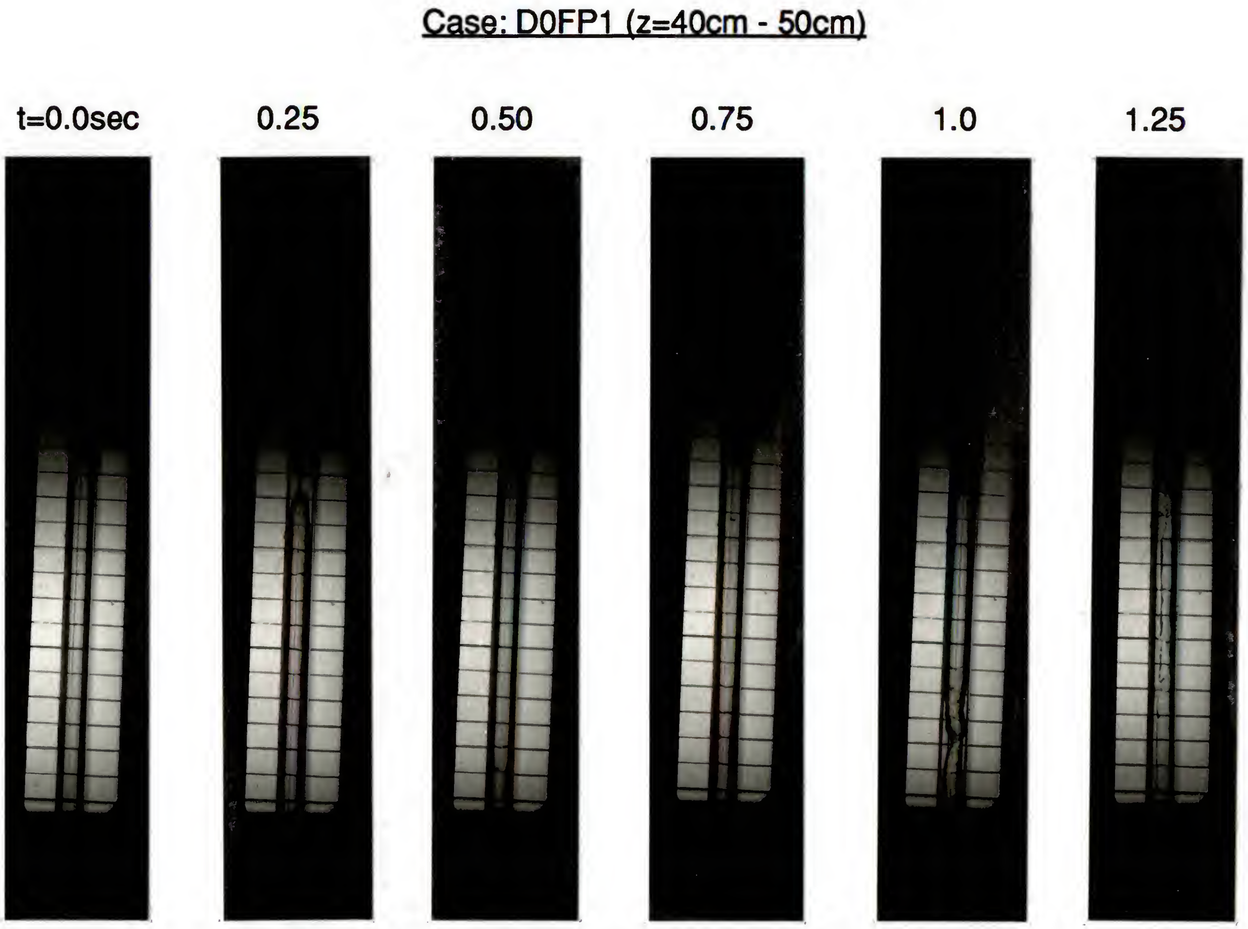

(a) DTin=4.6C, G=37.7kg/m^2/s, Xex=17.5%.

Figure 4-3 Flow pattern transitions during the free fall.

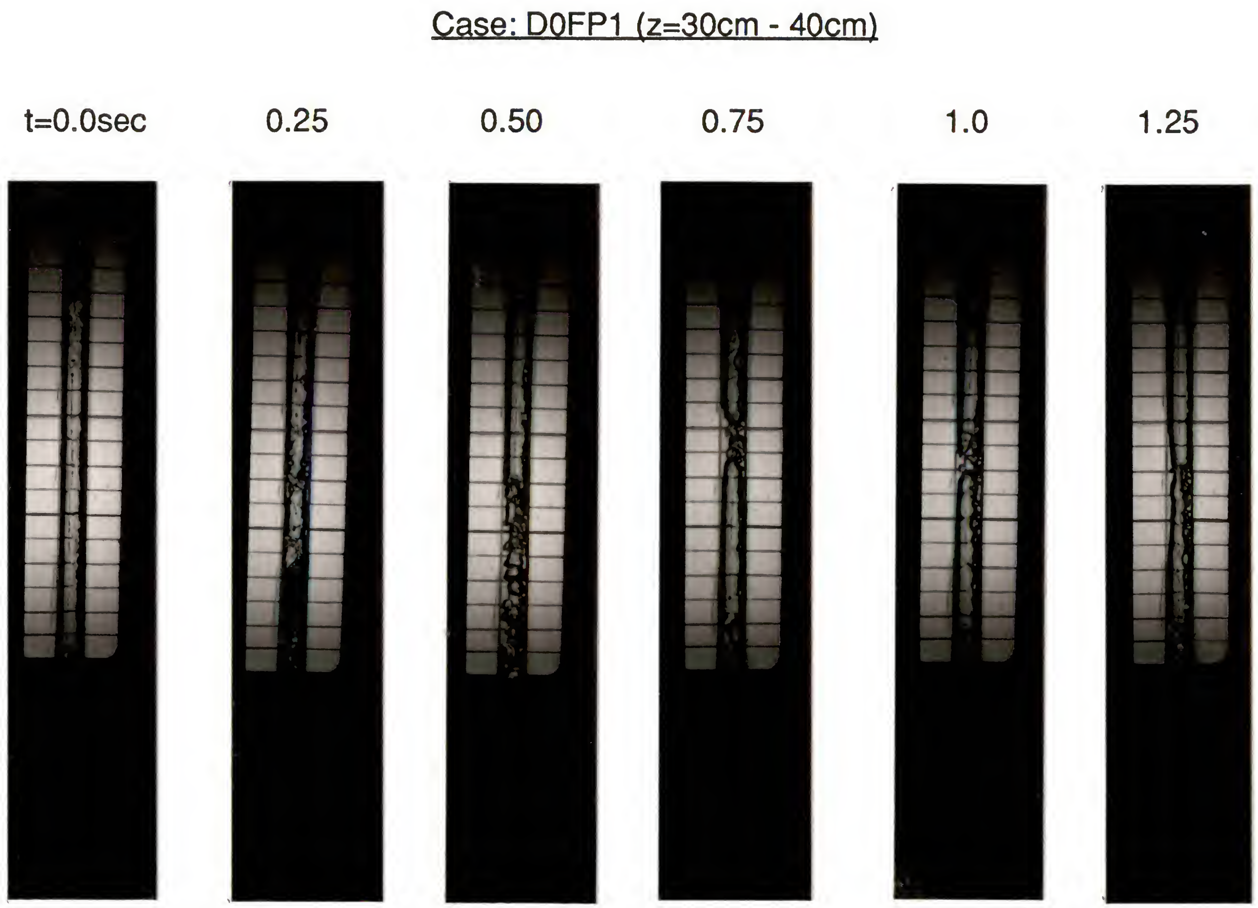

(b) DTin=4.6C, G=37.7kg/m^2/s, Xex=10.9%.

Figure 4-3 Flow pattern transitions during the free fall.

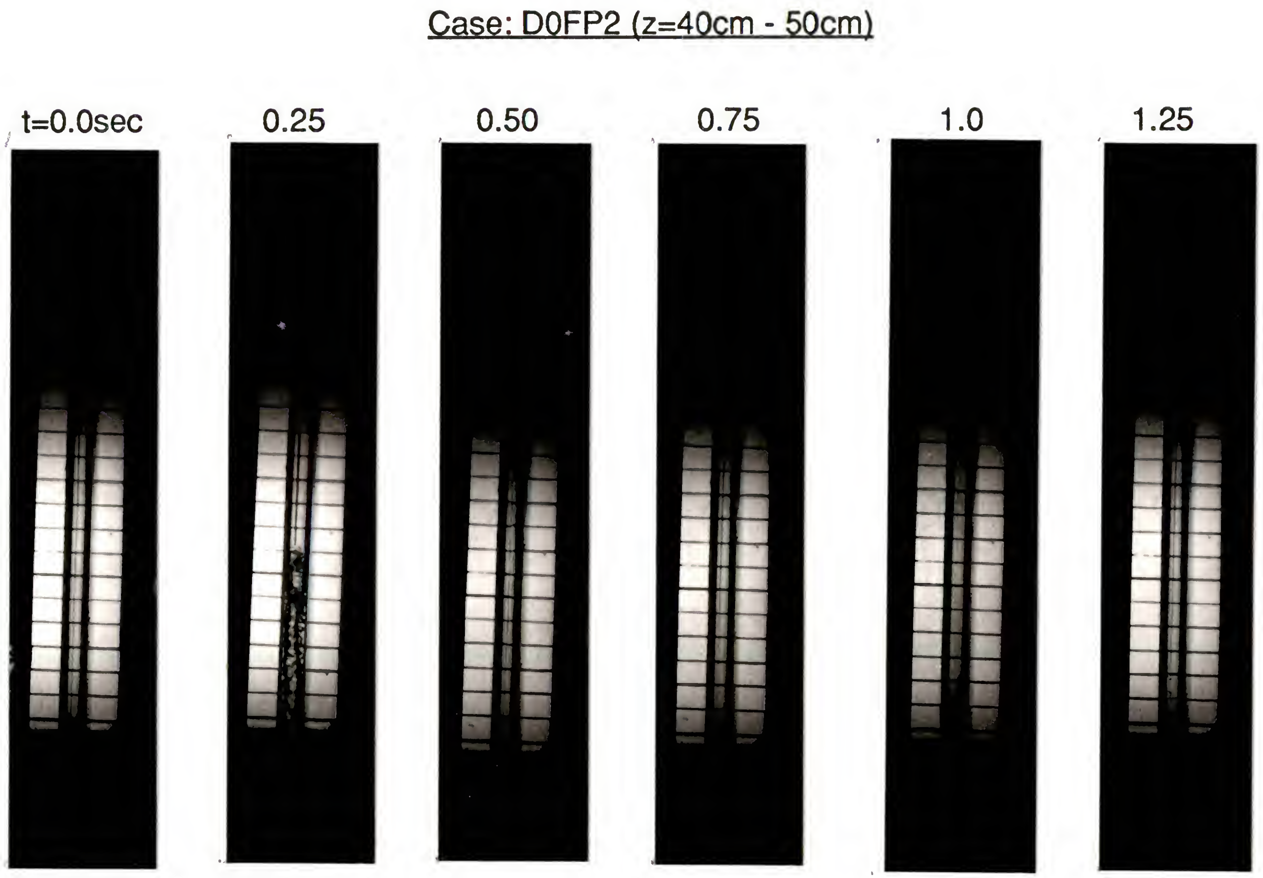

(c) DTin=17.0C, G=37.7kg/m^2/s, Xex=9.2%.

Figure 4-3 Flow pattern transitions during the free fall.

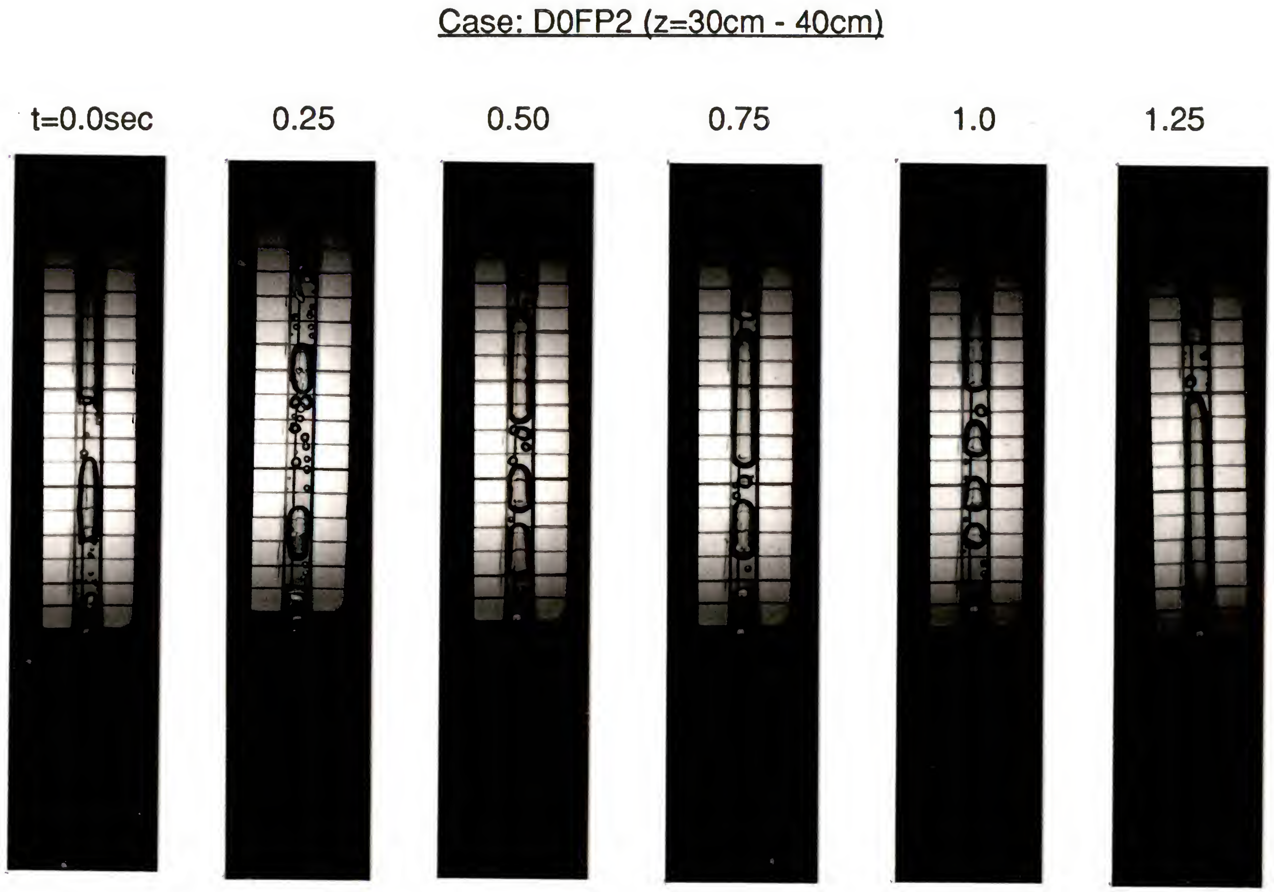

(d) DTin=17.0C, G=37.7kg/m^2/s, Xex=2.7%.

Figure 4-3 Flow pattern transitions during the free fall.

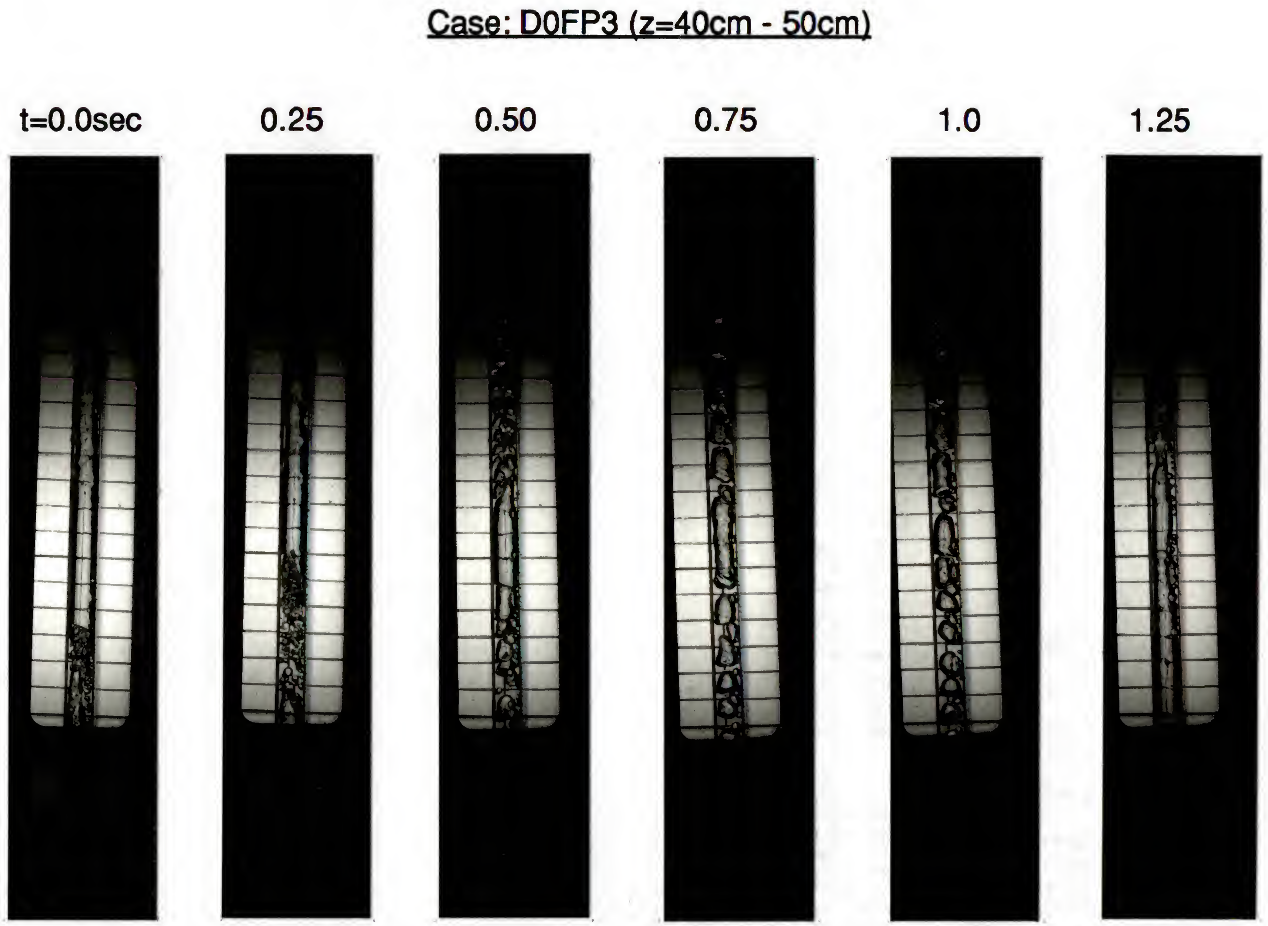

(e) DTin=4.6C, G=114.4kg/m^2/s, Xex=3.7%.

Figure 4-3 Flow pattern transitions during the free fall.

Case: D0FP3 (z=30cm - 40cm)

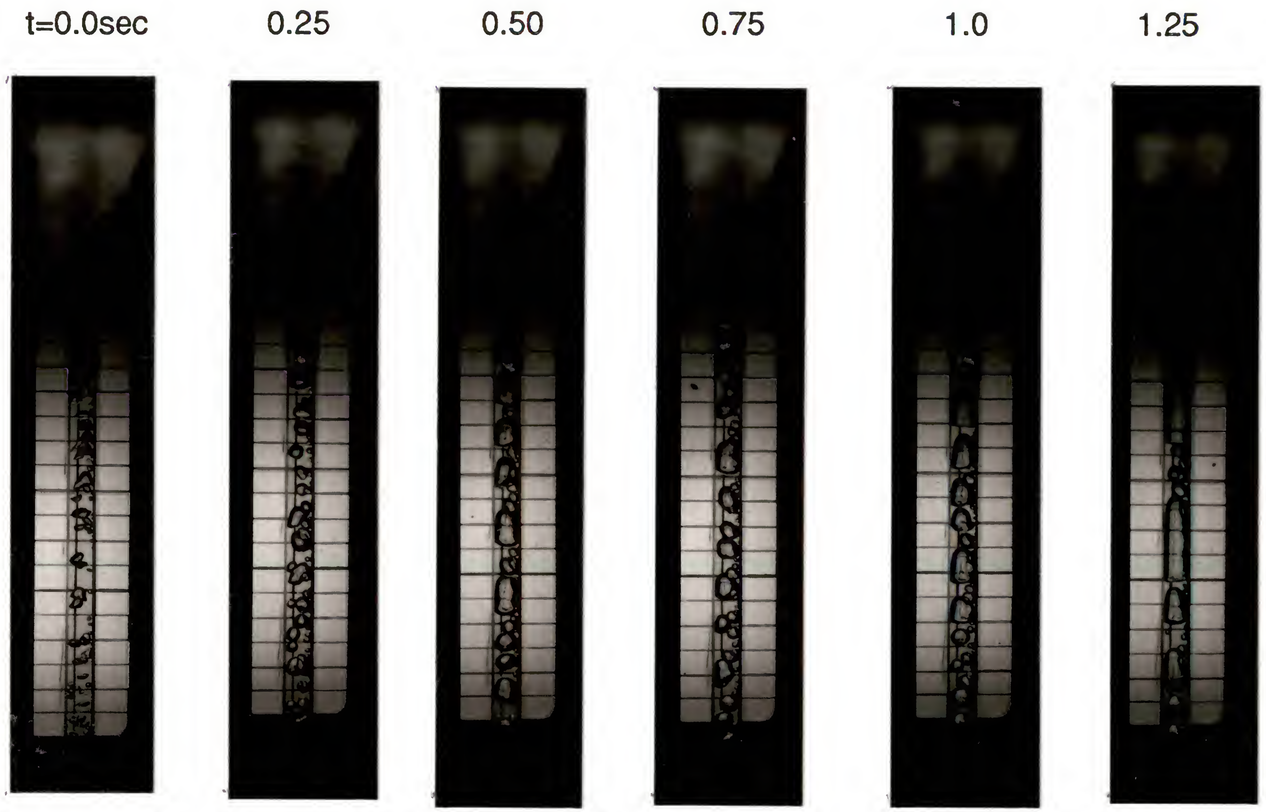

(f) DTin=4.6C, G=114.4kg/m^2/s, Xex=1.6%.

Figure 4-3 Flow pattern transitions during the free fall.

Case: D0FP4 (z=40cm - 50cm)

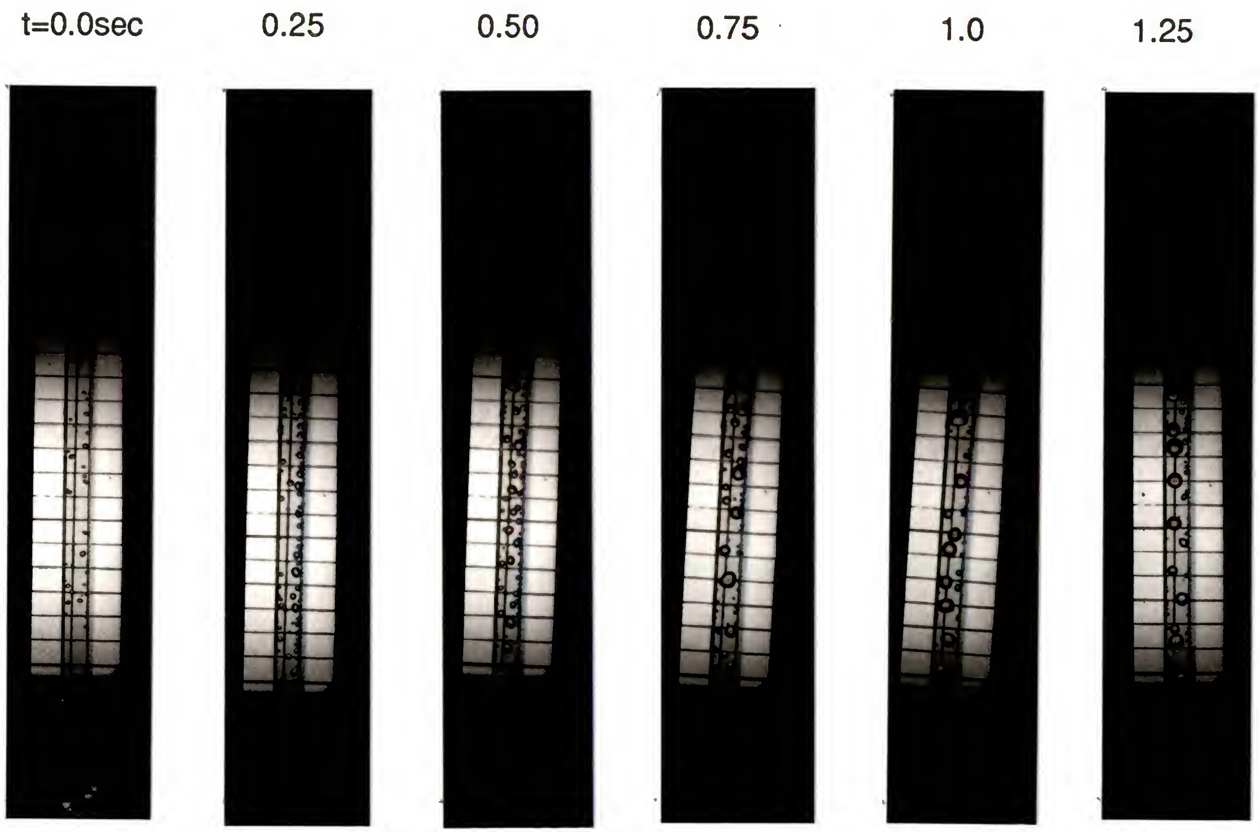

(g) DTin=16.9C, G=114.4kg/m^2/s, Xex=-4.5%.

Figure 4-3 Flow pattern transitions during the free fall.

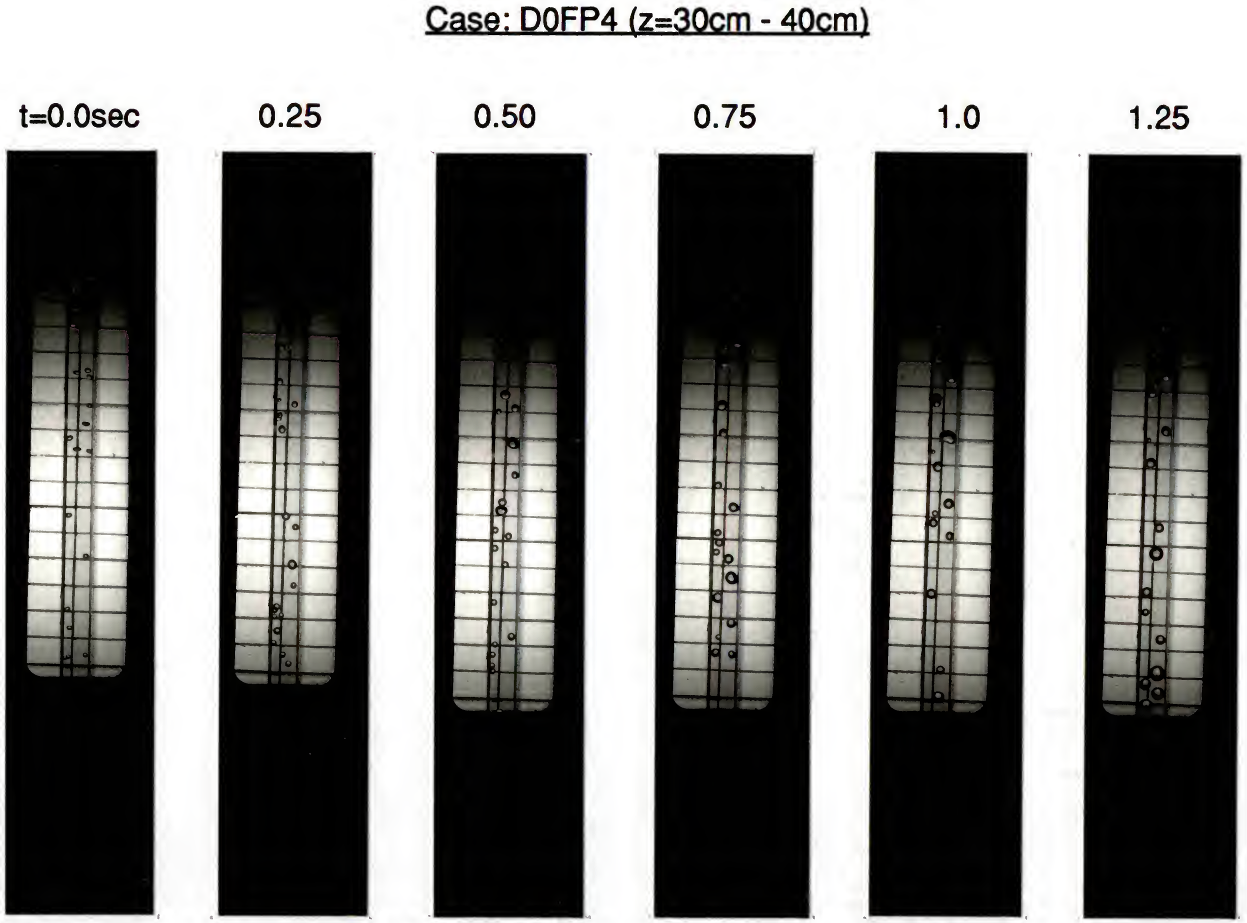

Case: D0FP4 (z=30cm - 40cm)

(h) DTin=16.9C, G=114.4kg/m^2/s, Xex=-6.7%.

Figure 4-3 Flow pattern transitions during the free fall.

recorded with a video camera at the exit of the test section through two transparent plastic blocks between which was a 2.6mmx38.4mm rectangular channel. This rectangular channel has the same cross sectional area as the circular boiling test section attached below. This prevents a pressure drop at the junction and is intended to provide two-dimensional void distribution across the cross section. A high-speed mode, video camera was used to investigate continuous motion of phase change and to measure bubble velocity in the dispersed flow. After several trials, a high-speed mode of 1/2000 second with back-lit setting was found to be appropriate to record the moving boundaries of bubbles.

During the experiment, the high-speed images were blurred due to power failure of a video light. The video camera was switched to an automatic mode and recording was continued. The recorded images qualitatively showed the fundamental difference of vapor phase distribution during the gravity transition. The observation of flow patterns in subcooled flow identified a similar change of vapor phase distribution to that observed in the drop tower experiment. For Case F1015 with the exit quality of -0.41%, the slug flow observed in normal gravity changed into the annular flow with smooth surface in microgravity. This observation agrees with the previous result from DOFP3. The conditions at the exit of the test section for F1020 and F1035 were highly subcooled. Formation of large bubbles, similar to those observed in DOFP4 in the drop tower experiment, was also observed during the microgravity period.

Through the two series of microgravity experiments, three types of typical flow patterns were also identified under 0.02g and 0.01g microgravity conditions. The flow pattern in the subcooled boiling region in both normal and microgravity was classified as bubbly flow, although the diameter of coalesced bubbles in microgravity was significantly larger than that in normal gravity. The concentrated bubbly flow and slug flow in normal gravity tends to shift into the annular flow in microgravity. The influence of gravity appeared less significant on the hydrodynamic aspect of annular flow.

Flow pattern mapping. Observed flow patterns in the drop tower experiments are plotted on the Dukler reduced-gravity flow pattern map as a function of liquid and vapor volumetric fluxes, U_{ls} and U_{vs}[53]. Among various flow regime maps[13], Dukler's map was chosen because the volumetric flux was a measurable quantity independent of gravity. Figure 4-4(a) and (b) show the distributions of flow patterns under normal and microgravity conditions, respectively. Although the number of data sets is small, each flow pattern is well classified on these maps. Large bubbles observed in the low-quality range were also classified as bubbly flow.

Transition boundaries. The relationship between the two velocities is given by

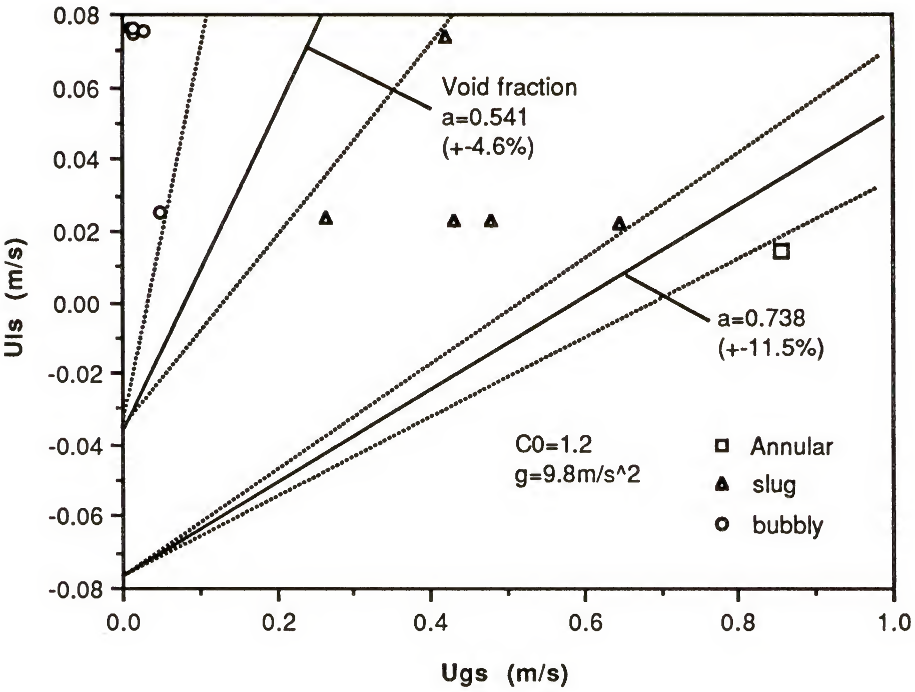

(a) g/gn=1.0

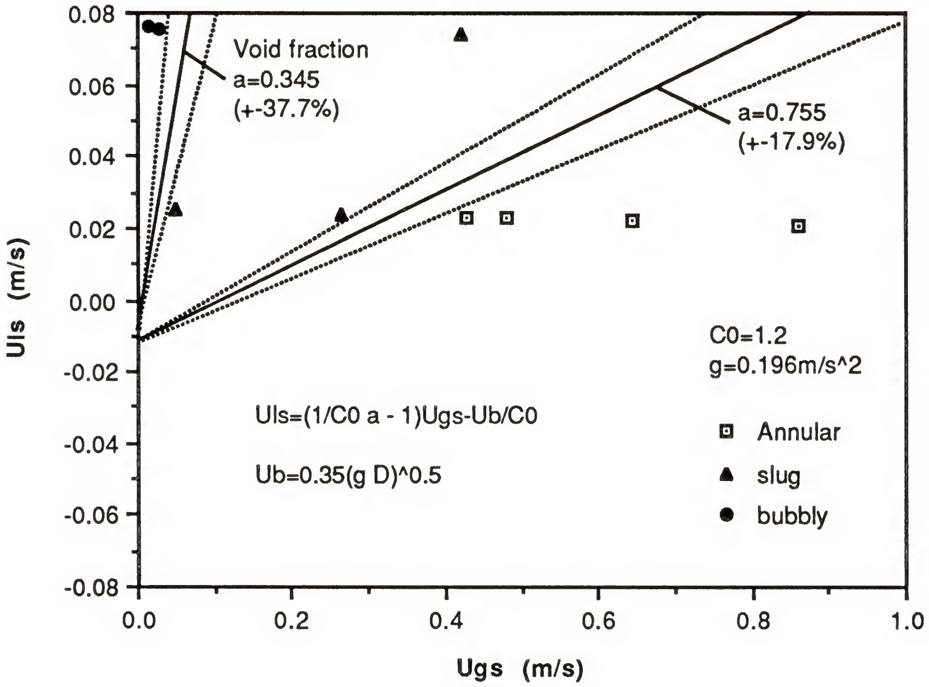

(b) g/gn=0.02

Figure 4-4 Flow pattern transitions on the Dukler flow regime map.

$$U_{ls} = \left(\frac{1}{C_0 \alpha} - 1 \right) U_{gs} - \frac{U_b}{C_0} \tag{4-5}$$

where U_b is the bubble rising velocity and expressed as

$$U_b = 0.35 \left(\frac{(\rho_f - \rho_g)\, g D}{\rho_f} \right)^{1/2} \tag{4-6}$$

for slug flow, while U_b for bubbly flow is given by[51]

$$U_b = 0.33\, g^{0.76} \left(\frac{\rho_f}{\mu_f} \right)^{0.52} R_b^{1.28} \tag{4-7}$$

for bubble diameters less than 1mm. For low pressures, Eq.(4-6) is reduced to $0.35(g \cdot D)^{1/2}$. C_0 in Eq.(4-5) is the distribution parameter defined in the drift flux model. A value of 1.2 was assumed throughout the analysis for simplicity. The transition boundaries from bubbly to slug and slug to annular flow were experimentally obtained and shown in Figure 4-4. The critical void fractions for each boundary was calculated from Eq.(4-5). The value of U_b was obtained by assuming $g=0.196 m/s^2$ in microgravity.

The boundaries between bubbly and slug flow are given by

$\alpha_{BS}=0.538\pm0.025$ (1.0g), and

$\alpha_{BS}=0.378\pm0.130$ (0.02g),

while those between slug and annular flow are

$\alpha_{SA}=0.757\pm0.085$ (1.0g), and

$\alpha_{SA}=0.794\pm0.135$ (0.02g).

It is interesting to note that these boundaries are close even though the acceleration is changed. The void fraction is a function of slip velocity and significantly varies when the gravity level is reduced. However, the critical void fractions are mainly determined by the geometry of flow channel and the velocity distribution of flow. It appears that the critical void fractions are independent of gravity change. In other words, the same flow pattern map can be used for variable gravity conditions when void fraction is used as a transition criterion. To verify the above hypothesis, more data must be collected under microgravity conditions.

Colin et al. [14] and Dukler et al. [53] proposed different values of 0.2 and 0.45, respectively, as a boundary between bubbly and slug flow based on their adiabatic, horizontal two-phase flow experiments carried out aboard a reduced-gravity aircraft. The present analysis qualitatively agreed with their results. This implies that the hydrodynamic mechanism leading to bubble coalescence is independent of gravity change. The boundary for the transition from slug to annular flow was not reported since their system was horizontal.

Another issue neglected in the above analysis is the estimation of the distribution parameter, C_0. As described in the previous section, the radial distribution of void fraction is quite different especially in the subcooled region. Selection of different values for C_0 leads to different criteria for boundaries. An estimation of the value of C_0 under microgravity conditions was attempted using the radial distribution of the void fraction and discussed in the following section.

4.2 Void Fraction

The void fraction was measured by image analysis of the same photographs used for identifying flow patterns. The Macintosh program IMAGE 1.28P converts the grayscaled images into binary files. By adjusting the threshold, the area of vapor and liquid phases were converted into black and white pixels, respectively. Since the visual observation of flow patterns described above identified a significant increase in void fraction, the present analysis on void fraction was focused only on the low quality range. Cases D0FP3 and D0FP4 with exit qualities of 3.7% and -4.5%, respectively, were selected for this purpose. In the high-quality region whose flow patterns are slug and annular, the irregular boundaries of vapor phase was difficult to define with the present method.

The binary images of flow patterns are shown in Figure 4-5. IMAGE 1.28p then counted the number of bubbles in the designated area to yield the average diameter of each bubble. The accumulated area of vapor phase was divided by the total area of the photographed region to obtain the average vapor volume fraction. Since the flow patterns of interest are discrete bubbly and slug flow in the low quality region, the

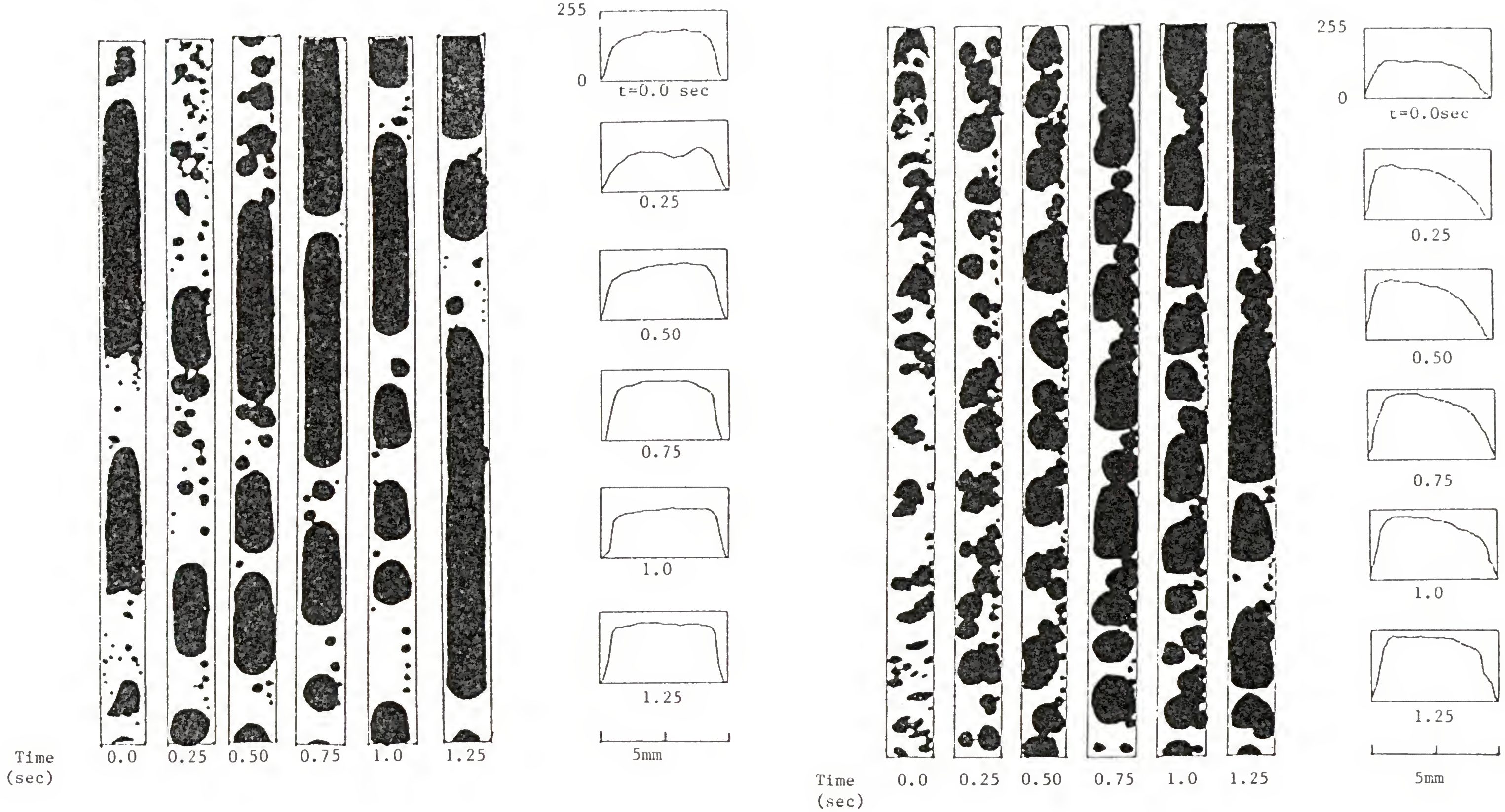

(a) (b)

Figure 4-5 Binary images of vapor phase distributions in the radial directions. (a) DOFP4 (z=40-50cm), (b) DOFP4 (z=30-40cm), (c) DOFP3 (z=40-50cm), and (d) DOFP3 (z=30-40cm).

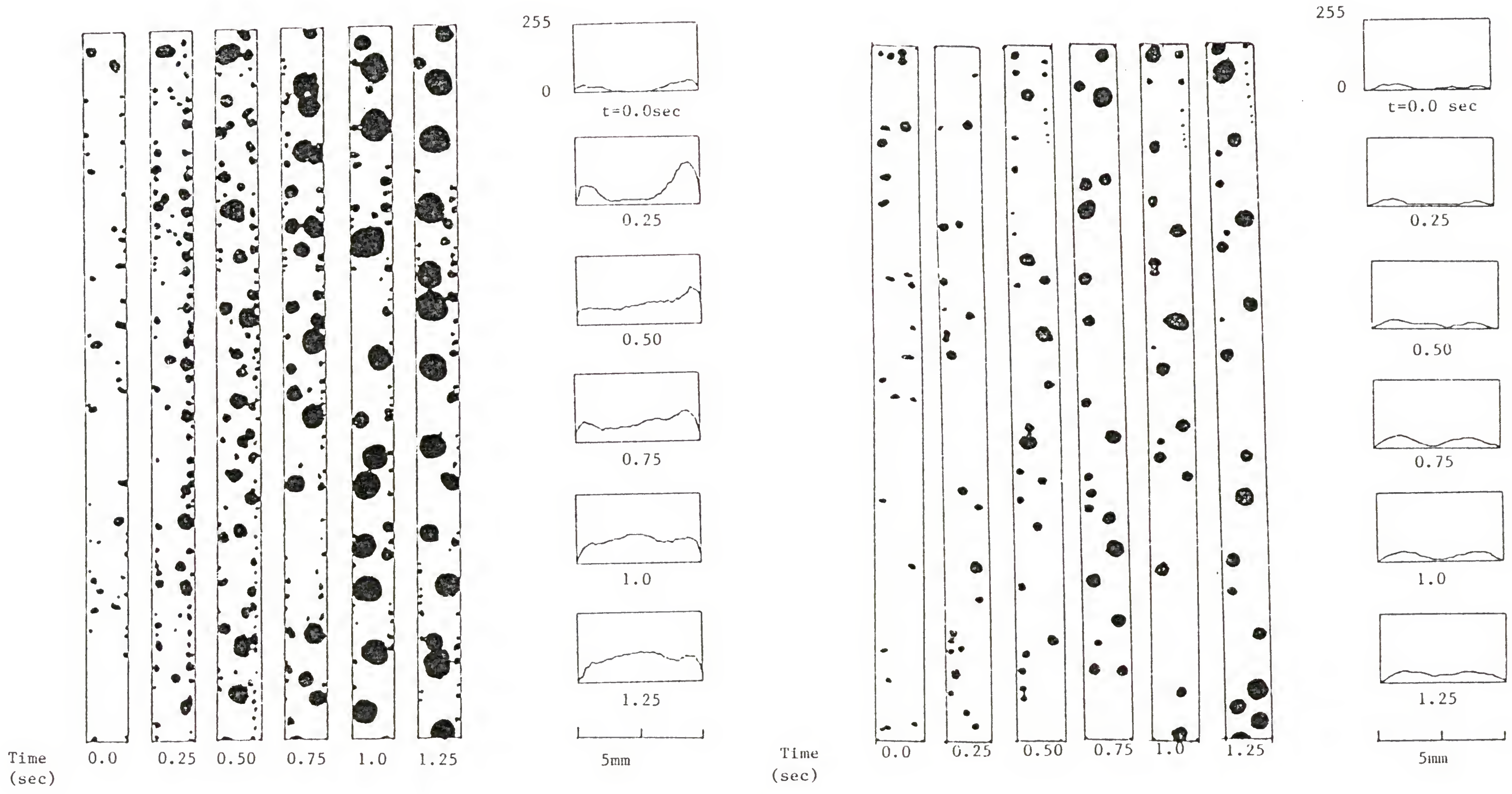

(c)

(d)

Figure 4-5 (cont.) Binary images of vapor phase distributions in the radial directions. (a) DOFP4 (z=40-50cm), (b) DOFP4 (z=30-40cm), (c) DOFP3 (z=40-50cm), and (d) DOFP3 (z=30-40cm).

error caused by the overwrapped vapor phase was assumed negligible.

The void fraction, defined as the area ratio of vapor phase across the cross section, is calculated from the volume fraction using the following relationship:

$$\frac{(1-\alpha)}{\alpha} = s\frac{(1-\beta)}{\beta} \qquad (4\text{-}8)$$

where s is the slip ratio given by

$$s = \left(\frac{\rho_f}{\rho_g}\right)^{0.205} Re^{-0.016} \qquad (4\text{-}9)$$

for normal gravity cases[25]. The above correlation for the slip ratio does not account for gravity change. The average void fraction in microgravity was significantly larger than that with normal gravity in the entire low quality range. However, the void fraction profiles for normal and microgravity are likely to merge in the high-quality region. This is confirmed by the photographs for Cases D0FP1 and D0FP2, in which the once-established annular or concentrated slug flow patterns in normal gravity remained as they were in microgravity. The experimental results showed that the hydrodynamic aspect of two-phase flow was significantly influenced by gravity change in the low-quality region. In the present study, the drift flux model, Sekoguchi's model, and the slip correlation were employed to predict void fraction profiles.

Drift flux model. The drift flux model proposed by Kroger and Zuber includes a gravity term explicitly upon evaluating the weighted mean drift velocity $<u_{gj}>$. The expression for $<u_{gj}>$ is flow-pattern dependent and different forms are proposed for particular flow patterns. For the case of one-dimensional, vertical up-flow of isolated bubbles with little coalescence[32]:

$$<u_{gj}> = 1.53(1-\alpha)^2 \left[\frac{\sigma g(\rho_f - \rho_g)}{\rho_f^2}\right]^{1/4}, \qquad C_0 = 1.0 \qquad (4\text{-}10)$$

while, for vertical-up flow in the bubbly-slug region,

$$<u_{gj}> = 1.41\left[\frac{\sigma g(\rho_f - \rho_g)}{\rho_f}\right]^{1/4}, \qquad C_0 = 1.2 \qquad (4\text{-}11)$$

where C_0 is the distribution parameter defined as

$$C_0 = \frac{<\alpha j>}{<\alpha><j>} \qquad (4\text{-}12)$$

At this moment, the distribution parameter characterizing the radial distribution of vapor phase in microgravity is unknown. For simplicity, the same values derived for normal gravity conditions were used throughout the present analysis. Note that $<u_{gj}>$ is proportional to $g^{1/4}$ for Eq.(4-11), and decreases by 62% under 0.02g. The void fraction for the drift flux model is given by

$$\alpha = \frac{\beta}{C_0 + \frac{<u_{gj}>}{<j>}} \tag{4-13}$$

It should be noted that in an extreme case of zero gravity ($g=0.0 m/s^2$), the above equation reduces to

$$<\alpha> = \frac{<\beta>}{C_0} \tag{4-14}$$

If C_0 is equal to 1.0, Eq.(4.14) yields a homogeneous model in which the slip ratio is equal to 1.0. The slip ratio in the drift flux model is given by:

$$s = \frac{1 - <\alpha>}{\frac{1}{C_0 + \frac{<u_{gj}>}{<j>}} - <\alpha>} \tag{4-15}$$

In the above equation, C_0 is the distribution factor and indicates the degree of vapor phase distribution across the cross section[47].

For example, a hypothetical case of adiabatic, laminar two-phase flow is considered. As shown in Figure 4-6(a), the second order polynomials are assumed for the volumetric flux (j/j_c) and the void fraction profile ($\alpha-\alpha_w/\alpha_c-\alpha_w$)

$$\frac{j}{j_c} = 1 - \left(\frac{r}{R}\right)^2 \tag{4-16}$$

$$\frac{\alpha - \alpha_w}{\alpha_c - \alpha_w} = 1 - \left(\frac{r}{R}\right)^2 \tag{4-17}$$

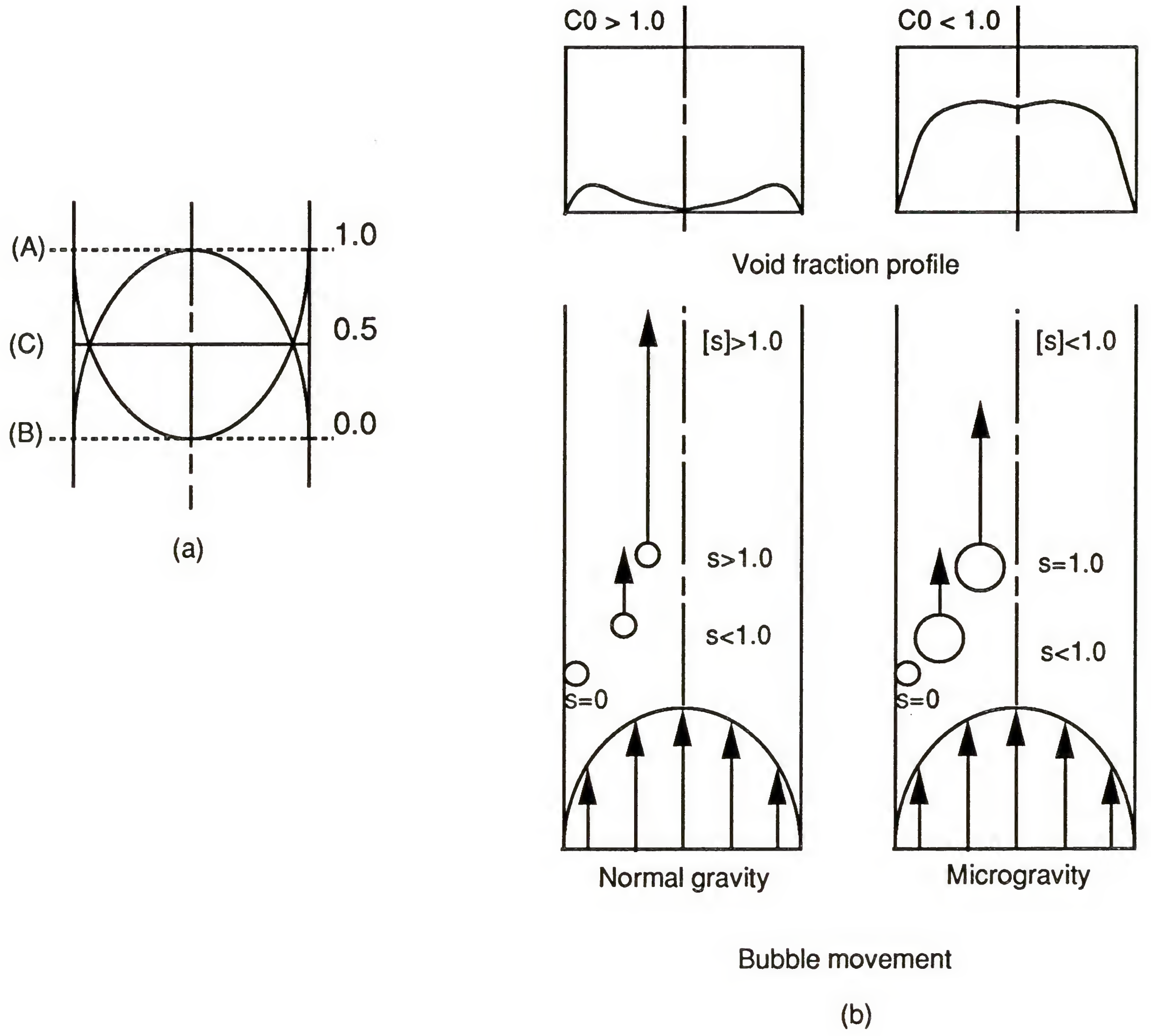

Figure 4-20 Local flow conditions near the bubble detachment under microgravity conditions.

Here, subscripts c and w denote the values at the center line and the wall, respectively. The profile of the total volumetric flux j approaches that of single-phase liquid flow when the void fraction is small. For simplicity, $\alpha_w=0$ is assumed for the adiabatic flow. Profile (A) in Figure 4-6(a) corresponds to the case where the vapor phase concentrates near the wall and simulates the flow pattern to be observed in the nucleate boiling region in a vertical pipe. The calculated value of C_0 from Eq.(4-12) yields 0.667. Profile (B) is the flow pattern to be observed in slug flow and the vapor phase concentrates near the center line where the liquid velocity is fastest. The value of C_0 in such a case is 1.60. When the vapor phase is uniformly distributed across the tube, as Profile (C), C_0 becomes 1.0.

The bubbly flow pattern under normal gravity conditions observed in the drop tower experiments showed a concentration of bubbles near the wall, while the concentration of vapor phase shifted toward the center line under microgravity conditions. Therefore, it is inferred that the value of C_0 in microgravity may be larger than that of normal gravity. To estimate the value of C_0, the radial void fraction distributions obtained in the drop tower experiments were approximated with the 6th-order polynomials and calculated from Eq.(4-12). The quadratic form of j in Eq.(4-16) was maintained for the present analysis. The distributions of void fraction in Case D0FP4 were selected as an example because the region photographed was the nucleate boiling region where the largest difference in void fraction was observed in microgravity. The constants for normal and microgravity void fraction profiles are as follows

	1.0g	0.02g
a_0	+0.00474	+0.43019
a_1	-0.06263	-1.34286
a_2	+0.51416	+19.9703
a_3	-2.07937	-105.916
a_4	+7.78731	+234.904
a_5	-10.7704	-229.471
a_6	+4.60682	+81.4233

The values of C_0 for normal and microgravity conditions are 0.997 and 1.272, respectively. As expected, the value of C_0 in normal gravity is slightly smaller than 1.0 due to the void concentration near the wall. However, C_0 became larger than 1.0 in microgravity mainly due to coalescence of large bubbles near the center line. According to Eq.(4-15), the average slip ratio becomes larger than 1.0 even under zero gravity condition. However, this prediction contradicts the physical interpretation of bubble movement described in Figure 4-6(b). Under zero gravity conditions in the nucleate boiling region, the maximum velocity of detached bubbles cannot exceed the liquid velocity. As a result, the overall slip ratio becomes less than 1.0. The drift flux model fails to predict the slip ratio in the nucleate boiling region when the gravitational acceleration approaches zero. However, for simplicity, the normal-gravity value of C_0 was assumed throughout the present calculation.

The void fraction profiles for Cases D0FP3 and D0FP4 under:

2.4g----- maximum gravity during the pull-up maneuver in the Learjet flight experiment,
1.0g----- normal gravity, of course,
0.02g---- microgravity level in the drop tower experiment,
0.01g---- microgravity level in the Learjet flight experiment, and
1.0E-6g-- residual microgravity level experienced in spacecraft in orbits.

are plotted in Figure 4-7, 4-8, and 4-9, respectively. From Figure 4-7(a), one can notice that the deviation of void fraction from the 1.0g prediction is more significant in microgravity than at higher gravities. Although all curves appear to merge at higher qualities, the difference in void fraction becomes larger as the quality becomes smaller. Under normal gravity conditions, the measured void fractions were significantly lower than those predicted by the drift flux model. This is mainly due to the small heat flux used in the present experiment. The amount of heat fluxes used in Kroger and Zuber's experiment was about 5 - 15 times larger than that of the present experiment. Besides, the material consisting of the heating surface was coated glass which has a fairly

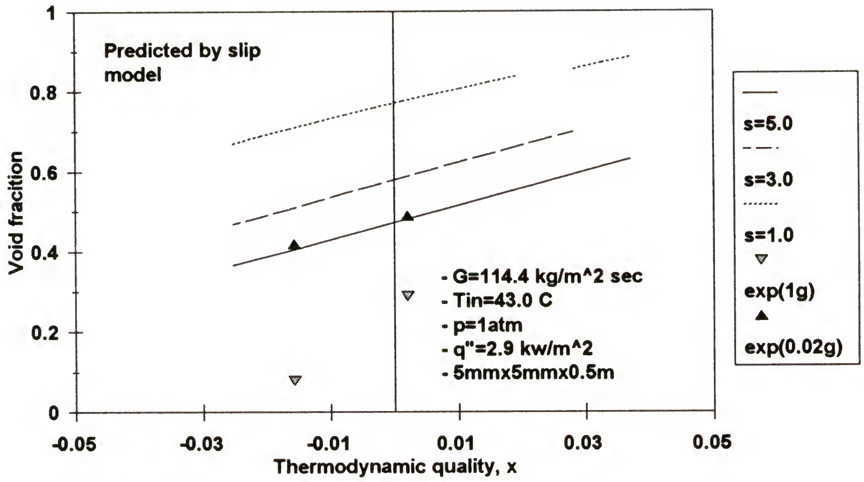

(a) z=0.4 - 0.5m

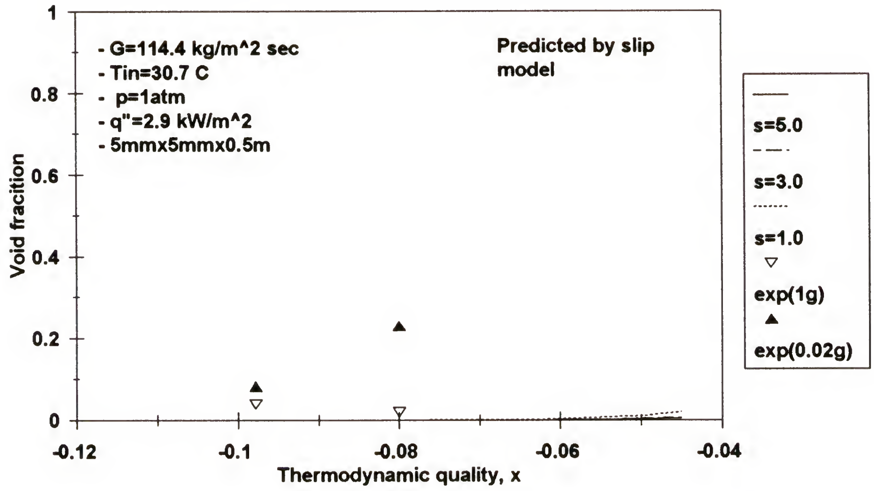

(b) z=0.3 - 0.4m

Figure 4-9 Void fraction profiles predicted by the slip model.

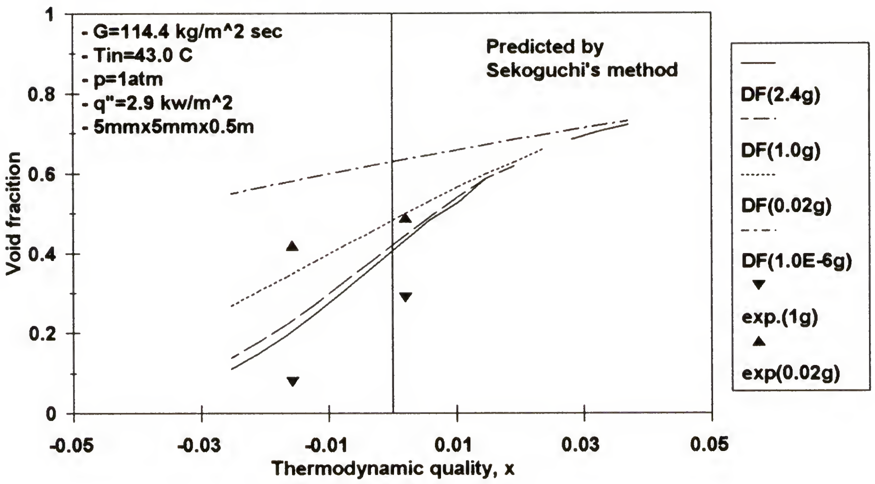

(a) z=0.4 - 0.5m

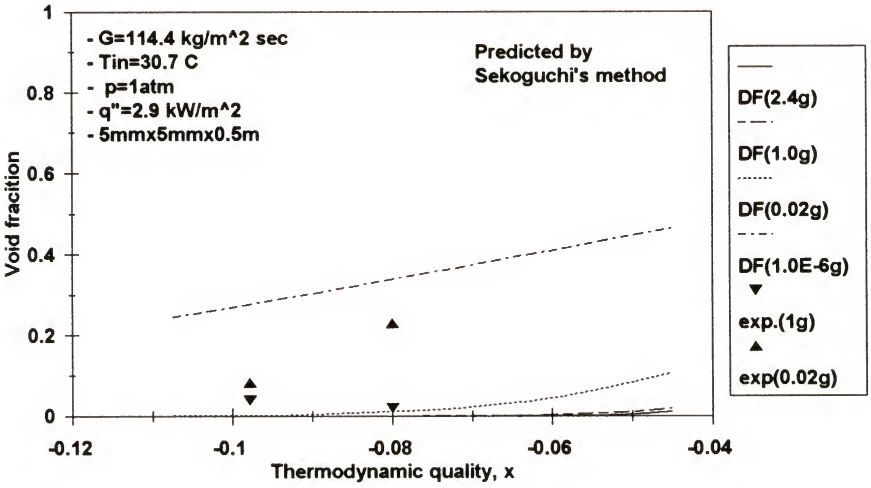

(b) z=0.3 - 0.4m

Figure 4-8 Void fraction profiles predicted by Sekoguchi's model.

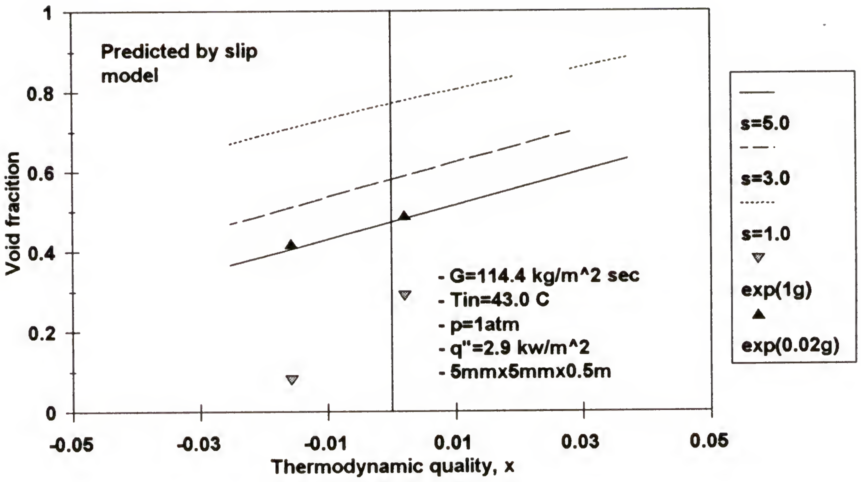

(a) z=0.4 - 0.5m

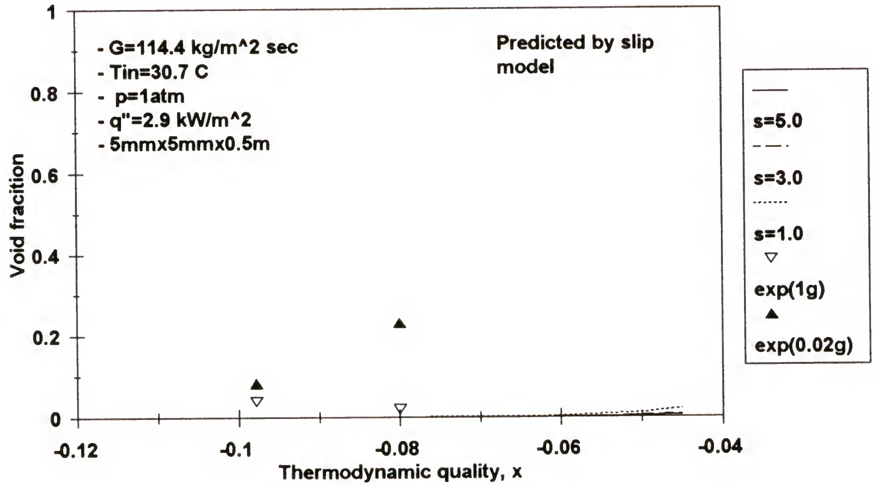

(b) z=0.3 - 0.4m

Figure 4-9 Void fraction profiles predicted by the slip model.

smooth surface. It is considered, therefore, that the number of activated nucleation sites in the present study was much smaller than that in Kroger and Zuber's experiment. Recondensation of vapor phase was estimated by Ahmad method and included in the calculation of exit qualities. The void fraction predicted for the imaginary case of 10^{-6}g is significantly larger than that of 1.0g. This indicates that the slip velocity still exists under 0.02g conditions and that assuming s=1.0 overestimates the void fraction in microgravity.

Sekoguchi's method. For Case D0FP4, the exit condition is still subcooled. In the subcooled region, the thermal equilibrium quality becomes negative and correlations used in saturated boiling are no longer valid for the negative quality. However, vapor phase exists even in this region and plays a significant role for heat transfer. Because of the existence of vapor phase, the net or actual quality has a positive value.

Sekoguchi, Tanaka, Esaki, and Imasaka developed a semi-theoretical model to predict the actual quality in the subcooled boiling region, assuming a temperature and velocity profile in the radial direction[33]. The methodology is summarized in Chapter 5.3.2 since it is closely related to the heat transfer problem. His model was particularly selected here because its theoretical nature provides an insight into the gravity dependance of the flow and heat transfer more explicitly than other entirely empirical correlations. His model solves the void fraction profile in the axial direction simultaneously through iteration process. For the void fraction, however, he employed Smith's correlation including a factor derived empirically and set to 0.4[34]. The gravity effects on void fraction are not explicitly shown in Smith's correlation.

The single-phase heat transfer coefficient consists of laminar flow and natural convection components. The latter is a function of the Grashof number and proportional to $g^{1/3}$. Through the gravity-dependent single-phase heat transfer coefficient, the true quality as well as void fraction incorporates the gravity effects in Sekoguchi's model.

In the saturated region, the thermal equilibrium quality alone was used for the above calculation.

The resulting void fraction profiles under variable gravity conditions are shown in Figure 4-8(a) and (b). For Case D0FP3, the void fraction profiles for various gravities merge in the lower quality region than that of the drift flux model. The difference of the predicted void fraction in 0.02g and that of 1.0g is less pronounced compared to the drift flux model. The void fraction in the saturated boiling region is still overestimated and its difference is larger than that of the drift flux model. In the highly subcooled region, the predictions qualitatively agreed with the experimental data of normal gravity. This is because Sekoguchi's method was exclusively developed for the subcooled boiling analysis.

Slip correlations. The slip ratio under normal gravity conditions is estimated by Eq.(4-9). For the present system in 1.0g, the value of s was 2.63. However, Eq.(4-9) is unable to predict the slip ratio under microgravity conditions. Three values of slip ratio(1.0, 3.0, and 5.0) were arbitrarily chosen and substituted into the following equation to obtain the void fraction:

$$\langle\alpha\rangle = \frac{1}{1+s\left(\frac{1}{x}-1\right)\left(\frac{\rho_g}{\rho_f}\right)} \tag{4-18}$$

The curves are plotted in Figure 4-9(a) and (b). The result shows that the slip ratio must be much larger to match the present experimental data. Besides, these curves tend to vary linearly and do not reflect the appropriate void fraction behavior around x=0.0. In the subcooled region, the prediction grossly underestimates the experimental data.

Other well-known models for subcooled boiling consists of Levy's and Larsen-Tong's models[35][36]. However, Levy's model requires subcooling at the bubble detachment point, which was unavailable in the present experiment. Levy considered the hydrodynamic force balance of a detaching bubble to estimate the liquid temperature at the top of the bubble. Since the magnitude of the buoyancy force is expected to vary in microgravity, the liquid temperature at the top of the detaching bubble is unknown. He concluded that the buoyancy force on bubble detachment was negligible through correlating his experimental data with his model. Therefore, gravity effects on boiling heat transfer are not clearly represented with his model unless the force balance is refined. Similarly, Larsen-Tong's model requires information about the thickness of a bubble boundary layer growing on the heating surface in order to calculate the heat flux transferred to the liquid core. This quantity was not measured in the present experiment.

The flow boiling experiment in microgravity showed significant differences in the average void fraction and the void distribution in the radial direction. Among the models described above, the drift flux model is capable of incorporating these changes in microgravity with less effort. This model includes the gravity term explicitly as a form of bubble rising velocity and is able to express the change of void fraction distribution in the radial direction by choosing an appropriate distribution parameter C_0 for variable gravity conditions.

Under a gravity level of 0.02g, all of the above models and experimental results showed a large increase in volume fraction in the subcooled region. As will be stated in Chapter 5, the onset of nucleate boiling seems insensitive to gravity change. These facts lead to a conclusion that the void fraction rapidly increases in the subcooled region under microgravity conditions, rather than gradually increasing as under normal gravity conditions. Such a sudden increase in void fraction at the beginning of the two-phase region may cause an instability.

The size of a coalesced bubble flowing with liquid is normally determined by hydrodynamic balance. However, growth of such large bubbles is restricted by the liquid temperature profile and geometry of the heating surface. The above analysis also suggests that under low gravity conditions there is a possibility for the slip ratio to become less than 1.0 in microgravity.

4.3 Velocity and Temperature Profiles

As a result of different void distributions under microgravity conditions, the velocity profile and heat transfer mechanism are expected to change, especially in the low-quality region. The histograms in Figure 4-5 show the average radial distributions of vapor phase scanned every 0.25 seconds and integrated in the axial direction for Cases D0FP3 and D0FP4. The integer on the y-axis is the count of black pixels on a single axial scanning line normalized for 2^8=256. In the bubbly flow regime in normal gravity, the bubbles generated on the wall form two peaks adjacent to the wall, while they are merged into one broad peak at the center in microgravity. For the slug flow in D0FP3, the radial distribution had not changed much, although the average volume fraction increased and the flow pattern approached the annular flow in microgravity.

An attempt was made to reflect the above change in flow patterns on the analysis of two-phase flow under microgravity conditions. To investigate the effect of phase change in microgravity on the velocity and temperature profiles, the contribution of vapor phase to the momentum and heat transfer must be specified. Sato, Sadatomi, and Sekoguchi developed a theoretical model to include the turbulent effect of bubbles for dispersed bubbly flow and verified their theory with an adiabatic vertical flow experiment using an air-water mixture[16][37][38]. Their analysis is useful for the present study since the contribution of the turbulence caused by bubbles is considered separately. In the following paragraph, their theory is briefly outlined.

They introduced an additional turbulent stress due to bubble agitation into the two-dimensional shear stress equation as follows

$$\tau = \rho_f (1-\alpha)(\nu_f + \epsilon' + \epsilon'') \frac{du_L}{dy} \tag{4-19}$$

where α is the local void fraction, u_L is the average liquid velocity in the flow direction, ν_f is the kinetic viscosity, ϵ' is the inherent eddy diffusivity of the turbulence, and ϵ'' is the eddy diffusivity due to bubble agitation. Using non-dimensional parameters, Eq.(4-19) is given by

$$\frac{du_L^+}{dy^*} = \frac{\tau^*}{(1-\alpha)\,(\nu_f + \epsilon' + \epsilon'')/(Ru_L^*)} \tag{4-20}$$

where each parameter in the above equation is expressed as

$$\begin{aligned} u_L^+ &= \frac{u_L}{u_L^*} \\ y^* &= \frac{y}{R} \\ \tau^* &= \frac{\tau}{\tau_w} \\ u_L^* &= \sqrt{\frac{\tau_w}{\rho_f}} \end{aligned} \tag{4-21}$$

Here, τ_w and u_L^* denote the wall shear stress and the friction velocity, respectively. The shear stress distribution τ^* in a vertical tube was obtained from the force balance between pressure and shear friction. The resulting form of the shear stress yields

$$\begin{aligned} \tau^* &= \frac{\tau}{\tau_w} \\ &= \left(1 - B\int_0^1 \alpha r^* dr^*\right) r^* + \frac{B}{r^*}\int_0^{r^*} \alpha r^* dr^* \end{aligned} \tag{4-22}$$

where $B = gR/u_L^{*2}$. Note that τ^* is reduced to unity when:

a) the void fraction becomes small and the integrations in Eq.(4-22) approach zero, or

b) the term B becomes zero regardless of void distribution as the gravity approaches zero.

In the present experiments, the residual gravities of 0.01 and 0.02g are still large enough to modify the shear stress distribution and cannot be neglected.

The eddy diffusivities for fully developed turbulent bubbly flow are expressed as follows

$$\epsilon' = \left(1 - \exp\left(-\frac{y^+}{R^+}\right)\right)^2 \times \left(1 - \frac{11}{6}\left(\frac{y^+}{R^+}\right) + \frac{4}{3}\left(\frac{y^+}{R^+}\right)^2 - \frac{1}{3}\left(\frac{y^+}{R^+}\right)^3\right) \nu_f k y^+ \qquad (4\text{-}23)$$

where the damping factor $(1\text{-}\exp(y^+/R^+)\}^2$ was added to account for the attenuation of turbulence and the eddy diffusivity near the wall. Based on the experimental data, Laufer[63] chose 0.4 and 16 for k and A^+, respectively.

For the eddy diffusivity due to bubble agitation, they proposed the following expression

$$\epsilon' = \left(1 - \exp\left(-\frac{y^+}{R^+}\right)\right)^2 k_1 \alpha \left(\frac{d_B}{2}\right) U_B \qquad (4\text{-}24)$$

where k_1 is the empirical constant and assumed to be 1.2, d_B the bubble diameter, and U_B the relative velocity of bubbles to the liquid velocity. Eq.(4-20), Eq.(4-22), Eq.(4-23) and Eq.(4-24) were solved simultaneously to obtain the velocity profile with the following boundary condition

$$u_L^+ = 0 \qquad \mathit{for} \quad y^+ = 0 \qquad (4\text{-}25)$$

Correction of τ_w was iterated until the mass flux G matched the given value.

A similar approach was employed to obtain the temperature distribution in the radial direction using the velocity distribution obtained above. The dimensionless form of the temperature profile is given by

$$\frac{dT_L^*}{dy^*} = -\frac{1}{2} Nu \frac{q''^*}{(1-\alpha)\left[1 + Pr_f\left(\frac{\epsilon' + \epsilon''}{\nu_f}\right)\right]} \tag{4-26}$$

where T_L^*, q''^*, and Nu are the dimensionless temperature, heat flux, and Nusselt number, respectively, defined as

$$T_L^* = \frac{(T_L - T_{CL})}{(T_w - T_{CL})} \tag{4-27}$$

$$q^* = \frac{q}{q_w} = \frac{R}{r} \frac{\int_0^r (1-\alpha)\, u_L\, r\, dr}{\int_0^R (1-\alpha)\, u_L\, r\, dr} \tag{4-28}$$

$$Nu = \frac{h_{TP} D}{k_f} \tag{4-29}$$

The two-phase flow heat transfer coefficient h_{TP} is given by $q_w''/(T_w - T_{CL})$. Under the following boundary condition at the wall,

$$T_L^* = 1, \qquad for \quad y^+ = 0 \tag{4-30}$$

Eq.(4-26) and Eq.(4-28) were solved simultaneously by the 4th order Runge-Kutta method. The value of T_w was initially guessed and iteration was repeated until T_{CL} converges into the measured value. To deal with the extremely large temperature gradient near the wall region, the radial distance was divided into 165 meshes using a non-uniform grid system.

In the above analysis, the void fraction profile must be given as input data. The above method was applied to the results of Case D0FP4 obtained in the first series of drop tower experiment. The flow rate was 114kg/m^2/sec and the channel width of the boiling test section was 5mm. The heat flux applied to the 0.5m test section was 2.93kW/m^2. The measured center line temperature was 46.0°C for both normal and microgravity conditions. Laminar flow analysis was used since the liquid Reynolds number was 1540 for Case D0FP4. To evaluate ϵ'', d_B and U_B need to be specified. The average values of bubble diameter under normal and microgravity conditions were read from the photograph, while the slip velocity U_B was replaced with the rising velocity of a single bubble to reflect the gravity effects. The values of d_B were 0.0011m and 0.0032m for normal(1.0g) and microgravity (0.02g) conditions, respectively.

The results from the above calculation in normal and microgravity for Case D0FP4 in the drop tower experiments are shown in Figure 4-10(a) through (e). Because of the slip velocity of vapor phase, bubbles with small diameters tend to concentrate near the wall under normal gravity. On the contrary, coalescence of bubbles seem to be promoted, forming larger bubbles under microgravity conditions. The average diameter of coalesced bubbles in microgravity at the same position was about 2.9 times larger than those of normal

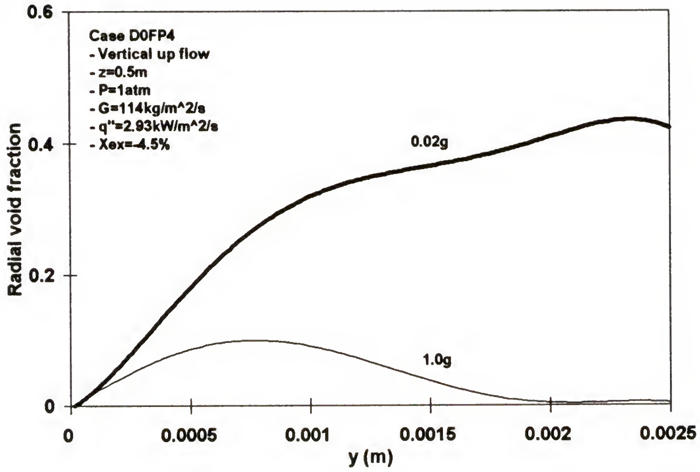

(a) Void fraction distributions

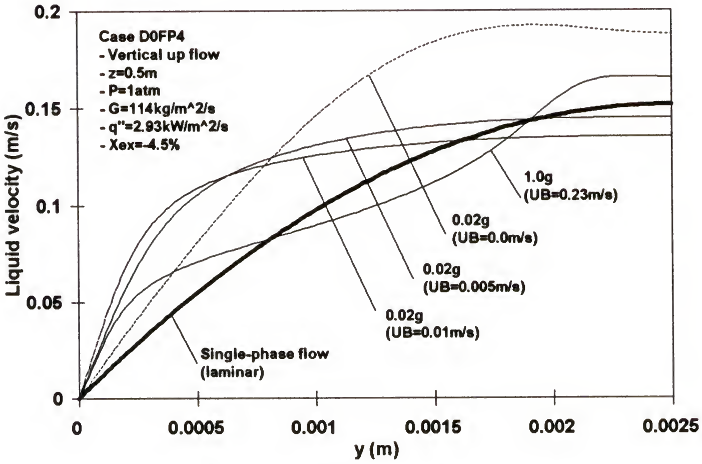

(b) Liquid velocity distributions

Figure 4-10 Two-phase flow properties under 1.0g and 0.02g for Case D0FP4 calculated by Sato's method.

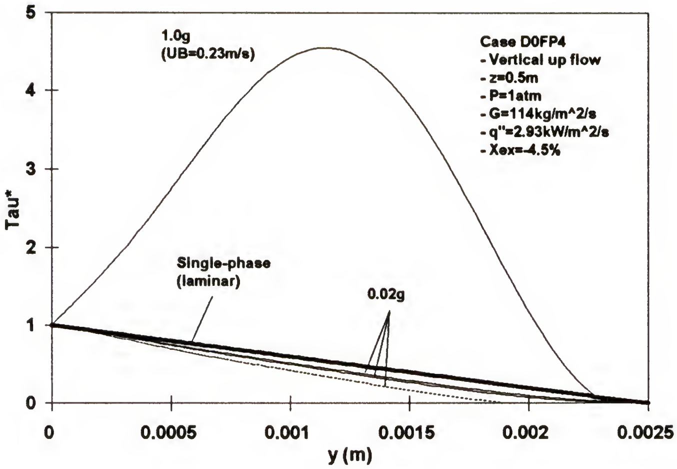

(c) Normalized shear stresses

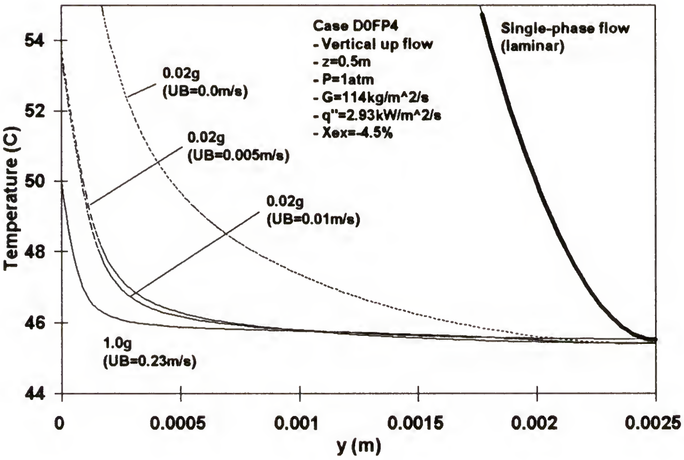

(d) Liquid temperature distributions

Figure 4-10 --- continued

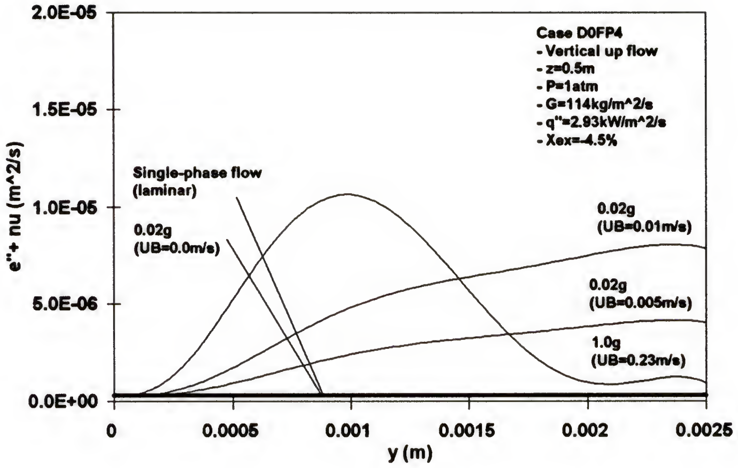

(e) Total eddy diffusivities

Figure 4-10 --- continued.

gravity. This is related to the Helmholtz instability of a free surface moving with a certain velocity.

Using the void fraction profile in Figure 4-10(a), the velocity distributions were calculated for both normal and microgravity conditions (Figure 4-10(b)). Compared to the single-phase laminar flow profile, liquid velocities of two-phase flow in both normal and microgravity became larger owing to concentration of voids near the wall. When a slip velocity existed, the velocity profile of microgravity two-phase flow approached that of turbulent flow even though the flow was laminar. However, the velocity profile for two-phase bubbly flow in microgravity without the slip velocity showed that the profile was similar to that of single-phase flow. Under such conditions, the existence of bubbles decreases the flow area and increases the liquid velocity if the mass flux is kept constant. Although the single-phase heat transfer increases, no contribution is made to the generation of turbulence by the bubbles under zero-gravity conditions. Shear stress distribution in microgravity were similar to those of single-phase laminar flow in normal gravity (Figure 4-10(c)). However, the profile for two-phase flow in normal gravity was significantly different from others. This is because the parameter B in Eq.(4-22) includes the gravity constant g and the profile for τ^* approaches that of single-phase flow regardless of the void fraction profile.

Table 4-3 Computed wall shear stresses and wall temperatures of laminar two-phase flow for Case D0FP4.

Case*	$\langle\alpha\rangle$**	d_B** (mm)	U_B (m/s)	$\tau_{w,cal.}$ (Pa)	$T_{w,cal.}$ (°C)	T_{lb} (°C)	Nu	τ_w/τ_{w1p}	Nu/Nu_{1p}	f***
1.0g (2-P)	0.04	1.1	0.23	0.120	50.0	26.1	54.6	2.07	20.3	0.951
0.02g (2-P)	0.23	3.2	0.0	0.083	61.9	26.5	13.7	1.43	5.1	0.0
0.02g (2-P)	0.23	3.2	0.01	0.146	53.8	26.5	28.0	2.52	10.4	0.510
0.02g (2-P)	0.23	3.2	0.01	0.181	53.6	26.5	28.7	3.12	10.6	0.519
1.0g (1-P)	0.0	---	---	0.058	127.9	26.1	2.7	1.0	1.0	---

* 1-P and 2-P indicate single- and two-phase flow, respectively.

** Measured from the flow patterns photographed in Case D0FP4.

*** Defined as $q_{ag}''/(q_{ag}''+q_{fc}'')$.

The calculated wall shear stresses for normal and microgravity two-phase flow are shown in Table 4-3. The ratio of the wall shear stress in two-phase flow to that of single-phase flow in normal gravity was 2.07. Under microgravity conditions, this ratio became less than 2.07 when U_B was less than 0.003m/s.

Temperature distribution in the radial direction was obtained using the velocity profile previously computed. Figure 4-10(d) shows the temperature profiles for both normal and microgravity two-phase flows. The temperature profile for single-phase laminar flow is also shown for reference. The calculated wall temperatures for microgravity conditions were higher than that under normal gravity, indicating that the heat transfer rate was deteriorated in microgravity. The wall temperatures and Nusselt numbers are computed and listed in Table 4-3. The ratio of Nu for two-phase flow to that of single-phase flow Nu/Nu_{1P} for 1.0g and 0.02g are:

$(h_{ag}+h_{fc})/h_{f0}=20.3$ for 1.0g, and

$(h_{ag}+h_{fc})/h_{f0}=10.4$ for 0.02g (U_B=0.005m/s).

where h_{ag} denotes the heat transfer coefficient accounting for bubble agitation, h_{fc} the heat transfer coefficient accounting for single-phase forced convection, and h_{f0} the heat transfer coefficient for liquid alone. This result indicates that heat transfer in the two-phase flow for the same amount of heat flux was deteriorated under microgravity conditions.

It is considered that the turbulence generated by the bubbles were weakened in microgravity in spite of the increase in bubble size. Figure 4-10(e) shows the intensity of total eddy diffusivity for bubbly flow. Since the eddy caused by bubble agitation is much larger than the kinetic viscosity ν_L, the total eddy diffusivity follows the void fraction profile. However, $\epsilon''+\nu_f$ in microgravity becomes smaller as the gravity constant becomes smaller. Below a certain value of gravity constant, $\epsilon''+\nu_f$ in microgravity becomes smaller than that of normal gravity although the average void fraction in 0.01g is much larger than that of normal gravity. Under zero-gravity conditions, the slip velocity disappears and ϵ'' becomes completely zero.

The same analysis was applied to Case F1035 in the Learjet flight experiment. The liquid Reynolds number for this case was 9616 and falls in the turbulent flow range. The heat flux used in this case is about 10 times larger than that of Case D0FP4. The eddy diffusivity inherent to the turbulent flow ϵ' is introduced in the calculation. Selection of Case F1035 is based on the fact that the pressure change during the gravity transition was smallest. Since the void fraction profile was unavailable for this series of experiments, the same void fraction profiles of Case D0FP4 was employed.

The resulting velocity profiles are shown in Figure 4-11(a). Because of the void fraction profile, the velocity near the wall is slightly increased in normal gravity. Under

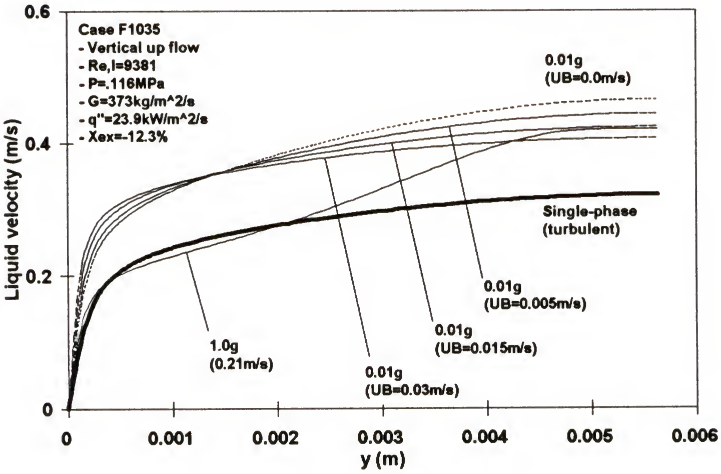

(a) Liquid velocity distributions

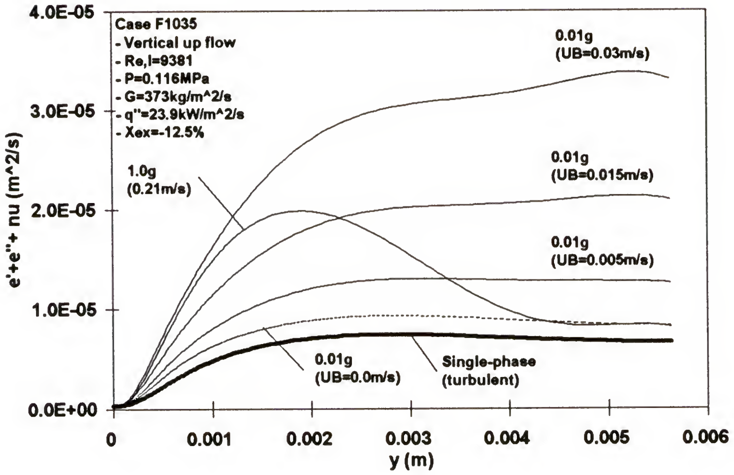

(b) Total eddy diffusivity

Figure 4-11 Two-phase flow properties under 1.0g and 0.02g for Case F1035 calculated by Sato's method.

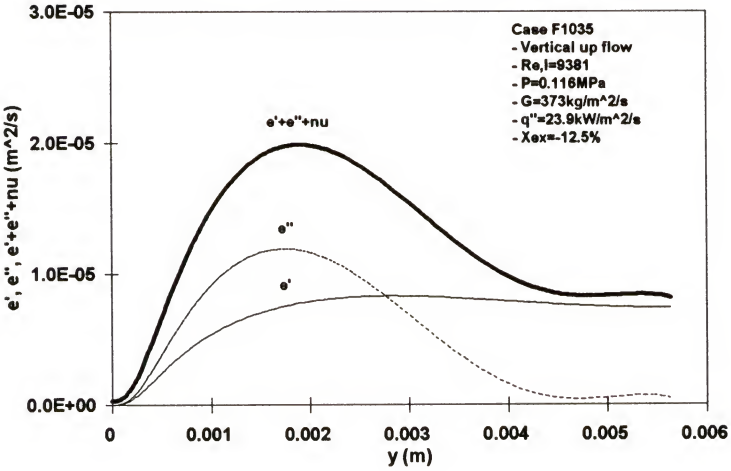

(c) Eddy diffusivities (1.0g)

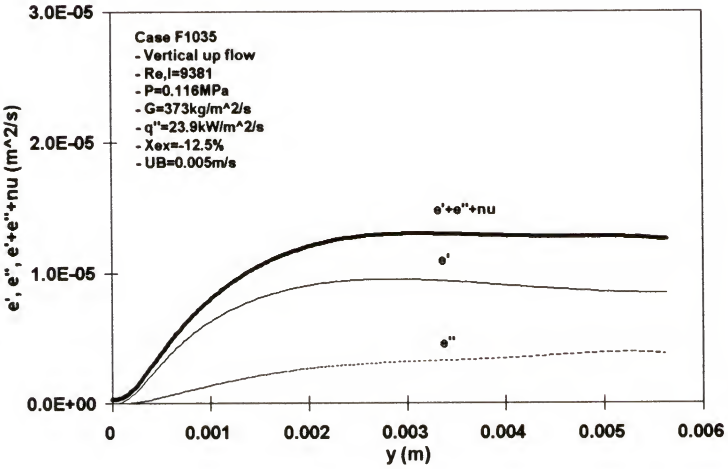

(d) Eddy diffusivities (0.01g)

Figure 4-11 --- continued

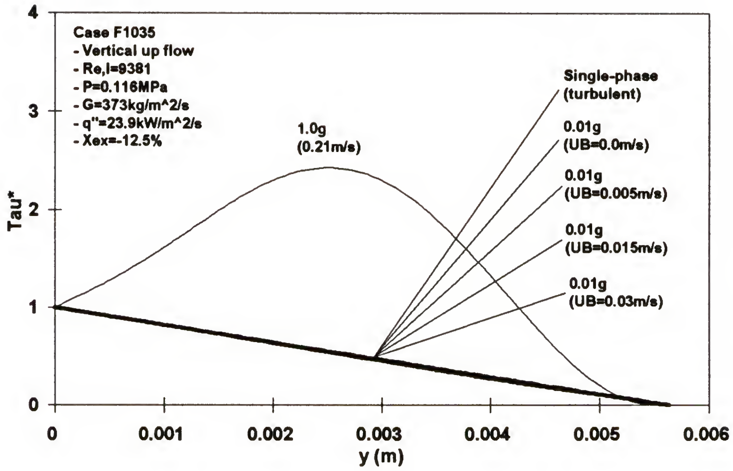

(e) Normalized shear stresses

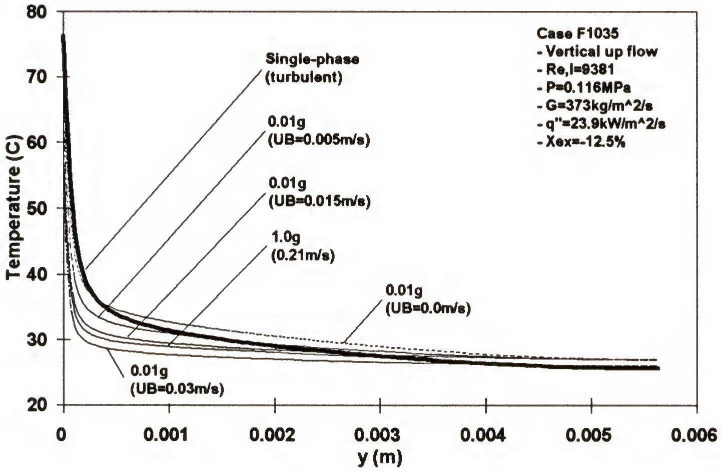

(f) Liquid temperature profiles

Figure 4-11 --- continued

Table 4-4 **Computed wall shear stresses and wall temperatures of turbulent two-phase flow for Case F1035.**

Case*	$<\alpha>$**	d_B** (mm)	U_B (m/s)	$\tau_{w,cal.}$ (Pa)	$T_{w,cal.}$ (°C)	T_{lb} (°C)	Nu	τ_w/τ_{w1p}	Nu/Nu_{1p}	f***
1.0g (2-P)	0.04	1.1	0.21	0.575	55.9	26.1	134.7	1.37	1.68	0.41
0.01g (2-P)	0.23	3.2	0.0	0.678	68.2	26.5	96.3	1.62	1.20	0.0
0.01g (2-P)	0.23	3.2	0.01	0.760	63.2	26.5	109.4	1.81	1.37	0.12
0.01g (2-P)	0.23	3.2	0.02	0.893	57.8	26.5	128.3	2.13	1.60	0.25
0.01g (2-P)	0.23	3.2	0.03	1.037	52.8	26.5	152.7	2.48	1.91	0.37
1.0g (1-P)	0	---	---	0.419	76.3	26.1	80.0	1.0	1.0	---

* 1-P and 2-P indicate single- and two-phase flow, respectively.

** Used the results from Case DOFP4.

*** Defined as $q_{ag}''/(q_{ag}''+q_{fc}'')$.

microgravity conditions, the profile is similar to that of single-phase flow. This is because ϵ'' becomes smaller and ϵ' became larger than ϵ'' in microgravity(Figure 4-11(b) and (d)). However, in normal gravity, ϵ'' and ϵ' were comparable to each other(Figure 4-11(c)). The shear stress distributions shown in Figure 4-11(e) were similar to those of Case DOFP4, except that the magnitude of τ^* in normal gravity was smaller. The calculated wall shear stresses for normal and microgravity conditions are shown in Table 4-4. The wall shear stress in zero-gravity was 1.18 times larger than that of normal gravity. The above computation indicates that larger frictional pressure drops are expected in microgravity since the relationship between the wall shear stress and the frictional pressure drop gradient is given by

$$\frac{\tau_{w,2\phi}}{\tau_{w,1\phi}} = \frac{\left[\dfrac{dP}{dz}\right]_{2\phi,f}}{\left[\dfrac{dP}{dz}\right]_{1\phi,f}} \qquad (4\text{-}31)$$

where $\tau_{w,2\phi}$ and $\tau_{w,1\phi}$ are the wall shear stresses for two-phase and single-phase flow, respectively. The measurement of pressure drops in microgravity will be discussed later in Section 4.4.

The temperature profiles in Figure 4-11(f) showed a decrease in heat transfer rate under microgravity conditions. The calculated wall temperatures under normal and microgravity conditions (U_B=0.005m/s) were 55.9°C and 63.2°C, respectively, for the measured bulk temperatures. The wall temperature for the single-phase turbulent flow was 76.3°C. The ratios of the two-phase bulk convection heat transfer to the single-phase convection heat transfer for 1.0g and 0.01g were:

$(h_{ag}+h_{fc})/h_{f0}=1.68$ for 1.0g, and

$(h_{ag}+h_{fc})/h_{f0}=1.37$ for 0.01g ($U_B=0.005$m/s).

The bulk convection heat transfer rate of two-phase flow in 0.01g was about 18.4% smaller than that of 1.0g. The above result indicates that the bulk convection of two-phase flow consisting of single-phase flow plus bubble agitation was deteriorated under microgravity conditions. It also shows that the contribution of bubble agitation to heat transfer becomes less significant in microgravity.

The total heat transfer rate including evaporation was measured in the Learjet flight experiment and their results are discussed in Chapter 5.

4.4 Pressure Drop

The pressure drop for two-phase flow consists of gravitational, accelerational, and frictional components. Among the three components, frictional pressure drop is of paramount importance since its gradient is directly related to the wall shear stress, hence heat transfer. In this chapter, the results from pressure drop measurements conducted in the drop tower facility is reported and compared with the prediction by a homogeneous model. Then, the influence of

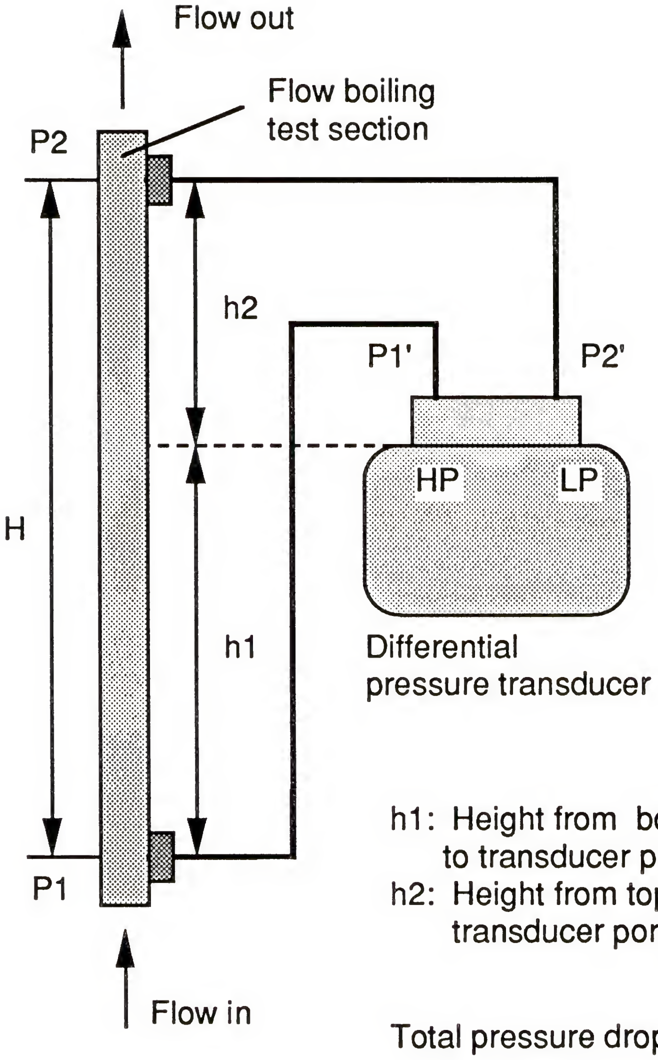

h1: Height from bottom pressure tap to transducer ports.
h2: Height from top pressure tap to transducer ports.

Total pressure drop:

$$(P1-P2) = \Delta Pread + \rho f\,(h1+h2)\,g$$
$$= \Delta P1 + \Delta P2 + \rho f\, g\, H$$

Figure 4-12 Pressure drop measurement along a vertical test section in the drop tower experiment.

gravity on the accelerational and frictional pressure drops is discussed.

The pressure drop along the axis of the 4mmI.D.x500mm SUS tube was measured by a diaphragm-type differential pressure transducer. Pressure taps were attached perpendicular to the flow at the exit and inlet of the test section. Two lead lines filled with liquid Freon 113 were connected to the high and low pressure ports of the transducer elevated by h1 from the inlet of the test section(Figure 4-12). The output of the transducer includes the static pressure of the liquid inside the vertical lead lines. The total pressure drop in the test section (P_1-P_2) is given by

$$(P_1 - P_2) = \Delta P_{read} + \rho_f g L \tag{4-32}$$

As long as the lead lines are filled with liquid at the same temperature, the elevation of the pressure transducer does not affect the measurement. Under variable gravity conditions for vertical flow systems, however, the static pressure changes significantly. Due to the fact that the static pressure in 1.0g for the drop tower experiment is approximately 50 times larger than that of 0.02g, continuous use of the same range in the pressure transducer for normal and microgravity conditions was impossible. A finer range was selected for measurement of the total pressure drop in microgravity. The output signal ranging from 0.96V to 5.0V was recorded in a high speed sampling recorder every 2 msec. in real time. The voltage output became 0.96V when the differential pressure was zero.

Table 4-5 Test conditions for pressure drop measurement in drop tower experiments.

Case	D0PD1	D0PD2	D0PD3	D0PD4	D0PD5	D1PD1	D1PD2
Mass flux ($kg/m^2/s$)	75	228	295	493	561	570	562
Subcooling (K)	4.3	3.1	4.0	3.5	4.0	3.5	4.5
Exit quality (%)	20.7	5.7	3.3	1.3	0.5	0.8	0.2
L_{1P}* (m)	0.066	0.145	0.242	0.343	0.447	0.397	0.382
Void fraction**	0.879	0.879	0.877	0.718	0.668	0.680	0.589
ΔP_{total} (measured) (Pa)	673	1234	1468	1850	1579	7890	7983
ΔP_{total}*** (predicted) (Pa)	967	1517	1257	1327	996	8216	8531
$1/X_{tl}$	1.841	0.530	0.373	0.207	0.165	0.166	0.141

* A 4mmIDx500mm SUS tube was used.

** Values were predicted by the drift flux model.

*** Homogeneous model was used.

Calibration of the pressure transducer was conducted under normal gravity conditions using a column of Freon 113 at room temperature.

The test conditions of the pressure drop measurements are summarized in Table 4-5. With heat flux constant, pressure drops for five different mass flow rates were measured. The exit quality ranged from 0.54% to 20.7%. Inlet temperatures were maintained near 43°C to provide about 5K of subcooling. A dc power of 26V was applied to the nichrome heater of 13.0 ohms resistance, supplying 52.0W of electrical power to the test section. Heat loss was estimated by reading thermocouple outputs inside and outside of the insulator wrapped around the tube. Of total heat input, 12% of heat flux was lost to ambient. The resulting net heat flux was 6.63kW/m^2.

Pressure drop recordings for the five cases are shown in Figure 4-13. The flow rate change during the free fall was within 2%. On the recording chart, three types of total pressure drop were read from the curve; a) the maximum value appearing in the middle of the free fall, b) the minimum value appearing at the end of the free fall, and c) the average value during 1.25 seconds of the free fall. The above three types of pressure drops measured during the free fall experiment are plotted in Figure 4-14 against the thermodynamic quality for the five cases. As the quality increases, the total pressure drop in microgravity increases in the low quality region less than 1%, while they tend to

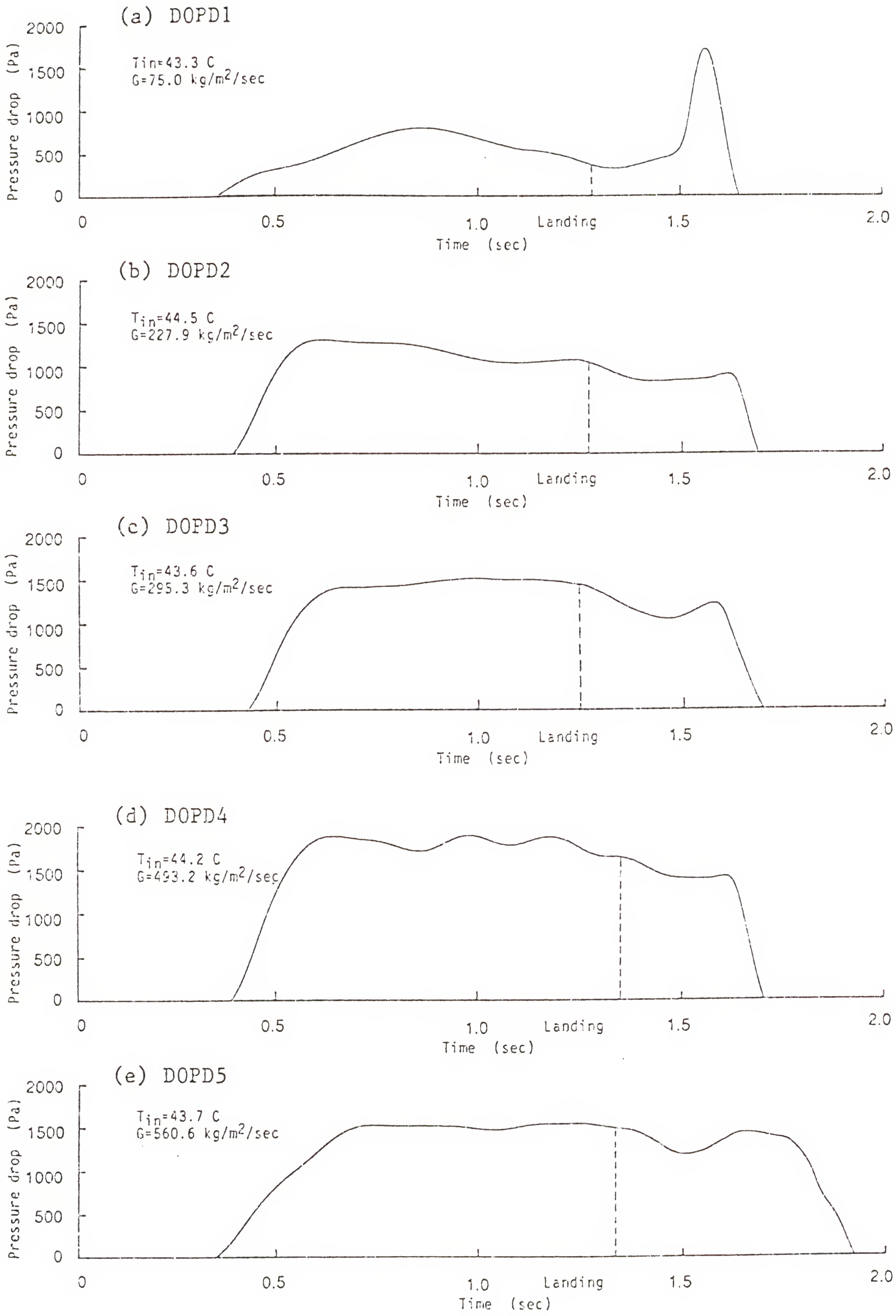

Figure 4-13 Total pressure drops measured in drop tower experiments. L=0.5m, D=5mmx5mm, q"w=2.93kW/m^2.

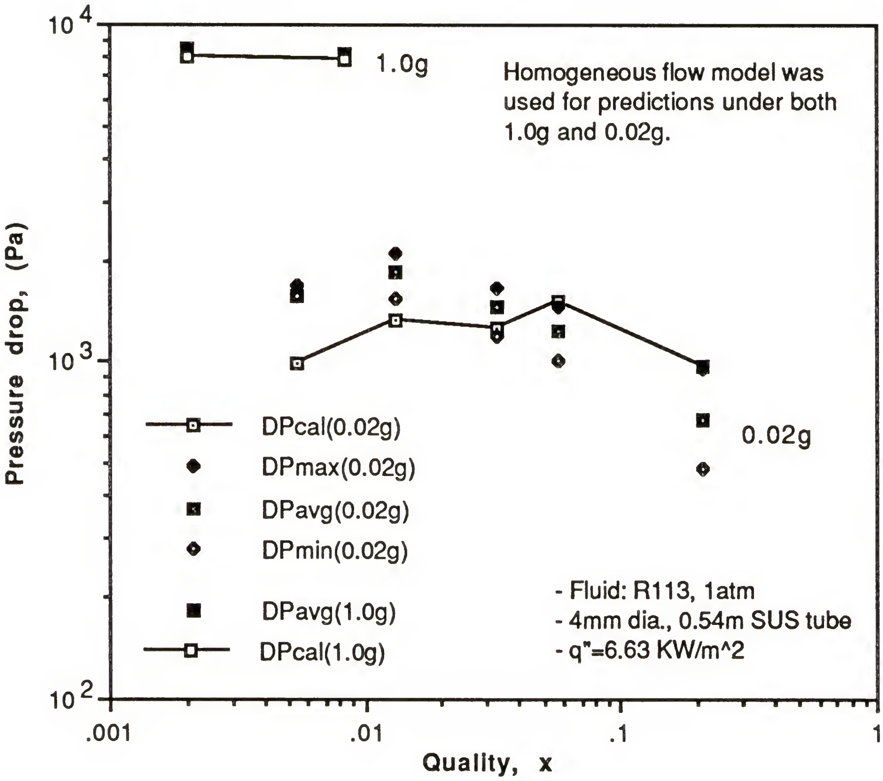

Figure 4-14 Total pressure drops in a vertical tube under 1.0g and 0.02g conditions.

decrease in the higher quality region. This is due to two competing factors: one is the decreasing mass flux and the other is the increasing quality and void fraction.

Two measurements of pressure drops in normal gravity are also shown in Figure 4-14. The pressure drops measured in normal gravity indicated much larger total pressure drop due to elevated static pressure.

A homogeneous model, in which the velocities of the vapor and liquid is considered equal, was used to calculate each component of the total pressure drop. The test section is simply divided into single and two-phase regions. For systems with an uniform heat flux, the length of the single-phase region is given by

$$\frac{L_{1P}}{L} = \frac{(h_f - h_{fi})}{\Delta h} \tag{4-33}$$

where Δh is the increase in enthalpy provided by the heater. Δh is computed from the total heat input Q and the mass flow rate m as follows

$$\Delta h = \frac{Q}{\dot{m}} \tag{4-34}$$

In the present system with a constant heat flux, the single-phase region becomes larger as the mass flow rate increases. At the boundary of the two regions, the thermodynamic quality is zero. In the two-phase region, the following are the expressions for each component of the pressure drop based on the homogeneous model

$$\Delta P_{2f} = \frac{2 f_{TP} L_{2P} G^2 v_f}{D}\left[1 + \frac{x}{2}\left(\frac{v_{fg}}{v_f}\right)\right] \qquad (4\text{-}35)$$

$$\Delta P_{2a} = G^2 v_f \left(\frac{v_{fg}}{v_f}\right) x \qquad (4\text{-}36)$$

$$\Delta P_{2g} = \frac{g \sin\theta \; L_{2P}}{v_{fg} x} \ln\left[1 + x\left(\frac{v_{fg}}{v_f}\right)\right] \qquad (4\text{-}37)$$

where f_{TP} is the two-phase friction factor defined as

$$f_{TP} = \frac{0.079}{Re_{TP}^{1/4}} \qquad (4\text{-}38)$$

for turbulent flow and

$$f_{TP} = \frac{16}{Re_{TP}} \qquad (4\text{-}39)$$

for laminar flow. An equation proposed by McAdams[39] was adopted here for the mean two-phase viscosity μ_{TP}

$$\mu_{TP} = x \, \mu_g + (1-x)\, \mu_f \qquad (4\text{-}40)$$

In the single-phase region, the accelerational component is negligible. The gravitational and frictional components are given by

$$\Delta P_{1g} = \rho_f g L_{1P} \qquad (4\text{-}41)$$

$$\Delta P_{1f} = \frac{2 f_{f0} G^2 v_f L_{1P}}{D} \qquad (4\text{-}42)$$

In Eq.(4-36), the single-phase friction factor f_{f0} defined as

$$f_{f0} = \frac{0.079}{Re^{1/4}} \tag{4-43}$$

for turbulent flow and

$$f_{f0} = \frac{16}{Re} \tag{4-44}$$

for laminar flow. In the above calculation, the value of g was set to be $0.196 m/s^2$ for the case of microgravity.

Due to lack of buoyancy force, the slip ratio is considered to be close to unity. Under such circumstances, calculation by the homogeneous two-phase flow model is expected to provide a reasonable estimate for pressure drops in microgravity. The predicted total pressure drops for corresponding cases are plotted in Figure 4-14 together with experimental data. The solid line indicates the predicted total pressure drops. The predicted values agrees with experimental results in the high quality region larger than 2%, while the prediction tends to underestimate in the low quality region. In the low quality region where the flow pattern is mainly bubbly flow, the increase in void fraction is significantly large, as shown in Figure 4-3(g). This result indicates that the void fraction and pressure drop in the subcooled region are no longer negligible.

To investigate further the influence of gravity on pressure drop, each component in the two-phase region for normal gravity and microgravity conditions was separated and compared to each other in Figure 4-15(a) and (b). In

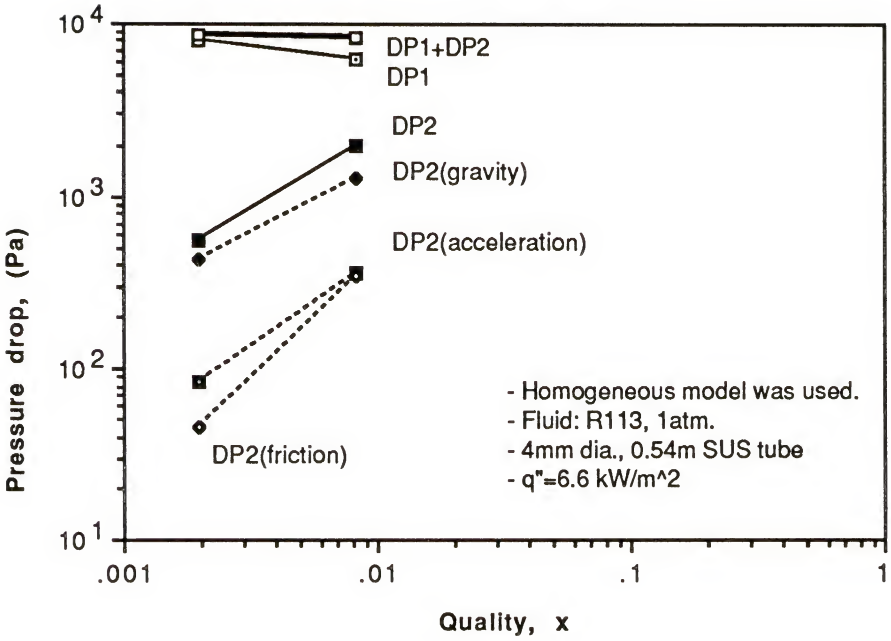

(a) 1.0g

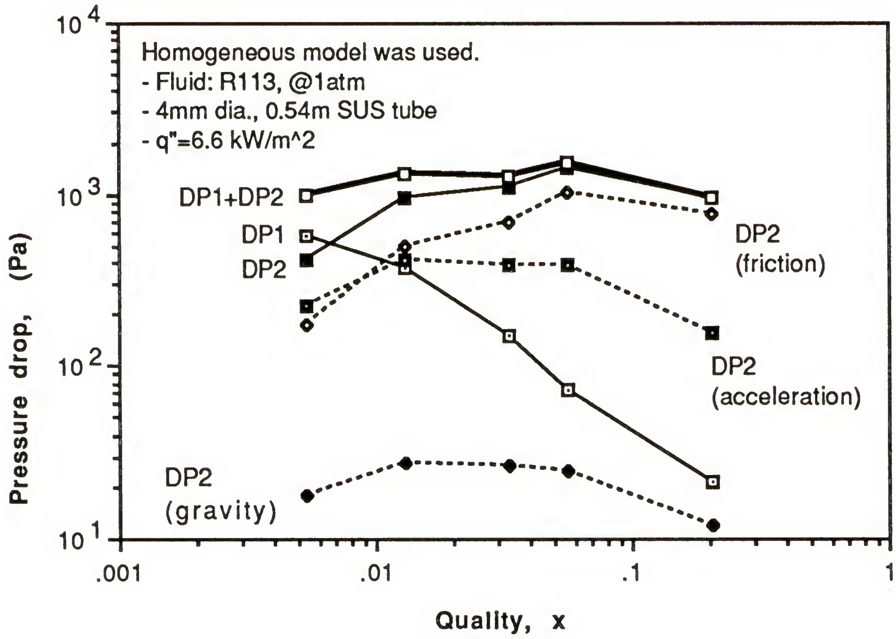

(b) 0.02g

Figure 4-15 Influence of gravity on pressure drop components in a vertical tube.

microgravity, the frictional component is dominant in both the two-phase and single-phase regions. Since ΔP_{2f} and ΔP_{2a} include the square root of the mass flux, both components tend to decrease in the high quality region where G is reduced to attain higher qualities for the present study. Single-phase pressure drop linearly decreases as L_{1P} becomes smaller. On the other hand, in normal gravity, the static pressure in the single-phase region is dominant for the present range of quality, and the increase in frictional and accelerational components in the two-phase region hardly contributes to the total pressure drop.

As indicated previously, the frictional component of the pressure drop is of paramount importance to the heat transfer problem in microgravity. The wall shear stress for a tube is correlated with the gradient of frictional pressure drop by

$$\tau_w = \frac{4}{D}\left(\frac{\Delta P}{\Delta z}\right)_{2f} \qquad (4\text{-}45)$$

With the measurement procedure used in the present experiment, $(\Delta P/\Delta z)_{2f}$ cannot be measured directly. Assuming that the void fraction profile is known, the calculated values of ΔP_1, ΔP_{2g}, and DP2a were subtracted from the measured total pressure drop to obtain ΔP_{2f}. Then, ΔP_{2f} was divided by L_{2P} to yield the average frictional pressure drop gradient. The same procedure was applied to the data obtained under normal gravity conditions. The result is shown in Figure 4-16, with the predictions. The maximum, average, and minimum values of total

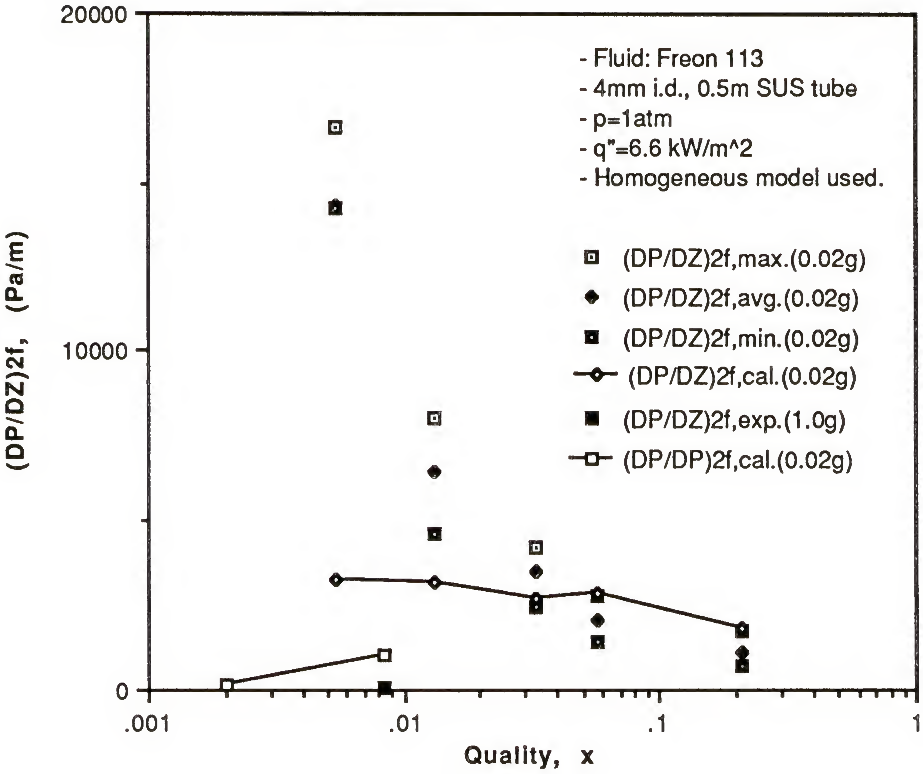

Figure 4-16 Frictional pressure drop gradient in a vertical tube under 1.0g and 0.02g conditions.

pressure drop measured during the microgravity period are plotted separately. $(\Delta P/\Delta z)_{2f}$ in the low quality region under microgravity conditions became significantly larger than those of normal gravity conditions. A conceivable reason for the increased $(\Delta P/\Delta z)_{2f}$ in the low quality region is, again, the formation of significantly large bubbles in the liquid flow. Taking into account the correlation provided by Eq.(4-45), the wall shear stress in microgravity in the low-quality region seems to become larger than that in normal gravity under the conditions of present experiment. This result indicates that the pressure drop in the subcooled region is no longer negligible under microgravity conditions.

Separated flow models can provide more accurate predictions if the void fraction profile along the flow is given. The axial evolution of void fraction was not available in the present experiment, although the volume fraction near the test section exit was determined from the photographs. The existing void fraction correlations are flow-pattern sensitive and tend to deviate from each other depending on the heat flux, mass flow rate, and geometry of heaters, especially in the low-quality region. The test conditions of the present study, characterized by low flow rate and low heat flux, are very unique and difficult to find existing correlations applicable to the present experiments. Because of the above reasons, the separated flow model was not used in the present study.

CHAPTER 5
GRAVITY EFFECTS ON SUBCOOLED BOILING HEAT TRANSFER

5.1 Flight Experiment Results

On September 16, 1992, two racks containing the flow boiling equipment and data acquisition system were aboard NASA's LeRC microgravity Learjet and subjected to a series of 10^{-2}g microgravity tests. Each microgravity trajectory lasted for approximately 18 seconds.

Test conditions of the Learjet experiments are summarized in Table 5-1. The ground test results with the preheater turned on showed that approximately three minutes were required for start-up. The thermal equilibrium qualities at the exit of the test section for these tests ranged from -0.04% to -12.1% and maintained within the subcooled region. The mass fluxes were changed from 165 to 384kg/m^2/sec. Without using the preheater, the inlet temperatures were kept between 15.2°C to 20.3°C. A constant dc current of 14.7A was supplied to the main heater. The electrical power input was 411W. The heat flux calculated from the current and the resistance measured was 24.3kW/m^2 at the operating temperatures. Heat loss to ambient was measured by reading temperatures inside and outside the insulator around the test section and found to be 0.4kW/m^2.

Table 5-1 Learjet flight experiment conditions[*].

Case No.	Period[**] (sec)	$T_{f,in}$ (°C)	$\Delta T_{sub,in}$ (°C)	$T_{f,out}$ (°C)	G(kg/m^2/s) (GPM)	P_{top}(MPa) (psig)	P_{btm}(MPa) (psig)	ΔP(MPa) (psi)
F10151	200.0 - 209.7	20.3	31.9	40.0	165 (0.166)	0.110 (3.455)	0.118 (4.663)	0.008 (1.203)
F10152	220.1 - 223.6	20.3	33.6	46.6	37 (0.038)	0.105 (2.736)	0.125 (5.580)	0.020 (2.844)
F10150	245.2 - 248.7	19.8	25.4	37.9	210 (0.209)	0.093 (1.007)	0.094 (1.094)	0.001 (0.087)
F10201	188.1 - 197.9	15.2	36.6	31.6	198 (0.199)	0.109 (3.235)	0.117 (4.390)	0.008 (1.155)
F10202	205.6 - 209.7	15.3	42.9	36.2	146 (0.146)	0.122 (5.192)	0.143 (8.194)	0.021 (3.002)
F10200	230.6 - 233.4	15.4	31.1	31.5	227 (0.228)	0.098 (1.699)	0.098 (1.728)	0.001 (0.028)
F10351	150.6 - 159.6	17.2	34.5	26.0	373 (0.374)	0.108 (3.123)	0.116 (4.357)	0.009 (1.234)
F10352	175.5 - 177.7	17.2	37.4	26.2	360 (0.362)	0.106 (2.896)	0.128 (6.011)	0.021 (3.115)
F10350	192.3 - 201.3	17.3	32.8	26.5	384 (0.385)	0.110 (3.463)	0.110 (3.490)	0.001 (0.027)

[*] Flight experiments were conducted on 9/16/93 at NASA LeRC.
[**] The times indicate the period when constant a pressure profile was established.

Although two flights were scheduled, only the first flight was completed because of a malfunction of the airplane control system. Five parabolas were flown during the single flight. The qualities and flow patterns at the exit of the test section are summarized in Table 5-2. During the five parabolas, two data sets in virtual memory obtained at the first and fourth trajectories were erased because the computer power was lost just before entering the low-gravity maneuver. The probable cause of the power loss is an unsecured electrical contact of the power supply inside the computer, which failed during the transition from 2.4g to 0g.

Figure 5-1(a) through (c) show the acceleration histories in x-(fore-aft), y-(right-left), and z-(up-down) directions recorded in a built-in accelerometer. Here, the z-axis is parallel to the flow direction in the vertical test section. It was attempted to null acceleration in the z-direction. The first and second curves in Figure 5-1 indicate the accelerations in the z-directions recorded in coarse(1/20g per scale) and fine(1/200g per scale) modes, respectively. Although the z-axis acceleration fluctuated during the initial period of each trajectory, it damped out within ±1/100g as time progressed. Acceleration along the x-axis was almost nullified, while that of the y-axis was maintained slightly positive to follow the parabolic trajectory.

Bulk temperature profiles, flow rates, pressure drops, and wall temperature profiles for Cases F1015, F1020, and

Table 5-2 Summary of experimental conditions for Learjet flight experiments[*].

Date	Case No.	Gravity level	Re_{10}	Heat flux (kW/m^2)	Exit quality	Actual quality[**]	Void fraction[**]	Flow pattern at the exit
9/16 1992	F10151	1.0g	4145	23.9	-0.004	0.010	0.45	Slug.
	F10150	±0.01g	5271	23.9	-0.044	0.006	0.51	Annular.
	F10201	1.0g	5006	23.9	-0.067	0.002	0.16	Bubbly.
	F10200	±0.01g	5734	23.9	-0.084	0.002	0.19	Large bubbly.
	F10351	1.0g	9381	23.9	-0.121	0.001	0.02	Bubbly.
	F10350	±0.01g	9656	23.9	-0.123	0.001	0.01	Large bubbly.

[*] Atmospheric pressure in the cabin was 0.0862 MPa.
[**] True quality and void fraction was computed by Sekoguchi's method.

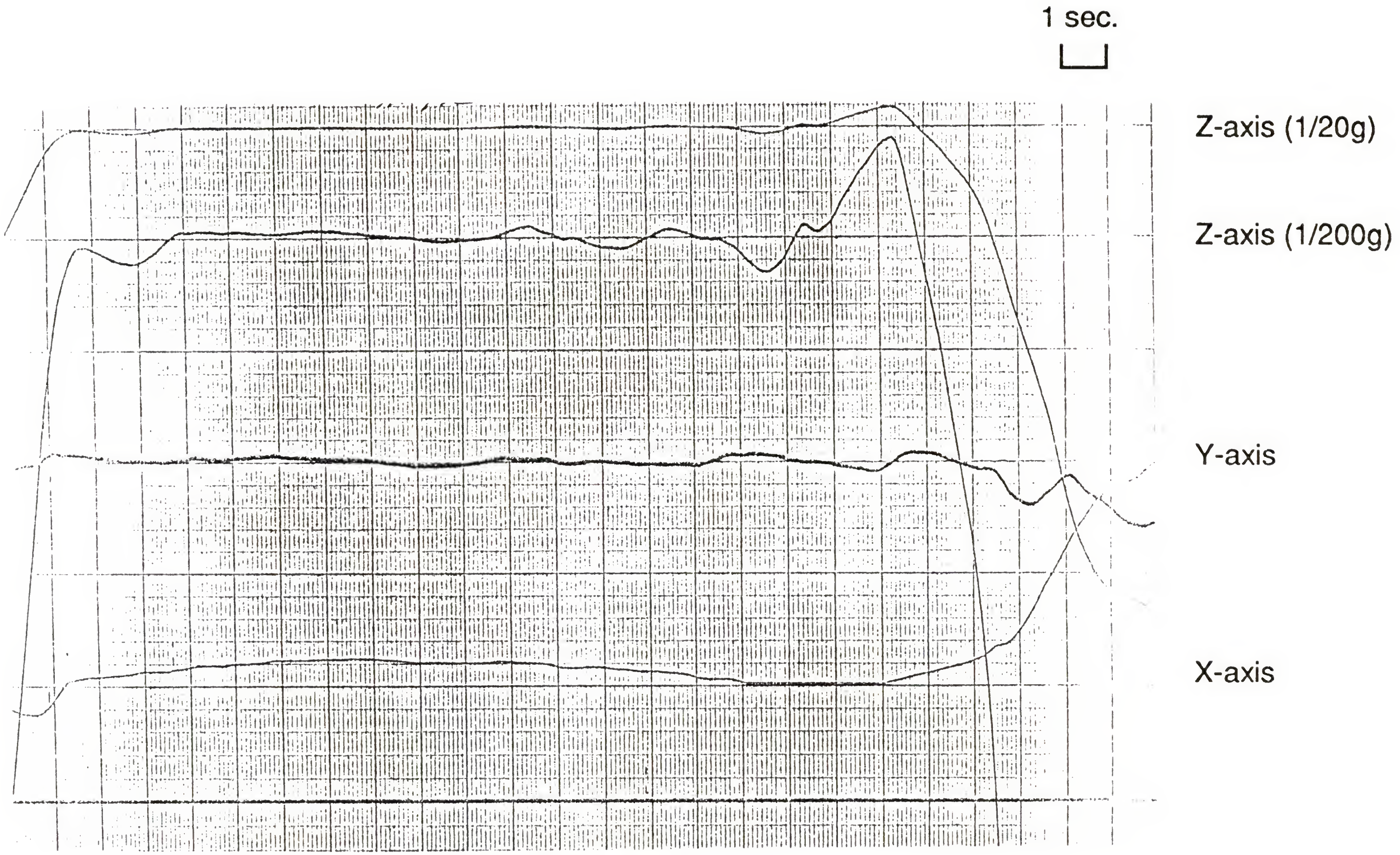

(a) Case F1015

Figure 5-1 Acceleration histories recorded by an on-board accelometer during the Learjet flight experiment.

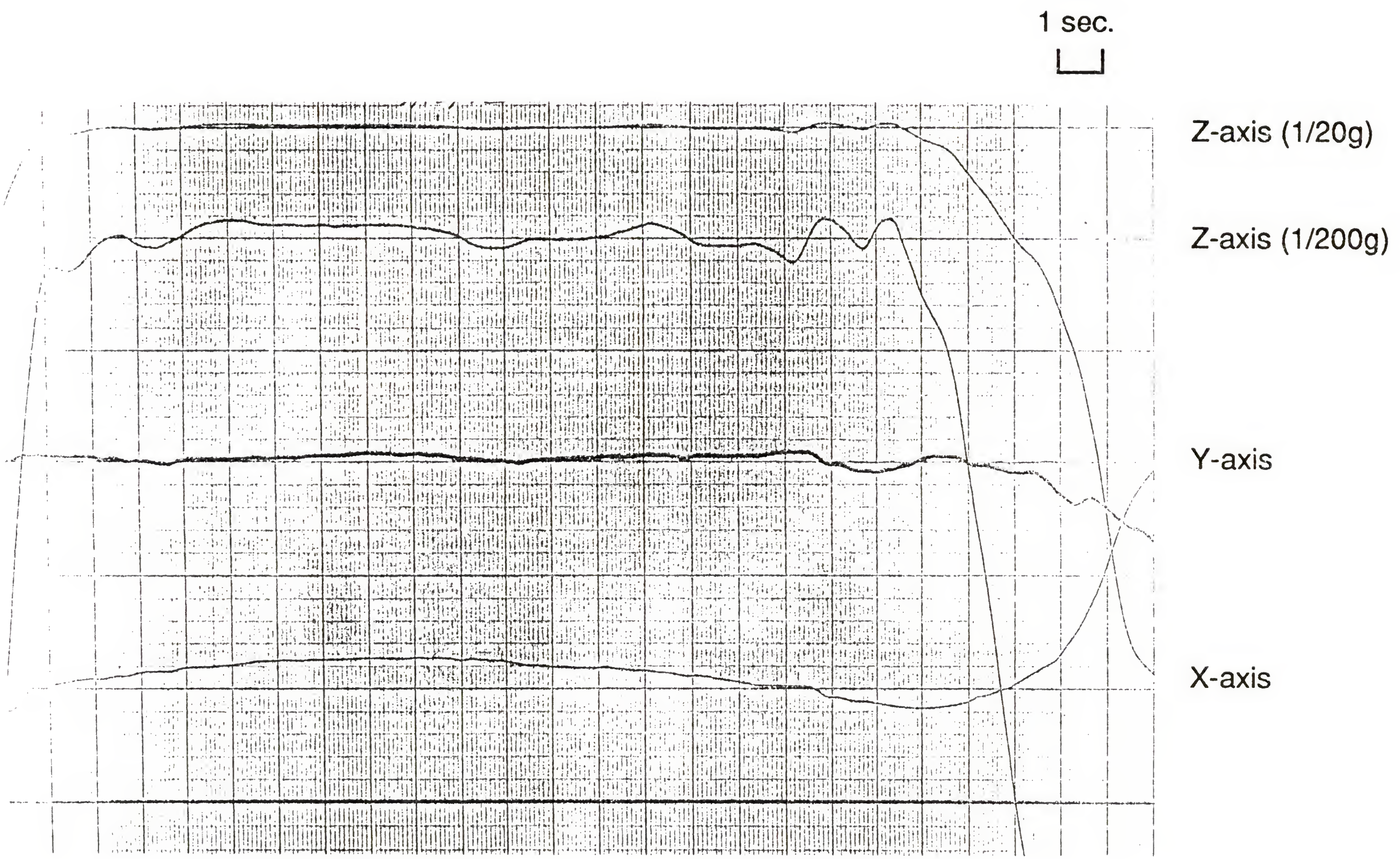

(b) Case F1020

Figure 5-1 Acceleration histories recorded by an on-board accelometer during the Learjet flight experiment.

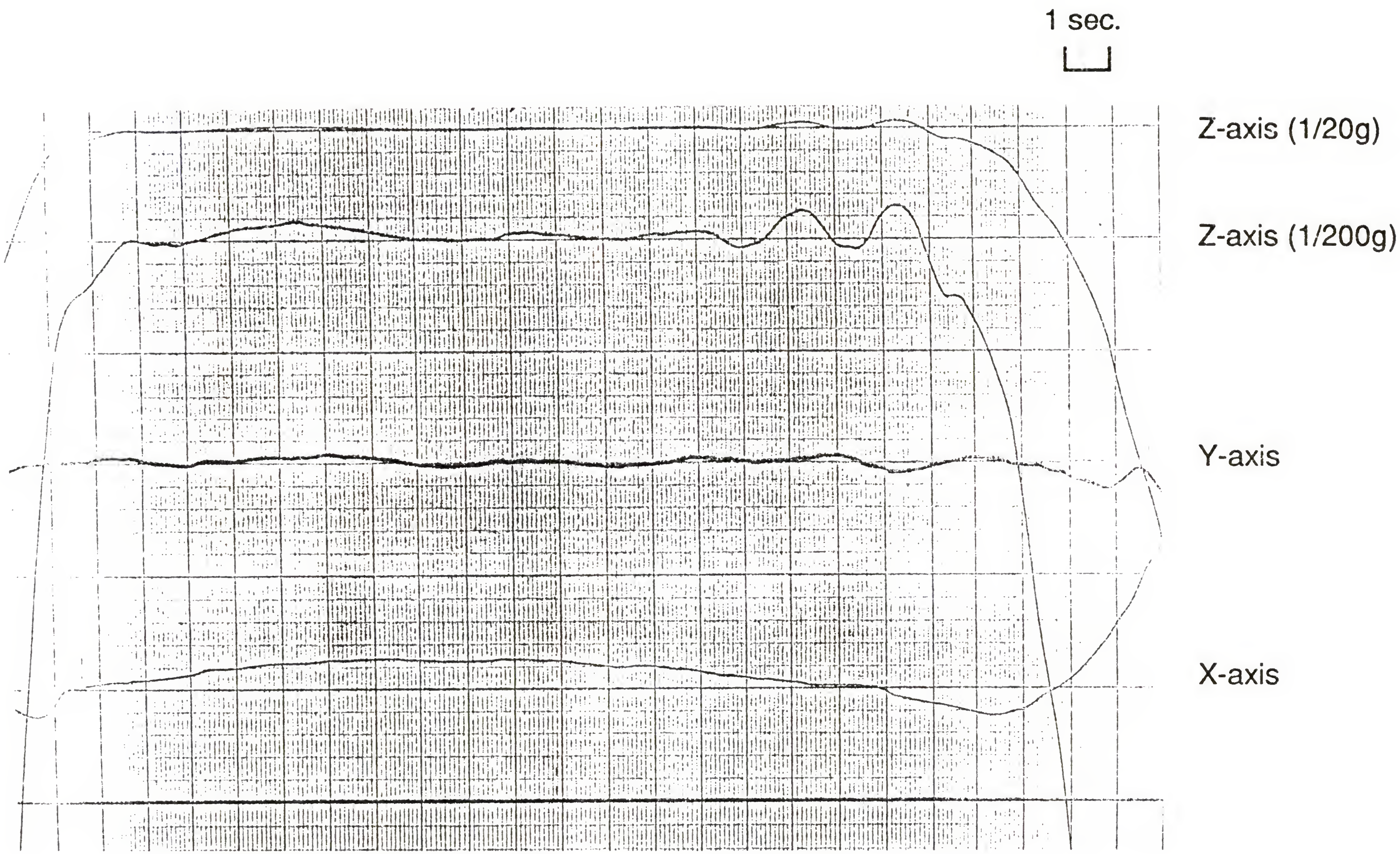

(c) Case F1035

Figure 5-1 Acceleration histories recorded by an on-board accelometer during the Learjet flight experiment.

F1035 are shown in Figure 5-2 through 5-4, respectively. Flow rates of 165, 198, and 373kg/m^2/sec were tested while maintaining a constant heat flux of 23.9kW/m^2.

Bulk temperatures at the exit of the test section for Case F1015 are shown in Figure 5-2(a). The profile indicates that the system requires about 200 seconds for start-up for the same inlet temperature. The exit bulk temperature rose rapidly at t=212sec because the flow stopped during the pushover before entering the microgravity trajectory. Upon entering the microgravity trajectory, the flow started again and the bulk temperature reached a steady state after a few fluctuations. The acceleration level estimated from the static pressure was 2.4g during this period. The observed flow pattern transition was slug to annular, indicating that the liquid was deficient in the upper portion of the test section. Expansion of the vapor phase allowed the liquid to stay in the lower portion of the test section during the high acceleration period. The decrease in flow rate became less significant during the succeeding subcooled boiling tests where liquid phase was continuous along the test section. The above incident implies that experiments for higher thermal equilibrium qualities may encounter flow-rate instabilities in vertical flow systems during the high acceleration period unless sufficient driving pressure is supplied. To avoid the flow interruption, the boiling condition at the test section

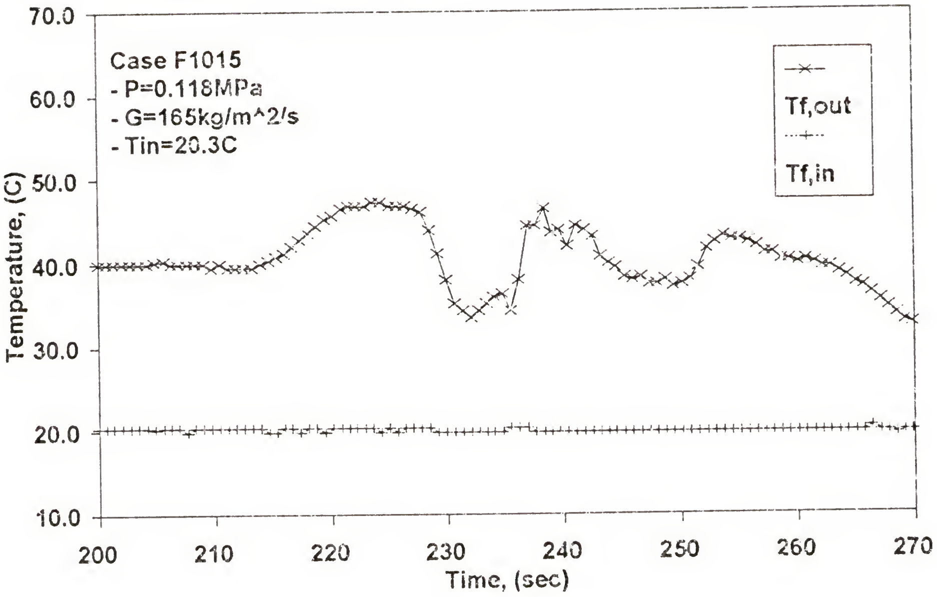

(a) Bulk temperatures

Figure 5-2 Variation of flow properties for Case F1015 during the flight experiment.

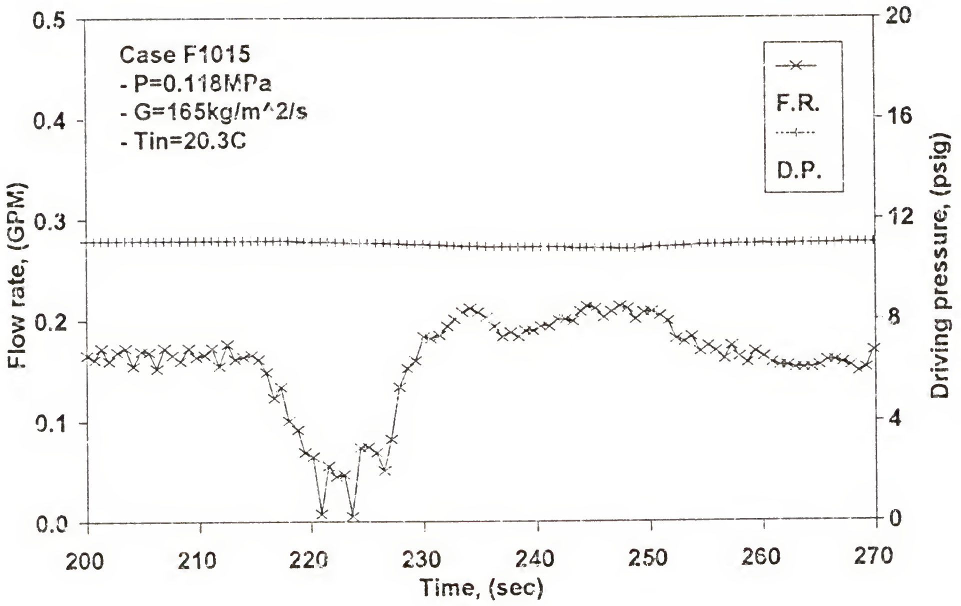

(b) Flow rate

Figure 5-2 Variation of flow properties for F1015 during the flight experiment.

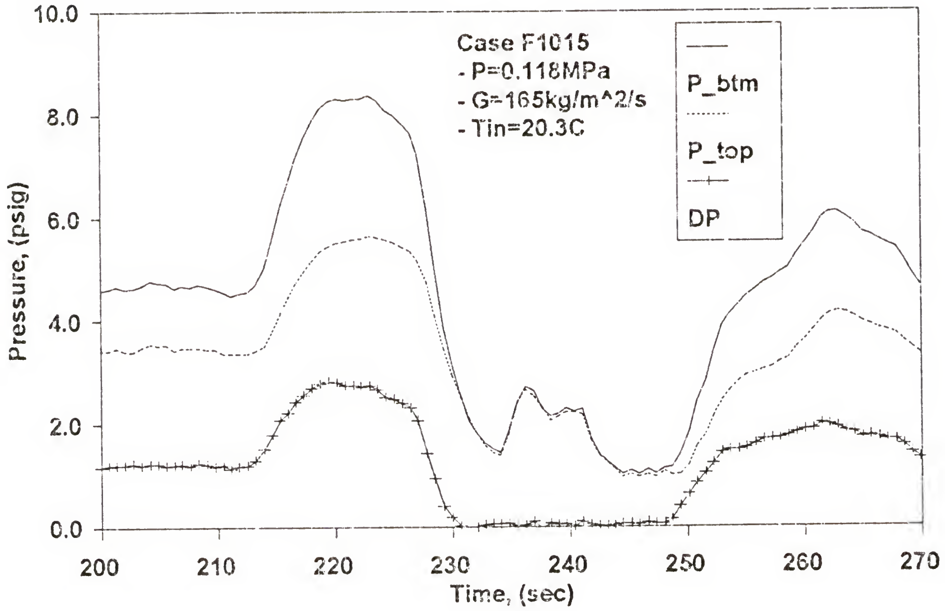

(c) Pressure drop

Figure 5-2 Variation of flow properties for Case F1015 during the flight experiment.

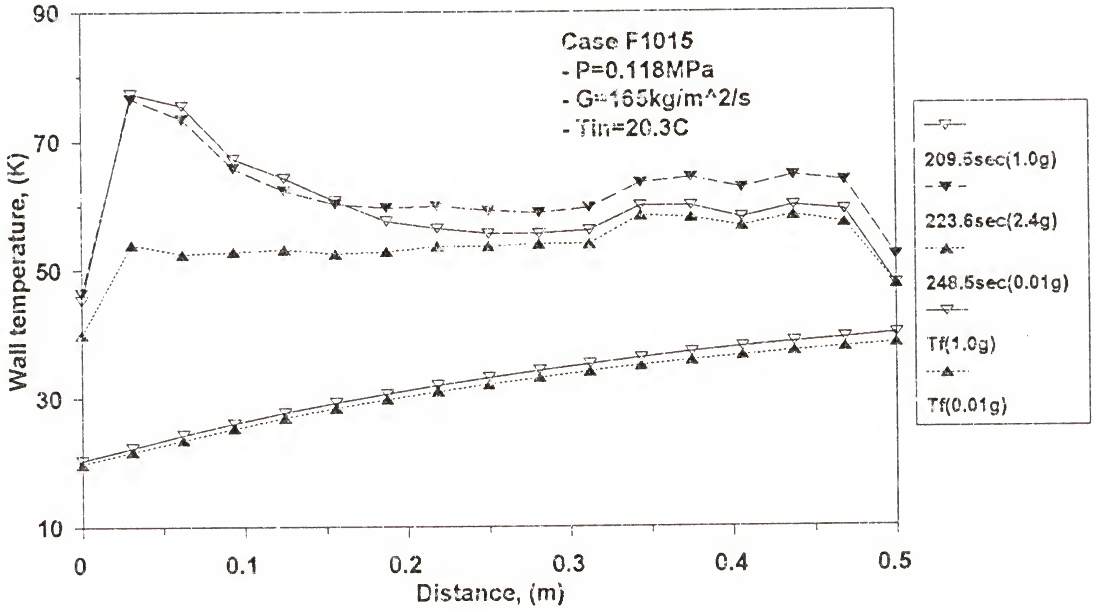

(d) Wall temperatures

Figure 5-2 Variation of flow properties for Case F1015 during the flight experiment.

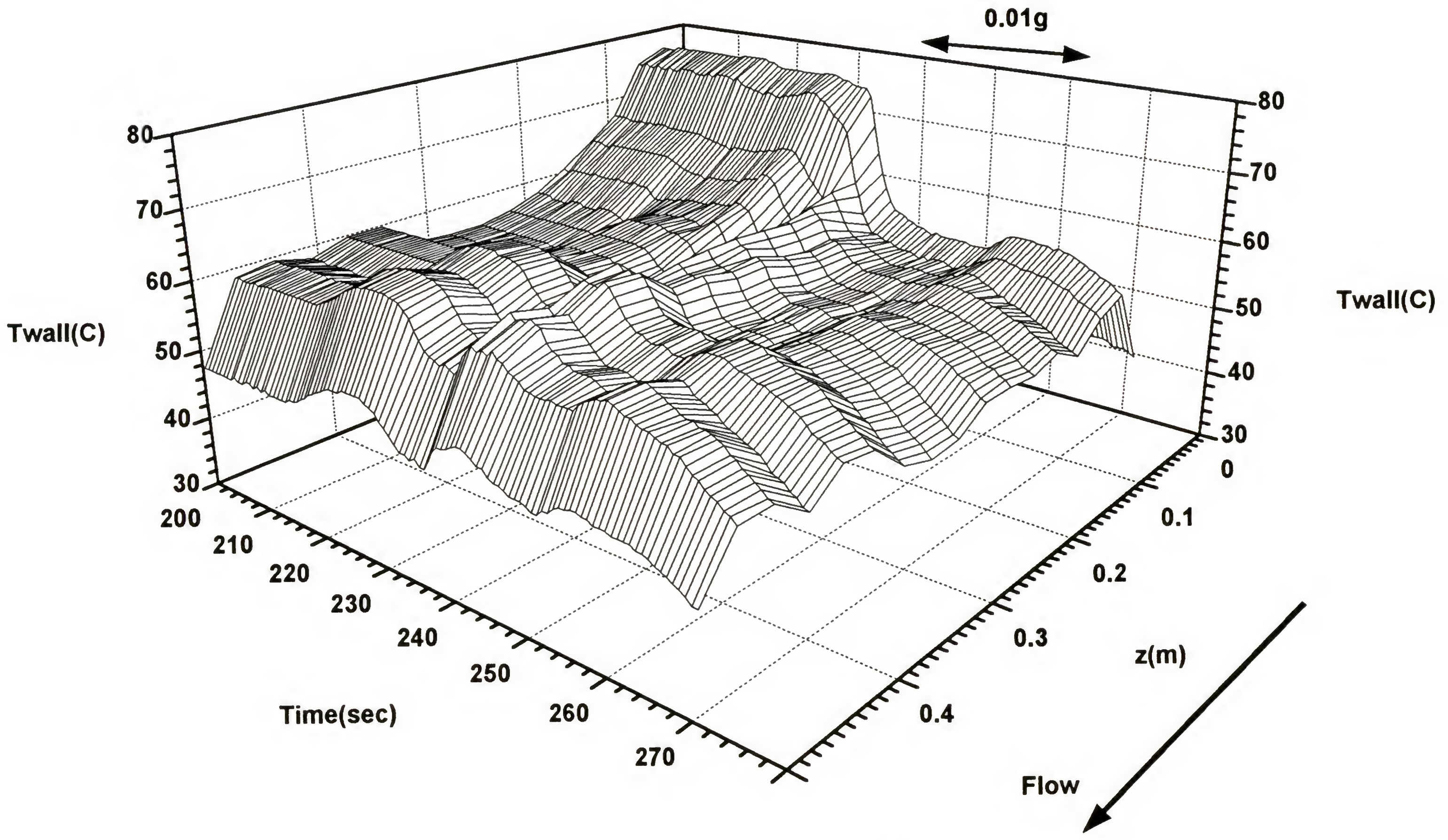

(e) Overall wall temperatures

Figure 5-2 Variation of flow properties for Case F1015 during the Learjet flight experiment.

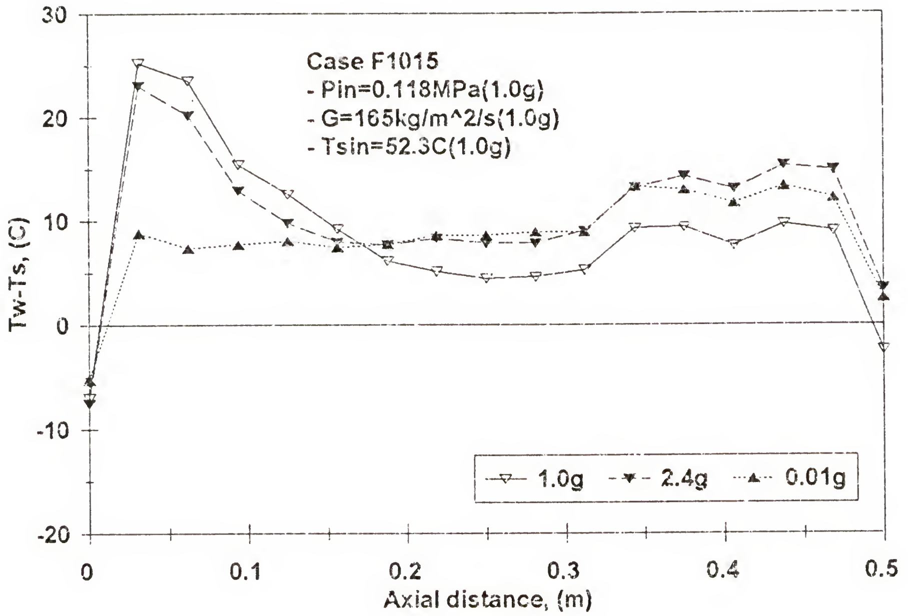

(f) Wall superheats

Figure 5-2 Variation of flow properties for Case F1015 during the flight experiment.

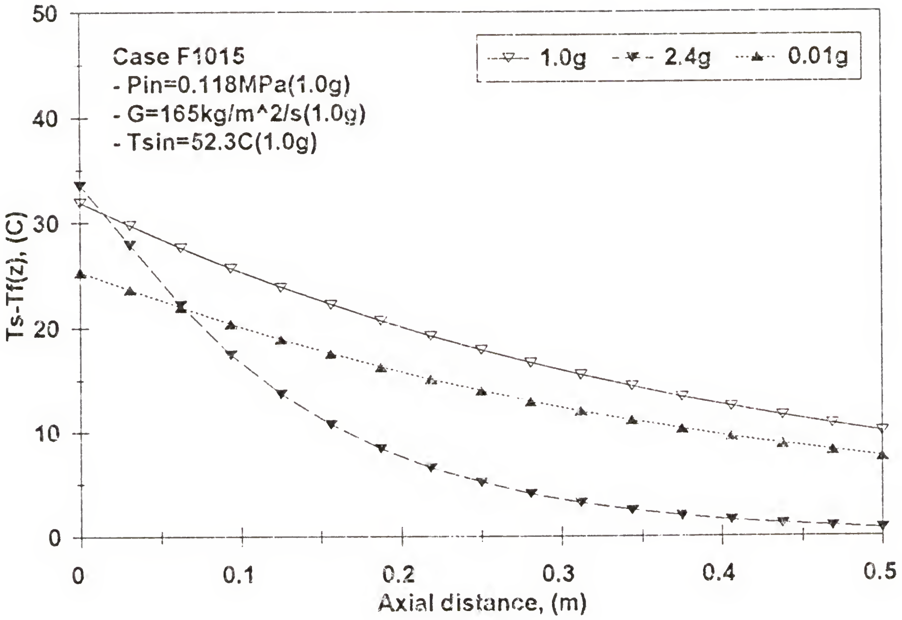

(g) Subcoolings

Figure 5-2 Variation of flow properties for Case F1015 during the flight experiment.

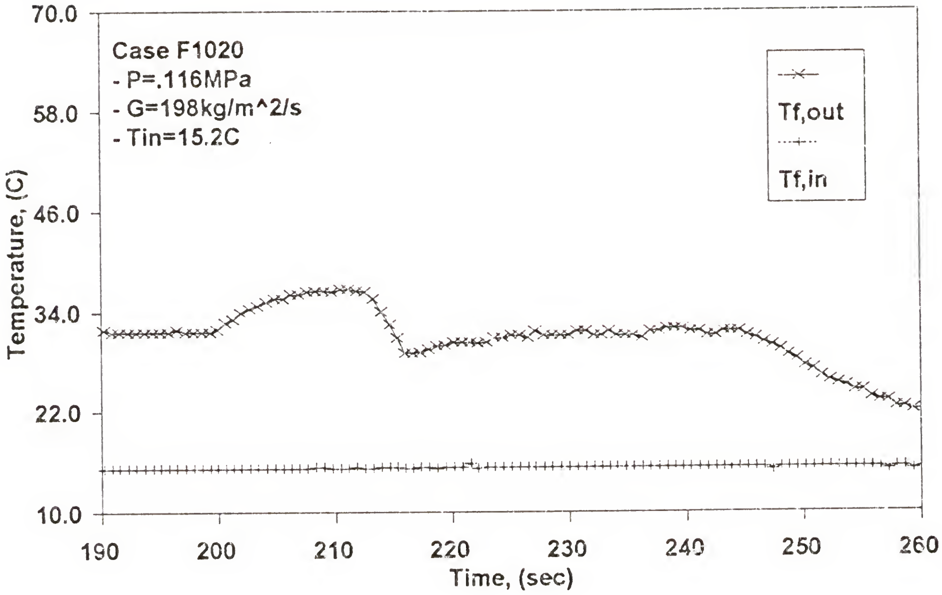

(a) Bulk temperatures

Figure 5-3 Variation of flow properties for Case F1020 during the flight experiment.

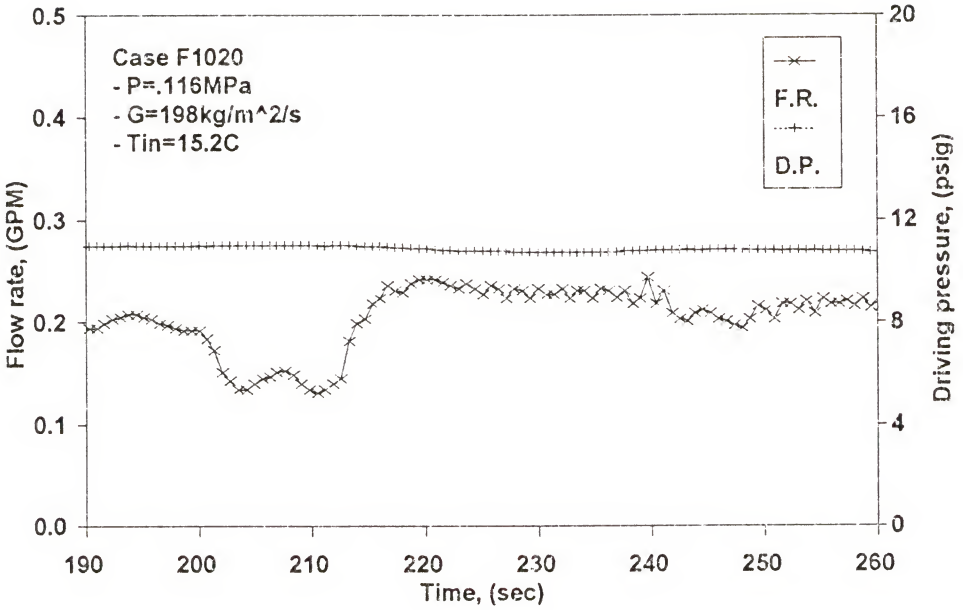

(b) Flow rates

Figure 5-3 Variation of flow properties for Case F1020 during the flight experiment.

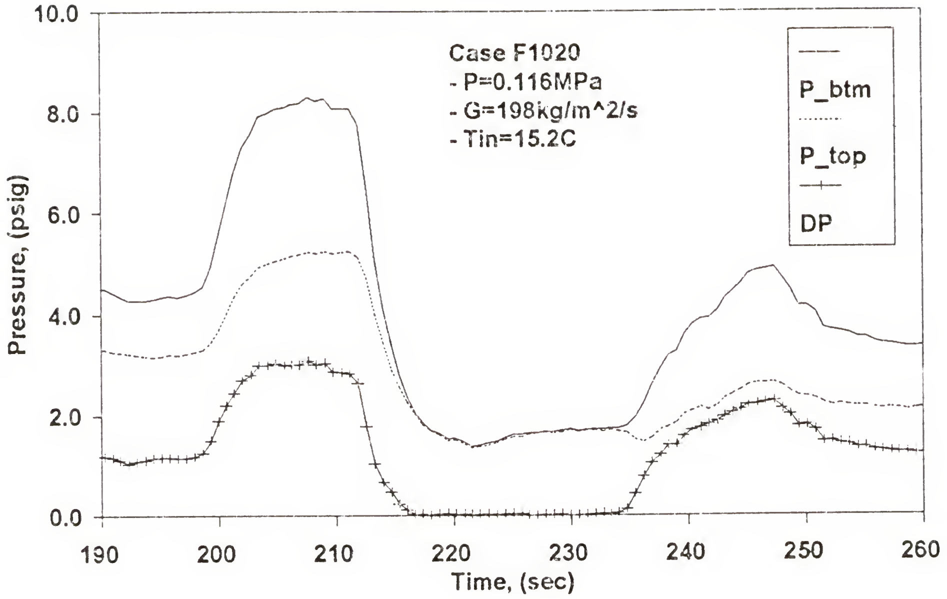

(c) Pressure drops

Figure 5-3 Variation of flow properties for Case F1020 during the flight experiment.

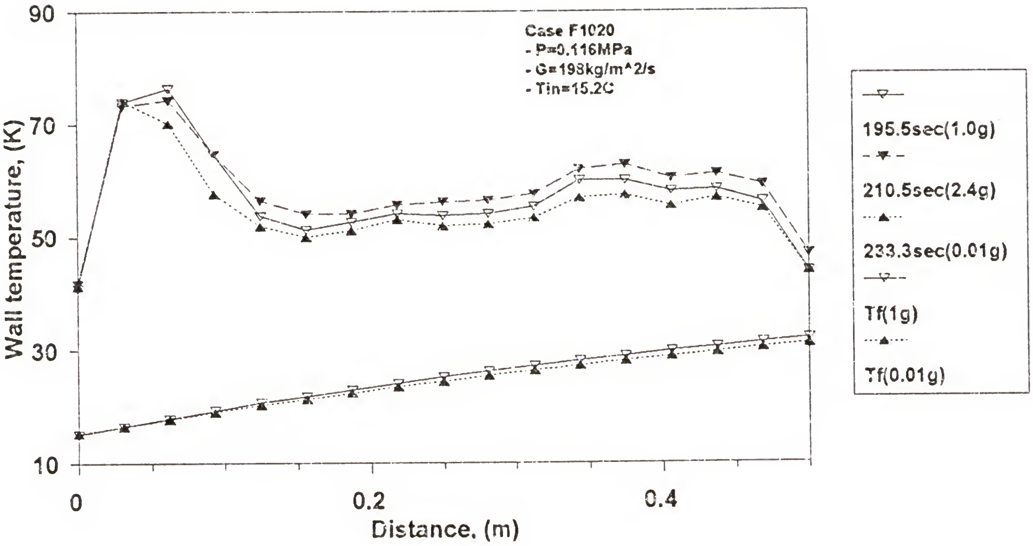

(d) Wall temperatures

Figure 5-3 Variation of flow properties for Case F1020 during the flight experiment.

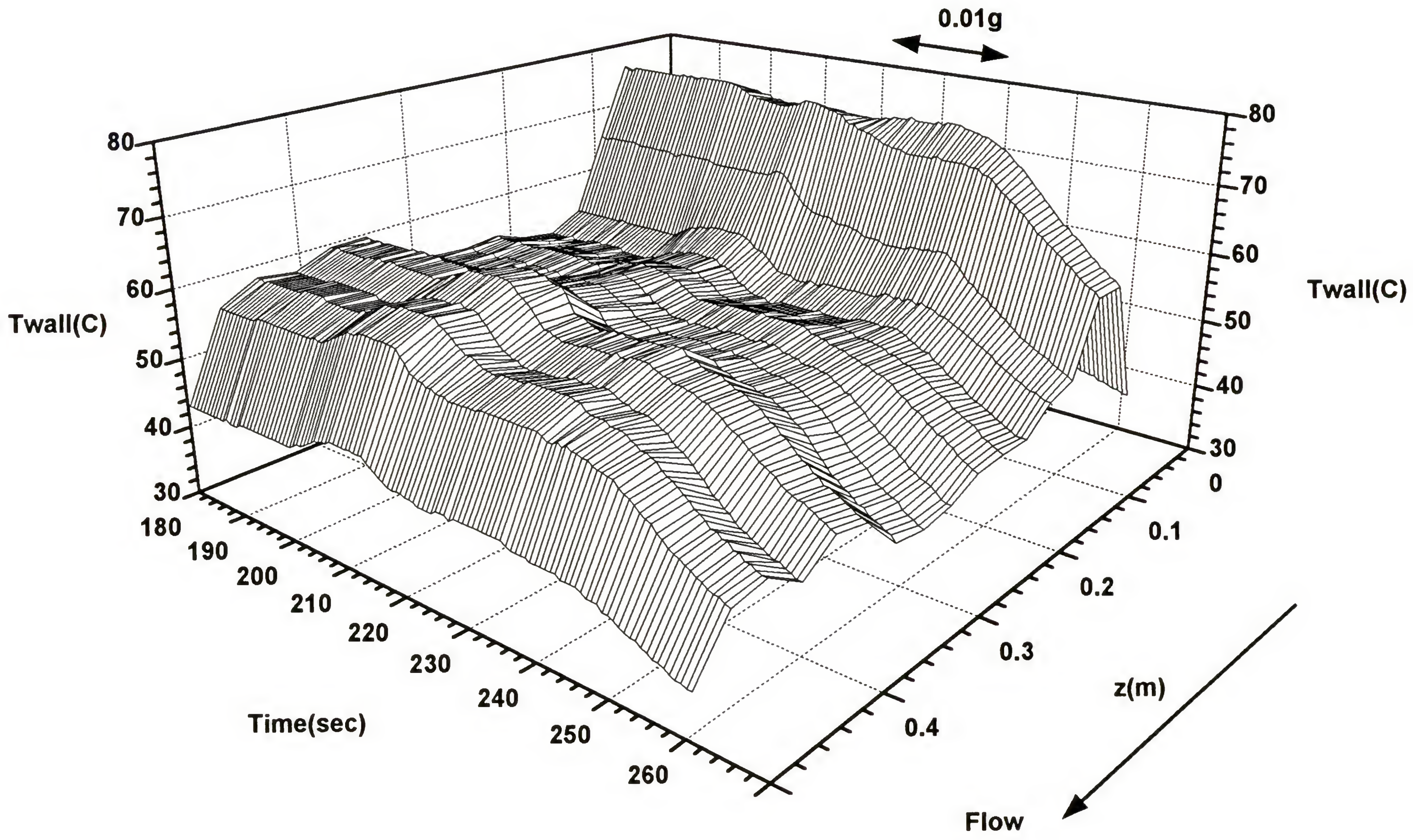

(e) Overall wall temperatures

Figure 5-3 Variation of flow properties for Case F1020 during the Learjet flight experiments.

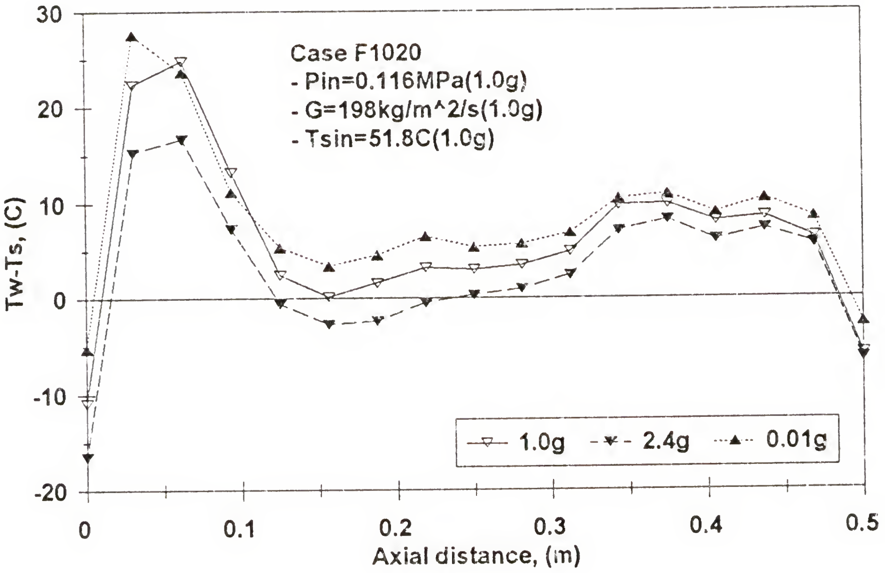

(f) Wall superheats

Figure 5-3 Variation of flow properties for Case F1015 during the flight experiment.

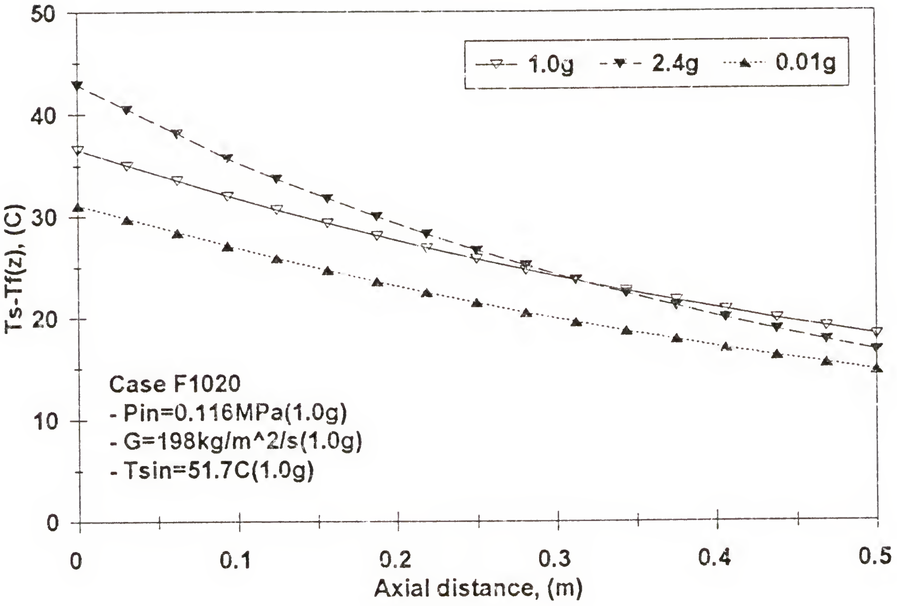

(g) Subcoolings

Figure 5-3 Variation of flow properties for Case F1020 during the flight experiment.

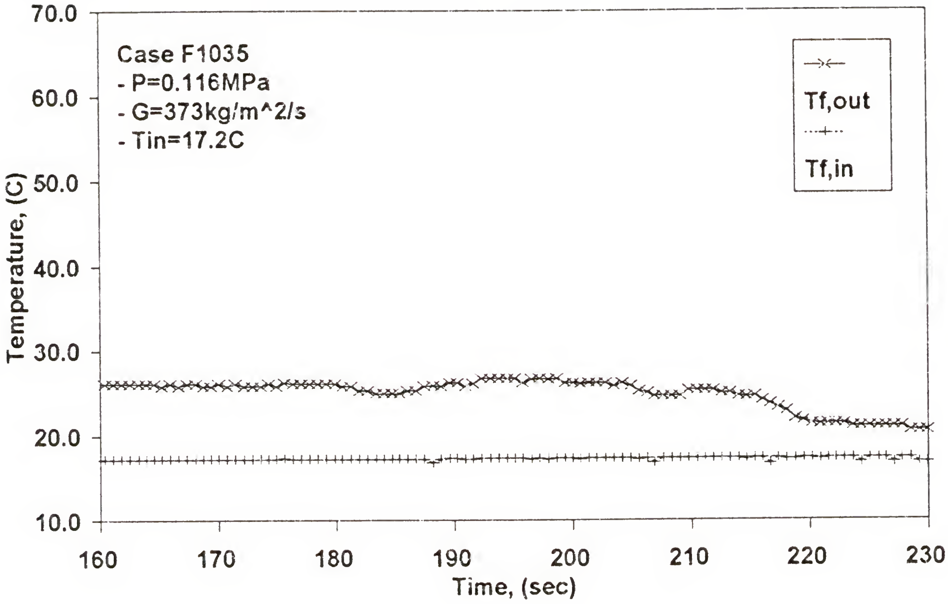

(a) Bulk temperatures

Figure 5-4 Variation of flow properties for Case F1035 during the flight experiment.

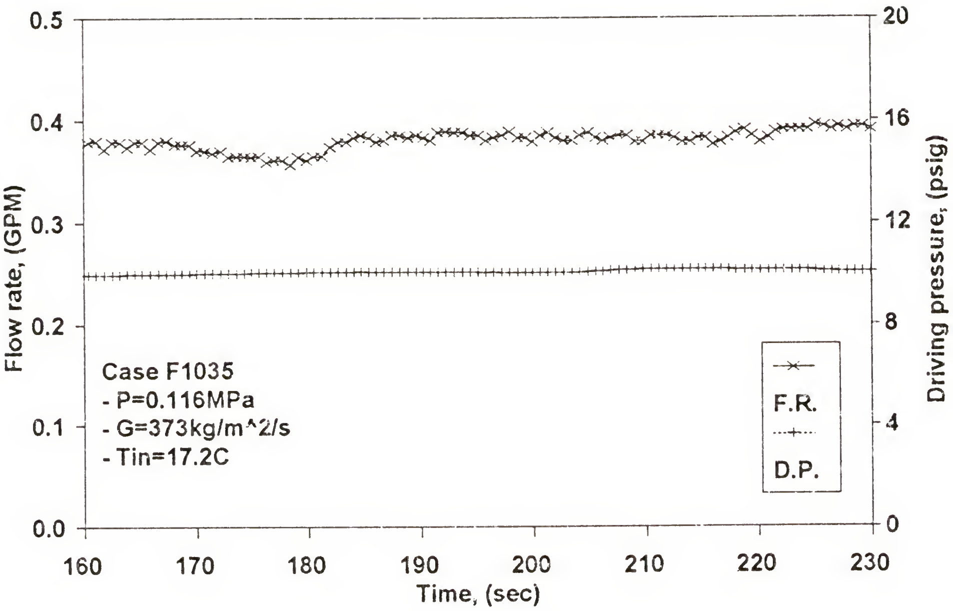

(b) Flow rates

Figure 5-4 Variation of flow properties for Case F1035 during the flight experiment.

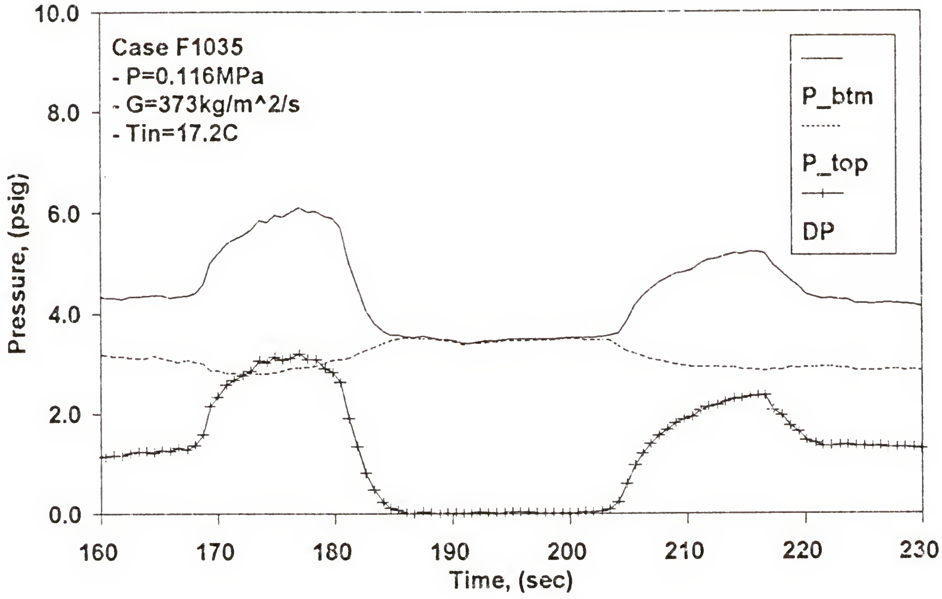

(c) Pressure drops

Figure 5-4 Variation of flow properties for Case F1035 during the flight experiment.

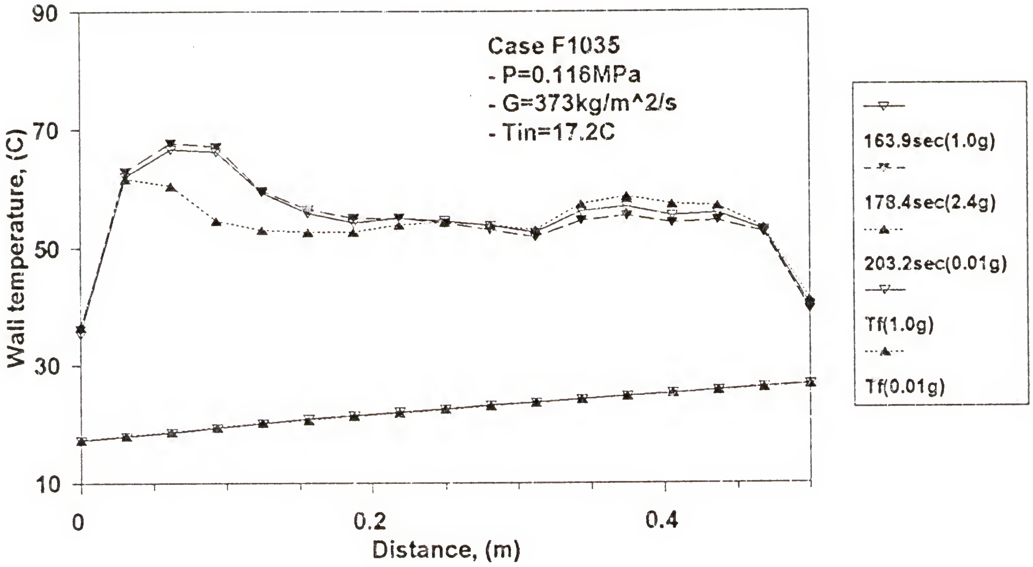

(d) Wall temperatures

Figure 5-4 Variation of flow properties for Case F1035 during the flight experiment.

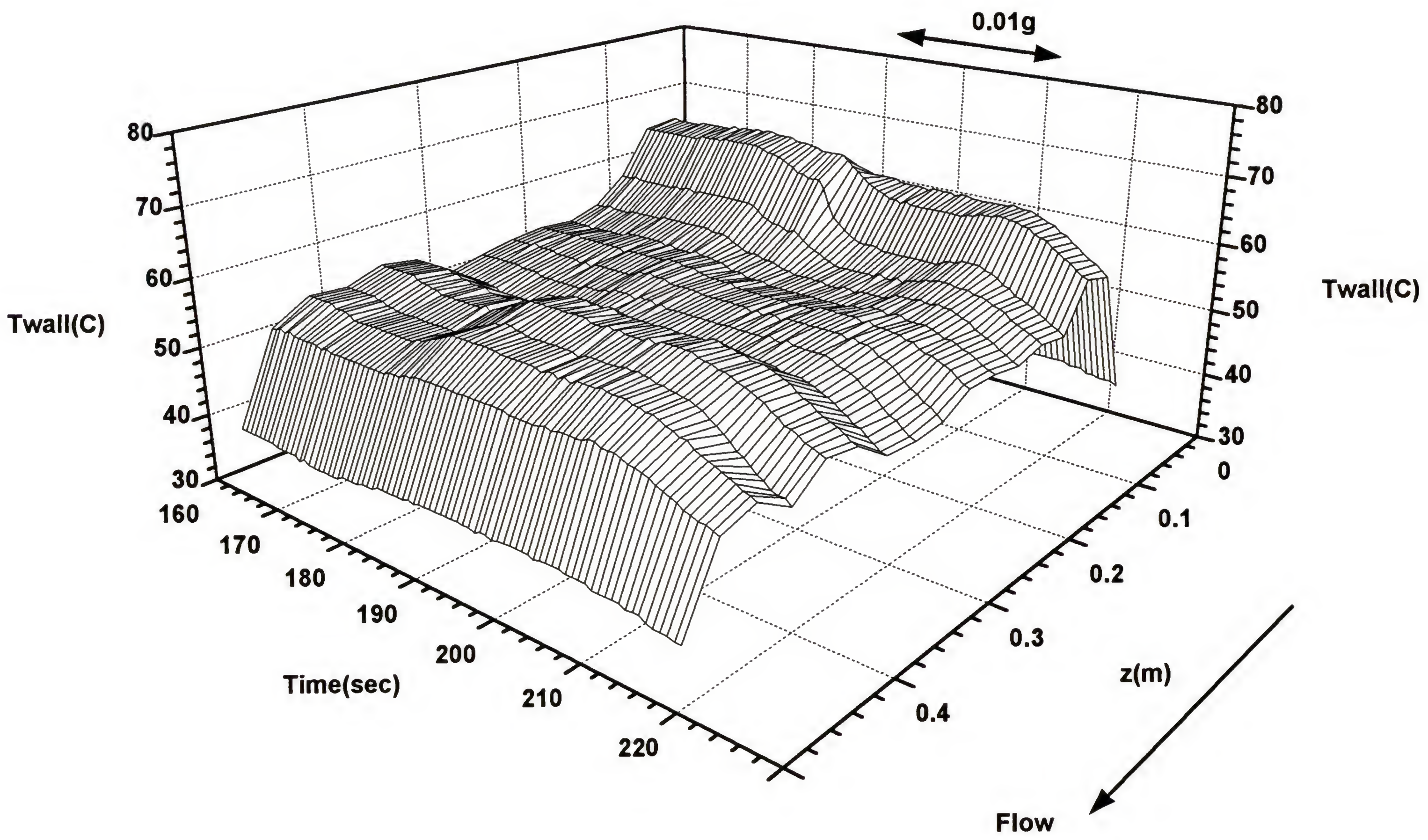

(e) Overall wall temperatures

Figure 5-4 Variation of flow properties for Case F1035 during the Learjet flight experiments.

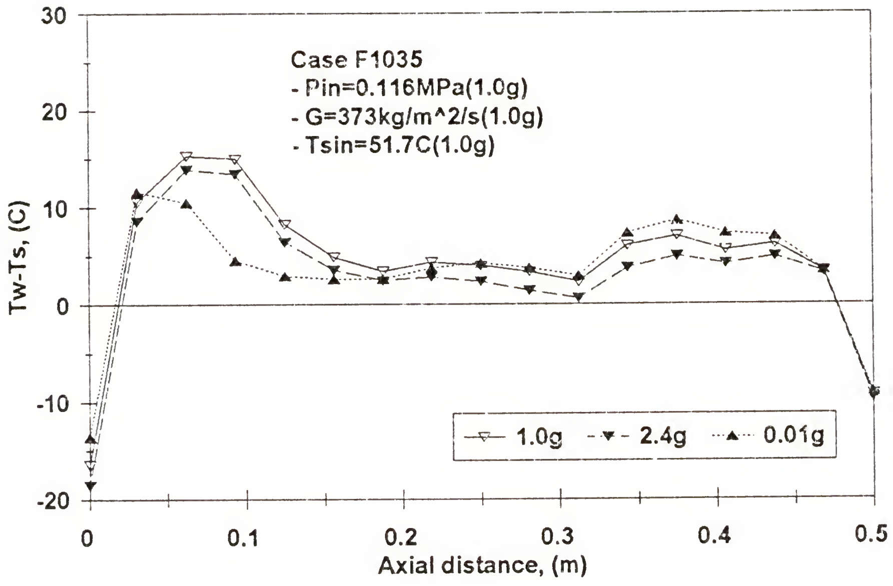

(f) Wall superheats

Figure 5-4 Variation of flow properties for Case F1035 during the flight experiment.

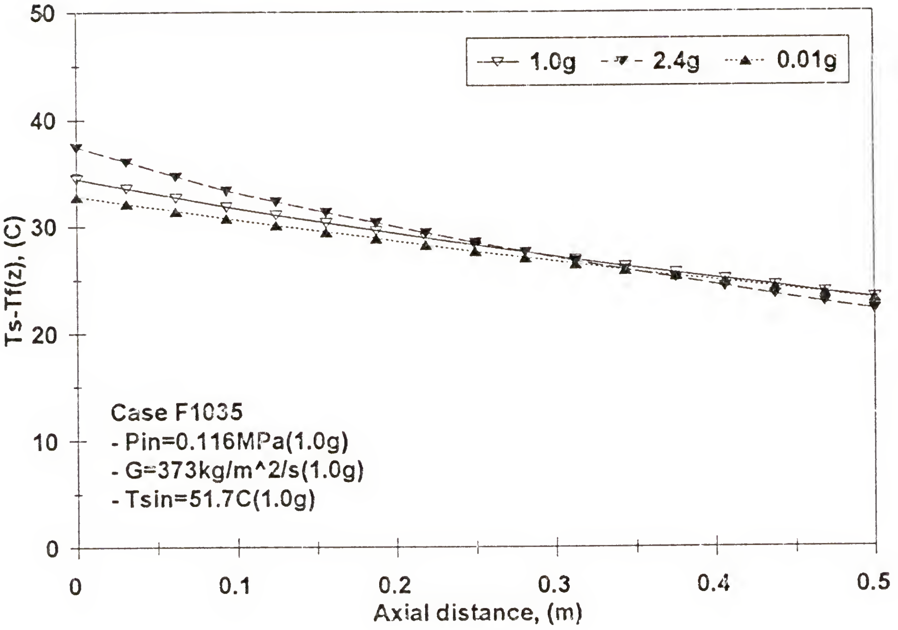

(g) Subcoolings

Figure 5-4 Variation of flow properties for Case F1035 during the flight experiment.

exit for the present system was confined to subcooled qualities.

The variation of gauge pressures located at the inlet and outlet of the test section during the experiments are shown in Figure 5-2(b). The ambient pressure in the cabin on that day was 0.85atm. Since all the test conditions at the exit fall in the subcooled region, the acceleration pressure drop was small compared with the static pressure drop. In normal gravity, the gravitational pressure drop was dominant compared to other components. According to error propagation formula, the uncertainty range of the differential pressure was ±38.5Pa based on the accuracy of ±27.5Pa for a single pressure transducer. Since the built-in accelerometer was independent of our data acquisition system, matching between the events and elapsed time was made by reading the pressure data.

As shown in Figure 5-2(c), the flow rates increased during the microgravity trajectories with the decrease in static pressures. Since the acceleration in microgravity became about 1/100 of normal gravity, the static pressure of Freon 113 in a 0.5m vertical tube changed from 7585Pa to 75.9Pa at room temperature. Correspondingly the flow rates increased by 27.1%, 14.6%, and 2.9% for Cases F1015, F1020, and F1035, respectively. This change was undesirable because the objective of the present study was to investigate the gravity effects on heat transfer with other conditions unchanged. Especially for Case F1015, the flow completely stopped at t=222.0sec. As can be seen from the pressure data, this coincides with the time when the highest acceleration was achieved. For Case F1035, however, the flow rate change as well as the pressure change was small enough to allow for comparison of microgravity data with normal gravity data. On the analysis of Cases F1015 and F1020, changes in the flow rate and pressure were considered.

To successfully operate the present system, the liquid phase must be continuous to avoid the flow interruption, or the driving pressure must be large enough to exceed the pressure losses in the loop. The calculation of pressure losses in the loop is shown in Appendix A.

Wall temperature and estimated bulk temperature distributions under normal and micro gravity conditions are shown in Figure 5-2(d). The bulk temperatures at the inlet and exit of the test section were measured by 1.6mmO.D. E-type thermocouples immersed in the flow. In the two-phase region, the axial bulk temperatures were estimated by Ahmad's equation without using the condensation parameter[40]. In the single-phase region, bulk temperatures were estimated simply by the following heat balance

$$T_f(z) = T_{fi} + \left(\frac{4\, q_w'' \, z}{G c_{pl} D} \right) \tag{5-1}$$

In the subcooled boiling region, the dimensionless subcooling is expressed as

$$\Delta T^{*} = \frac{\Delta T}{\Delta T_{d}} = \frac{(T_{s} - T_{f})}{(T_{s} - T_{d})} = e^{-c_{1}z^{*}} \qquad (5\text{-}2)$$

where C_1 is the heat transfer parameter and z^* is the dimensionless distance($=z/L_{2P}$). C_1 is defined as

$$C_{1} = \left(\frac{4\, h_{fc} L_{2P}}{G D c_{pl}} \right) \qquad (5\text{-}3)$$

where h_{f0} is the single-phase forced convective heat transfer coefficient, L_{2P} is the significant boiling length given by

$$L_{2P} = L - \frac{4\, G c_{pl}}{q_{w}'' D} (\Delta T_{in} - \Delta T_{d}) \qquad (5\text{-}4)$$

ΔT_{in} and ΔT_d denote the subcoolings at the inlet and the bubble detachment point, respectively. An array of 17 fine-gauge thermocouples were mounted on the 0.5m long, 0.71mm wall thickness copper tube at equal intervals. The outputs from the thermocouples were calibrated by 9th order polynomials. Accuracy of the temperature reading was ±0.5°C. Wall temperatures at both ends were lower than others because of pressure taps and tube fittings diffusing heat from the copper tube. Therefore, these 2 data points at each end were discarded.

For Case F1015, the wall temperatures decreased significantly along the test section in microgravity, indicating a large increase in heat transfer rate. Although the liquid flow once stopped and re-started, it was stabilized at the end of the microgravity trajectory of 18 seconds (Figure 5-2(b)). The flow pattern changed from slug flow to annular flow in microgravity. Our previous results in the drop tower experiments also showed a similar transition from slug to annular flow in microgravity.

As shown in Figure 5-2(d), a peak of the wall temperature profile near the test section inlet disappeared under microgravity conditions. From the data set obtained in this experiment, it is difficult to correlate the wall temperature profile to the void fraction profile in the flow direction. However, a similar subcooled experiment using Freon 113 was conducted by Hino and Ueda[41]. They measured wall temperature profiles and photographed the void fraction distributions simultaneously. It was found that the peak in the wall temperature curve corresponds to the onset of nucleate boiling point (ONB). The profiles in microgravity indicate that the wall temperatures at the ONB decreases significantly.

The wall temperatures in the subcooled region near the test section outlet under microgravity conditions decreased by 1-2°C. Since the system pressures have decreased during the transition from 2.4g to 0.01g, the change of saturation temperature was taken into account to investigate the gravity effect on heat transfer. The overall wall temperature transition along the test section is shown in Figure 5-2(e). The wall superheat and liquid subcooling are separately shown in Figure 5-2(f) and 5-2(g), respectively. The increase in wall superheats near the test section outlet indicates that the bulk convection heat transfer was decreased in microgravity.

Similar tendencies were observed in Figure 5-3 and 5-4 for Cases F1020 and F1035, respectively. Since the exit condition was highly subcooled for Case F1035, the static pressure change was minimal among the three data sets. Case F1035, therefore, exhibits the gravity effects with a minimum interference of pressure change.

Characteristic boiling regions. For highly subcooled liquid flowing in a heated channel, the heat transfer process evolves from forced convective single-phase flow to subcooled flow boiling, then to saturated flow boiling. The subcooled boiling region is further divided into 2 regions at the bubble detachment point: the highly subcooled region with low void fraction where bubbles are attached or slide along the wall, and the slightly subcooled region with large void fraction where the detached bubbles flow with the liquid.

As boundaries of the above regions, two characteristic points are defined. One is the onset of nucleate boiling (ONB) point at which the first bubble formation is observed, and the other is the bubble detachment point at which bubbles break off the wall and enhance the stirring motion in the liquid. Figure 5-5 shows the typical flow pattern and the variation of surface and liquid temperatures. The range of

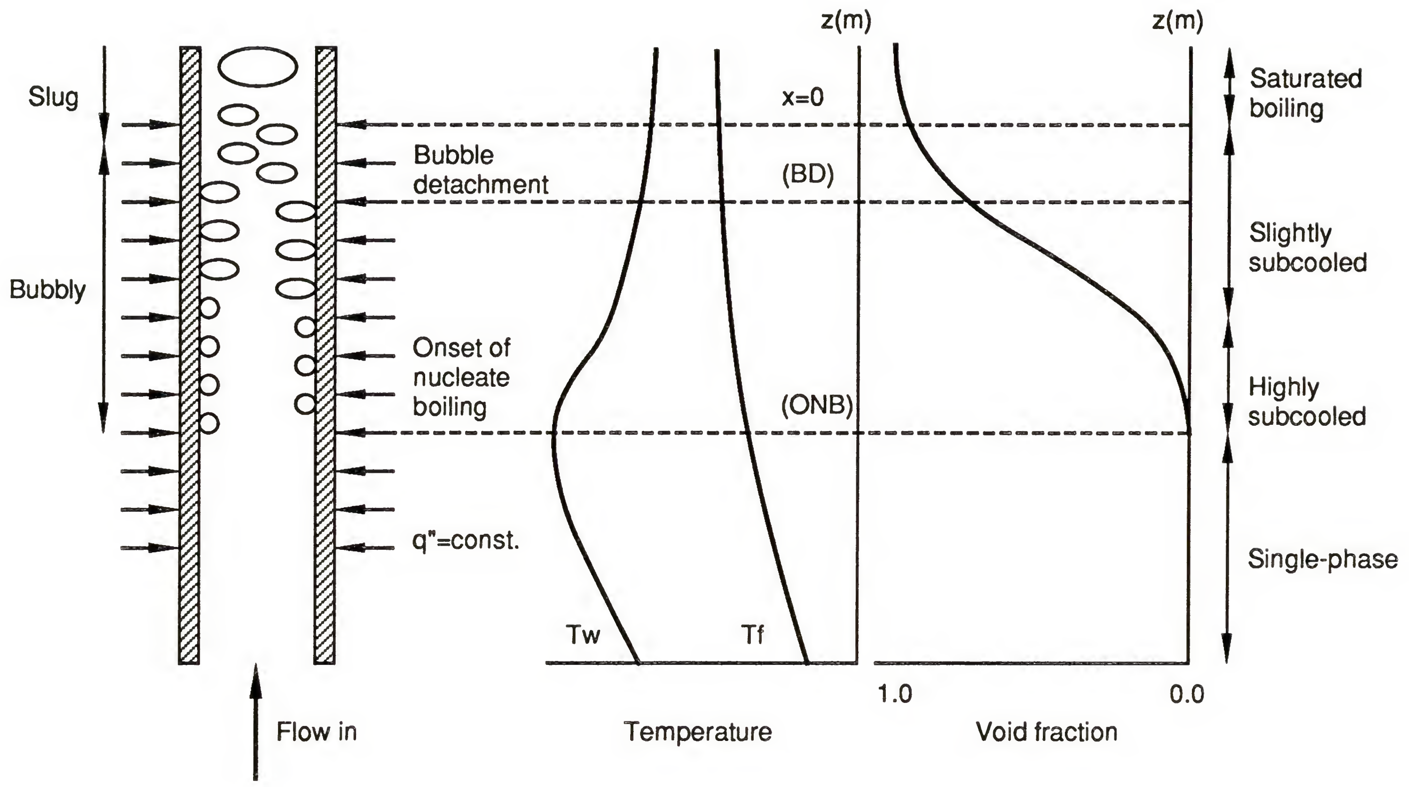

Figure 5-5 Flow boiling evolution in a vertical pipe in the subcooled region.

the present study is confined to the single-phase region, highly subcooled region, and a part of slightly subcooled region. In microgravity, the heat transfer mechanisms are considered to be different from those in normal-gravity. The existing models to predict the boundaries of the above regions cannot be applied to microgravity heat transfer without verification. In the following section, the gravity effects on the single-phase and subcooled heat transfer mechanisms will be discussed, followed by discussions of gravity effects on the onset of nucleate boiling.

5.2 Forced Convective Single-Phase Flow

A simple heat balance in this region yields the liquid temperature profile. Eq.(5-1) was used to estimate the liquid temperature within the single-phase region. The wall temperature is given by

$$T_w(z) = T_f(z) + \frac{q_w''}{h_{f0}} \tag{5-5}$$

where h_{f0} is the single-phase heat transfer coefficient. The minimum and maximum Reynolds numbers for the present tests were 4145 and 9656, respectively, which fall in the intermediate range between laminar and turbulent flow. The decrease in system pressure during the microgravity maneuver induced an increase in the mass flow rate. Although the inlet temperature was maintained constant throughout the experiment, this increase in mass flow rate altered bulk temperature profiles. Among three cases, F1035 showed a minimum decrease in bulk temperature of 0.6K at the test section exit, while a maximum decrease of 1.1K was observed for F1020.

5.2.2 Contribution of Natural Convection

It is assumed that the effects of gravity change is negligible on single-phase turbulent flow since no phase change is involved. However, natural convection heat transfer, which is driven by the buoyancy force, is significantly affected by the gravity change. In general, the Nusselt number is expressed as a function of Reynolds number Re, Prandtl number Pr, and Grashof number Gr defined as

$$Gr = \frac{D^3 \rho_f^2 g \beta \Delta T}{\mu_f} \tag{5-6}$$

During the microgravity trajectories, the acceleration level reached ±0.01. The corresponding Gr is approximately 1/100 of Gr under normal gravity. In laminar flow correlations, Nu is proportional to $g^{0.1}$ and a change in g by 1/100 reduces Nu by 37%. In a vertical flow system, if the flow rate is low and the liquid Reynolds number is less than 2000, the natural convection is significantly affected by the gravity level.

For the relatively low Reynolds numbers in this experiment, the contribution of natural convection heat transfer to that of laminar and turbulent heat transfer was estimated by Jackson's correlation[55] derived for intermediate Reynolds number ranges near the entrance region.

This correlation was chosen particularly because the contributions of laminar, turbulent, and natural convection for forced convective flow in a pipe was distinguishable

$$Nu=1.74\,[\,(0.785\,Re\,Pr\frac{D}{z}+Re^2Pr^{5/6}\times10^{-5})^2 + (Gr\,Pr)^{5/4}\times10^{-3}\,]^{1/5} \qquad (5\text{-}7)$$

The first, second, and third term on the RHS of Eq.(5-7) indicate the contributions of laminar, turbulent, and natural convection, respectively. The effects of gravity change in the single-phase flow on Nu were negligible since the relative magnitude of the natural convection accounts for less than 1%. In fact, the wall temperature profiles in this region showed no change during the gravity transition, as shown in Figure 5-3(d) and 5-4(d). In Case F1015, the present analysis was not applicable since the flow pattern changed from slug to annular flow.

5.2.3 Single-Phase Heat Transfer Coefficient

Due to the unique test conditions and configuration of the test section, none of the existing correlations successfully predicts the single-phase heat transfer rate for the present study. However, the single-phase heat transfer still accounts for substantial fractions in the subcooled region. Successful prediction of the gravity effects on boiling heat transfer depends on the accurate prediction of single-phase flow heat transfer.

A new correlation specifically applicable to our study was developed based on the turbulent flow heat transfer model proposed by Sieder-Tate. Nu_0 for fully developed turbulent flow is given by

$$Nu = 0.023\left[\frac{GD}{\mu_f}\right]^{0.8}\left[\frac{C_{pl}\mu_f}{k_f}\right]^{1/3}\left(\frac{\mu_f}{\mu_w}\right)^{0.14} \tag{5-8}$$

Since the inlet of the vertical tube is located 0.14m above the bend, the flow was not completely developed in the inlet region. Normally, turbulence caused by the edge of the tube increases the heat transfer rate. Eq.(5-8) alone underestimates the heat transfer rate in this region. According to [55], the local Nu(z) in the entrance region should be multiplied by the following correction factor

$$Nu(z) = 1.57\,Nu_0\left(\frac{D}{z}\right)^{0.054} \tag{5-9}$$

The validity of the above equation is Re > 8,000 and (L/D) < 60. The factor 1.57 was modified to fit the range of appropriate Reynolds numbers. Substitution of Eq(5-8) into Eq.(5-9) yields

$$Nu(z) = C_1 Re^{C_2} Pr^{1/4}\left(\frac{\mu_f}{\mu_w}\right)^{0.14}\left(\frac{D}{z}\right)^{0.054} \tag{5-10}$$

where C_1 and C_2 are constants to be determined experimentally through least square fitting. Three data sets obtained in the flight experiment were used to correlate Re with Nu in the transitional range between laminar and turbulent flow. The

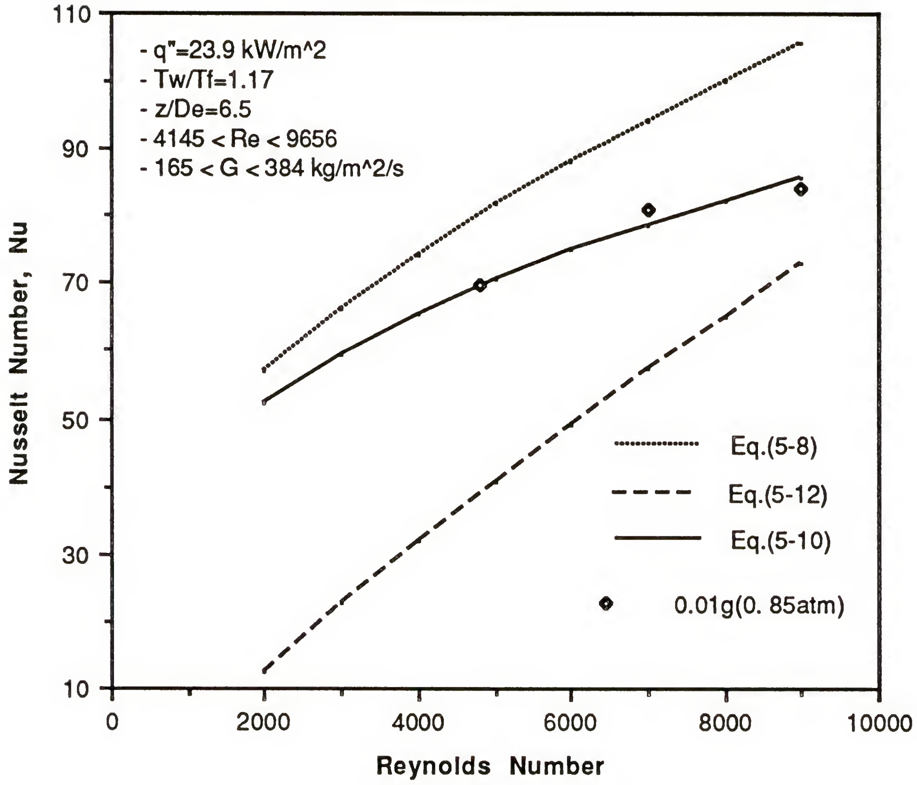

Figure 5-6 Single-phase heat transfer in a vertical tube in Learjet flight experiments.

result of curve fitting is shown in Figure 5-6. The pressure in the Learjet cabin was 0.0862MPa, while that of ground tests was 0.101MPa. The coefficients for the new correlation are

C_1=2.192, and

C_2=0.330.

The validity of the above correlation is confined to 4145 < Re < 9656 and q_w''=23.9kW/m^2. Nu for the experiments were calculated as follows

$$Nu(z)_{\exp} = \frac{q_w'' D}{k_f (T_w - T_f)} \tag{5-11}$$

The wall temperature T_w was measured on the outer surface of the tube, while the bulk temperatures between the inlet and outlet of the test section were estimated by Eq.(5-1).

Two other correlations for forced convective heat transfer were also plotted against Re. One is Jackson's correlation (Eq.(5-8)), and the other is that of Warmeatlas [42] derived for the transition between laminar and turbulent flow

$$Nu = \frac{(\alpha/8)(Re-1000)Pr}{1+12.7(\alpha/8)^{1/2}(Pr^{2/3}-1)} \times \left[1+\left(\frac{D}{L}\right)^{2/3}\right]\left(\frac{Pr}{Pr_w}\right)^{0.11} \times 0.86\left(\frac{D_w}{D_h}\right)^{-0.16},$$
$$\alpha = (1.82\log_{10}Re - 1.64) \tag{5-12}$$

Eq.(5-8) tends to overestimate the heat transfer rate since this relationship was developed for smaller Pr. The value of Pr for Freon 113 was on the order of 7.0. Eq.(5-12), on the other hand, underestimates the heat transfer rate for small Re. This is probably due to the relatively small flow rate used in the present experiment. Eq.(5-10) follows the variation of Nu over the entire range of Re in the present experiments.

It should be noted that this correlation was derived only for the present study from a limited number of data. Thus, this equation may not be applicable elsewhere.

5.2.4 Effects of Pressure on Nusselt Number

Vertical flow lines including the boiling test section were subject to the transition of gravity varying from 1.0g through 2.4g and to 0.01g during the trajectory. As shown in Table 5-1, the largest pressure decrease due to gravity change was 3.5psi experienced in Case F1015. This pressure change induced an increase in flow rate by 25.8%. As a result, Nu was increased by 7.7%. Using Eq.(5-10), the ratio of Nu under 1g and 0.01g conditions is given by

$$\frac{Nu_{0g}}{Nu_{1g}} = \left(\frac{Re_{0g}}{Re_{1g}}\right)^{0.33}\left(\frac{Pr_{0g}}{Pr_{1g}}\right)^{1/4} \tag{5-13}$$

The increase in Nu in the single-phase region for F1015, F1020, and F1035 were +4.6%, +5.0%, and +1.0%, respectively. This result indicates that the change of heat transfer rate observed for Case F1035 under microgravity conditions reflects the gravity effects with least effect of pressure change. The increase in flow rate for Case F1035 in microgravity was 3.0%, the smallest of the three cases.

If one hypothetically maintains the same flow rate with the above pressure change, Nu would decrease by 1.4%. In general, a decrease in pressure reduces the heat transfer rate. However, this decrease in Nu was exceeded by the effects of the increase in the flow rate.

5.3 Onset of Nucleate Boiling

In the beginning of the subcooled region, the wall temperatures in microgravity significantly decreased. In this section, theories of the onset of heterogeneous nucleation are introduced. Then the effect of pressure change on the ONB is examined to identify the gravity effects.

5.3.1 Superheat at ONB

Existing analytical solutions to predict the heat flux and the wall superheat at the onset of nucleate boiling were reviewed by Dougall and Lippert[56]. Among several theories, those proposed by Bergles and Rohsenow, Hsu, and Frost and Dzakowic were applied to the present study.

Hsu postulated that the criterion for nucleation is that the temperature of the liquid at the top of the bubble should exceed the equilibrium temperature of the vapor in the bubble[57]. If a full spectrum of cavity size is assumed to exist on the heating surface, the criterion is given by the tangent of liquid temperature profile

$$T_f(z) = T_w - \left(\frac{q_w'' y}{k_f} \right) \tag{5-14}$$

and the vapor equilibrium temperature profile

$$T_g = T_s (1 + \frac{A}{r_{crit}}) \tag{5-15}$$

where A is a combination of fluid properties. As values of A, the following values were employed

$$\frac{R_g T_s}{p_f} \left(\frac{2\sigma}{h_{fg}} \right) \qquad (Bergles\text{-}Rohsenow[59])$$

$$v_{fg} \left(\frac{2\sigma}{h_{fg}} \right) \qquad (Frost\text{-}Dzakowic[60]) \tag{5-16}$$

$$\frac{1}{1.25\rho_g} \left(\frac{2\sigma}{h_{fg}} \right) \qquad (Frost\text{-}Dzakowic[61])$$

At the tangent, the following relationships are satisfied

$$T_f = T_g \qquad and \qquad \frac{dT_f}{dy} = \frac{dT_g}{dy}, \qquad at \;\; y = nr_{crit} \tag{5-17}$$

where $n \cdot r_{crit}$ indicates the distance from the wall to the tangent of two profiles. Frost and Dzakowic and Hsu assumed that the temperature isotherm above the bubble is distorted due to the presence of the bubble and proposed Pr^2 and 2.0, respectively, for the value of n. Bergles and Rohsenow suggested n=1.0 without considering the isotherm distortion.

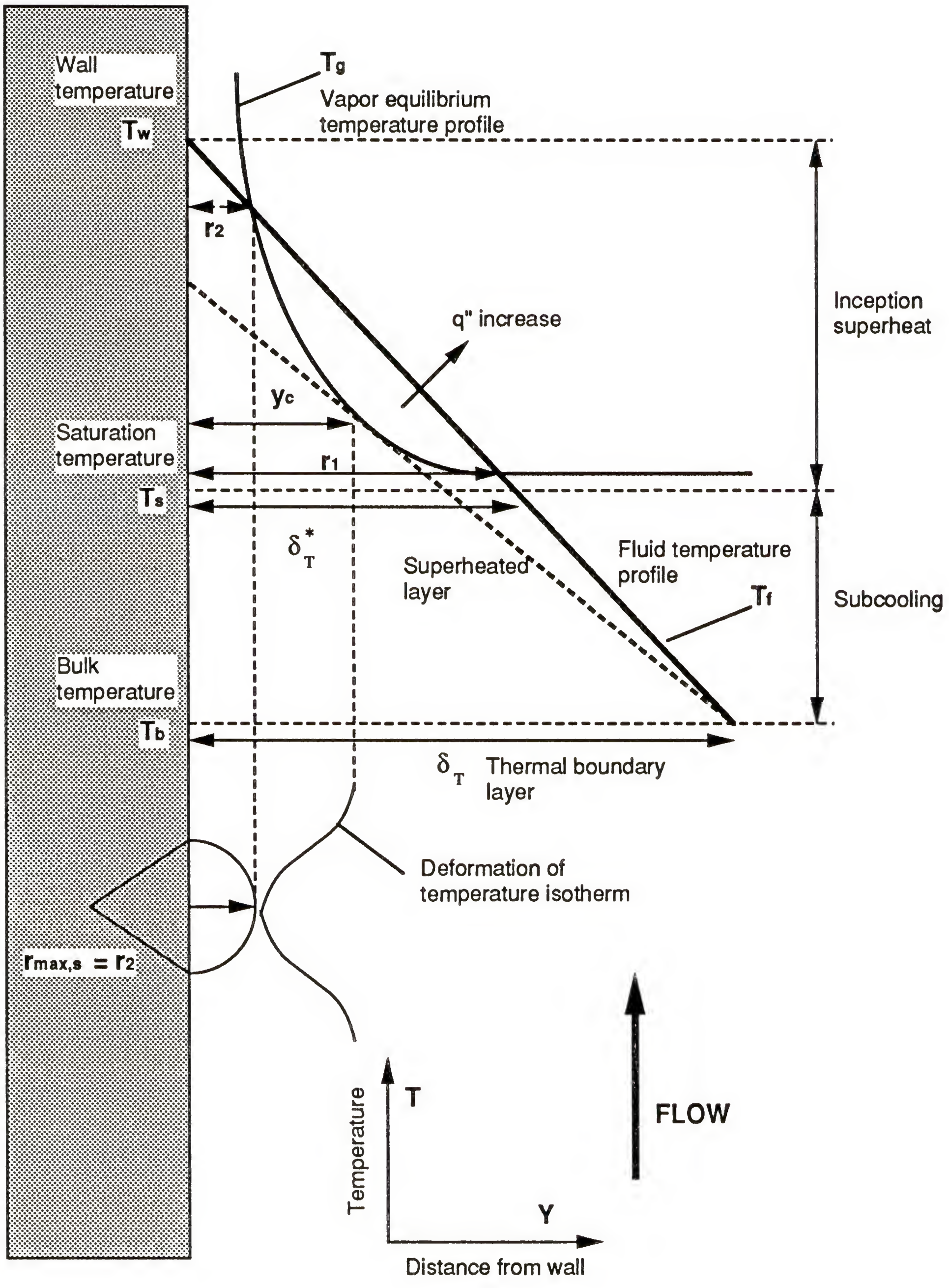

Figure 5-7 Liquid and vapor equilibrium temperature profiles at the onset of nucleate boiling.

Figure 5-7 illustrates the above conditions schematically. Eq.(5-14) and Eq.(5-15) were solved under the conditions of Eq.(5-17). The predicted wall superheat is given byThe

$$\Delta T_{\mathrm{sat}} = 2T_{\mathrm{s}}\left(\frac{h_{\mathrm{f0}}\, nA}{k_{\mathrm{f}}}\right) + \sqrt{\left(\Delta T_{\mathrm{sub}} + T_{\mathrm{s}}\frac{h_{\mathrm{f0}}\, nA}{k_{\mathrm{f}}}\right) 4T_{\mathrm{s}}\left(\frac{h_{\mathrm{f0}}\, nA}{k_{\mathrm{f}}}\right)} \qquad (5\text{-}18)$$

critical radius is expressed as

$$r_{\mathrm{crit}} = \frac{k_{\mathrm{f}}}{2\, n h_{\mathrm{f0}}}\left(1 - \frac{h_{\mathrm{f0}}\Delta T_{\mathrm{sub}}}{q_w^{\prime\prime}}\right) \qquad (5\text{-}19)$$

The wall superheats for the present study calculated by Eq.(5-18), however, significantly underestimated the experimental values (Figure 5-8) except those of Frost and Dzakowic. However, considering that Pr=7.2 for Freon 113, it is unlikely that the temperature isotherm is distorted sharply above the bubble within a thin thermal layer. According to Collier[**58**], the maximum size of cavities on the smooth copper tube is on the order of 0.1μm. The critical cavity sizes predicted by the above models are much larger than the cavities on the heating surface. In such a case, the condition given by Eq.(5-17) is not satisfied. To initiate nucleation, the liquid and wall temperatures should increase further until r_{min} in Figure 5-7 matches the existing maximum cavity size $r_{\mathrm{max,s}}$ on the heating surface. The wall superheat under this condition is given by

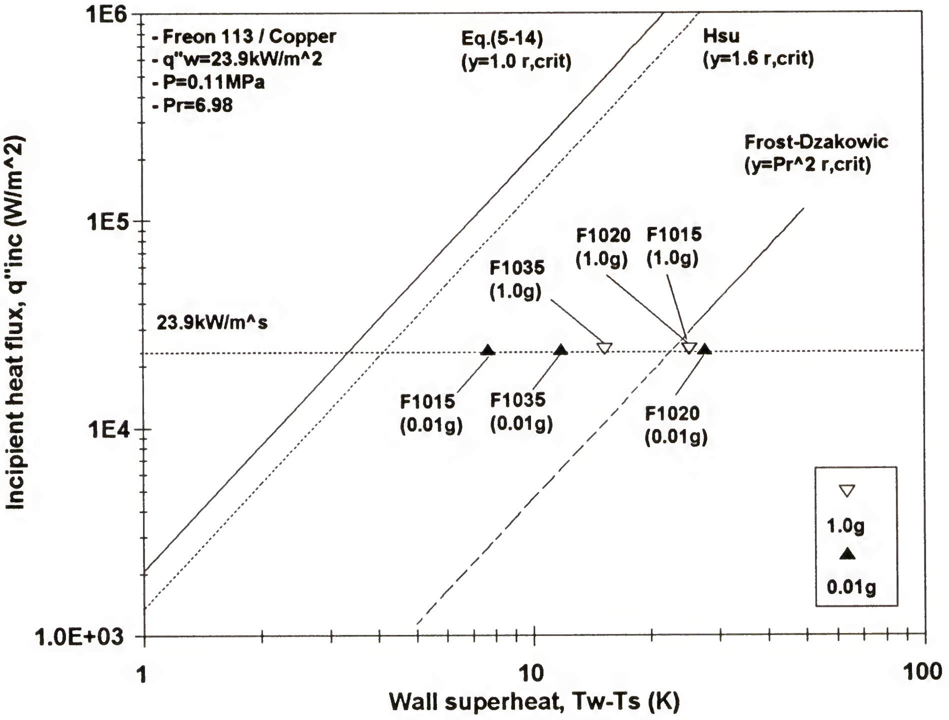

Figure 5-8 Onset of nucleate boiling measured in the Learjet flight experiment.

$$T_w - T_s = \frac{q_w'' n r_{max,s}}{k_f} + \frac{A T_s}{r_{max,s}} \tag{5-20}$$

where $r_{max,s}$ is calculated from

$$r_{max} = \frac{k_f}{2 n h_{f0}} \left(1 - \frac{h_{f0} \Delta T_{sub}}{q_w''} \right) - \frac{k_f}{h_{f0}} \sqrt{ \frac{1}{4 n^2} \left(1 - \frac{h_{f0} \Delta T_{sub}}{q_w''} \right) - \frac{h_{f0} T_s}{q_w'' n} \left(\frac{h_{f0} A}{k_f} \right) } \tag{5-21}$$

For simplicity, Hsu's model, in which the temperature isotherm without distortion, was employed in the following analysis.

The wall superheats for the present study calculated by Eq.(5-20) are tabulated in Table 5-3. The decrease in wall superheat observed during the microgravity period is predicted reasonably by the above model. It is found that $r_{max,s}$ and T_w-T_s are sensitive to the single-phase heat transfer coefficient and that the decrease in wall superheat is due to the increase in flow rate during the microgravity period, not due to the gravity change. In addition, the nucleation initiates within the laminar sublayer having a thickness on the order of 1μm. Formation of bubbles in a superheated layer is a metastable phenomenon and considered hardly affected by the change of buoyancy force.

The large discrepancy for Case F1015 is caused by the flow pattern change from slug to annular flow and the same model cannot be applied to this case.

Table 5-3 Critical radii for nucleation and predicted wall superheats at the ONB.

Case No.	T_s^* (C)	r_{max} x10^{-6} (m)	r_{min} x10^{-6} (m)	r_{crit} x10^{-6} (m)	δ_T^* x10^{-6} (m)	ΔT_{sat} by Eq. (5-18) (K)	ΔT_{sat} by Eq. (5-20) (K)	ΔT_{sat} measured (K)	ΔT_{sub} measured. (K)
F10151	52.1	113.1	0.196	56.4	70.1	2.3	28.8	25.2	29.9
F10150	45.2	115.2	0.245	57.8	24.9	2.4	29.9	8.7	23.8
F10201	51.5	100.7	0.226	50.1	69.2	2.4	24.5	24.8	32.8
F10200	46.5	92.7	0.291	46.5	59.3	2.6	22.3	23.5	29.9
F10351	51.3	65.7	0.345	33.0	42.7	2.7	14.3	15.3	32.7
F10350	50.1	59.9	0.397	30.1	32.5	2.8	12.6	11.6	32.2

* evaluated at the ONB.

5.3.2 Pressure Effects on Fluid Properties

The change of thermal properties of Freon 113 as a function of pressure is illustrated in Appendix C. For example, a decrease in the system pressure for Case F1015 during the gravity transition from 1.0g to 0.01g was 25.7%. The corresponding changes in the vapor density and the liquid viscosity are -7.1% and +6.4%, respectively. If the heat flux is unchanged, the superheat for nucleation decreases by 2.1% for the above pressure decrease. This change is too small compared to the wall superheat observed in the experiment. The same argument is applicable to other cases. Therefore, the change of properties due to the decrease in static pressure cannot cause the wall temperature decrease observed in the present study. It is considered that the decrease in wall superheats near the ONB was caused by the enhanced forced convection due to an increase in mass flux induced by reduced system pressure.

The effect of saturation temperature change on the nucleation criterion for Cases F1015, F1020, and F1035 is illustrated in Figure 5-9(a)-(c), respectively. The vapor equilibrium temperature asymptotically approaches the saturation temperature. When the system pressure decreases, this curve shifts downward since the asymptote T_s is reduced as the pressure is reduced. As the change of thermal conductivity was small and the heat flux was constant, the slope of the liquid temperature profile remained unchanged.

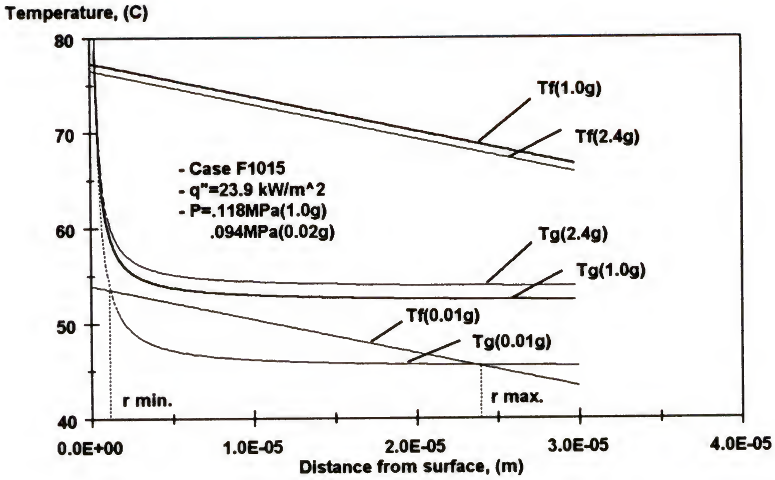

(a) Case F1015

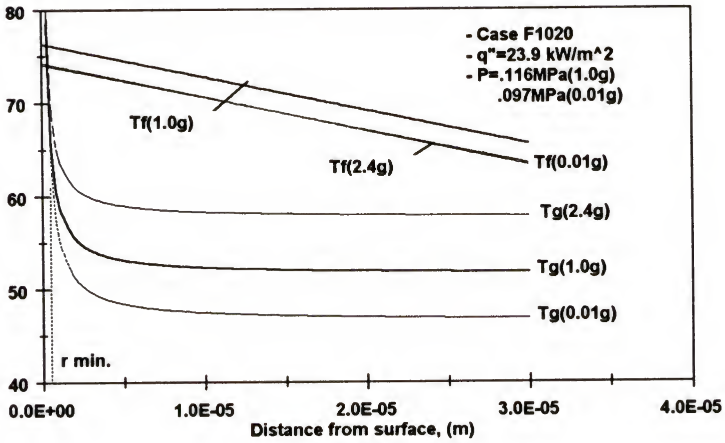

(b) Case F1020

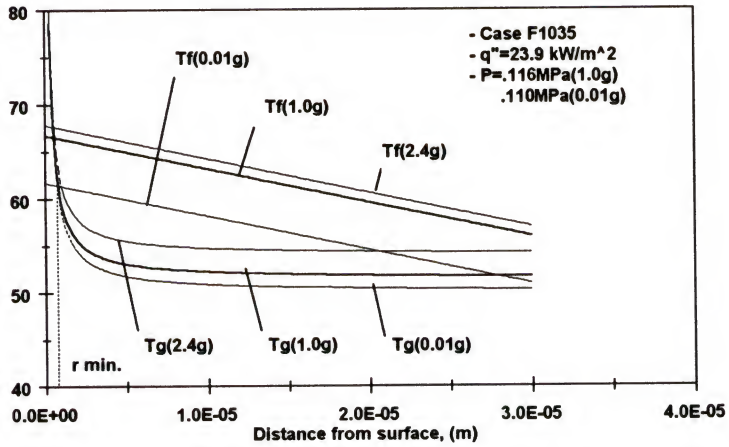

(c) Case F1035

Figure 5-9 Liquid and vapor equilibrium temperatures near the heating surface.

The wall temperatures decreased due to enhanced bulk convection. As a result, the range of cavity size to be activated became smaller. The change of r_{max} is insignificant for the wall superheat because such a cavity size is rare on the heating surface.

5.3.3 Superheated Layer Thickness Near the ONB

In pool boiling, suppression of the natural convection induces an increase in the thickness of the thermal layer near the heating surface. The difference in the thickness of the superheated layer in pool boiling and flow boiling systems under microgravity conditions is discussed in the following section.

Assuming that δ_T* is the thickness of superheated layer, one can obtain

$$\frac{k_f}{q_w''}(T_w - T_s) = \delta_T^* \tag{5-22}$$

from Eq.(5-14). The above relationship is valid when a linear temperature profile is assumed. The thickness of the superheated layer is thus easily estimated from Eq.(5-22), ranging approximately 30 - 70μm for the present study. When the heat fluxes are constant, δ_T* is only a function of wall superheat. The decrease in the wall superheat, caused by enhanced bulk convection, reduced the thickness of the superheated layer during the microgravity period.

The above facts characterize the difference of heat transfer at the ONB between the pool boiling and forced convection. Ervin et al.[22] conducted microgravity pool boiling experiments in a drop tower facility and observed transient nucleate boiling on a transparent gold film. Their measurement also included the wall temperature variation at the moment of boiling inception. They observed a formation of large superheated thermal boundary layers and an energetic propagation of bubble growth associated with the ONB, which were unique to the microgravity conditions. The result of wall temperature measurements showed that during such energetic bubble growth, wall superheat was larger than other modes of bubble formation. They suggested that this is due to larger internal energy stored inside the superheated layer. Similarly, Zell et al.[21] reported that the wall superheat at the ONB in microgravity was higher than that in normal gravity and that the heat transfer near the ONB in microgravity was deteriorated.

Under microgravity conditions, natural convection in pool boiling may disappear. This will cause thickening of superheated layer and the increase in wall temperature since only heat conduction is available in such a case. In normal gravity, the natural convection assists to diffuse the internal energy stored in the superheated layer otherwise to be transferred to the vapor phase.

In flow boiling systems with high subcoolings, forced convection, instead of natural convection, carries away a portion of internal energy in the superheated layer. Therefore, the energetic bubble formation described in Ervin's work do not occur even under microgravity conditions.

5.4 Subcooled Boiling Heat Transfer

5.4.1 Heat Balance

Bowring[46] assumed that the total heat flux in the subcooled region is described as a sum of forced convective heat flux q''_{fc} and boiling heat flux q''_{bo}

$$\begin{aligned} q''_{TP} &= q''_{fc} + q''_{bo} \\ &= q''_{fc} + q''_{ag} + q''_{ev} \end{aligned} \tag{5-23}$$

where the total two-phase heat transfer coefficient is defined by

$$h_{TP} = \frac{q''_{TP}}{(T_w - T_f)} \tag{5-24}$$

The forced convective heat transfer coefficient is given by

$$h_{fc} = \frac{q''_{fc}}{(T_w - T_f)} \tag{5-25}$$

and the boiling heat transfer coefficient is given by

$$h_{bo} = \frac{q''_{bo}}{(T_w - T_s)} \tag{5-26}$$

In Eq.(5-23), the boiling heat flux q''_{bo} for vertical flow systems is further divided into the heat flux transferred by evaporation q''_{ev} and the heat flux transferred by bubble agitation q''_{ag}.

In the existing correlations, the bubble agitation heat flux q''_{ag} is implicitly included in the boiling heat flux. However, q_{ag}'' induced by bubble motion is considered to vary significantly under variable gravity conditions. Therefore, contributions of q_{ev}'' and q_{ag}'' are separately discussed in the present study. Note that the heat transfer coefficients for two-phase and forced convective flow are defined for

$$(T_w - T_f) = (T_w - T_s) + (T_s - T_f) = \Delta T_{sat} + \Delta T_{sub} \tag{5-27}$$

while that of boiling contribution is defined only for the superheat $(T_w - T_s)$. In the two-phase region where liquid and vapor coexist, the forced convective heat transfer coefficient h_{fc} is larger than that in the single-phase region. Instead of using the single-phase Reynolds number, the two-phase Reynolds number including the vapor voidage was used

$$Re_{TP} = \left(\frac{u_{fc}\,\rho_f\,D}{\mu_f}\right) = \left(\frac{1-x}{1-\alpha}\right) Re_{f0} \tag{5-28}$$

Substituting the above equation into the Nusselt number correlation for single-phase flow, one obtains

$$h_{fc} = C_1 h_{f0} \left(\frac{1-x}{1-\alpha} \right)^{C_2} \qquad (5\text{-}29)$$

The values of 2.192 and 0.33, obtained for the present study, were used as C_1 and C_2, respectively. Eq.(5-29) indicates that h_{fc} increases as the void fraction increases in the low-quality region, while h_{fc} ceases to increase as the quality approaches unity. The physical significance of the above equation is that the local heat transfer is increased by the reduced flow area in the existence of growing void fraction. Substitution of Eq.(5-24) and Eq.(5-29) into Eq.(5-23) and rearranging, gives

$$\left(\frac{h_{TP}}{h_{f0}} \right) = \left(\frac{1-x}{1-\alpha} \right)^{0.33} \left(1 - \frac{q''_{bo}}{q''_{TP}} \right)^{-1} \qquad (5\text{-}30)$$

Sekoguchi[33] evaluated the term $(1-q''_{bo}/q''_{TP})^{-1}$ experimentally. Therefore, his method cannot be applied instantly to microgravity heat transfer problems without considering the gravity effects on q''_{bo}. One of the objectives of the present study is to investigate the gravity effects on the ratio (h_{TP}/h_{f0}). This ratio was selected as an index of comparison for microgravity boiling heat transfer since the single-phase heat transfer coefficient h_{f0} also varies depending on the flow conditions. In the following section, the terms $[(1-x)/(1-\alpha)]^{0.33}$ and $(1-q''_{bo}/q''_{TP})^{-1}$ in Eq.(5-30) will be evaluated separately to examine the gravity effects.

5.4.2 Forced Convective Heat Transfer in the Subcooled Region

The exit qualities for Cases F1015, F1020, and F1035 under 1.0g conditions are -0.4%, -6.7%, and -12.1%, respectively. The negative values indicate that the flow conditions were subcooled. To account for local boiling in the subcooled region, the actual quality x_a was introduced. Among several theories for x_a, we turn to Sekoguchi's work since his analysis is based on a theoretical model and specifically developed for subcooled flow boiling[33]. Assuming the 1/7th law for the temperature and velocity profiles, the actual quality x_a is given by

$$x_a = Bo^{*}\left[\frac{2}{7}\left(\frac{5}{6}\left(1+\frac{x}{Bo^{*}}\right)\right)^{9} - \frac{3}{35}\left(\frac{5}{6}\left(1+\frac{x}{Bo^{*}}\right)\right)^{16}\right] \tag{5-31}$$

where

$$Bo^{*} = Bo^{+}\left(\frac{1-x_a}{1-\alpha}\right)^{0.33} \tag{5-32}$$

$$Bo^{+} = Bo\left(\frac{Re^{0.67}\,Pr^{3/4}}{2.1917\left(\frac{\mu_f}{\mu_w}\right)^{0.14}\left(\frac{z}{D}\right)^{0.054}}\right) \tag{5-33}$$

$$Bo = \left(\frac{q_w''}{h_{fg}\,G}\right) \tag{5-34}$$

Again, instead of 0.8, the value of 0.33 was used in the definition of Bo^*. Although the original expression for Bo^+

uses the Dittus-Boelter equation, Eq.(5-10) was employed in this analysis.

Void fraction and Slip ratio. For the void fraction, Sekoguchi suggested the use of Smith's[34] correlation

$$\frac{1}{\alpha}=1+\phi\frac{\rho_g}{\rho_f}\left(\frac{1}{x_a-1}\right)$$
$$+(1-\phi)\,\frac{\rho_g}{\rho_f}\left(\frac{1}{x_a}-1\right)\left[\frac{\rho_f/\rho_g+\phi\,(1/x_a-1)}{1+\phi(1/x_a-1)}\right]^{1/2} \tag{5-35}$$

Smith recommended 0.4 as the value for ϕ. However, this factor ϕ implicitly includes the effects of the slip between the liquid and vapor phases under normal gravity conditions. Under microgravity conditions, the value of ϕ will be different because the slip ratio is smaller in microgravity. Instead of Eq.(5-35), Eq.(4-16) was employed in the present study. To incorporate the gravity effects on s, Eq.(4-11) derived by Zuber and Findlay was used[32]. Although the flow pattern of interest is bubbly flow, the above equation is widely applicable without reference to flow pattern.

For the change in gravity from 1.0g to 2.4g to 0.01g, the ratio $\langle u_{gj}\rangle/\langle u_{gj}\rangle_{1g}$ varies from 1 to 1.257 to .316, respectively. Since the gravity level during the microgravity experiment was 0.01g, the slip ratio approaches unity but still remains larger than 1.0, according to the drift flux model.

Eq.(5-31), Eq.(5-32), Eq.(5-33), and Eq.(5-34) were solved simultaneously to obtain x_a and α for variable gravities. Since the equations were recursive, 17 to 18

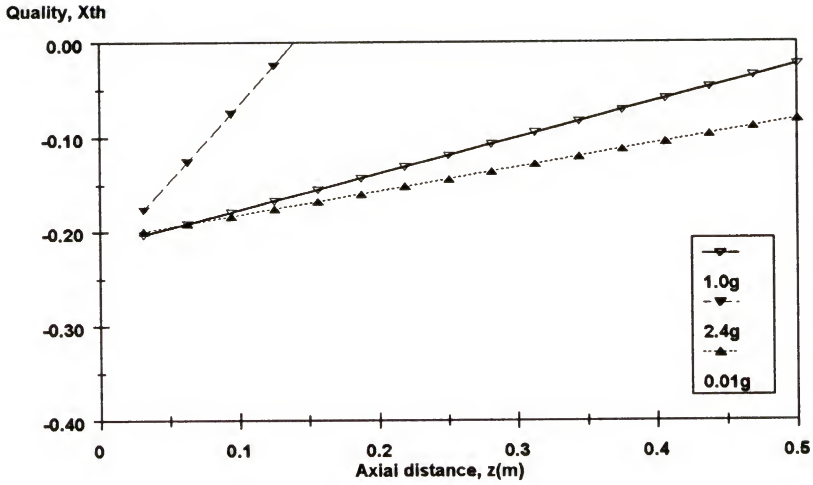

(a) Case F1015

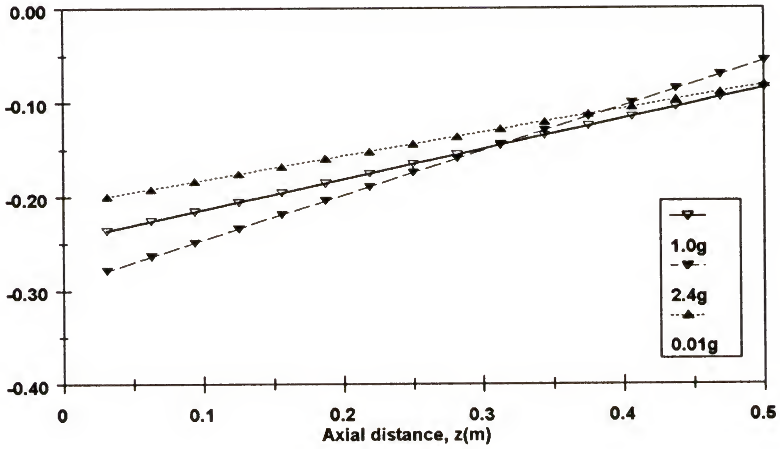

(b) Case F1020

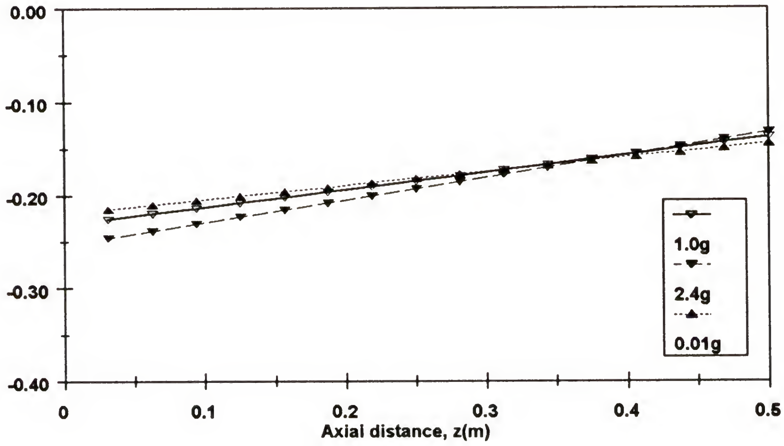

(c) Case F1035

Figure 5-10 Thermal equilibrium qualities for the Learjet flight experiments.

iterations were needed before convergence using the bi-section method. The thermal equilibrium qualities, void fractions, and actual qualities evaluated at the exit of the test section for each case were calculated simultaneously. The actual qualities ranged from 0.0068%(Case F1035) to 0.970% (Case F1015).

Figure 5-10(a) through (c) indicate the evolution of thermal equilibrium qualities along the test section for Cases F1015, F1020, and F1035, respectively. The qualities increased linearly since the heat input through the wall was uniform. The inlet qualities under microgravity conditions decreased since the flow rates increased due to the decrease in static pressure. The change in gradient of each curve is caused by the liquid enthalpy change due to varied pressure and liquid temperature.

The profiles for the actual qualities are different from thermal equilibrium qualities(Figure 5-11(a) through (c)). The actual quality, defined as the ratio of the enthalpy stored in the superheated layer to the total enthalpy carried by flow, is given by

$$x_a = \frac{c_{pl}\int_0^{y_s^*} (T-T_s)\, u_L (1-y^*)\, dy^*}{h_{fg}\int_0^1 u_L (1-y^*)\, dy^*} \qquad (5\text{-}36)$$

where $y_s^*=(y_s/R)$ is the dimensionless superheated layer thickness. Eq.(5-36) implicitly includes the effects of

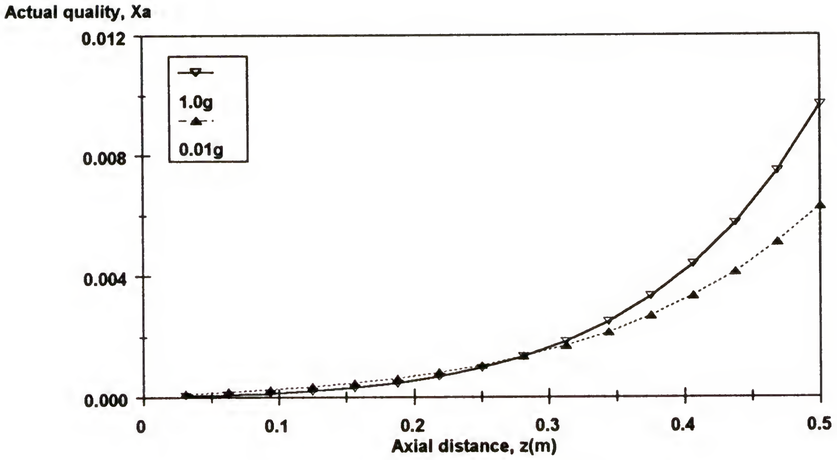

(a) Case F1015

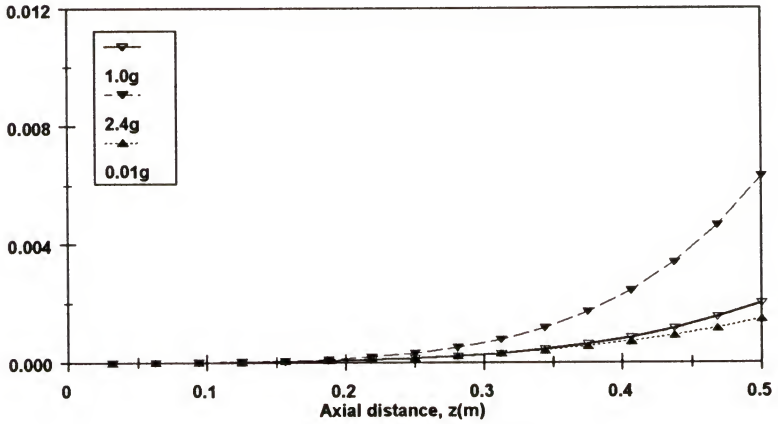

(b) Case F1020

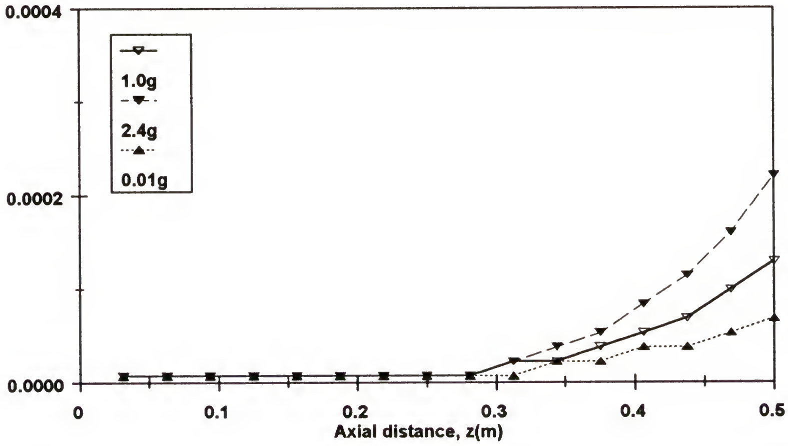

(c) Case F1035

Figure 5-11 Actual quality profiles calculated by the modified Sekoguchi's method.

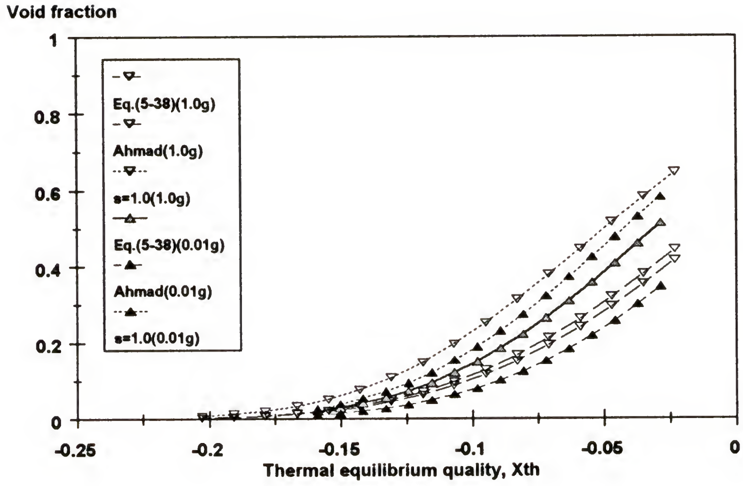

(a) Case F1015

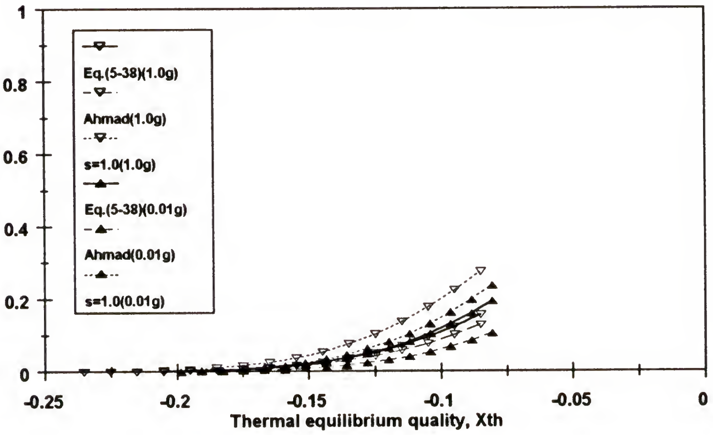

(b) Case F1020

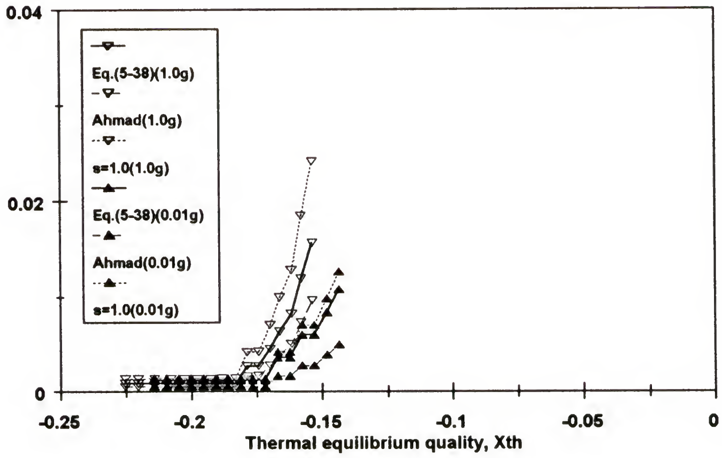

(c) Case F1035

Figure 5-12 Void fraction profiles predicted by Sekoguchi's and Ahmad's methods.

gravity through the void fraction and liquid velocity. Under microgravity conditions, the actual qualities for each case were lower than those of normal gravity since the increased bulk convection removes some part of the enthalpy otherwise built up in the superheated layer.

The void fraction profiles along the test section are shown in Figure 5-12(a) through (c). The void fraction becomes largest when the slip ratio is 1.0. However, the prediction by Eq.(4-16) indicates that the above assumption overestimates the void fraction. This results suggests that there still remains a relative velocity between the phases even in 0.01g. The void fraction calculated from Ahmad's correlation, which is only valid under normal gravity conditions, is also shown for reference.

Effect of Superheated Layer Thickness. It is particularly interesting to examine gravity effects on the thickness of the superheated layer, y_s^* in the subcooled region. Assuming the 1/7th law for the liquid temperature profile, y_s^* is given as

$$y_s^* = \left[k_m\left(1 + \frac{x}{Bo^*}\right)\right]^7 \qquad (5\text{-}37)$$

where K_m is a constant(=.833) and Bo^* is defined in Eq.(5-33). Bo^* includes the void fraction inside the term $[(1-x_a)/(1-\alpha)]^{0.33}$ and is affected by gravity through the change in slip ratio. The calculated superheated layer thicknesses are shown in Figure 5-13(a) through (c) for Cases F1015, F1020, and

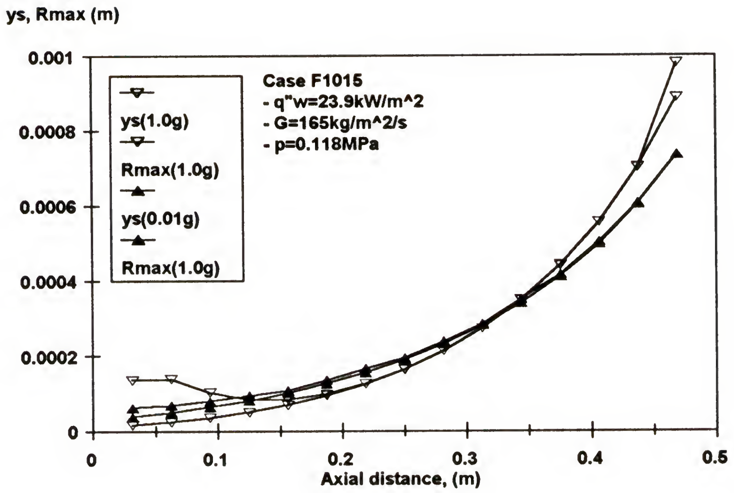

(a) Case F1015

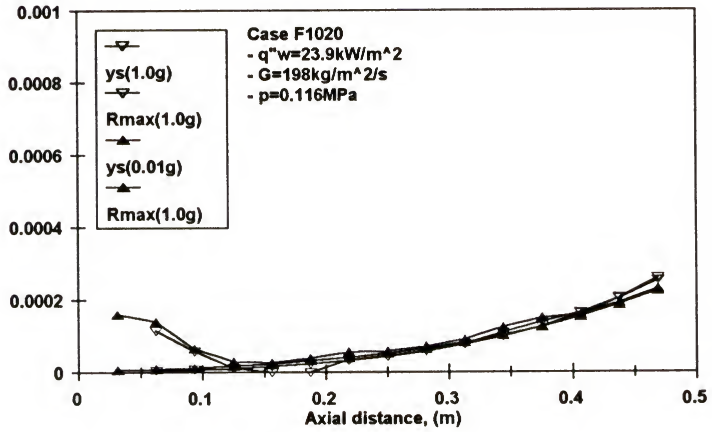

(b) Case F1020

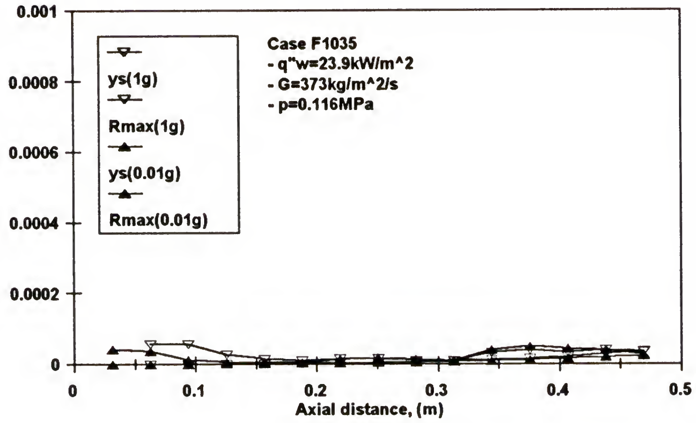

(c) Case F1035

Figure 5-13 Growth of superheated layer and bubble diameter in the axial direction.

F1035, respectively. Although y_s^* grows larger along the test section, y_s^* decreased only slightly in microgravity. This indicates that the build-up of enthalpy in the superheated layer, which was observed in pool boiling, would not occur in flow boiling since the enthalpy near the wall is carried away by forced convection. This is also supported by the following facts:

a) The contribution of natural convection to the total heat flux was less than 1% for the present study.

b) The radial velocity profiles calculated in Chapter 4 show that the change of the liquid temperature profile near the wall in microgravity was small for turbulent flow.

Using the actual qualities and void fractions obtained through the above method, the factor $[(1-x_a)/(1-\alpha)]^{0.33}$ was evaluated along the test section. Figure 5-14 (a)-(c) shows axial evolutions of this factor for each case. The value of $[(1-x_a)/(1-\alpha)]^{0.33}$ increases rapidly near the exit because the gradient of quality dx_a/dz is nearly constant throughout the test section, while $d\alpha/dz$ increases rapidly in the latter half of the test section. Due to significant increase in void fraction, the values of $[(1-x_a)/(1-\alpha)]^{0.33}$ in microgravity exceeded those in normal gravity for Cases F1015 and F1020. However, for Case F1035 in which the void fraction as well as the true quality was smaller than other cases, $[(1-x_a)/(1-\alpha)]^{0.33}$ was close to 1.0. This implies that single-phase heat transfer was still dominant for Case F1035.

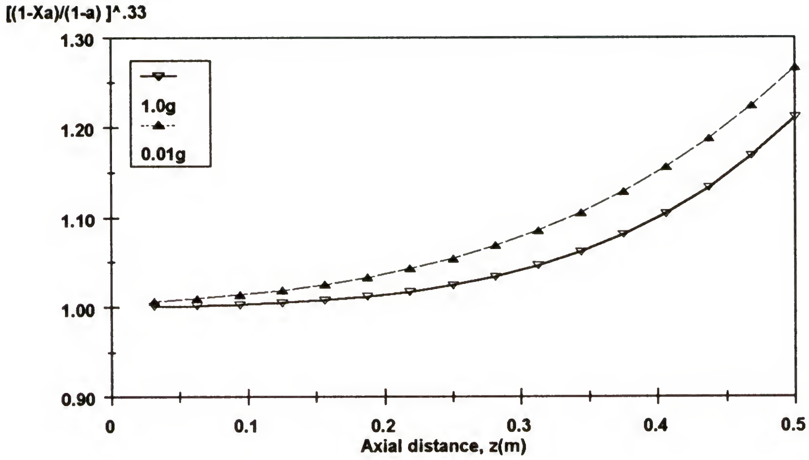

(a) Case F1015

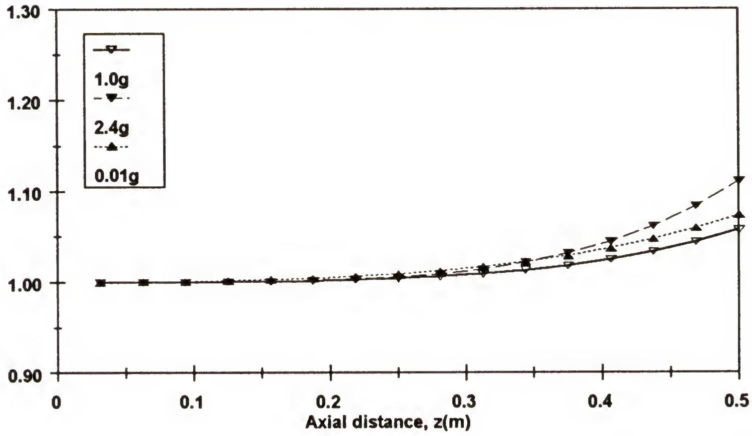

(b) Case F1020

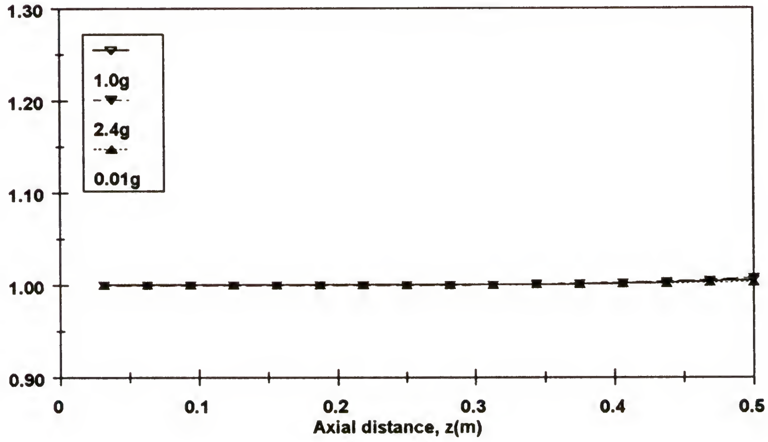

(c) Case F1035

Figure 5-14 Variation of forced convective factor under microgravity conditions.

5.4.3 Boiling Heat Flux

Estimation of the ratio of boiling heat flux to the total heat flux q''_{bo}/q''_w from the present data sets is difficult since the boiling conditions such as bubble diameters or the number of nucleation sites are unknown. However, the flow conditions such as flow rates, system pressures, and qualities were measurable with certain accuracy. Therefore, q''_{bo} can be obtained more accurately by subtracting q''_{fc} from the total heat flux, rather than calculating q''_{bo} independently. Figure 5-15(a) through (c) show the distributions of q''_{bo}/q''_w along the flow axis for Cases F1015, F1020, and F1035, respectively. For all cases, the forced convection ratio q_{fc}''/q_w'' increased in the subcooled region near the outlet of the test section under microgravity conditions. Conversely, the boiling heat flux ratio q_{bo}''/q_w'' decreased because the bubble agitation component q_{ag}'' became smaller. The evaporation heat flux q_{ev}'' calculated by the mass transport model was found to be much smaller than any other component in the present study, although q_{ev}'' was slightly increased in microgravity.

Figures 5-16(a) through (c) show the boiling curves for the subcooled boiling under microgravity conditions using Rohsenow's correlation. The value of g was set to $0.098 m/s^2$ for microgravity conditions. Rohsenow's correlation is given by

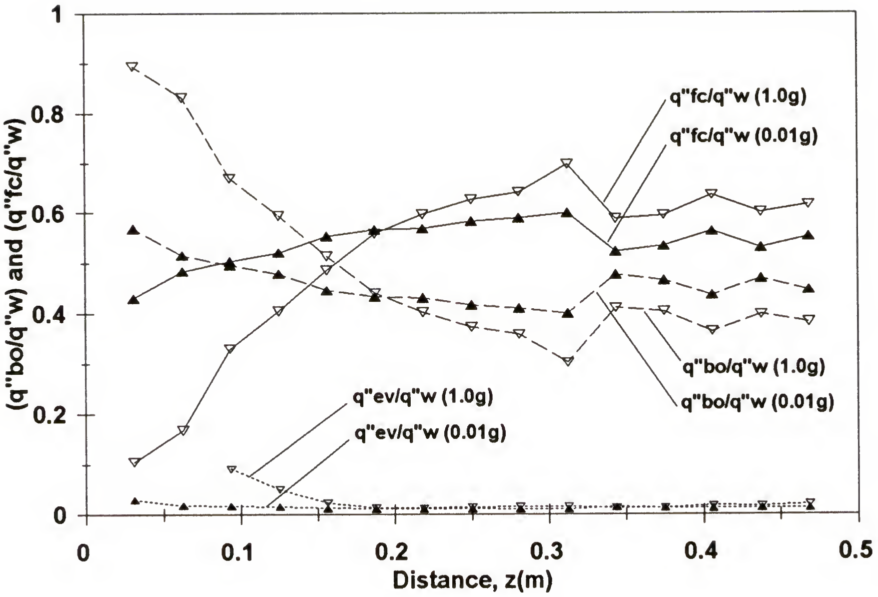

(a) Case F1015

Figure 5-15 Development of boiling heat flux in the axial direction.

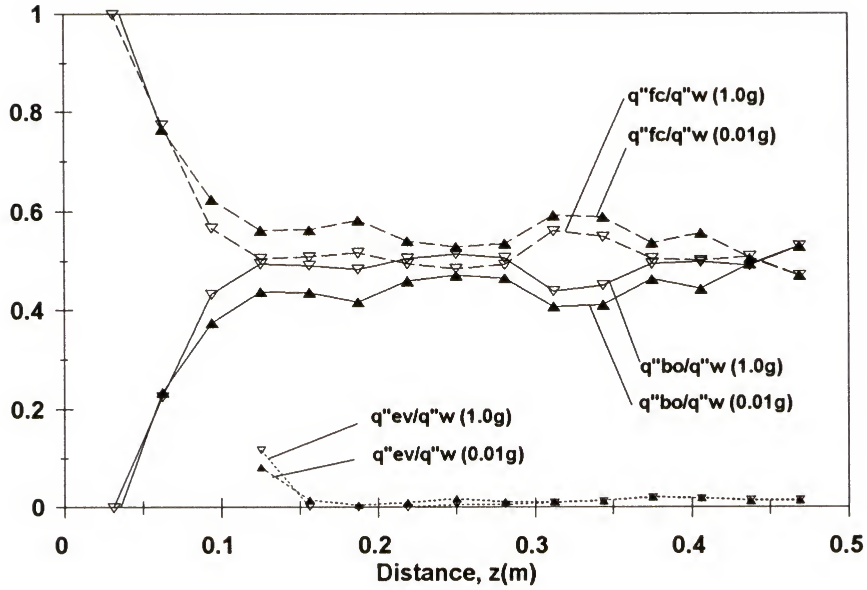

(b) Case F1020

Figure 5-15 --- continued.

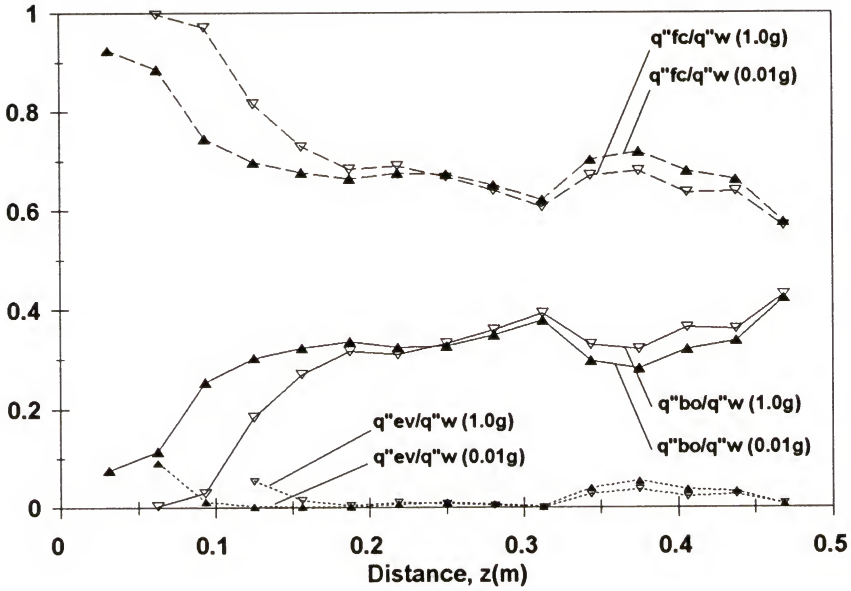

(c) Case F1035

Figure 5-15 --- continued.

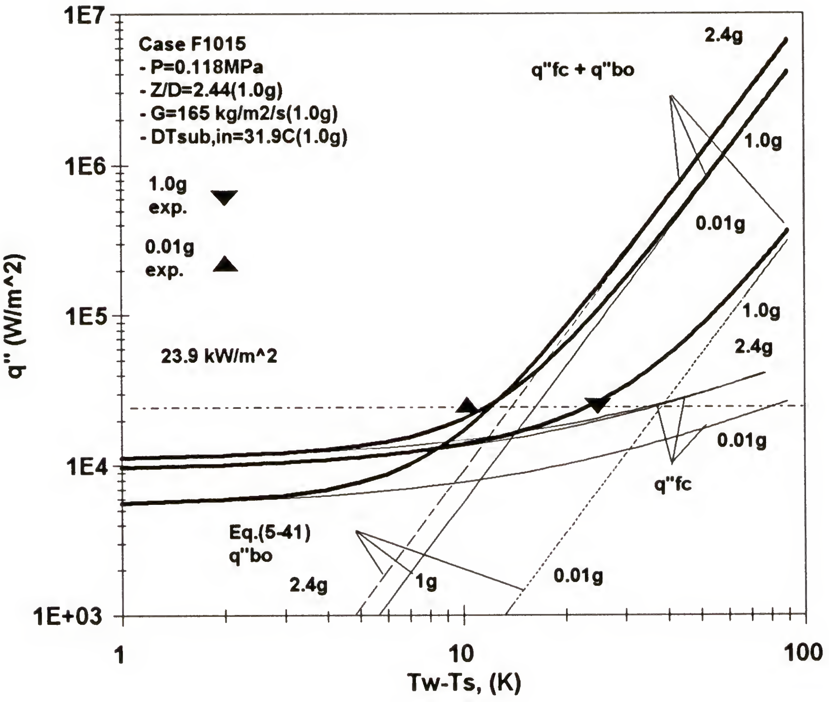

(a) Case F1015

Figure 5-16 Boiling curves under variable gravity conditions.

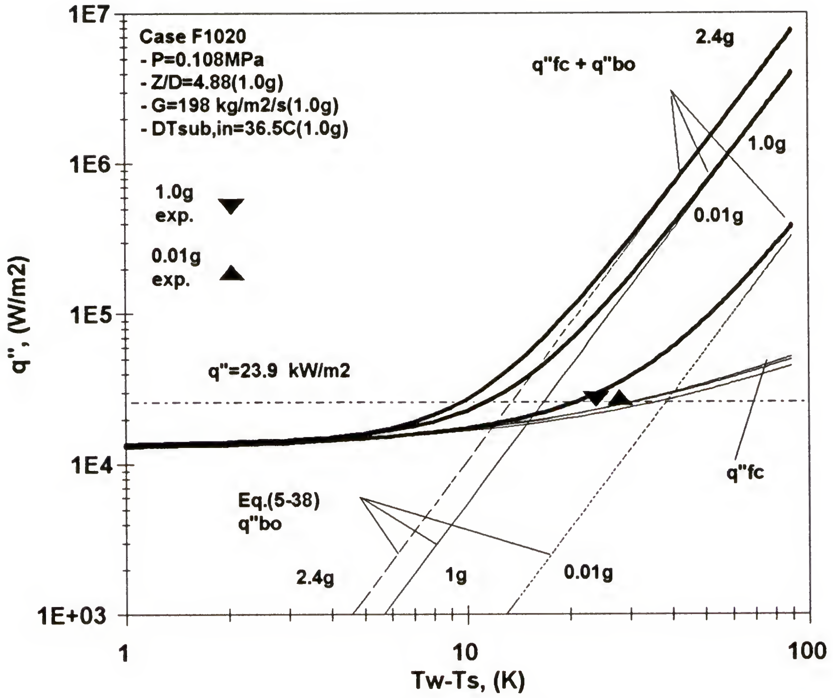

(b) Case F1020

Figure 5-16 --- continued.

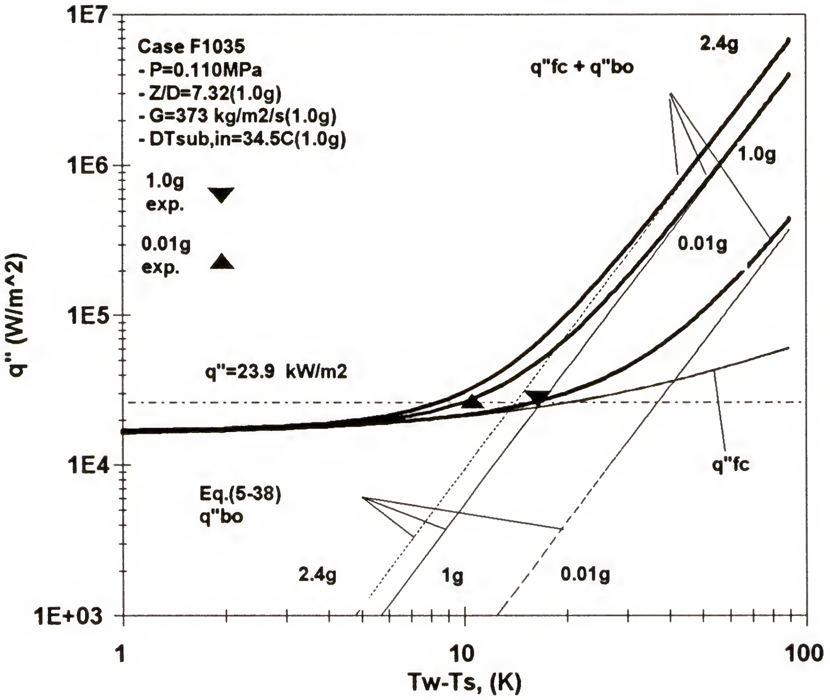

(c) Case F1035

Figure 5-16 --- continued.

$$\left[\frac{(T_w - T_s)\, c_{pl}}{h_{fg}}\right] = \frac{1}{C_f}\left[\frac{q''_{bo}\, b}{\mu_f\, h_{fg}}\right]^{1/3} Pr^{1.7} \qquad (5\text{-}38)$$

where $1/C_f$ is a constant depending on the surface condition and b is the characteristic diameter of bubbles given by

$$b = \sqrt{\frac{\sigma}{g\,(\rho_f - \rho_g)}} \qquad (5\text{-}39)$$

The above equation is derived as a result of the force balance between the surface tension and the buoyancy force, a classical model of bubble detachment in pool boiling. The use of this model in subcooled boiling heat transfer is not physically sound and the predictions grossly underestimate the wall superheat at the ONB under microgravity conditions. The force balance providing the detachment criterion should be revised for microgravity applications.

Evaporation heat flux q''_{ev}. In order to investigate the influence of gravity on the governing parameters of bubble growth, it is necessary to develop a model to describe the heat transfer mechanism for a single bubble in subcooled boiling. The mass transport model, first proposed by Snyder[45], was adopted in the present analysis. The importance of mass transfer inside the bubble under microgravity conditions was suggested by Zell et al.[21]. It is reported that subcooled pool boiling was effectively continued in a reduced gravity environment where the buoyancy force was absent. It is interesting to note that heat was continuously transferred from the wall even if the bubble stays on the surface. If a single bubble carries the enthalpy equivalent to one bubble volume, heat transfer in pool boiling would become immediately inefficient under microgravity conditions where bubble detachment no longer takes place. This is a strong evidence to support the mass transport mechanism for their subcooled pool boiling experiment.

The mass transport model was then incorporated in the bubble growth model proposed by Unal[50]. Dynamics of bubble growth in subcooled flow is determined by the heat balance. Upon the initiation of a bubble at the activated nucleation site, heat is mainly supplied to the bottom part of the bubble by both heat conduction through the interface and evaporation from the microlayer beneath the bubble. Simultaneously, heat is removed at the top of the bubble that is exposed to the low-temperature liquid. This condensation mechanism is observed only for subcooled boiling and allows an extremely high heat flux in the subcooled boiling region.

Unal[48] developed a bubble growth model based on microlayer evaporation. The heat balance between evaporation from the microlayer and condensation at the upper part of the bubble was considered and the conduction through the bubble interface was neglected since the conduction heat transfer is small compared to evaporation. In order to incorporate the mass transport mechanism, Unal's model was modified with the following assumptions:

a) The liquid flow was fully developed and the velocity and temperature profiles were similar to those of single-phase flow. This assumption was justified since the number of nucleation sites was relatively small for the flow boiling system with large subcooling and low heat fluxes.

b) Heat flux was constant and wall temperatures were given as input data to compute the maximum bubble diameter and growth rate.

c) For simplicity, a constant contact angle was used. Deformation of the bubble during the growth period was neglected.

d) Inertia-controlled bubble growth to be observed at the beginning of bubble growth was neglected since this period was extremely short compared to the period of asymptotic growth mode that followed.

e) The dry area in the microlayer was neglected. As van Stralen[49] pointed out, the dry patch in the microlayer was hardly observed at atmospheric pressure.

f) The interaction between bubbles was neglected.

g) The thickness of the superheated layer was calculated by the temperature profile obtained by the 1/7th law.

Formulation of the model. A schematic diagram of the proposed model is shown in Figure 5-17. In this figure, b_h indicates the relative height of the superheated layer thickness to the bubble height. The lower part of the bubble

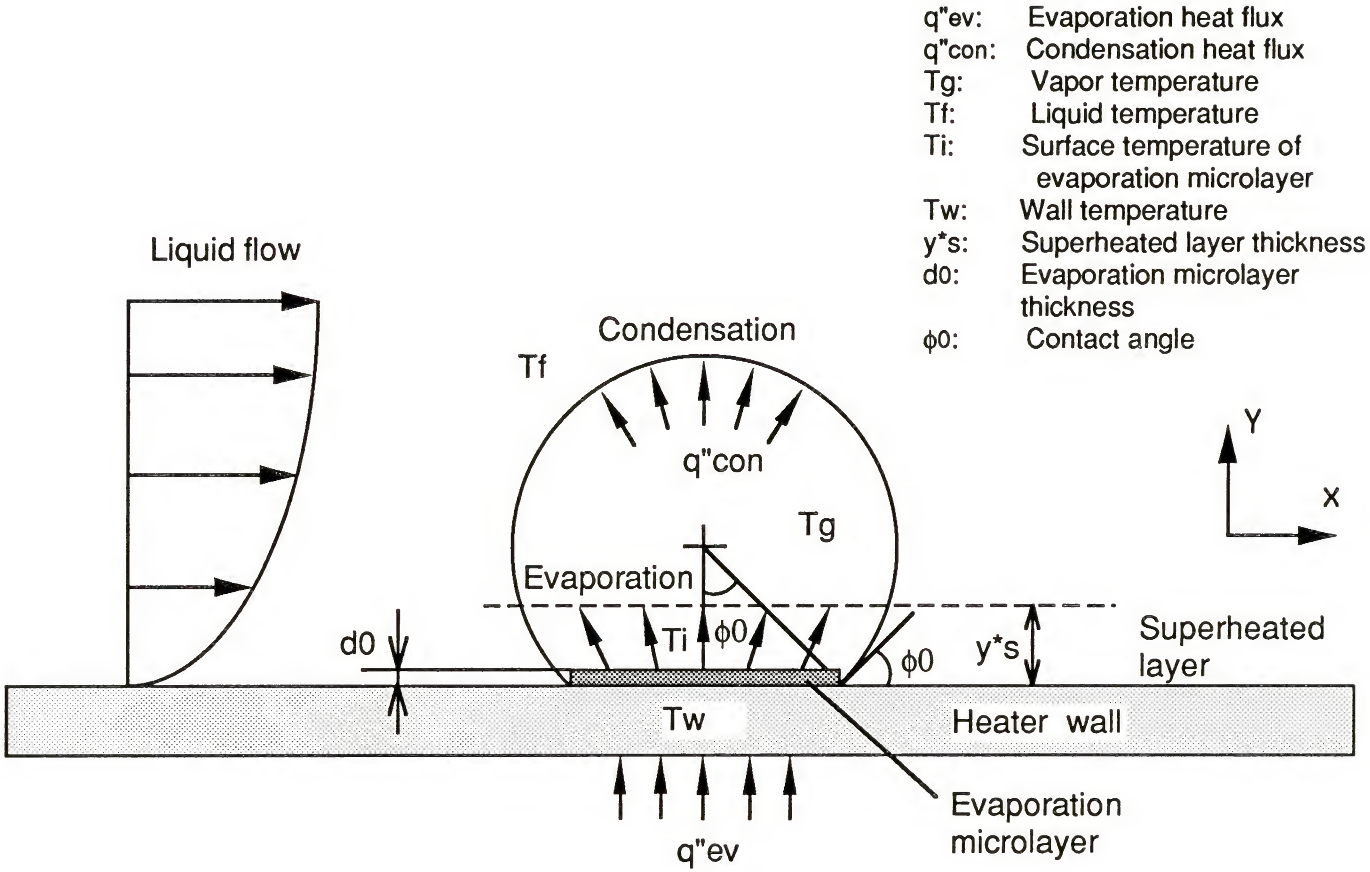

Figure 5-17 Schematic diagram of the heat balance for a single bubble in subcooled flow.

up to $y=2R^*b_h$ is immersed in the superheated layer, while the upper part from $y=2R^*b_h$ is subjected to the subcooled liquid. The energy balance for a single bubble on the heating surface in the subcooled flow is described as

$$q''_{ev} \cdot A_B - q''_{con} \cdot A_C = \left(\frac{dV}{dt}\right) \rho_g h_{fg} \tag{5-40}$$

where q''_{bo} is the boiling heat flux provided from the heating surface, q''_{con} the condensation heat flux removed from the bubble, A_B the base area of the bubble available for evaporation, A_C the area exposed to subcooled liquid, V the vapor volume, ρ_g the vapor density, and h_{fg} the latent heat of vaporization. The transient conduction heat flux q''_{bo} is obtained from the approximate problem in which a semi-infinite liquid column of temperature T_i makes contact on the heating surface of temperature T_w

$$q''_{ev} = \left(\frac{\pi}{2}\right) \frac{k_f \theta_0}{(\pi a t)^{1/2}} \tag{5-41}$$

where k_f the thermal conductivity of the liquid, a the thermal diffusivity of liquid, and θ_0 is the superheat $(T_w - T_i)$ in the microlayer. The condensation heat flux q''_{con} derived by Unal[50] for subcooled flow at 0.1MPa was used in this analysis

$$q''_{con} = h_{con} \Delta T_{sub} = \frac{C h_{fg} (D/2)}{v_{fg}} \tag{5-42}$$

where C is a constant obtained experimentally equal to 63.4 for the present study, and ΔT_{sub} the subcooling at the top of the bubble. The value of ΔT_{sub} was considered zero in the superheated layer, while outside the superheated layer, it was calculated from the previously assumed temperature profile of the liquid. Considering the geometric factor and rearranging, Eq.(5-40) is expressed as

$$\frac{dR}{dt} = \frac{C\Delta T_{sub}}{(1-\rho_g/\rho_f)}\left(\frac{f_2}{f_3}\right)R + \frac{\sqrt{\pi}}{4}2\sqrt{a}\,Ja\left(\frac{f_1}{f_3}\right)t^{-1/2} \qquad (5\text{-}43)$$

where f_1, f_2, f_3 are geometric factors and functions of the contact angle ϕ_0

$$f_1 = \frac{\sin^2\phi_0}{2} \qquad (5\text{-}44)$$

$$f_2 = 1 + \cos\phi_0 - 2b_h \qquad (5\text{-}45)$$

$$f_3 = 1 + \frac{3}{2}\cos\phi_0 - \frac{1}{2}\cos^3\phi_0 \qquad (5\text{-}46)$$

When ΔT_{sub} is zero, Eq.(5-43) reduces to a diffusion bubble growth in saturated boiling with $\phi_0=\pi/2$

$$\frac{dR}{dt} = \frac{\sqrt{\pi}}{4}2\sqrt{a}\,Ja\left(\frac{1}{2}\right)t^{-1/2} \qquad (5\text{-}47)$$

where Ja is the Jacob number defined as

$$Ja = \frac{(T_w - T_s)\,c_{pl}\,\rho_f}{h_{fg}\,\rho_g} \qquad (5\text{-}48)$$

When subcooling is not negligible, Eq.(5-43) becomes a first-order non-linear differential equation since ΔT_{sub} is a function of the bubble radius R. Eq.(5-43) was solved numerically by using the 4th order Runge-Kutta method under the following initial condition

$$R=0 \qquad at \quad t=0 \tag{5-49}$$

The initial radius of the bubble is on the same order of the cavity size (≈1 μm) and was neglected compared to that of the bubble under growth.

To calculate the superheat of the evaporation microlayer θ_0, the surface temperature T_i needs to be specified. The initial thickness of the evaporation microlayer**[49]** d_0 is described as

$$d_0 = \frac{1}{2}\psi^2\left(\frac{k_f}{h_{fc}}\right) \tag{5-50}$$

where h_{fc} denotes the heat transfer coefficient in the subcooled region. φ denotes the ratio of wall superheat to the total temperature difference given by

$$\varphi = \left(\frac{\theta_0}{\theta_0 + \theta_0^*}\right) \tag{5-51}$$

where $\theta_0=(T_w-T_{sat})$ and $\theta_0^*=(T_{sat}-T_f)$. It is assumed that this thickness remained almost the same throughout the bubble life since the evaporation rate was small[49].

To account for mass transport inside the bubble, the mass flux due to evaporation needs to be determined. The evaporation rate between two liquid surfaces at different temperatures[45] is given by

$$\frac{\dot{m}}{A_B} = \alpha \left[\frac{R_0}{2 \pi R_{113}} \right]^{1/2} \left[\frac{T_i^{1/2}}{v_g(T_i)} - \frac{T_g^{1/2}}{v_g} \right] \tag{5-52}$$

where m is the mass transfer rate (kg/sec), A_B the area of evaporation (m^2), T_i the surface temperature of the superheated microlayer (K), T_g the temperature of vapor inside the bubble (K), R the universal gas constant (8.3143J/mol/K), R_{113} the molecular weight of Freon 113 (187.376kg/mol), and α the accommodation coefficient which accounts for freshness of the surface and considered unity for such a case as nucleate boiling. The vapor equilibrium temperature T_g was determined by Eq.(5-19). The heat flux due to evaporation is, therefore, given as

$$h_{fg} \frac{\dot{m}}{A_B} = q''_{ev} \tag{5-53}$$

The above amount also must be equal to the heat conduction through the microlayer to maintain the constant heat flux

$$h_{fg} \frac{\dot{m}}{A_B} = k_f \frac{(T_w - T_i)}{d_0} \tag{5-54}$$

Here, the heat capacity of the evaporation microlayer is neglected since its thickness is on the order of few microns. The only unknown parameter in the above equation is the interface temperature T_i. Eq.(5-52) and Eq.(5-54) was solved numerically by the bi-section method to obtain the interface temperature T_i. It was found that T_i was higher than the vapor temperature T_g by a fraction of degree for the present study.

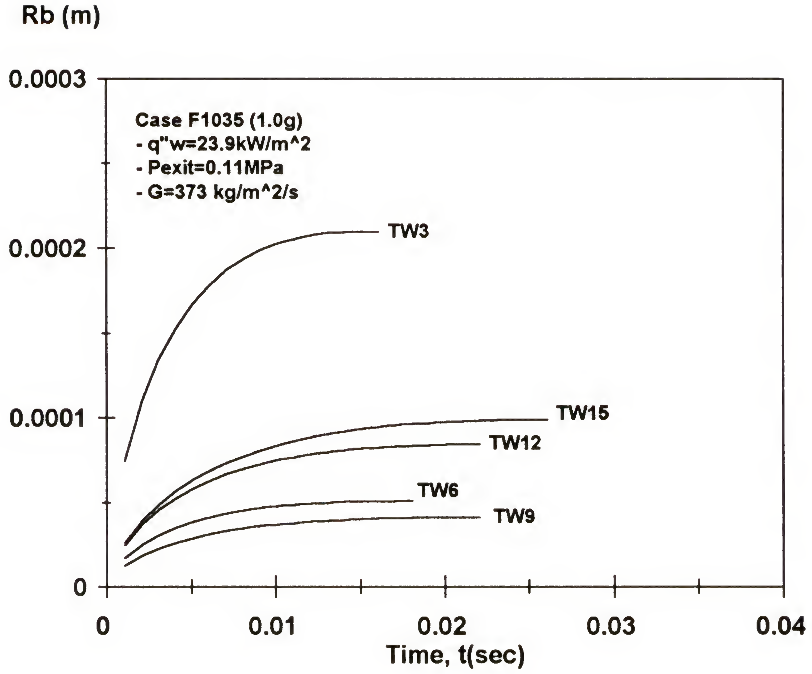

(a) g/g0=1.0

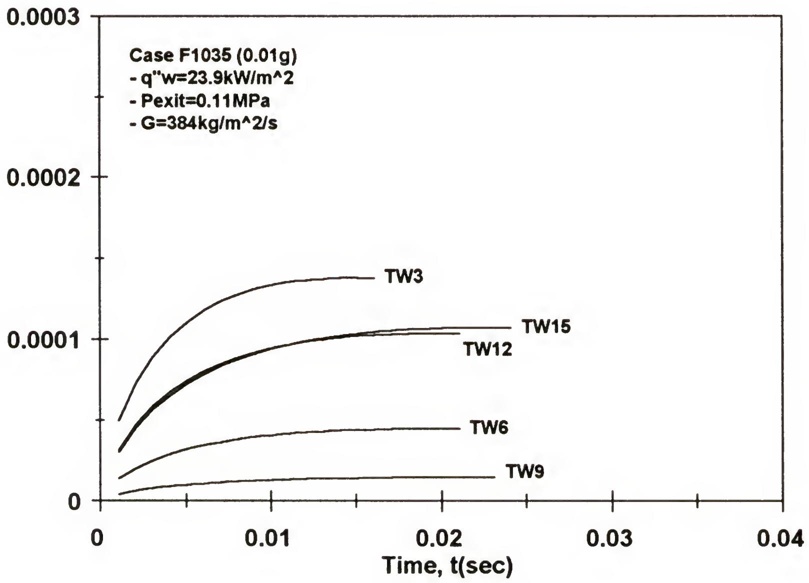

(b) g/g0=0.01

Figure 5-18 Typical bubble growth predicted by the mass transport model for Case F1035.

The measured wall temperatures were used to give the superheat θ_0 in the above calculation. Typical bubble growth for Case F1035 is shown in Figure 5-18. Within the superheated layer, the bubble grows proportional to $t^{-1/2}$. Its growth rate decreases after the top portion of the bubble was exposed to the subcooled liquid. Unlike saturated boiling, the bubble size is limited by the thickness of the superheated layer. In addition to the wall superheat, the growth rate is determined by the growth factor $2\sqrt{a}*Ja$. The variation of this factor as a function of pressure is shown in Appendix C. For example, this factor increases by approximately 19.5% for the pressure change experienced in Case F1020. This indicates that a bubble grows faster and larger within the same period under reduced pressure conditions, enhancing the evaporation heat transfer.

In the mass transport model, evaporation and condensation processes continue until the bubble is detached from the wall either by the drag force of the liquid flow or by the buoyancy force. At the moment of bubble detachment, the growth rate approaches zero. Therefore, in the present analysis, it is assumed that the bubbles leave the heating surface when the maximum diameter is reached.

The local evaporation heat flux q''_{ev} calculated from Eq.(5-53) was extremely high. For example, the calculated local evaporation heat flux at the inlet and the exit are 86.8kW/m^2 and 27.2kW/m^2, respectively for Case F1015. This is because the heat resistance becomes extremely low in the evaporation microlayer. The boiling heat flux in Eq.(5-38) is the averaged heat flux over the entire heat transfer area. The relationship between the local evaporation heat flux and the average evaporation heat flux is given by

$$q''_{\mathrm{ev,avg}} = \eta\, q''_{\mathrm{ev,local}} \tag{5-55}$$

where η is the area ratio of evaporation area to the total heat transfer area. η is defined as

$$\eta = (\pi R_i^2)\,\frac{N}{A_T} \tag{5-56}$$

where R_i is the base radius of a single bubble, N the total number of nucleation sites on the surface, and A_T is the total heat transfer area. Since η is very small compared to 1.0 in subcooled boiling, $q''_{\mathrm{ev,\ avg}}$ becomes a fraction of the total heat flux. In the following text, q''_{ev} will indicate the average value unless otherwise specified.

The evaporation process is sensitive to pressure change but hardly affected by the gravity change in the subcooled flow boiling. The initial thickness of the evaporation microlayer is slightly increased when bulk convection is deteriorated in microgravity, but the influence on the overall heat transfer is insignificant. The growth rate is indirectly increased when the wall superheat is elevated as a result of deteriorated bulk convection in microgravity. However, under the conditions where bubble detachment is hydrodynamically controlled, the effect of gravity change on heat transfer will be significant.

Heat flux due to bubble agitation, q''_{ag}. For a vertical subcooled flow boiling system under normal gravity conditions, the distributed bubbles rising faster than the surrounding liquid phase introduce turbulent motion in addition to eddies inherent to turbulent flow. It is considered that the above turbulent effect due to bubble motion becomes smaller under microgravity conditions since the slip velocity of the vapor phase approaches zero. However, coalescence of the detached bubbles is promoted in the absence of relative velocity and resulting bubble size grows larger than that of normal gravity.

As is discussed in Chapter 4, the turbulence caused by bubble agitation is proportional to the bubble diameter d_B and the slip velocity U_B. Under extremely small gravity conditions, U_B approaches zero and there is no turbulence caused by bubble agitation. In intermediate low-gravity conditions, however, the influence of $d_B \times U_B$ on eddy generation is unknown. Besides, the decrease in static pressure changes the shear stress distribution in the liquid flow. These differences are especially pronounced in vertical flow systems under reduced gravity conditions and alter the velocity and temperature profiles.

The relative magnitude of q''_{ev} to q''_{ag} is hard to define with the limited data available from the present experiments.

Bowring proposed an empirical relationships for the ratio (q''_{ag}/q''_{ev}) by analyzing experimental void fraction data for water[46]

$$\epsilon = \frac{q''_{ag}}{q''_{ev}} = 1 + 3.2\left(\frac{\rho_f}{\rho_g}\right)\left(\frac{C_{pl}}{h_{fg}}\right) \qquad (5\text{-}57)$$

The above equation is valid for 1-9.5bar (14.7-140psia). Substituting the thermal properties of Freon 113 at the saturation temperature, the ratio becomes 4.1 for Case F1035. This indicates that the heat flux due to bubble agitation q''_{ag} is about 4.1 times larger than the evaporation heat flux q''_{ev}. However, the ratio ϵ obtained from the mass transport model was much larger than 4.1 as shown in Figure 5-15. This is because the heat flux used in the present study was smaller than that of Bowring's experiment. His model predicts that q''_{ag} prevails in the majority of the subcooled region under normal and microgravity conditions.

The empirical factor 3.2 in Eq.(5-57), an effective temperature rise of the water pulled in and pushed out by the bubble, is considered a function of bubble size. The ratio ϵ will be larger in microgravity because the bubble agitation heat flux becomes smaller. Another experiment to investigate the influence of gravity exclusively on q''_{ag} is proposed and described in Chapter 6.

q''_{ev} predicted by Larsen-Tong's correlation. A semi-analytic model to account for the evaporation heat flux in subcooled flow boiling was proposed by Larsen and Tong[36].

This model is based on the formation and growth of the bubble boundary layer considering a heat balance between the heat removed by the liquid core and the external heat input. The heat flux removed by liquid flow at the edge of the bubble boundary layer q''_2, is given by

$$q_2'' = -\sqrt{\frac{16.5}{8}}\left(\frac{0.8}{Pr}\right)\frac{(r_2/R)\theta_c}{\mathrm{In}(1-r_2/R)}Re^{-0.3} \times\left[1-\alpha_b(1-(r_2/R)^2)\right]^{-0.7} \tag{5-58}$$

where r_2 is the distance from the center line to the edge of the bubble boundary layer and α_b is the average void fraction in the bubble boundary layer. Larsen and Tong assumed that r_2 is equal to the laminar sublayer thickness of fully developed turbulent liquid flow. In the present analysis, r_2 is computed using the superheated layer thickness, while α_b is obtained from

$$\alpha_b = \alpha/(1-(r_2/R)^2) \tag{5-59}$$

q''_2 represents the single-phase convection in a flow area gradually reduced by the growing bubble boundary layer. Note that this theory is developed for the horizontal flow and the bubble agitation mechanism normally observed in a vertical flow system is not included. Thus, the evaporation heat flux is expressed as the difference between the total heat flux and q''_2

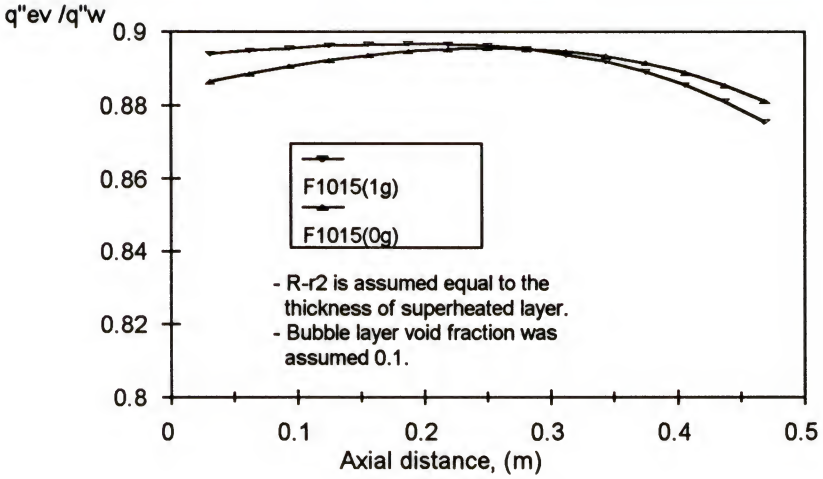

- R-r2 is assumed equal to the thickness of superheated layer.
- Bubble layer void fraction was assumed 0.1.

(a) Case F1015

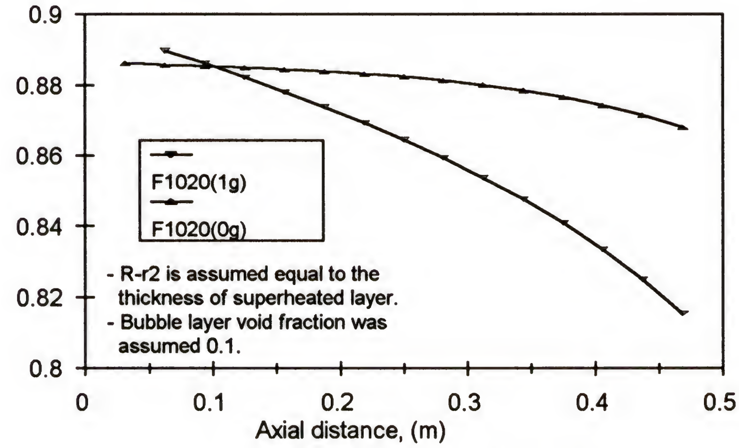

- R-r2 is assumed equal to the thickness of superheated layer.
- Bubble layer void fraction was assumed 0.1.

(b) Case F1020

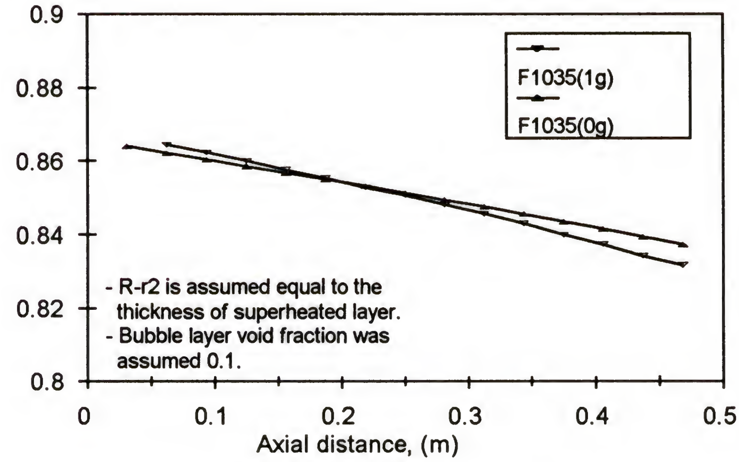

- R-r2 is assumed equal to the thickness of superheated layer.
- Bubble layer void fraction was assumed 0.1.

(c) Case F1035

Figure 5-19 Contribution of evaporation heat flux predicted by Larsen-Tong' correlation.

$$q''_{ev} = q''_{w} - (r_2/R)\, q''_2 \qquad (5\text{-}60)$$

Eq.(5-58) was applied to Cases F1015 through F1035 and the results are shown in Figure 5-19. It also should be noted that Eq.(5-58) does not include gravity effects explicitly.The calculation results for Cases F1015, F1020, and F1035 are, therefore, regarded as those for hypothetical experiments performed under normal gravity using the same flow conditions. The predicted evaporation rate was enhanced mainly because of reduced pressure, not reduced gravity.

This correlation tends to overestimate the values for evaporation heat flux since the empirical constants are chosen for fully developed subcooled flow boiling with large heat fluxes.

q''_{bo} predicted by Chen's correlation. The well-known Chen's correlation for saturated boiling heat transfer was employed to estimate the subcooled boiling heat transfer for the present experiment. Setting the suppression factor S equal to 1.0, the nucleate boiling heat transfer coefficient h_{bo} for subcooled boiling was calculated using the measured wall temperature data. h_{bo} is expressed as

$$h_{bo} = 0.00122 \left[\frac{k_f^{0.79}\, C_{pl}^{0.45}\, \rho_f^{0.49}}{\sigma^{0.5} \mu_f^{0.29}\, h_{fg}^{0.24}\, \rho_g^{0.24}} \right] \Delta T_{sat}^{0.24}\, \Delta P_{sat}^{0.75}\, S \qquad (5\text{-}61)$$

where ΔT_{sat} denotes the wall superheat, while ΔP_{sat} is the saturation pressure difference evaluated at wall temperature and at the bulk temperature. The results are shown in Figure

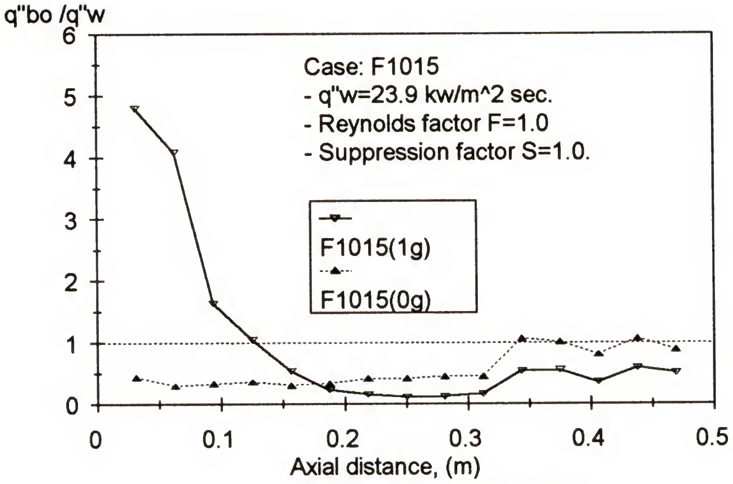

(a) Case F1015

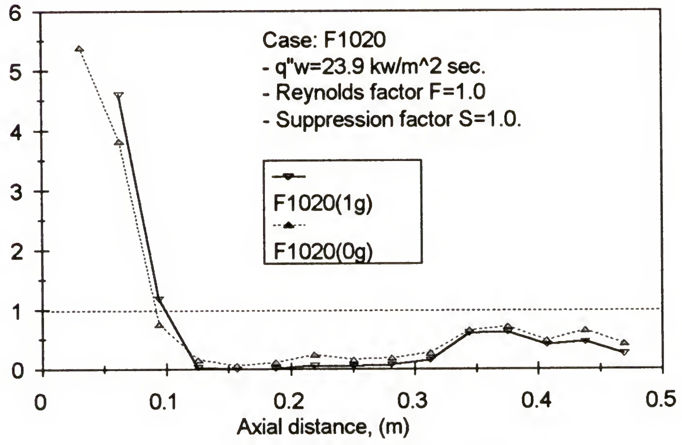

(b) Case F1020

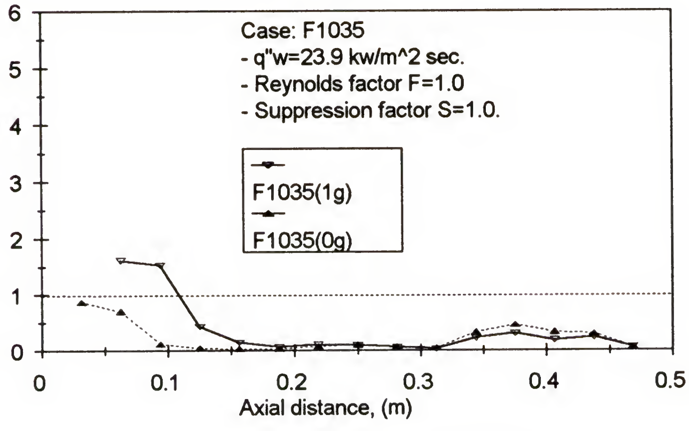

(c) Case F1035

Figure 5-20 Contribution of boiling heat flux predicted by Chen's correlation.

Table 5-4 Boiling and evaporation heat fluxes at TW15 estimated by Chen's and Larsen-Tong's methods.

	z(m)	q''_{bo}/q''_w(W/m^2)[*] measured	q''_{bo}(W/m^2) by Chen	q''_{ev}(W/m^2)[**] by Larsen-Tong	T_w-T_s[***]
F10151	0.438	14445	14193	21057	9.6
F10150	0.438	12727	25734	21161	13.3
F10201	0.438	9797	10965	19718	8.5
F10200	0.438	9766	15750	20831	10.4
F10351	0.438	8655	5635	19940	6.1
F10350	0.438	8078	7378	20064	7.0

[*] Sekoguchi's method was employed.
[**] Gravity effect is included as bubble boundary layer thickness, r2.
[***] Data at TW15(z=0.438m).

	z(m)	(0.01g/1.0g) measured	(0.01g/1.0g) Chen	(0.01g/1.0g) Larsen-Tong	(0.01g/1.0g) T_w-T_s[***]
F1015	0.438	0.886	1.813	1.005	1.385
F1020	0.438	0.997	1.436	1.056	1.224
F1035	0.438	0.933	1.309	1.006	1.148

5-20. It should be noted that the boiling heat flux h_{bo} consists of evaporation and bubble agitation. The predicted values tend to overestimate the heat transfer rate because this correlation was developed for saturated flow boiling with high heat fluxes where the evaporation heat flux is dominant over the bubble agitation heat flux. These calculation results are used to estimate the pressure effects on h_{bo} without considering the influence of gravity on boiling.
The predicted values of q''_{bo} in the outlet region were compared with the measurements and tabulated in Table 5-4. Since the Chen's correlation includes no effect of gravity, these calculation results are interpreted as the data that would be obtained in hypothetical experiments performed under normal gravity conditions using the same flow conditions. Chen's correlation predicts an increase in the boiling heat flux under microgravity conditions, which is opposite to the measurements. This is because q_{ev}'' is dominant in Chen's experiments, while q_{ag}'' is dominant in the present experiments. The increase in q_{ev}'' under microgravity conditions as predicted by Larsen-Tong's model agreed with the present measurements.

5.5 Gravity Effects on Boiling Mechanisms

The total heat flux consists of contributions of evaporation, bubble agitation, and forced convection of the liquid phase. For flow boiling systems provided with a constant heat flux, the following heat balance must be satisfied

$$q_w'' = const. = q_{ev}'' + q_{ag}'' + q_{fc}'' \tag{5-62}$$

If the ratio f is defined as follows,

$$f = \frac{q_{ag}''}{(q_{ag}'' + q_{fc}'')} \tag{5-63}$$

Eq.(5-63) is rewritten as

$$\left[\frac{1}{\epsilon}\left(\frac{f}{1-f}\right)+\left(\frac{f}{1-f}\right)+1\right]\left(\frac{q_{fc}''}{q_w''}\right)=1 \tag{5-64}$$

where ϵ is the ratio of the agitation heat flux to the evaporation heat flux as defined in Eq.(5-57). The value of f near the test section exit was calculated for Case F1035 for various values of U_B in Section 4.3. Under the conditions of Case F1035, the value of ϵ was equal to 4.1 in normal gravity. For simplicity, the same value for ϵ was assumed in the microgravity calculations. Eq.(5-64) yields the relative magnitudes of q_{ev}'', q_{ag}'', and q_{fc}'' when appropriate values are substituted for f and ϵ.

The resulting fractions of each contribution in the slightly subcooled region for Case F1035 are tabulated in Table 5-5. Note that the method described here is applied only to bubbly flow in the subcooled boiling at the exit of the test section. The selection of Case F1035 was made based on the least effect of pressure change. Under normal gravity

Table 5-5 Fractions of subcooled heat transfer components under 1.0g and 0.01g for Case F1035 at TW15 (z=0.4375m).

U_B (m/s)	$\epsilon^{*}=$ q_{ag}''/q_{ev}''	$f^{**}=$ $q_{ag}''/(q_{ag}''+q_{fc}'')$	q_{ev}''/q_w''	q_{ag}''/q_w''	q_{fc}''/q_w''	$(1-q_{bo}''/q_w'')^{-1}$	$[(1-x_a)/(1-\alpha)]^{0.33}$	h_{TP}/h_{fo}
0.210(1.00g)	4.1	0.406	0.090	0.369	0.540	1.848	1.004	1.855
0.0(0.01g)	4.1	0	0	0	1.0	1.0	1.005	1.005
0.005(0.01g)	4.1	0.124	0.029	0.121	0.849	1.176	1.004	1.181
0.015(0.01g)	4.1	0.250	0.057	0.236	0.707	1.414	1.003	1.418
0.030(0.01g)	4.1	0.372	0.083	0.341	0.576	1.736	1.002	1.739

* Bowring's correlation was used for both 1.0g and 0.01g cases.
** Radial void distribution obtained in Case D0FP4 was employed.

conditions, q_{fc}'' and q_{ag}'' account for 54% and 36% of the total heat flux, respectively. The contribution of the evaporation heat flux was 9%. Under microgravity conditions, the above fractions change significantly, mainly due to the increased void fraction and smaller slip velocity. In Table 5-5, three different cases were calculated by changing the value of U_B. The fraction of q_{ag}'' increases as the magnitude of the eddy generated by bubbles increases. The case for U_B=0.015m/s appears to most closely simulate the actual case since this value is close to the bubble rising velocity computed by the following relationship proposed by Peebles and Garber[51]

$$u_b = 0.33\, g^{0.76} \left(\frac{\rho_f}{\mu_f} \right)^{0.52} R_b^{1.28} \qquad (5\text{-}65)$$

$$for \quad 2 \le Re_b \le 4.02\, Y^{-0.214}$$

where the bubble Reynolds number Re_b and Y are defined by $2R_b u_b \rho_f/\mu_f$ and $g\mu_f^4/(\rho_f \sigma^3)$, respectively. The fractions of q_{fc}'' and q_{bo}'' in normal and microgravity are shown Figure 5-21 and compared with the measurements. The boiling heat flux q''_{bo} in the present experiment was obtained using Sekoguchi's method and given by

$$\left(\frac{q_{bo}''}{q_w''} \right) = 1 - \left(\frac{1 - x_a}{1 - \alpha} \right)^{0.33} \frac{(T_w - T_f)_{exit}}{(T_w - T_f)_{ONB}} \qquad (5\text{-}66)$$

where $(T_w-T_f)_{exit}$ and $(T_w-T_f)_{ONB}$ were the temperature differences measured at z=0.468m from the test section inlet and at the ONB, respectively. The fraction of q_{fc}'' in microgravity

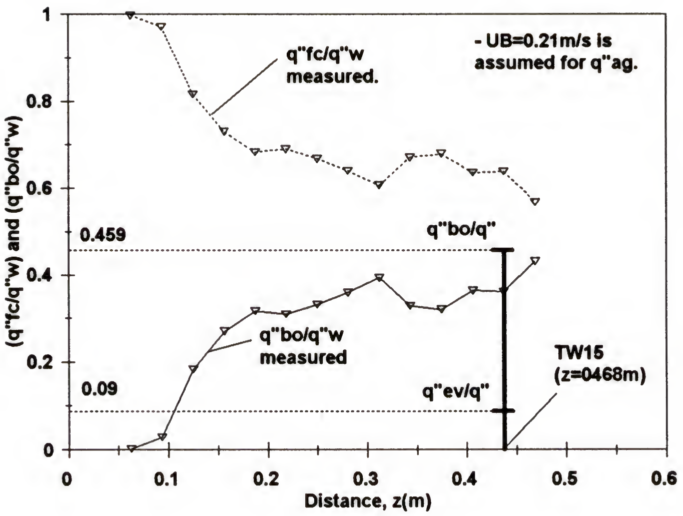

(a) g/g0=1.0

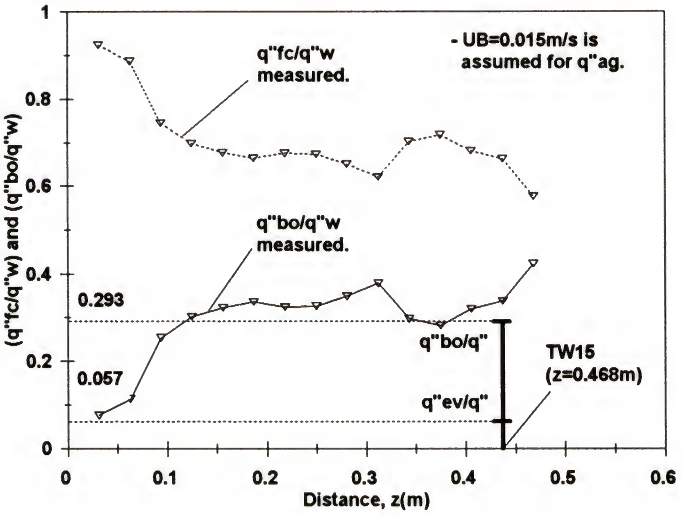

(b) g/g0=0.01

Figure 5-21 Ratios of heat flux components for Case F1035 predicted by the present analysis.

increased slightly compared to that of normal gravity. However, the fraction of q_{ag}'' decreased significantly due to loss of the buoyancy force. The forced convection heat flux q_{fc}'' accounted for 70.7% of q_w'', while the bubble agitation heat flux q_{ag}'' accounted for 23.6%. The heat flux due to evaporation q_{ev}'' was 5.7%.

Based on the fractions computed above, the ratio of the boiling heat flux (q_{bo}''/q_w'') was calculated for Case F1035 to obtain the two-phase heat transfer ratio (h_{TP}/h_{f0}). For the subcooled flow boiling with small void fractions, the influence of gravity on the forced convection term $[(1-x_a)/(1-\alpha)]^{0.33}$ was negligible. As a result, the term $(1-q_{bo}''/q_w'')^{-1}$ became dominant in determination of (h_{TP}/h_{f0}) under the conditions of Case F1035. This result is plotted in Figure 5-22 and indicates that the predictions qualitatively agree with the measurements under the conditions of F1035.

The two-phase flow heat transfer has been treated as a function of the Lockhart-Martinelli parameter X_{tl} and the Boiling number defined by $Bo=q_w''/(G\cdot h_{fg})$. The ratios h_{TP}/h_L obtained under normal and microgravity conditions are also plotted in Figure 5-22 as a function of $1/X_{tl}$. The same experiments were repeated 12 times on the ground under the conditions similar to those of the flight experiment. The atmospheric pressure in the laboratory was 1atm, while that in the Learjet cabin during the experiment was 0.85atm. Although the number of data was small, the ratios h_{TP}/h_L obtained in

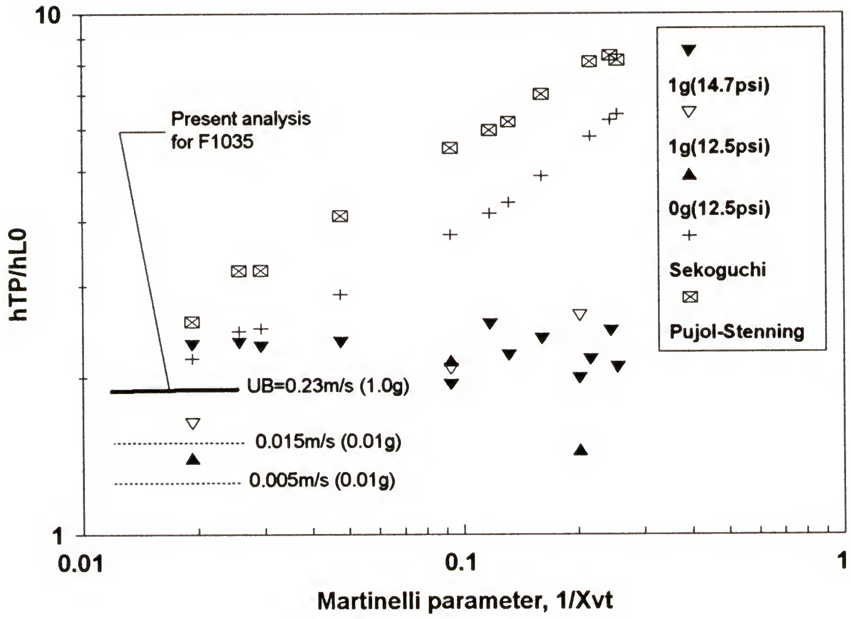

Figure 5-22 Two-phase flow heat transfer rate measured under normal(1.0g) and microgravity(0.01g) conditions.

microgravity tend to become smaller than those of normal gravity. A correlation derived by Pujol and Stenning for Freon 113 in a vertical up-flow system is shown as well[52]. Their correlation is given by

$$\frac{h_{TP}}{h_{f0}} = 0.9\left[Bo \times 10^{4} + 4.45\left(\frac{1}{X_{lt}}\right)^{0.37}\right] \tag{5-67}$$

Prediction made by Sekoguchi's method without modification is also plotted in Figure 2-22. Both correlations overestimated the ratio h_{TP}/h_L mainly because their correlations were derived for higher flow rates and higher heat fluxes.

The boiling heat flux q_{bo}'' comprises evaporation q''_{ev} and bubble agitation q''_{ag}. It is observed that q''_{ev} became larger in the inlet region where the superheat is large, while q''_{ag} becomes dominant in the exit region where the small wall superheat reduces the contribution of q''_{ev}.

In the subcooled region near the test section outlet, bubble agitation is significant and the wall superheat is small. To explain the gravity effects on subcooled heat transfer, the heat balance in the boiling test section was considered. The wall superheat for the subcooled flow boiling system is expressed as

$$(T_w - T_s) = \frac{q_w''}{h_{ev} + h_{ag} + h_{fc}} - \frac{h_{ag} + h_{fc}}{h_{ev} + h_{ag} + h_{fc}}(T_s - T_f) \tag{5-68}$$

For subcooled flow boiling with negligible contribution of q_{ev}'', such as for Case F1035, Eq.(5-68) is further reduced to

$$(T_w - T_s) = \frac{q_w''}{h_{ag} + h_{fc}} - (T_s - T_f) \tag{5-69}$$

As shown in Table 5-5, h_{ag} decreases significantly in microgravity, while h_{fc} increases due to the enlarged void fraction. As a result, the first term on the right hand side of Eq.(5-69) is increased. The second term on the right hand side of Eq.(5-69) remains constant unless system pressure is changed. The above discussion suggests an increase in wall superheat under microgravity conditions, which corroborates the measurement of wall superheats shown in Figure 5-2(f), 5-3(f), and 5-4(f).

In the region adjacent to the ONB point, the wall temperatures are higher than in other regions. Although the thickness of the superheated layer is thin, the number of activated nucleation sites is considered larger than in other regions. Under microgravity conditions, the wall superheats decreased as predicted by the ONB model previously described. Although the decrease in pressure as well as saturation temperature enhances the evaporation heat transfer, the decrease in wall superheat suppresses evaporation. Since the effect of wall superheat decrease is more significant than the pressure change, the resulting heat transfer due to evaporation h_{ev} decreased.

The analysis in this chapter has shown that gravity affects the flow boiling in various ways. The three heat transfer mechanisms (evaporation, bubble agitation, and forced convection) were discussed in view of their dependence on gravity. Each component is a function of:

$$h_{ev} = f_1 \left(\Delta T_{sat},\ P\ ,\frac{N}{A_T}\ ,f_b\ ,y_s^*\ ,\alpha\ ,Re\ ,Pr\ \right) \tag{5-70}$$

$$h_{ag} = f_2 \left(d_B\ ,U_B\ ,\alpha \right) \tag{5-71}$$

$$h_{fc} = f_3 \left(Re\ ,Pr\ ,\alpha\ ,x_a \right) \tag{5-72}$$

Among these parameters, the change of the void fraction affected all heat transfer mechanisms of flow boiling under variable gravity conditions. The detached bubble diameter d_B and slip velocity U_B were found to be significantly affected by gravity change. It is also found that the bubble agitation heat flux, normally included in the boiling heat transfer in the existing correlations, plays an important role. However, U_B and d_B are not independent of each other and a certain relationship appears to exist between U_B and d_B. For better understanding of physical phenomena, the bubble generation and void distribution should be visually observed in the future experiments.

The bubble detachment mechanism was not discussed because the point of the net vapor generation was thermally controlled under the conditions used in the present study, according to Saha and Zuber's criterion[54]. However, gravity effects on the bubble detachment will be significant under the conditions where the detachment criterion is hydrodynamically controlled.

CHAPTER 6
SUMMARY AND RECOMMENDATIONS

6.1 Discussions

Existing correlations. Most of correlations describing various phases of flow boiling have been derived under normal gravity conditions assuming a constant value for the gravitational acceleration. The exponents of Reynolds number, Prandtl number, and Grashof number obtained through the dimensional analysis are expected to assume different values for very low level of gravitational acceleration. It is somehow uncertain that the same dimensionless groups be involved in the correlations describing flow and heat transfer under microgravity conditions. For example, the predictions made by Rohsenow's correlation underestimated the wall superheats measured in microgravity as shown in Figure 5-16 (a) - (c). This is due to the fact that the correlation contains the force balance of a detaching bubble in pool boiling. Numerous observations of pool boiling experiments in microgravity show that bubble detachment is quite different from that in normal gravity. In addition, the mechanism of bubble detachment in flow boiling is more complicated than in pool boiling. According to Rohsenow's correlation, the predicted heat flux is proportional to $g^{1/2}$.

However, the present study indicated a weaker dependence on g in the range of microgravity conditions. In the absence of gravity, the contribution of buoyancy-induced heat transport is decreased and other mechanisms such as latent heat transport and bulk convection of the liquid phase become dominant. The experimental results qualitatively reflect the above tendency.

Drop tower experiment. Although a fair number of experimental investigations of adiabatic two-phase flow under microgravity conditions have been conducted, limited data on flow boiling with heat addition is available. The drop tower experiment of the present study was designed to observe the microgravity flow patterns of Freon 113 in a vertical channel with a constant heat flux. The use of transparent Cl_2Sn heating elements coated inside the flow channel provided a uniform heat flux distribution along the channel and simultaneously allowed taking pictures of flow patterns with a 35mm still camera. This configuration allowed for an unambiguous observation of bubble growth on the heating surface with flow, which was unavailable in the previous adiabatic two-phase flow experiments. The difference between adiabatic and nonadiabatic experiment was quite noticeable in the bubbly flow region. The Cl_2Sn elements with a thickness of $50\mu m$ was suitable for transient heat transfer experiments within a limited period of time because the heat capacity of the heater was negligibly small. The vertical flow was chosen since the transient time from normal gravity to microgravity in the vertical channel is shorter than the horizontal flow.

Observed flow patterns. A continuous transition from bubbly to annular flow patterns was also observed in the vertical flow boiling channel under microgravity conditions. However, the detailed structures of each pattern are different from those in normal gravity.

In bubbly flow, two types of bubbles were observed: nucleation bubbles on the heating surface and coalesced bubbles in the bulk liquid flow. The average size of nucleation bubbles under growth in microgravity was larger than those in normal gravity, indicating that the contribution of the buoyancy force to bubble detachment was nevertheless significant under the low flow conditions of the present study. It was also noticed that the number of visible nucleation sites was increased under microgravity conditions. This is due to an increase in wall temperature caused by reduced bulk convection. The main reason of the reduction in bulk convection is the absence of buoyancy force, which otherwise accelerates bubbles relative to the liquid phase. As a result, the turbulence generated by the bubbles is significantly decreased under microgravity conditions.

Coalescence of the detached bubbles was also significant under microgravity conditions. It also observed that the bubble coalescence is more prominent in microgravity where the relative velocity between bubbles and the liquid phase becomes small. This assertion is supported by the observation of bubbly flow during the 2.4g period in the flight experiment. It was also observed that the bubbles with smaller diameter moved faster in 2.4g than those in normal gravity. The size of coalesced bubbles is a function of the relative velocity between the phases, which is controlled by the gravitational acceleration.

The structure of annular flow in microgravity was quite different from that in normal gravity. The interface was wavy and small bubbles were trapped in the thin liquid films. The wavy interface was formed since the disturbance caused by the vapor motion was not diminished easily in the absence of gravity. As suggested by Klauser[25], gravity affects the annular flow heat transfer through the liquid film thickness. The formation of small bubbles seems to be due to a decrease in the heat transfer rate caused by the thickening of the liquid film under microgravity conditions.

In the slug flow region, the spherical shape at the ends of the vapor slug indicates that the relative velocity was close to zero.

Radial distribution of the vapor phase. The increase in the void fraction was expected by the theory of two-phase flow since the slip ratio approaches one in microgravity. However, the flow pattern observation also identified a significant difference in the radial distribution of the vapor phase in the bubbly flow region under microgravity conditions. This is due to the existence of large coalesced bubbles moving near the center line. After detachment from the wall, if the bubbles move faster than the surrounding liquid with a velocity gradient, the bubbles are driven toward the wall by the lift force. The peaks of the vapor phase distribution near the wall are thus formed in normal gravity. However, the magnitude of the lift force becomes smaller in microgravity because the relative velocity approaches zero. The detached bubbles migrate across the cross section and form larger bubbles. As a result, a broader, single peak is formed near the center line in microgravity.

In this study, a certain dependence between the coalesced bubble diameter and the gravitational acceleration was observed. However, a conclusive explanation of the coalescing process of multiple bubbles based on the limited number of data in this work is not feasible.

The drift flux model was considered and the values of distribution parameter C_0 under normal and microgravity conditions were calculated. It is evident that the value of C_0 becomes larger than one in the bubbly flow region under microgravity conditions because of the vapor phase concentration near the center line. When the drift flux model is used, the change in the value of C_0 impacts the heat transfer calculation which is dependent on the average void fraction. It was found that the gravity change affects the void fraction through both the radial distribution and the relative velocity of the vapor phase.

Velocity and temperature distributions. One of the unique features of Sato's method is that the contribution of bubble agitation to the total heat transfer is separately discussed. Normally, this term is included in the boiling heat transfer with the evaporation heat transfer. Sato's approach is appropriate for the present analysis since it is through bubble motion that gravity affects the two-phase flow heat transfer. The calculated velocity profile for 0.02g showed an increase in liquid velocity near the wall. The calculated wall temperature for 0.02g was higher than that for 1.0g, indicating a decrease in the heat transfer rate.

Sato proposed that the eddy diffusivity due to bubble agitation is a product of the void fraction α, the average bubble diameter d_B, and the relative velocity U_B. It was found that the velocity and temperature profiles were sensitive to the choice of the above variables. Improper selection of the value for U_B lead to numerical divergence. In this analysis, the measured values in the drop tower experiment were used as input data. However, the observation of bubbly flow under variable gravity conditions suggested that a certain relationship exists between d_B and

U_B. It should be noted that the values of these parameters cannot be chosen independently.

Pressure drop. As shown in Figure 4-15, the accelerational component of pressure drop was increased in microgravity because the average void fraction was increased. Also, the frictional pressure drop was increased in microgravity, especially in the low-quality region. This result qualitatively agrees with the results of the wall shear stress calculation obtained by Sato's method. This is because the liquid phase flowing in the reduced flow area was accelerated and the velocity gradient became larger in microgravity. The increase in the void fraction due to the reduced gravity affects both the accelerational and frictional components of the pressure drop in the two-phase flow.

Subcooled heat transfer experiment. Observation of the flow patterns in the drop tower experiment indicated a significant change in the two-phase flow structures in the subcooled region under microgravity conditions. The second series of experiments, the reduced-gravity airplane tests, were conducted to investigate the gravity effects on subcooled heat transfer. A number of previously performed two-phase flow boiling experiments using pump-driven closed loop systems had transient times on the order of minutes upon gravity change. These transient times are several times longer than the microgravity period available on the microgravity airplanes. As results of the insufficient transient times, several investigators reported conflicting results on microgravity heat transfer. To shorten the transient time, the present system employed an once-through, pressure-driven piston system and maintained the same conditions at the inlet of the boiling test section throughout the trajectories. The selection of vertical flow also helped reduce the transient time because the flow pattern was already axi-symmetric in normal gravity.

For the analysis of subcooled heat transfer, the flow rate, the void fraction, the system pressure, bulk temperatures, and wall temperatures on the boiling test section were measured under microgravity conditions.

The measured wall temperature profiles indicated that the wall superheat at the onset of nucleate boiling was decreased, while that in the subcooled region increased during the microgravity trajectories. The analysis of the onset of nucleate boiling showed that the former change was due to the enhanced bulk convection caused by an increase in the flow rate, not to the gravity change. However, the latter change of the wall superheat in the subcooled region was induced by the gravity change. It was observed in the drop tower experiment that bubble motion becomes lethargic in vertical flow under microgravity conditions. Sato's calculation showed that the turbulence generated by bubble motion yields a major contribution to subcooled heat transfer. It is concluded that the reduced gravity deteriorates subcooled heat transfer in vertical flow boiling through the lethargic motion of the bubbles. It is interesting to note that, in an extreme case of zero gravity, the velocity and temperature profiles in vertical flow approach those of single phase flow for the same mass flux because the turbulence generation due to bubbles is no longer available.

Gravity effects on subcooled boiling. The subcooled heat transfer mechanisms consist of forced convection of the liquid phase, bubble agitation, and evaporation. The contributions of each heat transfer component were calculated using Sekoguchi's method. The bubble agitation heat flux was significantly decreased under microgravity conditions. On the other hand, the forced convective heat flux was increased due to the increased void fraction.

The ratio of the evaporation heat flux to the bubble agitation heat flux was obtained by Bowring's correlation. The values of the above ratio were on the order of 4.0. The evaporation heat flux, calculated based on Bowring's correlation, accounted for less than 10% of the total heat flux under the conditions of the present study. This ratio is relatively small compared to that in saturated boiling because the bubble diameter on the heating surface is smaller in the subcooled region. According to the analysis based on Sekoguchi's method, the bubble diameter in subcooled flow is limited by the thickness of the superheated layer, which is controlled by the bulk convection.

The analysis in Section 5.4.3 showed that gravity affects the bubble growth rate through the thickness of superheated layer surrounding the lower part of the bubble. The thickness of the superheated layer estimated by Sekoguchi's method was slightly increased in microgravity owing to the deteriorated bulk convection.

The effect of gravity on the bubble detachment was not discussed in this study. The flow conditions near the bubble detachment point were classified as the thermally controlled region defined by Saha and Zuber[54]. When the inlet subcoolings are much smaller than those of the present study, the bubble detachment will be controlled hydrodynamically. In such a case, loss of the buoyancy force is expected to have a significant impact on the evaporation heat flux.

6.2 Conclusions

a) Experimental rigs

1. Flow patterns and bubble growth on the heating surface were observed under microgravity conditions in a 15m drop tower facility. Total pressure drops along the boiling test section were measured and the results were analyzed.

2. The second series of flow boiling rig was designed, fabricated, and tested aboard the NASA's reduced-gravity Learjet. Wall temperatures, bulk temperatures, and pressure drops in vertical up-flow were measured.

b) Flow analysis

3. Stable boiling in the subcooled region was observed during the 18 seconds of microgravity. Flow rates were slightly increased due to the static pressure balance of the vertical flow lines.
4. Bubbly, Slug, Annular flow patterns were observed under microgravity. Flow characteristics and structures of flow regimes were significantly different from those under normal gravity conditions.
5. Under similar flow conditions, the average void fraction in vertical up-flow was higher due to the decreased slip velocity.
6. In the bubbly flow region, radial void fraction profile exhibited two peaks near the heating surface under normal gravity conditions. A broad, single peak was observed under microgravity conditions.
7. The accelerational and frictional components of pressure drop increased in the low-quality region. Gravity change affects the pressure drop through the flow pattern change and void fraction.

c) Heat transfer analysis

8. Gravity effects were negligible in single-phase flow and at the onset of nucleate boiling under the conditions of present study. The decrease in wall temperature at the onset of nucleate boiling was caused by the decrease in system pressure and the increase in flow rate.
9. The wall superheat in the subcooled region was increased under microgravity conditions. This is due to the decrease in bubble-induced turbulence in the absence of gravity. The above fact indicates an increase in evaporation heat flux.
10. Enlarged bubble size and the reduced slip velocity oppositely contributed to the bubble-induced turbulence. The total bubble-induced turbulence diminished as the gravity level became smaller. As a result, there was a reduction in the heat transfer rate in vertical up-flow under microgravity conditions.
11. The influence of gravity on turbulent flow heat transfer was smaller than that of laminar flow due to inherent turbulence in turbulent flow.
12. Total two-phase heat flux ratio (h_{TP}/h_{f0}) of subcooled boiling in vertical up-flow was decreased under microgravity conditions.

6.3 Recommendations

a) Variable heat flux. In the present experiment, the flow rate was slightly changed while using the same value of uniform heat flux. However, wall superheats for various heat fluxes are needed to develop the boiling curve for microgravity applications. In particular, the data near the onset of nucleate boiling followed by the nucleate boiling region should be gathered and analyzed since Rohsenow's correlation fails to predict the boiling heat flux in this region.

The heat flux used in the present study was about 10 times smaller than other studies. Thus, we could not compare our results with the published results because the number of activated nucleation sites was by far less than others. Besides, most correlations for the two-phase heat transfer rate or void fraction tend to overestimate our results. To perform a reproducible and accurate microgravity experiment, the first task should be directed toward generating the data which can be analyzed by existing correlations under normal gravity conditions. In the Learjet cabin, a maximum of 80A of 28V dc is available from the on-board power supply. The current of 14.7A was used to provide a heat flux of 23.9kW/m^2 into the 0.5m test section in the present study. Since electrical power available on the Learjet is limited, a maximum of approximately 240kW/m^2

will be the upper limit of heat flux for the present equipment.

b) Inlet section length and flow rate. Heat flux near the inlet region is normally higher than that of the fully developed region. As shown in Sekoguchi's method, single-phase heat transfer prevails upon the entire region of the test section. Successful prediction of the boiling component of heat flux depends on an accurate measurement of single-phase heat transfer. The inlet section of the test tube should be long enough for the flow to fully develop.

In the present study, the liquid Reynolds number ranged from 4000 to 9000, which is larger than the laminar flow criterion of 2000 but not large enough for fully developed turbulent flow. In this intermediate range, the effects of laminar flow and natural convection still remain. Higher flow rates should be used since most existing models were developed for fully developed turbulent flow. The pressure-driven piston system used in this investigation provides a maximum mass flux of $500 kg/m^2/s$ for about one minute and the corresponding Re is over 13,000. In such a case, the heat flux is not large enough to achieve saturation conditions at the exit of the test section. A new heater providing higher heat fluxes needs to be installed.

We experienced a flow interruption during the 2.4g period of flight experiment under low flow rate conditions. This is because the static pressure loss exceeded the driving pressure in the piston. To prevent flow interruption, pressure should be large enough compared to the static pressure loss in a vertical tube. This can be done by adjusting the pressure regulator and replacing check valves on the pistons preset at 11psig for the present experiment.

c) Observation of vapor phase growth. Void fraction profiles in the radial and axial direction convey important information for analysis of flow structure and pressure drop mechanism under microgravity conditions. More sophisticated models for pressure drop calculation requires the growth of the void fraction in the axial direction must be accurately accounted for. In addition, bubble growth at the onset of nucleate boiling and bubble size at the moment of detachment needs to be observed to understand the gravity effects on subcooled boiling. In this work, the void fraction was measured at the exit of the test section. To observe the evolution of the vapor phase in a boiling channel, Hino and Ueda[41] used a transparent plastic annular flow channel with a cylindrical heater at the center (Figure 6-1). Their system gives a clear view of vapor phase evolution all along the tube. The use of similar geometry is recommended for the future studies.

d) Contribution of bubble agitation. One of the main mechanisms influenced by gravity is the heat transfer due

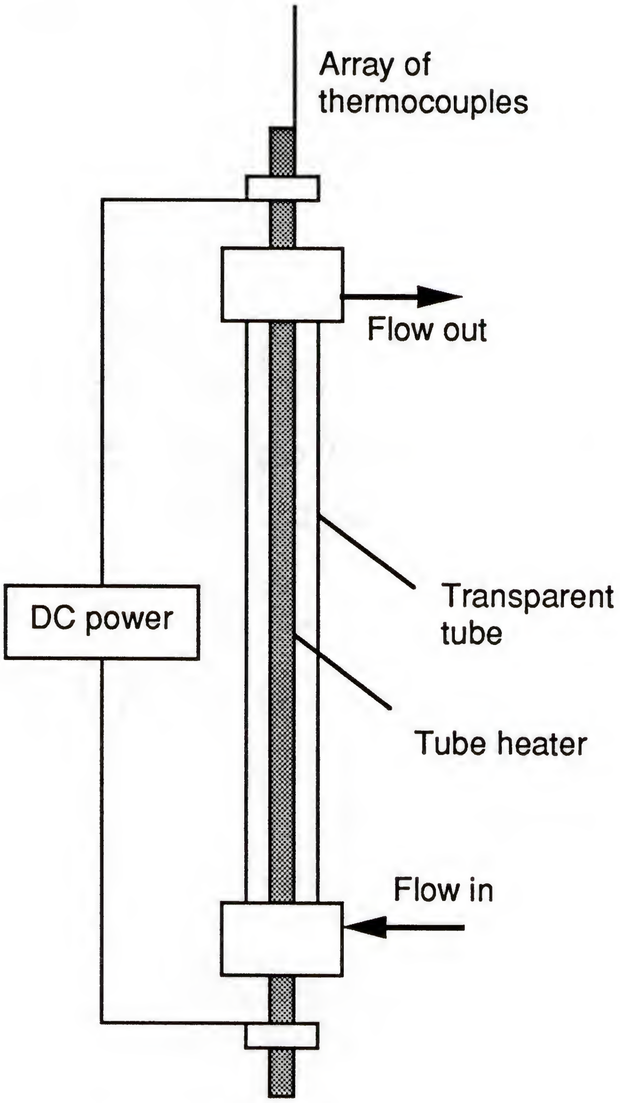

Figure 6-1 Transparent annular flow channel for observation of vapor phase evolution.

to bubble agitation. Sato et al. described the eddy diffusivity due to bubble agitation as a function of the average bubble diameter and the relative velocity of vapor phase to the liquid phase. The average bubble diameter was obtained from the photographs taken in our experiment, while the relative velocity of vapor phase was still unknown under reduced gravity conditions. The drift flux model was used to obtain the relative velocity. Under an ideal case of zero-gravity, the relative velocity disappears. For the practical cases, however, the residual gravity on the order of 10_{-6}g always exists even in spacecraft in orbit. In the present study, it is expected that small magnitudes of relative velocity still remain under the gravity levels of 0.02g and 0.01g for the drop tower and the Learjet flight experiments, respectively. Thus, the competitive effects of enlarged bubbles and the reduced relative velocity on the eddy diffusivity under microgravity conditions needs to be further examined.

An experimental apparatus is proposed to investigate the contribution of bubble agitation to the total heat flux. Figure 6-2 shows a schematic of the air-water two-phase flow system. At the bottom of the test section, air is supplied through orifices to simulate the vapor bubbles. A specific heat flux, small enough not to initiate boiling, is supplied from outside the tube. An array of sensitive thermocouples

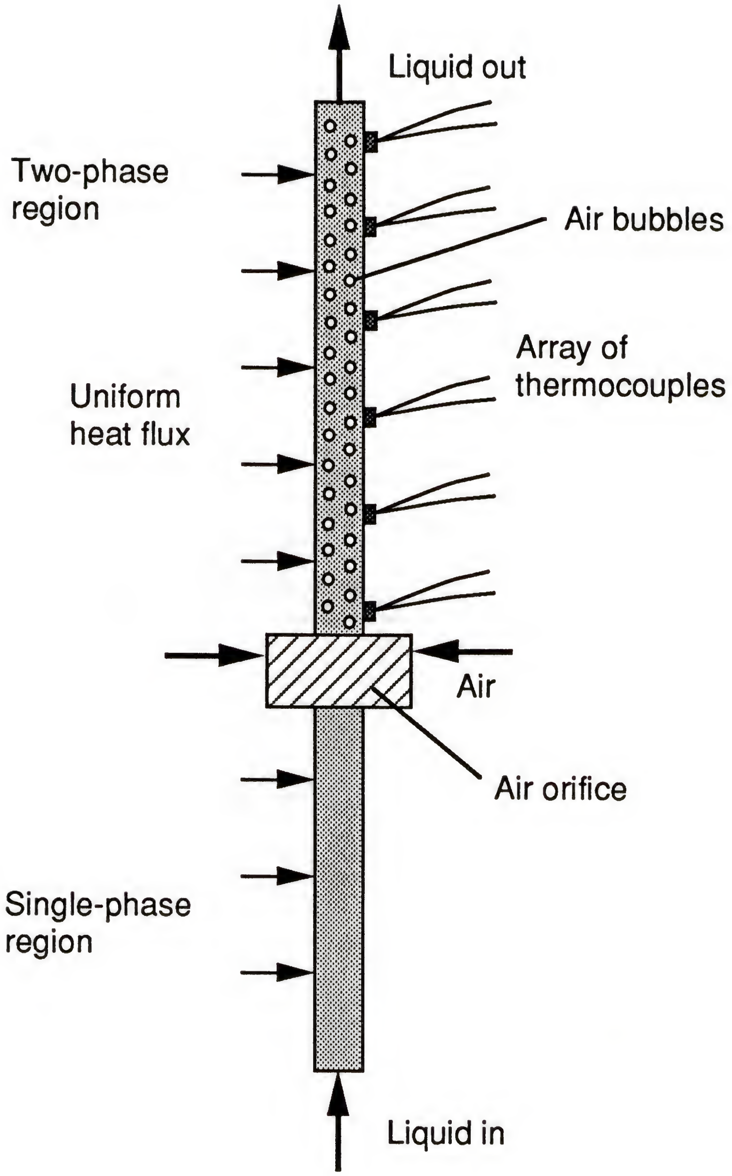

Figure 6-2 A proposed two-phase flow channel for measurement of bubble-induced heat transfer.

mounted on the tube surface will detect the wall temperature change caused by bubble agitation. In the above system, the heat transfer mechanism involves forced convection by liquid and turbulence caused by bubble agitation. Since nucleate boiling is excluded here, the contribution of bubble-induced heat transfer will be measured with high accuracy. The influence of gravity on the bubble-induced heat transfer will be understood by conducting the above experiment and observing bubble behavior under microgravity conditions.

APPENDIX A
STATIC PRESSURE CALCULATION IN THE VERTICAL FLOW SYSTEM

The static pressures in the vertical tubes in the Learjet experiment changed significantly during the gravity transition. This change caused a decrease in system pressure, which would not occur in the single-phase flow system. During the flow boiling experiment with low flow rates in high gravity levels, flow interruption occurred because of the insufficient driving pressure in the piston system. To prevent the flow interruption for future experiments, the static pressure balance was calculated for the present flow boiling system.

Figure A-1 shows a schematic diagram of the flow lines and piston system used in the Learjet experiment. Assuming that accelerational and frictional pressure drops are negligible compared to static pressure drop, the static pressures at points P1 through P10 are computed as follows:

$$P_{10} = P_0 - (20''-h_0)\ \rho_f'\ g + P_{loss,C2}$$

$$P_9 = P_{10} + 20''\ \rho_f'\ g$$

$$P_8 = P_9 - 23''\ \rho_m'\ g$$

$$P_7 = P_8 + 8.5''\ \rho_m'\ g$$

$$P_6 = P_7 - 17''\ \rho_m'\ g$$

$$P_5 = P_6 + 29''\ \rho_m\ g + 5.5''\ \rho_f\ g$$

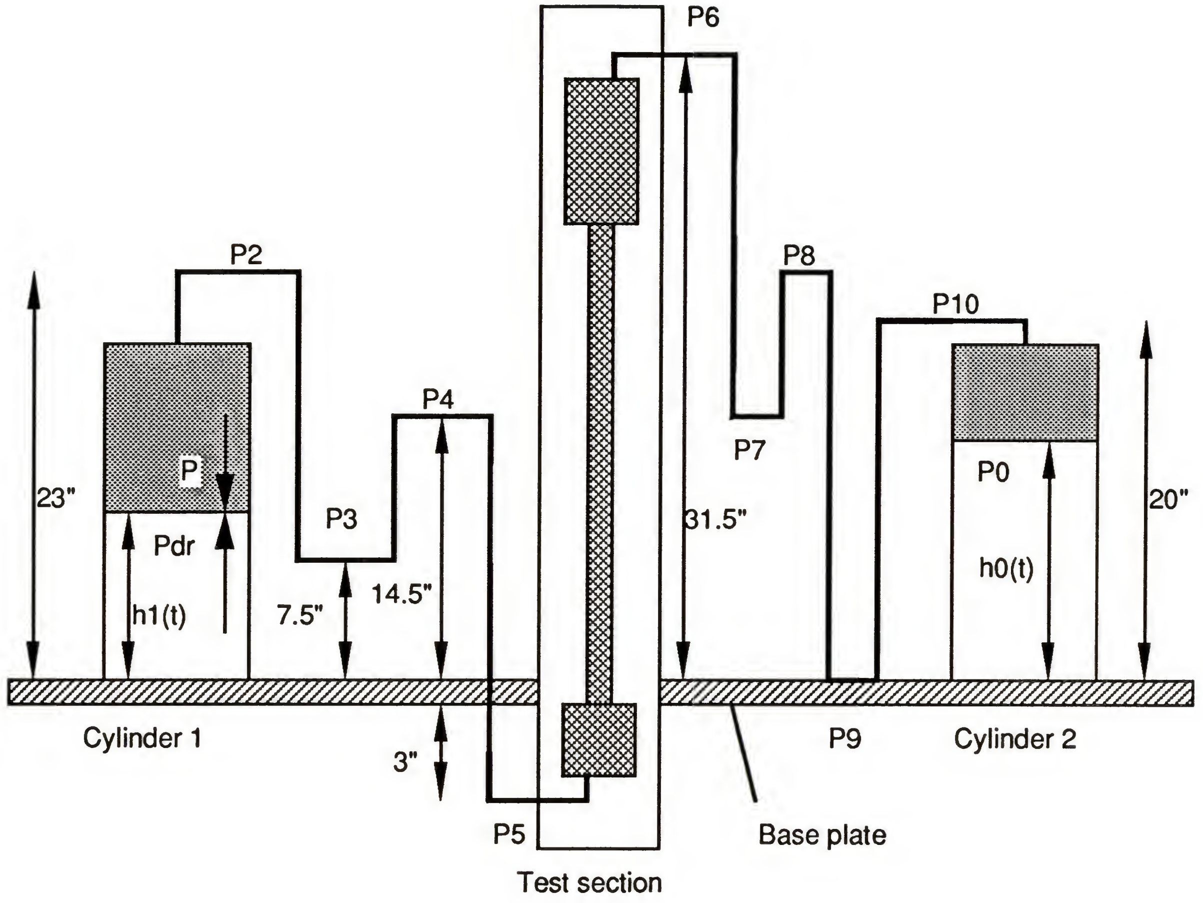

Figure A-1 Static pressure balance in a varying gravity field.

$P_4 = P_5 - 17.5'' \rho_f g$

$P_3 = P_4 + 7'' \rho_f g$

$P_2 = P_3 - 15.5'' \rho_f g + P_{loss,V2}$

$P = P_2 + (23''-h_1) \rho_f g + P_{loss,C1}$

where ρ_f, ρ_f', ρ_m, and ρ_m' are the average densities of liquid at the test section inlet, condenser exit, inside the test section, and condenser exit, respectively. $P_{loss,V2}$, $P_{loss,C1}$, and $P_{loss,C2}$ are the pressure losses due to the throttle valve, the piston head in Cylinder 1, and the piston head in Cylinder 2, respectively. Assuming further $\rho_f \approx \rho_f'$ and $\rho_m \approx \rho_m'$, the summation of the above equations yields

$$P_{drv} \geq P_{loss} + \left[31.5'' \rho_f \alpha - (h_1 - h_0) \rho_f\right] g \qquad \text{(A-1)}$$

where P_{drv} is the driving pressure supplied from a high-pressure air tank, P_{loss} is the total pressure loss due to the throttle valve and friction of cylinder piston heads, and α is the void fraction. In order to maintain flow in the system, P_{drv} must exceed the pressure loss and the static pressure head described in the right hand side of Eq.(A-1). It indicates that the static pressure head increases as the void fraction increases. The value of (h_1-h_0) is at most 10". It is considered that the total of the r.h.s. of Eq.(A-1) exceeded the driving pressure under the conditions of Case F1015, where the void fraction was large. In addition, the acceleration level g became 2.4 times larger than that of normal gravity during the pushover maneuver before entering the microgravity trajectories, only to increase the value of the right hand side of Eq.(A-1).

To prevent the flow interruption, it is suggested to;

a) increase the driving pressure P_{drv} large enough to overcome the pressure loss, or

b) confine the experimental conditions to the small void fraction range.

In the present experiment, the latter approach was taken since the driving pressure was limited to 11psi by pre-set check valves on the cylinders. Future experiments will reinforce the cylinder structure to sustain higher driving pressures.

APPENDIX B
ERROR ANALYSIS

The data from the experiment is meaningful only within the limits of the accuracy. An analysis on the errors was conducted using the error propagation formula.

The basic measured quantities and their respective uncertainty intervals are summarized in Table B-1. The confidence interval of the derived quantities are calculated in the following section.

a) Exit quality. The exit quality X_{ex} is given by

$$X_{ex} = \frac{\Delta h + h_{in} - h_s}{h_{fg}} \tag{B-1}$$

where the increase in the enthalpy Δh is expressed as $Q/(G\cdot\rho)$ [kJ/kg]. The heat input Q is obtained from the measured voltage V and current I. The error associated with Q is obtained by referring the individual uncertainties of V and I in Table B-1. The resulting relative error in Q is

$$\frac{W_Q}{Q} = \pm 0.0345$$

The error involved in the mass flux G stems from the uncertainty in the turbine flow meter and the resolution of the 8-bit data acquisition system. The combined accuracy of G becomes

Table B-1 Values and confidence intervals of measrued quantities.

Quantity	Confidence interval
1. Pressure	5.50±0.05 psig
2. Mass flux	0.370±0.002 GPM
3. Temperature	65±1 °C
4. Voltage	28.0±0.25 V
5. Current	15.0±0.5 A
6. Length of tube	500±2 mm
7. Radius of tube	12.8±0.1 mm

$$\frac{W_G}{G}=\pm 0.0341$$

The values of enthalpy at various temperatures were read from the ASME steam table. The accuracy of these values are conservatively assumed ±0.02. Using the values obtained in Case F1035, the interval of uncertainty for the exit quality is

$$\frac{W_X}{X}=\pm 0.133$$

It is noted that the addition and subtraction of enthalpy cause an increase in uncertainty although those of individual values are small.

b) Pressure measurement. The value of uncertainty for the high-accuracy pressure transducers provided by the manufacturer is ±0.1%, including thermal and hysteresis effects. The signal from the transducers are introduced to the data acquisition system with a resolution of 2.44mV in the range of ±5V. The uncertainty from the data acquisition system alone is ±0.0049. The total error of the pressure measurement is

$$\frac{W_P}{P}=\pm 0.0011$$

This error is to be applied to the actual readings at the inlet and outlet of the test section.

The pressures between the inlet and outlet P_b were estimated by the following equation

$$\frac{W_{P_b}}{P_b} = (P_{in} - P_{out})\ \frac{z}{L} + P_{in} \qquad \text{(B-2)}$$

where z is the distance from the inlet, L is the total length, P_{in} and P_{out} are the inlet and outlet pressures, respectively. Using the value of the pressure in the middle of the test section, the uncertainty of P_b yields

$$\frac{W_{P_b}}{P_b} = \pm 0.0016$$

The errors involved in the frictional pressure drop measurement are larger than those in the pressure measurement. The major sources of the error are the vapor quality and the Reynolds number. The uncertainty of the vapor quality was discussed in the previous section. The uncertainty of the Reynolds number is estimated ±0.12 in the present study. The relatively large error of the Reynolds number comes from the uncertainty of the viscosity. The pressure drop in the single-phase region is calculated by Eq.(4-41) and Eq.(4-42). The estimated uncertainties in this region are

$$\frac{W_{\Delta P_{1g}}}{\Delta P_{1g}} = \pm 0.035$$

$$\frac{W_{\Delta P_{1f}}}{\Delta P_{1f}} = \pm 0.138$$

For the two-phase flow region, the individual errors from accelerational and gravitational components, calculated by

Eq.(4-36) and (4-37), are accumulated. The uncertainties of each component in the two-phase region yield

$$\frac{W_{\Delta P_{2g}}}{\Delta P_{2g}} = \pm 0.192$$

$$\frac{W_{\Delta P_{2a}}}{\Delta P_{2a}} = \pm 0.118$$

The frictional component is obtained by subtracting the above components from the measured total pressure drop. Thus, the resulting total uncertainty for the two-phase frictional pressure drop becomes

$$\frac{W_{\Delta P_{2f}}}{\Delta P_{2f}} = \pm 0.340$$

Significant errors tend to build up during the subtraction of the pressure components.

c) Temperature measurement. The voltage signal from the OMEGA's E-type thermocouple is converted into the unit of temperature using a 9th-order polynomial provided by the manufacturer. The nominal accuracy of the polynomial in the manual is ±0.5°C. Since the relative error of the temperature measurement is larger than that of the data acquisition system, the latter was neglected in this calculation.
The bulk temperature T_b is obtained by the following equation

$$T_b = (T_{out} - T_{in})\frac{z}{L} + T_{in} \tag{B-3}$$

Using the error propagation formula, the error in the bulk temperature yields

$$\frac{W_{T_b}}{T_b} = \pm 0.025$$

d) Void fraction measurement. The diameters of individual babbles were automatically measured by Particle Analysis in Macintosh's Image v1.31 by choosing an appropriate scale. The error of this visual measurement stems from the resolution of the images. The scale was calibrated so that 9.40 pixels exist in 1.0mm. This introduces an error of ±0.106mm in the measurement of bubbles. The measured diameter of the bubbles ranged

$$0.19mm \le D_i \le 4.2mm$$

As is noticed, the uncertainty increases as the bubble diameter becomes smaller. The resulting accuracy of the void fraction measurement ranges

$$\pm 0.043 \le \frac{W_\alpha}{\alpha} \le \pm 0.426$$

The influence of the error occurred on measuring the diameters of small bubbles is considered insignificant since the accumulated volume of large bubbles are dominant in the void fraction measurement.

APPENDIX C
THERMAL PROPERTIES OF FREON 113

Variation of thermal properties of Freon 113 was not negligible for the change of system pressures encountered in the Learjet experiment. This change in the properties affects thermodynamic calculation, bubble growth, and heat transfer. The properties covered in this chapter are liquid and vapor densities, latent heat of vaporization, specific heat, viscosity, thermal conductivity, thermal diffusivity, Prandtl number, Jakob number, and $Ja \cdot \alpha^{0.5}$. The last properties are important to assess the influence of pressure change on bubble growth.

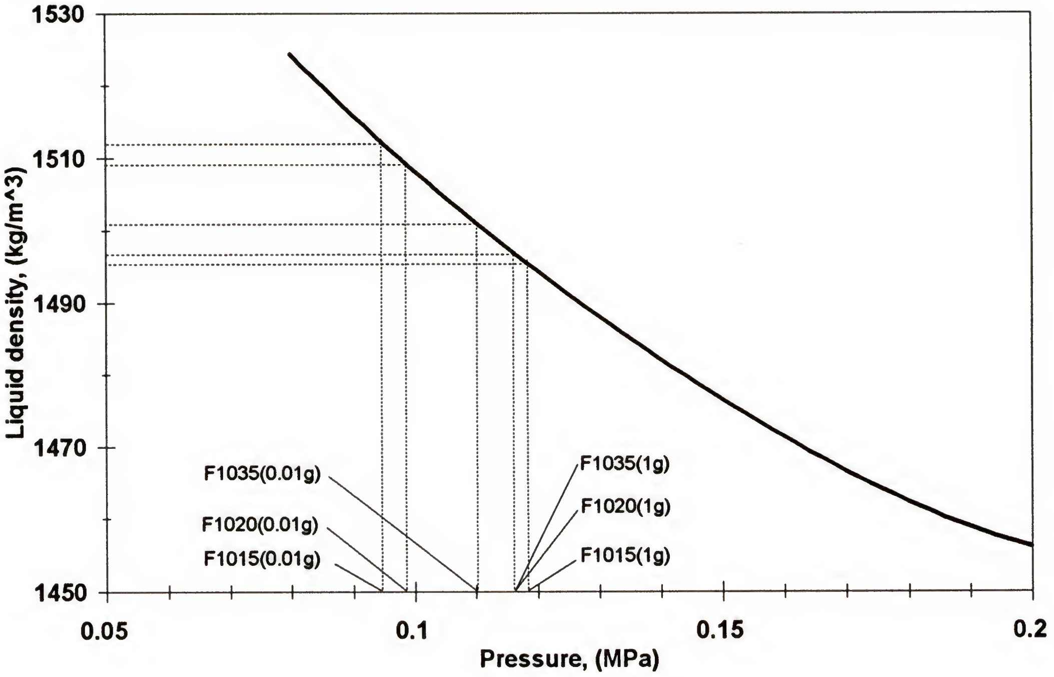

Figure B-1 Variation of liquid density as a function of pressure.

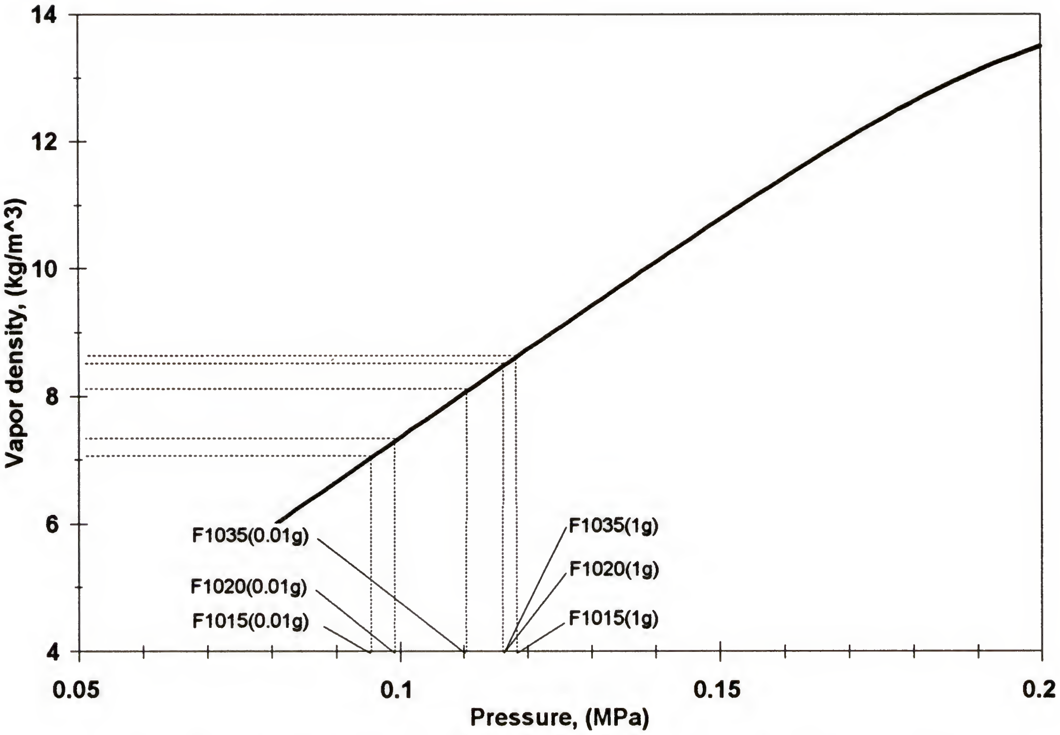

Figure B-2 Variation of vapor density as a function of pressure.

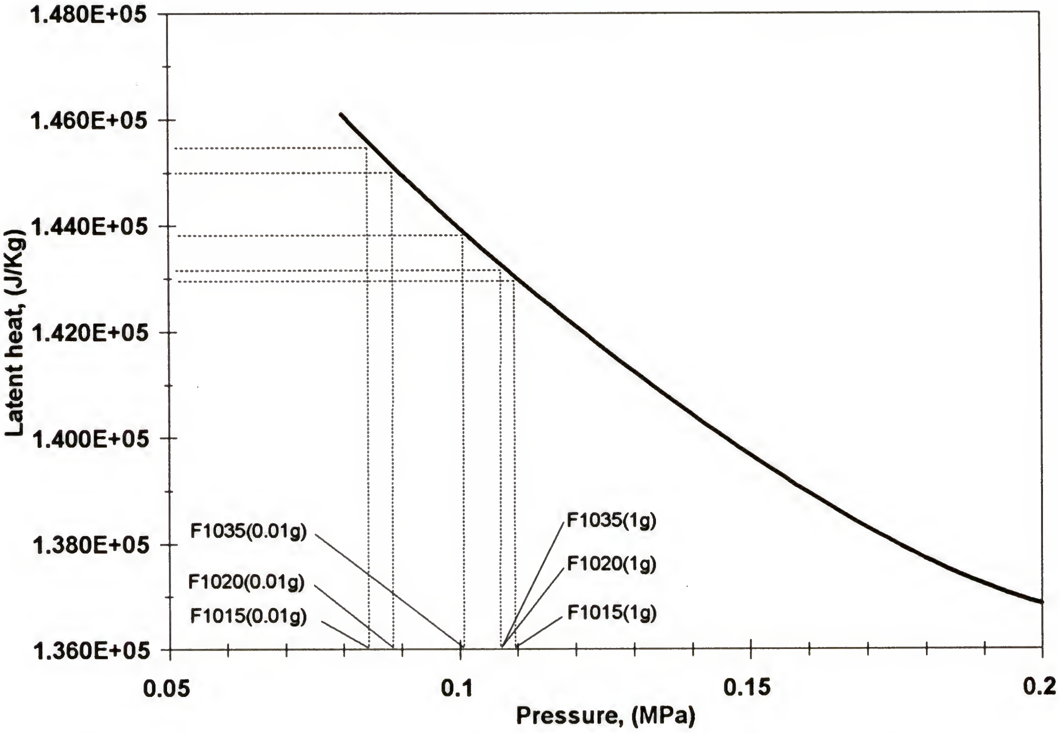

Figure B-3 Variation of latent heat as a function of pressure.

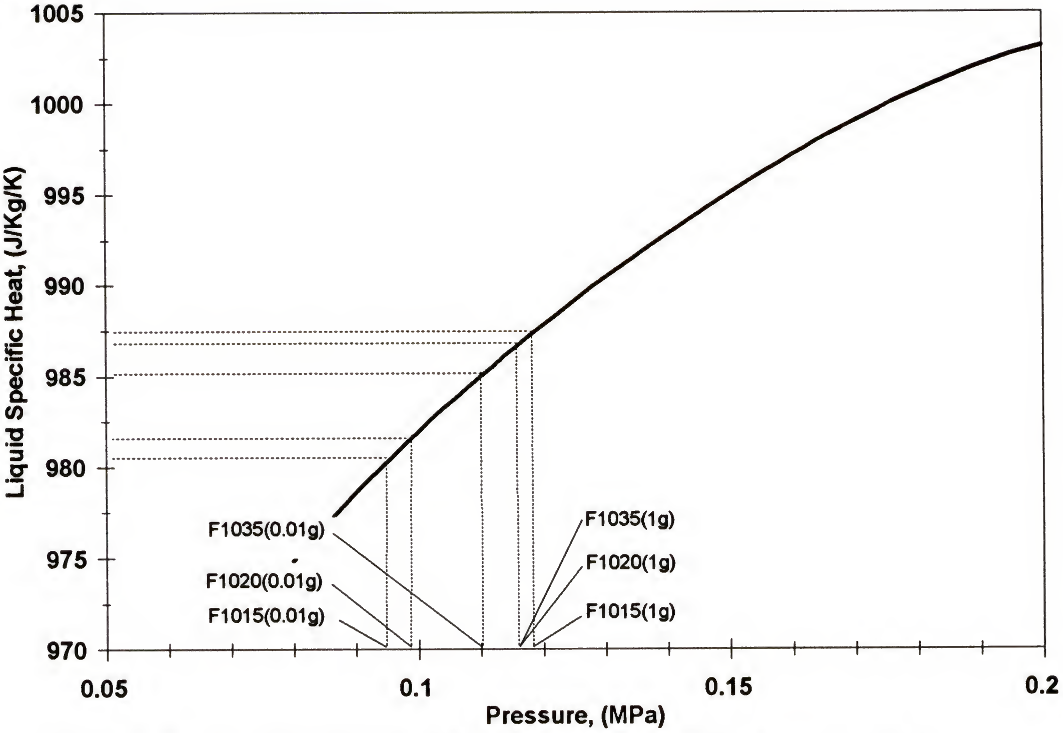

Figure B-4 Variation of liquid specific heat as a function of pressure.

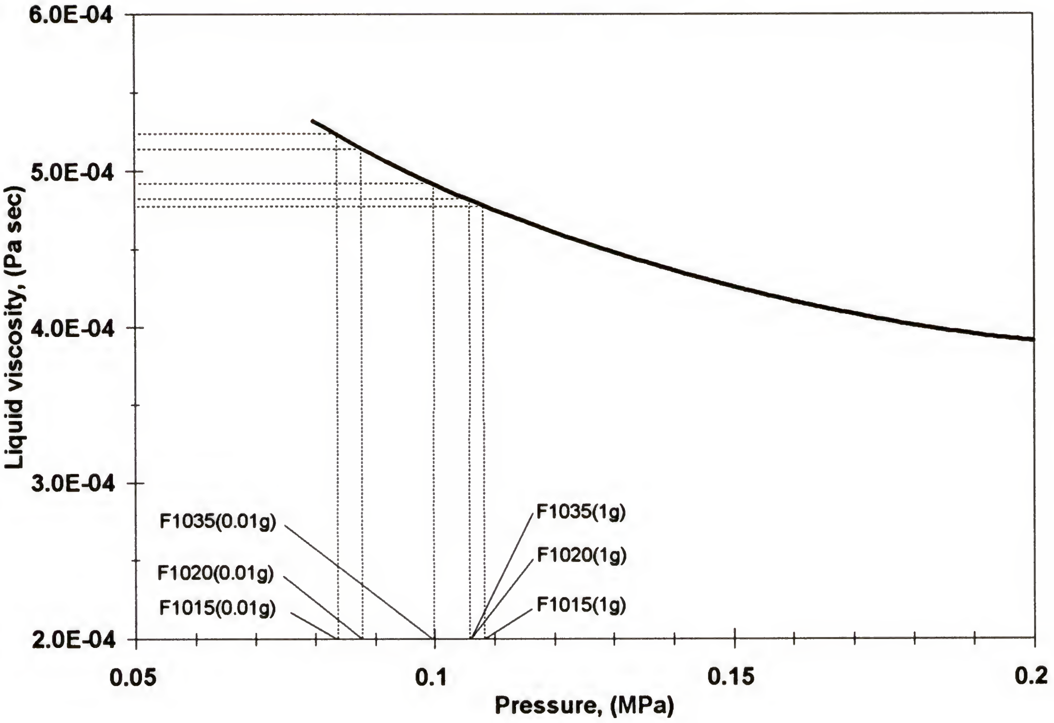

Figure B-5 Variation of liquid viscosity as a function of pressure.

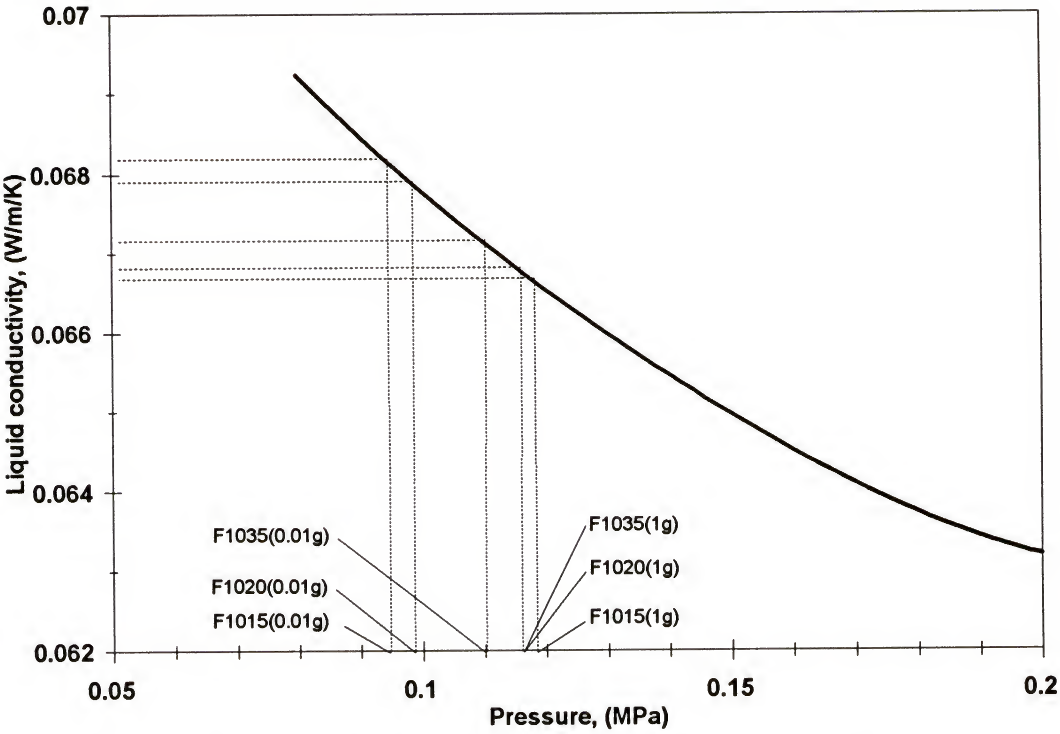

Figure B-6 Variation of liquid thermal conductivity as a function of pressure.

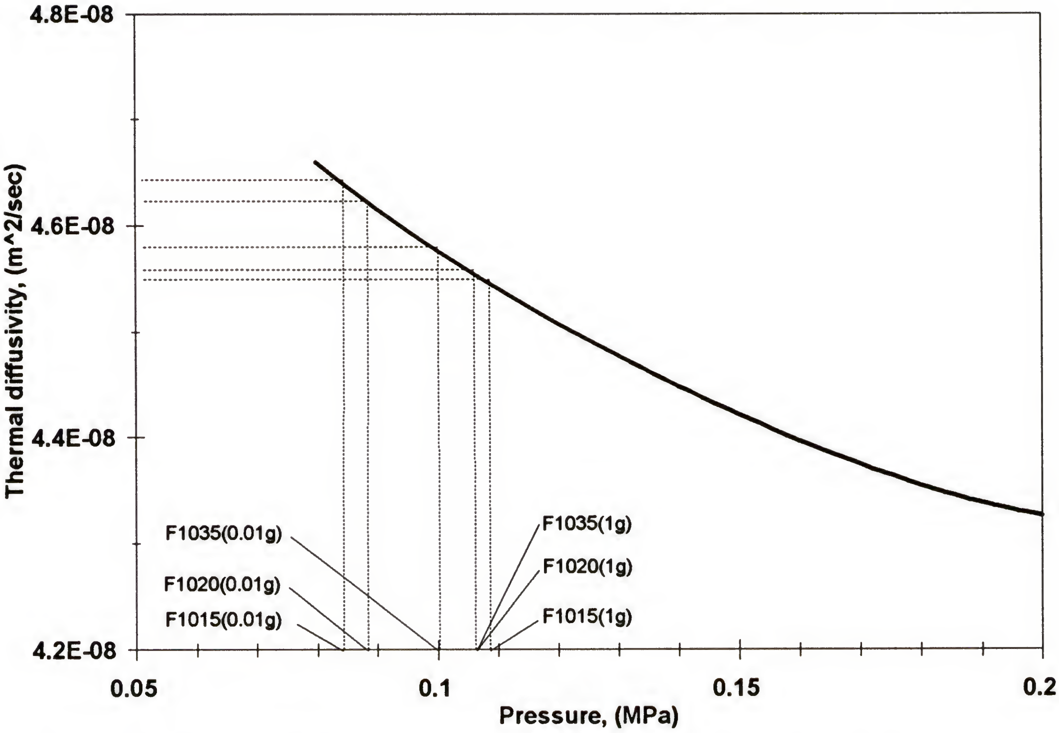

Figure B-7 Variation of thermal diffusivity as a function of pressure.

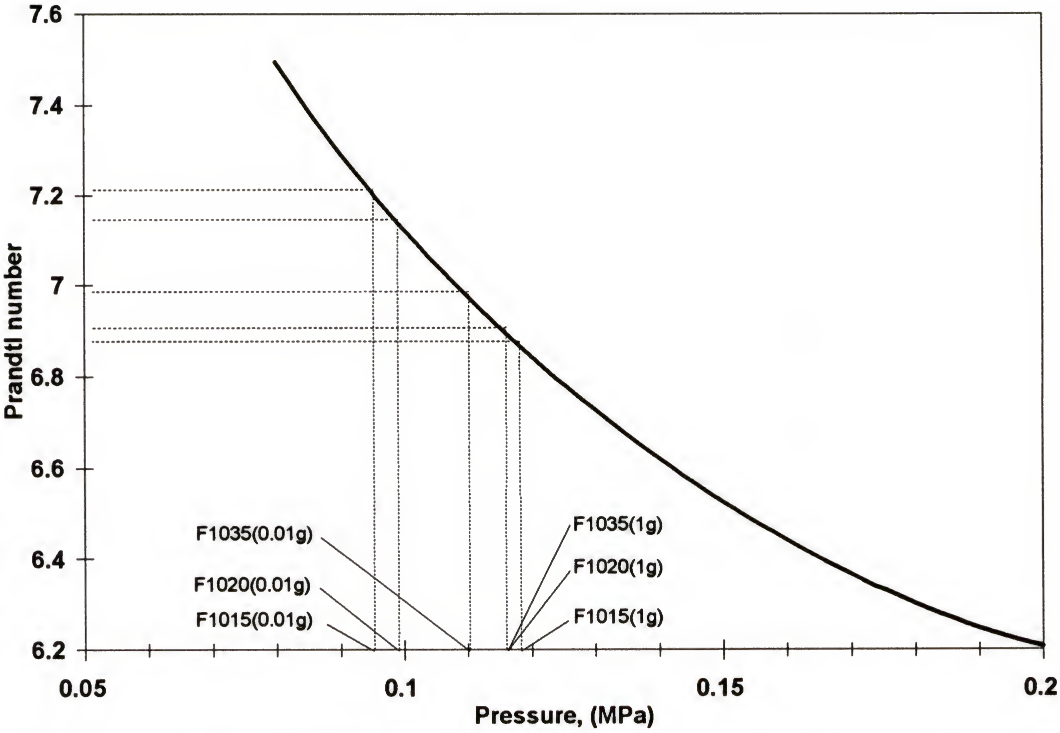

Figure B-8 Variation of Prandtl number as a function of pressure.

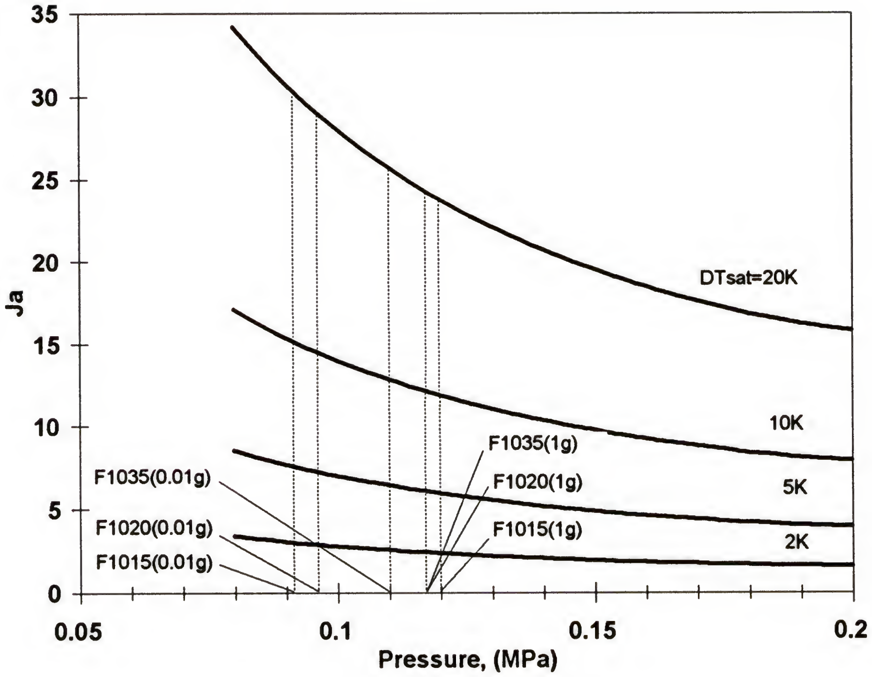

Figure B-9 Variation of Jakob number as a function of pressure.

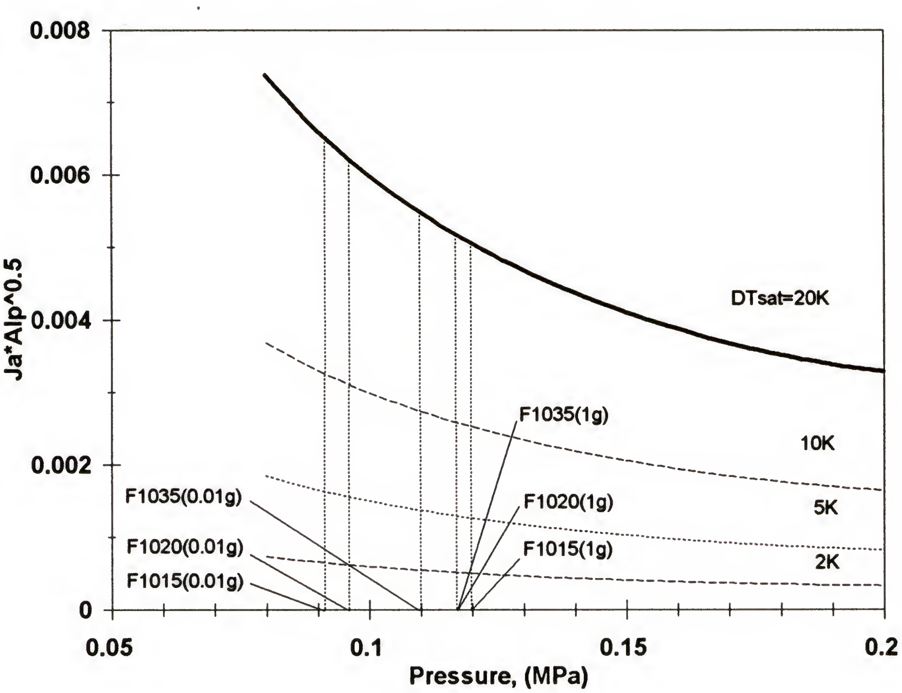

Figure B-10 Variation of Ja*a^0.5 as a function of pressure.

REFERENCE LIST

[1] Chub, D.L. and Calfo, F.L., "Scaling results for the liquid sheet radiator", Proc. 24th IECEC, vol.1, pp.45-50 (1989)

[2] Begg, L.L. and Engdahl, E.H., "Advanced radiator concepts", Proc. 24th IECEC, vol.1, pp.75-80 (1989)

[3] Borger, W.U. and Massie, L.D., "Space systems requirements and issues: The next decade", Proc. 25th IECEC, vol.1, pp.1-5 (1990)

[4] Siegel, R., "Effects of reduced gravity on geat transfer", Advances in Heat Transfer, vol.27, pp.143-228, Academic Press, New York (1966)

[5] Sherley, J.E., "Nucleate boiling heat transfer data for liquid hydrogen at standard and zero gravity", Advances in Cryogenic Engineering, vol.8, p.495, Plenum Press, New York (1963)

[6] Merte, Jr, H. and Clark, J.A., "Boiling heat transfer with cryogenic fluids at standard, fractional, and near-zero gravity", J. Heat Transfer, vol.86, p.351 (1964)

[7] Clodfelter, R.G., "Low-gravity pool-boiling heat transfer", APL Report, TDR-64-706 (1964)

[8] Siegel, R. and Keshock, E.G., "Effects of reduced gravity on nucleate boiling bubble dynamics in saturated water", AIChE J., vol.10, p.509 (1964)

[9] Keshock, E.G. and Siegel, R., "Forces acting on bubbles in nucleate boiling under normal and reduced gravity conditions", NASA TN D-2299 (1964)

[10] Zuber, N., "Hydrodynamic aspects of boiling heat transfer," Ph.D. dissertation, University of California, Los Angeles, (1959)

[11] Papell, S.S., Simoneau, R.J., and Brown, D.D., "Buoyancy effects on the critical heat flux of forced convective boiling in vertical flow," NASA TN D-3672 (1966)

[12] Evans, D.G., "Visual study of swirling and nonswirling two-phase two-component flow at 1 and 0 gravity," NASA TM X-725 (1963)

[13] Chen, I., Downing, R.S., Parish, R., and Keshock, E., "A reduced gravity flight experiment: Observed flow regimes and pressure drops of vapor and liquid flow in adiabatic piping," AIChE Symp. Ser. No263, vol.84 (1988)

[14] Colin, C., Fabre, J., and Dukler, A.E., "Gas-liquid flow at microgravity conditions - I, Dispersed bubble and slug flow," Int. J. Multiphase Flow, Vol.17, No.4, pp.533-544 (1991)

[15] Reinarts, T.R., Best, F.R., and Hill, W.S., "Definition of condensation two-phase flow behaviors spacecraft design", 7th Symposium on Space Nuclear Power Systems, pp.1216-1225 (1992)

[16] Sato, Y. and Sadatomi, M., "Momentum and heat transfer in two-phase bubble flow-I: Theory", Int. J. Multiphase Flow, vol.7, pp.167-177 (1981)

[17] Jakob, M., Heat Transfer, vol.1, Wiley, New York (1949)

[18] Rohsenow, W.M., "A method of correlating heat transfer data for surface boiling of liquids," Trans. ASME, Ser. C, vol.74, p.969 (1952)

[19] Frederking, T.H., and Clark, J.A., "Natural convection film boiling on a sphere," Advances in Cryogenic Engineering,"vol.8, p.501, Plenum, New York (1963)

[20] Schwartz, S.H. and Adelberg, M., "Some thermal aspects of a contained fluid in a reduced gravity environment," Symp. Fluid Mechs. Heat Transfer under Low Gravitational Conditions, Paper No.3349, Palo Alto, California (1965)

[21] Zell, M., J. Straub, and Weinzierl, A., "Nucleate pool boiling in subcooled liquid under microgravity -Results of TEXUS experimental investigations," Proc. 5th European Symposium on Material Sciences under Microgravity, ESA SP-222 (1984)

[22] Ervin, J.S., Merte, H.Jr., Keller, R.B., and Kirk, K., "Transient pool boiling in microgravity," Int. J. Multiphase Flow, vol.35, No.3, pp.659-674 (1992)

[23] Zuber, N., "The dynamics of vapor bubbles in nonuniform temperature fields," Int. J. Multiphase Flow, vol.2, No.83 (1961)

[24] Fritz, W., "Maximum volume of vapor bubbles," Z. Physik., vol.36, p.379 (1935)

[25] Klausner, J.F., "The influence of gravity on pressure drop and heat transfer in flow boiling," Ph.D. dissertation, University of Illinois (1989)

[26] Klausner, J.F. and Zeng, L.Z., "Bubble departure in pool and flow boiling systems: A review and latest developments," Proc. 2nd ASME/JSME Nuclear Engineering Joint Conference, pp.1-6 (1993)

[27] Sridhar, K.R., Chao, B.T., and Soo, S.L., "Pressure drop in fully developed, duct flow of dispersed liquid-vapor mixture at zero gravity," Acta Astronautica, vol.21, No.9, pp.617-627 (1990)

[28] Papell, S.S., "An instability effect on two-phase heat transfer for subcooled water flowing under conditions of zero gravity", Am. Rocket Soc. Space Power Systems Conf. Paper 2548-62 (1962)

[29] Feldmanis, C.J., "Pressure and temperature changes in closed loop forced convection boiling and condensing processes under zero gravity conditions", Proc. Inst. Environ. Sci. (1966)

[30] Crowley, C.J. and Sam, R.G., "Microgravity experiments with a simple two-phase thermal system," 7th Symposium on Space Nuclear Power Systems, pp.1207-1213 (1991)

[31] Standley, V.H. and Fairchild, J.F., "Microgravity experiments with a simple two-phase thermal system," 7th Symposium on Space Nuclear Power Systems, pp.1224-1229 (1991)

[32] Zuber, N. and Findlay, J.A., "Average volumetric concentration in two-phase flow systems," Trans. ASME Ser.C, J. Heat Transfer, pp. 453-468 (1965)

[33] Sekoguchi, K., Tanaka, O., Esaki, S. and Imasaka, T., "Prediction of void fraction in subcooled and low quality boiling regions," Bulletin of JSME, vol.23, pp. 1475-1482 (1980)

[34] Smith, S.L., "Void fractions in two-phase flow: A correlation based upon an equal velocity head model," Proc. Instin. Mech. Engrs., vol.184-Pt-1, pp.647-664 (1970)

[35] Levy, S., "Forced convection subcooled boiling - Prediction of vapor volumetric fraction," Int. J. Heat

Mass Transfer, vol.10, pp.951-965 (1967)

[36] Larsen, P.S. and Tong, L.S., "Void fractions in subcooled flow boiling," Trans. ASME Ser.C, J. Heat Transfer, pp. 471-476 (1969)

[37] Sato, Y., Sadatomi, M. and Sekoguchi, K., "Momentum and heat transfer in two-phase bubble flow-II: A comparison between experimental data and theoretical calculations," Int. J. Multiphase Flow, vol.7, pp.179-190 (1981)

[38] Sato, Y., and Sekoguchi, K., "Liquid velocity distribution in two-phase bubbly flow," Int. J. Multiphase Flow, vol.2, pp.79-95 (1975)

[39] McAdams, W.H. et al., "Vaporization inside horizontal tubes - II - Benzene-oil mixtures," Trans. ASME Ser. C, vol.64, p.193 (1942)

[40] Ahmad, S.Y., "Axial distribution of bulk temperature and void fraction in a heated channel with inlet subcooling," Trans. ASME Ser. C, vol.92, No.4, pp.595-609 (1970)

[41] Hino, R. and Ueda, T., "Studies on heat transfer and flow characteristics in subcooled flow boiling-Part 1. Boiling characteristics," Int. J. Multiphase Flow, Vol.11, No.3, pp.269-281 (1985)

[42] Schmidt, E., VDI-Warmeatlas, 2nd ed., secs. Gb and Gc, VDI, Dusseldorf (1974)

[43] Davis, E.J. and Anderson, G.H., "The incipient of nucleate boiling in forced convection flow," AIChE Journal, vol.12, No.4, pp.774-780 (1966)

[44] Bergles, A.E., Bakhru, N. and Shires, J.W., "Cooling of high-power-density computer components," Research Report No.60, Dept. Mech. Eng., M.I.T., November (1968)

[45] Snyder, N.W., and Robin, T.T., "Mass-transfer model in subcooled nucleate boiling," Trans. ASME Ser. C, vol.92, No.4, pp.595-609 (1970)

[46] Bowring, R.W., "Physical model based on bubble detachment and calculation of steam voidage in the subcooled region of a heated channel", OECD Halden Reactor Project Report HPR-10 (1962)

[47] Kroeger, P.G. and Zuber, N., "An analysis of the effects of various parameters on the average void fractions in subcooled boiling," Int. J. Heat Mass Transfer, vol.11, pp.211-232 (1968)

[48] Unal, H.C., "Maximum bubble diameter, maximum bubble-growth time and bubble-growth rate during the subcooled nucleate flow boiling of water up to 17.7MN/m_2," Int. J. Heat Mass Transfer, vol.19, pp.643-649 (1976)

[49] Stralen, S.V. and Cole, R., Boiling Phenomena, vol.1 and vol.2, Hemisphere, New York (1979)

[50] Unal, H.C., "Bubble departure diameter, bubble growth time and bubble growth rate during the subcooled nucleate flow boiling of water up to 177bar," Ref. No.73-02829, Central Technical Institute TNO, P.O. Box 342, Apeldoorn, The Netherlands (1973)

[51] Peebles, F.N. and Garber, H.J., "Studies on the motion of gas bubbles in liquids," Chem. Eng. Prog., vol.49, No.2, pp.88-97 (1953)

[52] Pujol, L. and Stenning, A.H., "Effect of flow direction on the boiling heat transfer coefficient in vertical tubes," Symp. Ser. of Canadian Soc. for Chem. Eng'ng, vol.1, No.1, pp.401-453, Plenum Press, New York (1960)

[53] Dukler, A.E., Fabre, J.A., McQuillen, J.B., and Vernon, R., "Gas-liquid flow at microgravity conditions: Flow pattern and their transitions," Int. J. Multiphase Flow, vol.14, pp.389-400 (1988)

[54] Saha, P. and Zuber, N., "Point of net vapor generation and vapor void fraction in subcooled boiling," Proc. 5th Int. Heat Tran. Conf., Tokyo, vol.4, pp.151-157 (1974)

[55] Cumo, M., and Naviglio, A., Thermal Hydraulics, vol.1, p.136, CRC Press, Boca Raton, FL (1988)

[56] Dougall, R.S., and Lippert, T.E., "Boiling inception in trichlorotrifluoroethane during forced convection at high pressures," NASA CR-2170 (1972)

[57] Hsu, Y.Y., "On the size of range of active nucleation cavities on a heating surface," Trans.ASME J of Heat Transfer, vol.84, p.207 (1962)

[58] Collier, J.G., Convective Boiling and Condensation, p.126, McGraw-Hill, New York (1982)

[59] Bergles, A.E., and Rohsenow, W.M., "The determination of forced convection surface-boiling heat transfer," J. of Heat Transfer, vol.86, pp.365-372 (1964)

[60] Frost, W., and Dzakowic, G.S., "An extension of the method for predicting incipient boiling on commercially

finished surfaces," ASME paper No.67-HT-61 (1967)

[61] Hsu, Y.Y., "On the size range of active nucleation cavities on a heating surface," J. of Heat Transfer, vol.84, No.3, August, pp.207-216 (1962)

[62] Cochran, T.H., and Aydelott, J.C., and Frysinger, T.C., "The effect of subcooling and gravity level on boiling in the discrete bubble region," NASA TND-3449 (1966)

[63] Laufer, J., "The structure of turbulence in fully developed pipe flow," NACA TR-1174 (1954)

BIOGRAPHICAL SKETCH

Masaki Misawa was born on May 1, 1962, the second child of four to Kiyoo and Kayoko Misawa in Yamagata Prefecture, Japan. He spent his youth in Yamagata city, an agricultural center of north-east Japan. He graduated from Yamagata East High School in 1980. He entered the University of Tokyo where he earned his B.S. degree in aerospace engineering in March, 1984. Upon completion of B.S. degree, he entered the graduate school at the University of Tokyo and received M.S. degree from the Department of Nuclear Engineering in March, 1986. After attending the Ph.D program in nuclear engineering until July, 1988, he joined the Department of Nuclear Engineering Sciences at the University of Florida, Gainesville, as a research assistant. He was awarded a 1988 Rotary International Scholarship. He is a member of Alpha Nu Sigma honorary society and a student member of the American Nuclear Society.

I certify that I have read this study and that in my opinion it conforms to acceptable standards of scholarly presentation and is fully adequate, in scope and quality, as a dissertation for the degree of Doctor of Philosophy.

Samim Anghaie

Samim Anghaie, Chair
Professor of Nuclear Engineering
Sciences

I certify that I have read this study and that in my opinion it conforms to acceptable standards of scholarly presentation and is fully adequate, in scope and quality, as a dissertation for the degree of Doctor of Philosophy.

Nils J. Diaz
Professor of Nuclear Engineering
Sciences

I certify that I have read this study and that in my opinion it conforms to acceptable standards of scholarly presentation and is fully adequate, in scope and quality, as a dissertation for the degree of Doctor of Philosophy.

Edward T Dugan

Edward T. Dugan
Associate Professor of Nuclear
Engineering Sciences

I certify that I have read this study and that in my opinion it conforms to acceptable standards of scholarly presentation and is fully adequate, in scope and quality, as a dissertation for the degree of Doctor of Philosophy.

Calvin C. Oliver

Calvin C. Oliver
Professor of Mechanical
Engineering

I certify that I have read this study and that in my opinion it conforms to acceptable standards of scholarly presentation and is fully adequate, in scope and quality, as a dissertation for the degree of Doctor of Philosophy.

James F. Klausner

James F. Klausner
Assistant Professor of
Mechanical Engineering

I certify that I have read this study and that in my opinion it conforms to acceptable standards of scholarly presentation and is fully adequate, in scope and quality, as a dissertation for the degree of Doctor of Philosophy.

Jean Casagrande
Professor of Linguistics

This dissertation was submitted to the Graduate Faculty of the College of Engineering and to the Graduate School and was accepted as partial fulfillment of the requirements for the degree of Doctor of Philosophy.

August 1993

for
Winfred M. Phillips
Dean, College of Engineering

Dean, Graduate School